

**THE SYNTHESIS AND THE PHOTOPHYSICAL PROPERTIES OF NEW HETEROMETALLIC  
PLATINUM(II)-IRIDIUM(III) COMPLEXES AND THEIR POLYMERS**

par

**Ahmed M. Soliman**

Mémoire présenté au département de chimie en vue  
de l'obtention du grade de maître ès sciences (M.Sc.)

FACULTÉ DES SCIENCES  
UNIVERSITÉ DE SHERBROOKE

Sherbrooke, Québec, Canada, February, 2012

**THE SYNTHESIS AND THE PHOTOPHYSICAL PROPERTIES OF NEW HETEROMETALLIC  
PLATINUM(II)-IRIDIUM(III) COMPLEXES AND THEIR POLYMERS**

by

**Ahmed M. Soliman**

Thesis submitted to the Chemistry Department as a part of  
the fulfillment required to the Masters degree (M.Sc.)

FACULTÉ DES SCIENCES  
UNIVERSITÉ DE SHERBROOKE

Sherbrooke, Québec, Canada, February, 2012

*To My Parents, I Love you.*

*To my sister Hanan and my brother Wael, you are my everything.*

*Research is converging on the conclusion that great accomplishment, and even what we call genius, is typically the results of years of passion and dedication and not something that flows naturally from a gift. Hard work and discipline contribute much more to science achievement than IQ does.*

C.S. Dweck

*If you want to conquer the ocean and reach out for new continents don't tell your men to get wood and nails to build a ship, just instill in them the yearning for the expanse of the seas and distant lands.*

Antoine de Saint-Exupery

## ABSTRACT

Platinum(II) and charged cationic iridium(III) complexes have attracted great interest as luminophores in a myriad of applications. Notably, each class of these complexes has been incorporated into organic light emitting diodes (OLEDs), light-emitting electrochemical cells (LEECs), nonlinear optical materials and photovoltaic devices. This thesis reports the synthesis of hybrid Pt-Ir-containing organometallic complexes and polymers with the goal of obtaining high performance luminophores for electroluminescent devices. As a first step towards the polymer construction, the synthesis of a series of homometallic and heterometallic monomeric complexes has been performed. A survey of the synthesis and detailed photophysical characterization of the polymer and their model monomers are reported. Comparison of the spectroscopic signature of the complexes state are hybrids between the metal-to-ligand charge transfer ( $^1\text{MLCT}$  and  $^3\text{MLCT}$ ) of the  $[\text{Ir}(\text{bpy})(\text{ppy})_2]^+$  and  $[\textit{trans}\text{-Pt}(\text{CCAr})_2(\text{PBu}_3)_2]$  chromophores. This conclusion is supported by computational studies, DFT (density functional theory) and TDDFT (time-dependent density functional theory).

## ABSTRACT

Les complexes de platine(II) et les complexes cationiques d'iridium(III) présentent un grand intérêt en tant que luminophores dans une myriade d'applications. Chacun de ces types de complexes ont notamment été incorporé dans des diodes organiques émettrices de lumière (OLEDs), cellules électrochimiques émettrices de lumière (LEECs), matériaux optique non linéaire et appareils photovoltaïques. Cette thèse rapporte la synthèse de complexes organométalliques contenant des hybrides Pt-Ir et des polymères ayant pour but d'obtenir des luminophores de hautes performances pour des appareils d'électroluminescence. Comme première étape vers la construction de polymère, la synthèse d'une série de complexes monomériques homométalliques et hétérométalliques a été effectuée. La revue de synthèse et la caractérisation des détails photophysiques des polymères et de leur modèle monomérique ont été rapportées. La signature spectroscopique des états complexes sont des hybrides entre transfert de charges de métal à ligand ( $^1\text{MLCT}$  and  $^3\text{MLCT}$ ) des chromophores  $[\text{Ir}(\text{bpy})(\text{ppy})_2]^+$  et  $[\textit{trans}\text{-Pt}(\text{CCAr})_2(\text{PBU}_3)_2]$ . Cette conclusion est supportée par étude computationnelle, DFT (théorie des fonctions de densité) et TDDFT (théorie des fonctions de densité dépendante du temps).

## ACKNOWLEDGEMENT

Profs. Eli Zysman-Colman and Pierre D. Harvey, I can't thank you enough for everything you did for me in the two years and a half of my M.Sc. studies. I am grateful for your guidance, generosity and emotional support. I have found all your advices to be relevant and impactful. I do really appreciate how patient you were. Thanks for always being available. You helped me to adore the scientific research and I am grateful for the career change that you assist me to track.

Thank you to my father, Dr. A. Moez. You are always there when I needed you and patiently listening to all my worries and stresses. Grateful thanks to my mother. I was enthusiastic every day at work to succeed and make you proud of what I achieved one day. To my sister Hanan, the sweetest girl I have ever seen and the closest to me. My brother Wael, the fastest guitarist I have ever played with and who inspired me to start playing drums, I do miss you much.

A special thanks to all my colleagues. I would like to start with Sébastien, an amazing researcher with leadership ability, and a very close friend on the personal side. Thanks for teaching me synthesis and photophysics. Your support either personally or professionally was endless. You gave more than what you get and I owe you a lot in my life. A special thanks to Gabriel, we shared a lot of great conversations together. I would never forget our journey to Quebec City to attend the big music show together. I wish you great success in your future. A sincere thanks to Lisa for the funny time we spent in the lab and for supporting my goals especially in the first year and a half of my masters. Thanks Etienne, I was fortunate to have such an amazing friend like you. I would like also to thank Celine for the nice British music that she used to put in the lab, Loic, for being such a close friend and for making life more pleasurable, Clarisse, Anissa, Maxime, Shawn, Gabrielle and Simon.

Many thanks to Dr. Shawkat Aly and Bin Du for their photophysics teachings, Simon Lamare and Tommy Kenny for their synthesis advices, Antony for being an amazing friend and encouraging me to learn French, Antoine for the awesome times we had and the music we shared, Peng Lu and Adam for the funny time in the lab. Special thanks go to Mohammed. Unfortunately, I only spent two great sessions with you, but I hope you a huge success in your masters.

In the chemistry department, I am grateful to all professors, especially Profs. Claude Spino and Armand Soldera for their advices, all the students and friends and all the professionals and technicians. I would have a special thank to Dr. Daniel Fortin for the DFT computations, Dr. René Gagnon for the mass spectrometry analysis and Dr. Jean-Marc for his advice during the course of my M.Sc. work.

Finally, thanks to the Université de Sherbrooke for having admitted me to the M.Sc. program and to the CQMF (centre québécois sur les matériaux fonctionnels), FQRNT (fonds de recherché sur la nature et les technologies) and the CEMOPUS (Centre d'Excellence sur les Matériaux Optiques et Photoniques de l'Université de Sherbrooke) for their financial support which is absolutely essential for such research.



# TABLE OF CONTENT

ABSTRACT	v
ACKNOWLEDGMENT	vii
TABLE OF CONTENT	ix
LIST OF ABBREVIATIONS	xi
LIST OF FIGURES	xii
LIST OF TABLES	xv
LIST OF SCHEMES	xvi
LIST OF EQUATIONS	xvii
INTRODUCTION	1
<b>I.1</b> Thesis layout	3
<b>I.2</b> Multi-metallic complexes	5
<b>I.2.1</b> Pt containing multi-metallic complexes	5
<b>I.2.2</b> Ir containing complexes	11
<b>I.2.3</b> Ir and Pt complexes	15
<b>I.3</b> Organometallic polymers	17
<b>I.3.1</b> Pt containing organometallic polymers	18
<b>I.3.2</b> Ir containing organometallic polymers	21
<b>I.3.3</b> Ir- Pt-containing organometallic polymers	24
<b>I.4</b> THEORY	27
CHAPTER 1: SYNTHESIS	35
<b>1.1</b> Synthesis of the bipyridine ligand	35
<b>1.2</b> Synthesis of Pt complexes and Pt containing polymer	39
<b>1.3</b> Synthesis of Pt-Ir model complexes and Pt-Ir containing polymers	44
CHAPTER 2: PHOTOPHYSICS AND DFT CALCULATIONS	47
<b>2.1</b> Photophysical properties of Ir complexes	48
<b>2.2</b> Photophysical properties of Pt complexes	51
<b>2.3</b> Photophysical properties of Pt-Ir-containing complexes	55
<b>2.4</b> Comparison of the photophysical properties of Pt, Ir and Pt-Ir complexes	58

2.5 Comparison of the photophysical Properties of monomers (31, 22, 34, ) and polymers (24 and 35)	62
2.6 DFT calculations	68
GENERAL CONCLUSION	83
REFERENCES	85
EXPERIMENTAL SECTION AND REFERENCES	90
ANNEX 1: SPECTRA OF NUCLEAR MAGNETIC RESONANCE OF PROTONS	112
ANNEX 2: SPECTRA OF NUCLEAR MAGNETIC RESONANCE OF CARBONS	135
ANNEX 3: SPECTRA OF NUCLEAR MAGNETIC RESONANCE OF PHOSPHORE	155

## LIST OF ABBREVIATIONS

<b>ACN</b>	Acetonitrile
<b>Bpy</b>	2,2'-Bipyridine
<b>CT</b>	Charge transfer
<b>DCM</b>	Dichloromethane
<b>DFT</b>	Density field theory
<b>Dpp</b>	2,3-bis(2-pyridyl)pyrazine
<b>Equiv.</b>	Equivalent
<b>GCMS</b>	Gas chromatography coupled with mass spectrometer
<b>HOMO</b>	Highest occupied molecular orbital
<b>HRMS</b>	High resolution mass spectrometer
<b>HSOMO</b>	Highest semi-occupied molecular orbital
<b>ILCT</b>	Intra-ligand charge transfer
<b>Ir</b>	Iridium
<b>LC</b>	Ligand centered
<b>LRMS</b>	Low resolution mass spectrometer
<b>LUMO</b>	Lowest unoccupied molecular orbital
<b>MLCT</b>	Metal-to-ligand charge transfer
<b>μs</b>	Microsecond
<b>NMR</b>	Nuclear magnetic resonance
<b>ns</b>	Nanosecond
<b>OLED</b>	Organic light emitting diode
<b>Phen</b>	Phenanthroline
<b>Ppy</b>	2-Phenylpyridine
<b>Pt</b>	Platinum
<b>TDDFT</b>	Time-dependent density field theory
<b>Terpy</b>	Terpyridine
<b>TMS</b>	Trimethylsilane

## LIST OF FIGURES

<b>Figure A.1.</b> Structures of the Zeise's salt ( <b>1</b> ) and Cacodyl compound ( <b>2</b> ).	1
<b>Figure I.1.</b> Structure of several Pt(II) and Fe(II) complexes reported by R. Ziessel.	5
<b>Figure I.2.</b> Comparison of the absorption spectra of <b>3-5</b> in DMF at room temperature.	6
<b>Figure I.3.</b> Complexes bearing Pt(II), Ru(II) and Re(III).	6
<b>Figure I.4.</b> Comparison of the absorption spectra of <b>7</b> and <b>12</b> (left) and <b>7</b> and <b>13</b> in ACN at room temperature.	8
<b>Figure I.5.</b> Structures of the Polypyridyl Pt complexes reported by Ziessel and Castellano	8
<b>Figure I.6.</b> Structures of the Pt <sub>3</sub> Fe and Pt <sub>3</sub> Zn complexes reported by Ziessel and Castellano.	9
<b>Figure I.7.</b> The changes in emission spectra of <b>14</b> upon addition of Fe(II) ( <b>a</b> ) and Zn(II) ( <b>b</b> ).	10
<b>Figure I.8.</b> Ru(II) or Os(II) containing Pt complexes	11
<b>Figure I.9.</b> The structures of <b>22-26</b> reported by Williams and illustration of the charge transfer process in <b>22</b> and <b>23</b> .	11
<b>Figure I.10.</b> Structure of the polymetallic complexes <b>25</b> and <b>26</b> .	12
<b>Figure I.11.</b> Photo-induced energy transfer processes occurring in the Ru(II) and Os(II) based complexes.	13
<b>Figure I.12.</b> Structure of complex PH <sub>2</sub> (D)-Ir (A <sub>1</sub> )-PAu (A <sub>2</sub> ) ( <b>27</b> ) with the direction of the photo-induced charge transfer.	14
<b>Figure I.13.</b> Structures of Pt and Ir complexes.	15
<b>Figure I.14.</b> Comparison of the absorption spectra of <b>28-32</b> in CH <sub>2</sub> Cl <sub>2</sub> at room temperature.	16
<b>Figure I.15.</b> Comparison of the emission spectra at 298K in CH <sub>2</sub> Cl <sub>2</sub> ( <b>a</b> ) and 77K in diethyl ether/isopentane/ ethanol (2:2:1 v/v) ( <b>b</b> ) of <b>28-32</b> .	16
<b>Figure I.16:</b> Structures of the Pt complex <b>33</b> and polymer <b>34</b> .	18
<b>Figure I.17.</b> General structure of cyclometalated Pt polymers <b>35a</b> and <b>35b</b> .	19
<b>Figure I.18.</b> General structure of polymers <b>36a</b> and <b>36b</b> .	20
<b>Figure I.19.</b> Classes of Ir(III)-containing polymers.	21
<b>Figure I.20.</b> General structure of polymers <b>36a</b> and <b>36b</b> .	21
<b>Figure I.21.</b> General structure of Ir(III) polymer <b>38</b> .	22
<b>Figure I.22.</b> Structure of the Ir(III)-containing polymer <b>39</b> .	23
<b>Figure I.23.</b> Structure of charged Ir(III)-containing polymer <b>40</b> .	24
<b>Figure I.24.</b> Absorption and emission of the complexes <b>41</b> , <b>42</b> , <b>43</b> and <b>44</b> at 298K in CH <sub>2</sub> Cl <sub>2</sub> .	26

<b>Figure 1.25.</b> Energy level diagram illustrating the radiative and the non-radiative processes.	28
<b>Figure 1.26.</b> Schematic representation of the various radiative and non-radiative rate constants transitions implied in the quantum yield and emission lifetime calculations.	29
<b>Figure 1.27.</b> (a) Potential energy diagram for a diatomic molecule illustrating the Franck-Condon excitation. (b) Intensity distribution among vibronic bands as determined by the Franck-Condon principle.	32
<b>Figure 1.28.</b> 298K (A) and 77 K (B) absorption spectrum showing the removal of the hot bands.	33
<b>Figure 1.1.</b> Structures of the target bipyridine ligands <b>5</b> and <b>10</b> .	34
<b>Figure 1.2.</b> Structures of the Pt complexes <b>16</b> , <b>20</b> and <b>22</b> .	39
<b>Figure 1.3.</b> <sup>1</sup> H NMR spectra between <b>15</b> and <b>16</b> complexes in CDCl <sub>3</sub> .	40
<b>Figure 1.4.</b> Structure of the polymer reported by Schanze and collaborators.	43
<b>Figure 1.5.</b> Synthesis and GPC results for polymer <b>24</b> .	43
<b>Figure 1.6.</b> Structures of the Ir complexes <b>27</b> and <b>28</b> and Pt-Ir complex <b>29</b> .	44
<b>Figure 1.7.</b> Synthesis and GPC results of Pt-Ir polymer <b>35</b> .	46
<b>Figure 1.8.</b> GPC trace of Pt-Ir polymer <b>35</b> .	46
<b>Figure 2.1.</b> Absorption spectra of complexes <b>30</b> , <b>31</b> and <b>36</b> in 2-MeTHF at 298K.	48
<b>Figure 2.2.</b> Emission spectra of <b>30</b> , <b>31</b> and <b>36</b> in 2-MeTHF at 298K.	49
<b>Figure 2.3.</b> Emission spectra of <b>30</b> , <b>31</b> and <b>36</b> in 2-MeTHF at 77K.	50
<b>Figure 2.4.</b> Structure of complex <b>37</b> characterized photophysically by Schanze et al.	51
<b>Figure 2.5.</b> Absorption spectra of complexes <b>16</b> , <b>20</b> and <b>22</b> in 2-MeTHF at 298 K.	52
<b>Figure 2.6.</b> Emission spectra of <b>16</b> , <b>20</b> and <b>22</b> in 2-MeTHF at 298K.	53
<b>Figure 2.7.</b> Emission spectra of <b>16</b> , <b>20</b> and <b>22</b> in 2-MeTHF at 77K.	53
<b>Figure 2.8.</b> Absorption spectra of Pt-Ir-containing complexes in 2-MeTHF at 298 K.	55
<b>Figure 2.9.</b> Emission spectra of compounds <b>32-34</b> in 2-MeTHF at 298K.	56
<b>Figure 2.10.</b> Emission spectra of compounds <b>32-34</b> in 2-MeTHF at 77K.	57
<b>Figure 2.11.</b> Structures of the complexes described in this section.	58
<b>Figure 2.12.</b> Absorption spectra of <b>16</b> , <b>20</b> , <b>30</b> , <b>32</b> , <b>33</b> , and <b>36</b> in 2-MeTHF at 298K.	59
<b>Figure 2.13.</b> Emission spectra of <b>16</b> , <b>20</b> , <b>30</b> , <b>32</b> , <b>33</b> , and <b>36</b> in 2-MeTHF at 298K.	60
<b>Figure 2.14.</b> Emission spectra of <b>16</b> , <b>20</b> , <b>30</b> , <b>32</b> , <b>33</b> , and <b>36</b> in 2-MeTHF at 77K.	61
<b>Figure 2.15.</b> Structure of the complexes described in this section.	62
<b>Figure 2.16.</b> Comparison of the absorption spectra of <b>22</b> , <b>24</b> , <b>31</b> , <b>34</b> and <b>35</b> in 2-MeTHF at 298 K.	63
<b>Figure 2.17.</b> Comparison of the emission spectra of <b>22</b> , <b>24</b> , <b>31</b> , <b>34</b> and <b>35</b> in 2-MeTHF at 298K.	64

<b>Figure 2.18.</b> Comparison of the emission spectra of <b>22</b> , <b>24</b> , <b>31</b> , <b>34</b> and <b>35</b> in 2-MeTHF at 77K.	65
<b>Figure 2.19.</b> Structure of the Pt-containing polymer studied by Schanze <i>et al.</i>	66
<b>Figure 2.20.</b> Representations of the frontier MOs <b>28</b> and <b>27</b> along with calculated energies (eV) for each.	69
<b>Figure 2.21.</b> Calculated (blue) and experimental (red) absorption spectra for <b>28</b> . The calculated spectrum appears as a form of bars for the 0-0 transitions by assigning 1000 cm <sup>-1</sup> for each bar.	71
<b>Figure 2.22.</b> Calculated (blue) and experimental (red) absorption spectra for <b>27</b> . The calculated spectrum appears as a form of bars for the 0-0 transitions by assigning 1000 cm <sup>-1</sup> for each bar.	72
<b>Figure 2.23.</b> Representations of the frontier MOs of <b>20</b> and <b>22</b> along with calculated energies (eV) for each.	73
<b>Figure 2.24.</b> Calculated (blue) and experimental (red) absorption spectra for <b>20</b> . The calculated spectrum appears as a form of bars for the 0-0 transitions by assigning 1000 cm <sup>-1</sup> for each bar.	76
<b>Figure 2.25.</b> Calculated (blue) and experimental (red) absorption spectra for <b>22</b> . The calculated spectrum appears as a form of bars for the 0-0 transitions by assigning 1000 cm <sup>-1</sup> for each bar.	76
<b>Figure 2.26.</b> Representations of the frontier MOs of <b>32</b> , <b>33</b> and <b>34</b> along with calculated energies (eV) for each.	77
<b>Figure 2.27.</b> Calculated (blue) and experimental (red) absorption spectra for <b>32</b> . The calculated spectrum appears as a form of bars for the 0-0 transitions by assigning 1000 cm <sup>-1</sup> for each bar.	80
<b>Figure 2.28.</b> Calculated (blue) and experimental (red) absorption spectra for <b>33</b> . The calculated spectrum appears as a form of bars for the 0-0 transitions by assigning 1000 cm <sup>-1</sup> for each bar.	81
<b>Figure 2.29.</b> Calculated (blue) and experimental (red) absorption spectra for <b>34</b> . The calculated spectrum appears as a form of bars for the 0-0 transitions by assigning 1000 cm <sup>-1</sup> for each bar.	81
<b>Figure 2.30.</b> Pentanuclear complex <b>36</b> .	84
<b>Figure 2.31.</b> New series of fluorinated complexes <b>37</b> , <b>38</b> , <b>39</b> and <b>40</b> .	84

## LIST OF TABLES

<b>Table I.1.</b> Photophysics of the Pt complex <b>33</b> and polymer <b>34</b> .	19
<b>Table 1.1.</b> Optimization of <b>15</b> and <b>16</b> yields upon using different equiv. of <i>trans</i> Pt(PBu <sub>3</sub> ) <sub>2</sub> Cl <sub>2</sub> .	40
<b>Table 2.1</b> Photophysical properties of Ir complexes.	51
<b>Table 2.2.</b> The calculation of the energy difference between the peak and shoulder positions in the emission spectra of <b>16</b> , <b>20</b> and <b>22</b> in 2-MeTHF at 298 K.	54
<b>Table 2.3.</b> Photophysical properties for complex <b>37</b> .	54
<b>Table 2.4.</b> Photophysical properties of complexes <b>16</b> , <b>20</b> and <b>22</b> .	55
<b>Table 2.5.</b> Photophysical properties of the Pt-Ir-containing complexes.	57
<b>Table 2.6.</b> Photophysical properties of compounds <b>16</b> , <b>20</b> , <b>30</b> , <b>32</b> , <b>33</b> , and <b>36</b> .	61
<b>Table 2.7.</b> Photophysical properties of <b>22</b> , <b>24</b> , <b>31</b> , <b>34</b> and <b>35</b> .	65
<b>Table 2.8.</b> Photophysical properties of all complexes and polymers investigated in this chapter.	66
<b>Table 2.9.</b> Energy and composition of TD-DFT calculated transitions of <b>28</b> .	70
<b>Table 2.10.</b> Energy and composition of TD-DFT calculated transitions of <b>27</b> .	71
<b>Table 2.11.</b> Energy and composition of TD-DFT calculated transitions of <b>20</b> .	74
<b>Table 2.12.</b> Energy and composition of TD-DFT calculated transitions of <b>22</b> .	75
<b>Table 2.13.</b> Energy and composition of TD-DFT calculated transitions of <b>32</b> .	78
<b>Table 2.14.</b> Energy and composition of TD-DFT calculated transitions of <b>33</b> .	79
<b>Table 2.15.</b> Energy and composition of TD-DFT calculated transitions of <b>34</b> .	79

## LIST OF SCHEMES

<b>Scheme I.1.</b> Synthesis of Pt-Ir polymer.	4
<b>Scheme I.2.</b> Synthesis of the mixed-metal Ir(III) and Pt(II) organometallic polymers.	25
<b>Scheme 1.1.</b> Retrosynthesis of Pt-Ir polymer ( <b>35</b> ).	34
<b>Scheme 1.2.</b> Synthesis of 5,5'-dibromo-2,2'-bipyridine via a Stille-Kelley coupling reaction.	35
<b>Scheme 1.3.</b> Synthesis of 5,5'-dibromo-2,2'-bipyridine ( <b>13</b> ) using Br <sub>2</sub> .	35
<b>Scheme 1.4.</b> A trial to obtain 5,5'-diethynyl-2,2'-bipyridine from 2,5 dibromopyridine <b>1</b> .	36
<b>Scheme 1.5.</b> The formation of <b>5</b> starting from 2,5 dibromopyridine <b>1</b> .	37
<b>Scheme 1.6.</b> Synthesis of 5,5'-diethynyl-2,2'-bipyridine ( <b>10</b> ) from 2,5 dibromopyridine ( <b>1</b> ).	38
<b>Scheme 1.7.</b> Synthesis of Pt complex <b>15</b> and <b>16</b> .	39
<b>Scheme 1.8.</b> Synthesis of 1-ethynyl-4-methylbenzene <b>19</b> .	41
<b>Scheme 1.9.</b> Synthesis of Pt complex <b>20</b> .	41
<b>Scheme 1.10.</b> The first method for the synthesis of complex <b>22</b> .	42
<b>Scheme 1.11.</b> Alternative synthesis of complex <b>22</b> .	42
<b>Scheme 1.12.</b> Synthesis of the precursor [(ppy) <sub>2</sub> IrCl] <sub>2</sub> dimer.	44
<b>Scheme 1.13.</b> Synthesis scheme for complexes <b>30-34</b> .	45



## LIST OF EQUATIONS

Equation 1	29
Equation 2	30
Equation 3	30
Equation 4	30
Equation 5	30
Equation 6	31
Equation 7	31
Equation 8	31
Equation 9	31

## INTRODUCTION

Organometallic chemistry is the study of chemical compounds containing at least one metal-carbon bonds. It is a sub-branch of inorganic coordination chemistry, although it also plays a major role in organic and materials chemistry. There are many applications of great importance for this area in chemistry. Some of the applications among others, include LED,<sup>1</sup> photovoltaic devices,<sup>2</sup> and chemical sensors.<sup>3</sup> It also plays an important role in other branches of chemistry such as biology.<sup>4,5</sup>

The metal-carbon bond in organometallic compounds is generally of character intermediate between ionic and covalent. They are very important in industry and relatively stable in solutions to undergo reactions.

The first transition metal organometallic compound to be discovered was Zeise's salt (**1**) in 1827 (Figure A.1).<sup>6</sup> However, it was not considered as the first because its structure was not known until the discovery of X-ray diffraction in the second half of the 19th century. Ten years later, Bunsen, a German chemist who was a pioneer in photochemistry and the discoverer of caesium (in 1860) and rubidium (in 1861), has studied in more details the nature and reactions of the first organometallic compound. It was Cacodyl (**2**).<sup>7</sup>

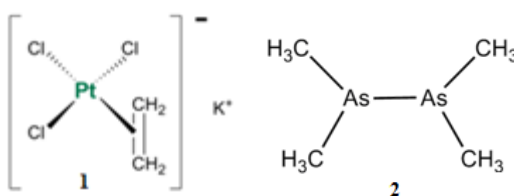


**Figure A.1.** Zeise's salt (**1**) and Cacodyl compound (**2**).

In 1849, the first organozinc compound was prepared.<sup>8</sup> The preparation of the first organomercury (Me<sub>2</sub>Hg)<sup>9</sup> and organolead materials (Et<sub>4</sub>Pb)<sup>10</sup> were reported in 1852 and 1853, respectively. In 1859 and 1863, organoaluminum<sup>11</sup> and organosilicon<sup>12</sup> compounds were prepared, respectively. Before the end of the 19<sup>th</sup> century, Ni(CO)<sub>4</sub><sup>13</sup> and Fe(CO)<sub>5</sub><sup>14</sup> were synthesized by Ludwig Mond by the direct reaction of the metal with CO.

Organometallic compounds can be also used in synthesis such as Grignard reagents. This reagent was discovered by the French Chemist and Nobel laureate Victor Grignard in 1900.<sup>15</sup> The reaction is an important means of preparing organic compounds from smaller precursor molecules.

In 1951, the discovery of ferrocene and its analogues was a breakthrough.<sup>17</sup> Ernst Fischer was sceptical of the iron nature of the proposed compound. He used X-ray diffraction to determine its true structure, in which two five-sided carbon rings sandwich a single iron. At that time, there was a steady stream of compounds being described in the literature combining metals and organic ligands, with novel structures, reactivities and applications in catalysis. Later on, he was able to isolate the first carbene<sup>18</sup> and carbyne<sup>19</sup> complexes in 1964 and 1973 respectively.

Among other achievements in organometallic chemistry was the elucidation of the structure of coenzyme vitamin B<sub>12</sub> by Dorothy Hodgkin, a British crystallographer.<sup>20</sup> Eleven years later; its total synthesis was reported by Robert Woodward.<sup>21</sup>

Organoplatinum compounds contain a carbon to platinum chemical bond. Its chemistry and that of organopalladium are somewhat similar, but organoplatinums are more stable and therefore less useful in catalysts. Zeise's salt was the first organoplatinum compound to be discovered.

Organoiridium compounds contain iridium-carbon chemical bonds. Iridium(III) is capable of forming a wide range of complexes, including mono-, bis- and tris-cyclometallated complexes. The latter is an interesting feature among all polyimine coordination complexes of the transition metals<sup>22</sup> and more complexes are known to be bidentate ligands than terdentate. Ir(bpy)<sub>3</sub><sup>3+</sup> was first described by Martin and collaborators in 1958.<sup>23</sup> The lack of a precise characterization at that time led Chiswell and his collaborators to reinvestigate the synthesis of [Ir(phen)<sub>3</sub>]<sup>3+</sup> in 1964 under similar conditions, although uncertainty remained regarding the purity of their end product.<sup>24</sup>

These types of Iridium(III) containing materials are phosphorescent and have wider range of applications in photovoltaics and electroluminescent devices such as OLEDs. They showed high efficiency in OLED devices, along with host material and fluorescent dye.<sup>25</sup>

## I.1 Thesis layout

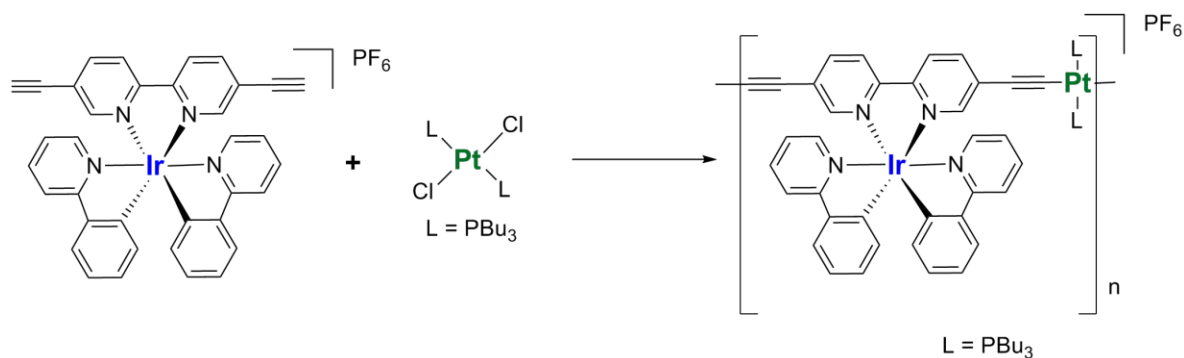
My main research work is lying under the branch of organometallic chemistry and uses a combination of organic and inorganic synthesis and coordination and materials' chemistries. Some analytical techniques such as absorption and emission spectroscopy have been used, in conjunction with theoretical calculations.

Iridium is one of the rarest elements in the Earth's crust, with annual production and consumption of only three tonnes.<sup>26</sup> Preparing new Ir(III) complexes is one of Ir applications and the scope of this project. These complexes have attractive photophysical and physicochemical profiles. These are the high quantum efficiencies, relatively short emission lifetimes and easily adjustable HOMO - LUMO energy gap. These properties made it one of the best choices as emissive molecules for electroluminescent devices.

Platinum is the chemical element with the chemical symbol Pt and an atomic number of 78. It is a dense, malleable, ductile, precious, gray-white transition metal. North Africa accounts for 80% of the production of this metal.<sup>27</sup> Complexes of Pt(II) coordinated by PBU<sub>3</sub> ligands as the *trans* isomer (Scheme I.1) were synthesized and photophysically characterized in this work. The *trans*-form appears to be more stable form. This trend was due to unfavourable steric interactions between the bulky phosphine ligands in the *cis*-form. When these complexes are coordinated to alkynes, high delocalization of the  $\pi$  electrons over the chain occurs. Also, the stability of this type of Pt complexes towards air, moisture,<sup>28a</sup> and high temperatures (over 200 C°),<sup>29</sup> and their good electrical conductivity<sup>28b</sup> are interesting features. The presence of long butyl chains connected to the phosphine is of great importance in the monomers and polymers solubility.<sup>30</sup>

This work concerns the study of hybrid charged Pt-Ir-containing monomers and polymers. As a first step towards the construction of new multi-metallic polymeric complexes (Scheme I.1), a covalent bond of an Ir(III) fragment onto the bis(ethynyl)bipyridine has been performed. Then by adding the *trans*-Pt(PBU<sub>3</sub>)<sub>2</sub>Cl<sub>2</sub> unit in a 1:1 ratio, the new polymeric complex containing both metals is now reported. In order to understand the photophysical behaviour of the polymer, monomers have also been synthesized and characterized photophysically. This structure using both metals is strongly luminescent and keeps the conjugation between them, and enables the charge transfer behaviour and

even tailors a hybrid excited state of the two moieties. Such hybrid excited state between Pt and Ir center is totally new.



**Scheme I.1.** Synthesis of Pt-Ir polymer.

The design of composite organometallic materials made of Ir(III) with another metal such as Pt(II) is rare. We can find no report of a polymer containing both metals in which the iridium complex unit is charged.<sup>31</sup> Besides the advantages of incorporating Pt(II) complexes that have been discussed above, studies shown the use of these cationic Ir (III) complexes in efficient red, green and blue electroluminescent devices.<sup>32</sup> A key challenge in these devices is to develop a design that has controlled color tuning without affecting the devices quantum efficiency. In our studies, the Ir(III) center is placed beside the main chain. The properties that result from incorporating these 2 metals in the monomers and along the polymers backbone, with their photophysical properties could have a great impact in photonic materials especially the one concerned with OLED.

This thesis comprises two chapters. Chapter one will report the synthesis and the characterization of organometallic monomers and polymers containing Pt, Ir and Pt-Ir units that have been successfully demonstrated during my M.Sc. studies. Chapter two deals with the photophysical studies of these complexes (Pt, Ir and Pt-Ir monomers and polymers) and supported by DFT computational studies.

## I.2 Multimetallic complexes

Alkynes have been demonstrated to be useful bridging ligands for the design of multicomponent architectures including multi-metallic complexes. This can occur by introducing a metal component through metal-acetylide  $\sigma$ -bonding. On the other hand, metal chelation may occur through pyridyl groups. In this section a review of some examples of Pt, Ir and Pt-Ir multi-metallic complexes and their photophysical properties is provided.

### I.2.1 Pt containing multi-metallic complexes

In 2006, Raymond Ziessel and collaborators reported the synthesis and preliminary photophysical properties of terpyridine–Pt(II) alkyne complexes bearing different appended moieties of terpyridines (Figure I.1).<sup>33</sup>

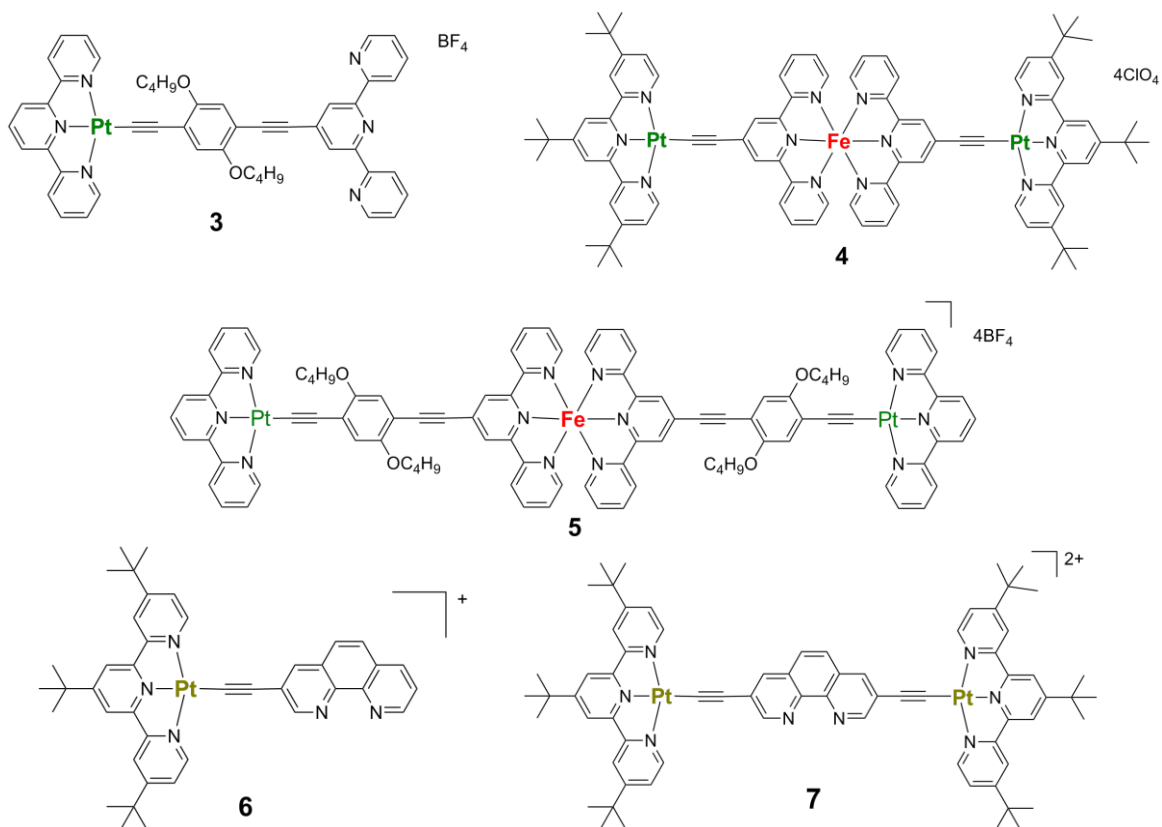


**Figure I.1.** Structure of several Pt(II) and Fe(II) complexes reported by R. Ziessel.<sup>33</sup>

Upon chelating **3** with Fe(II) to form **5**, the Pt  $^3$ MLCT band has shifted to high energy by 40 nm to 435 nm (Figure I.2). The new weak low energy band at 580-590 nm for **4** and **5** is attributed to Fe MLCT from the triplet state (i.e.  $^3$ MLCT).

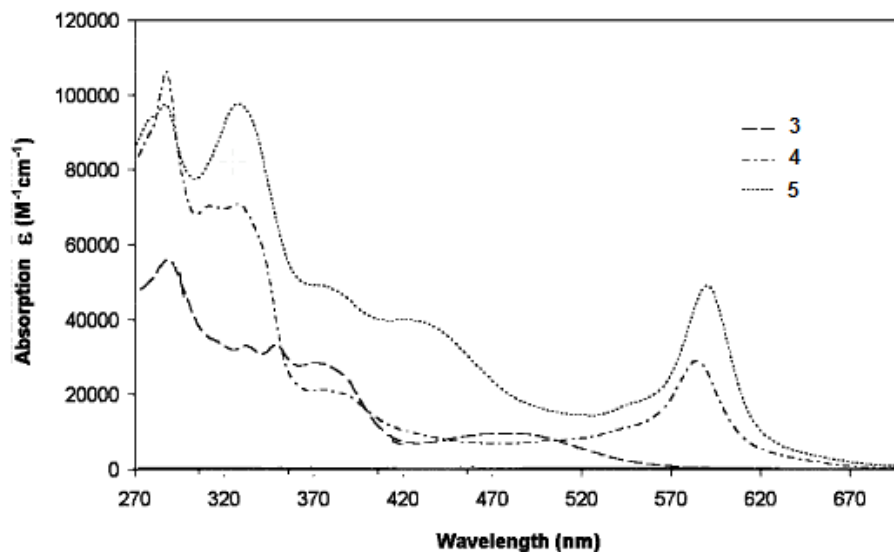


**Figure I.2.** Comparison of the absorption spectra of **3-5** in DMF at room temperature.<sup>33</sup>

In 2008, an interesting work has been published by Zhong-Ning Chen and co-workers that describes the photophysical properties of diads and triads made of Pt, Ru and Re subunits (Figure I.3).<sup>34</sup>

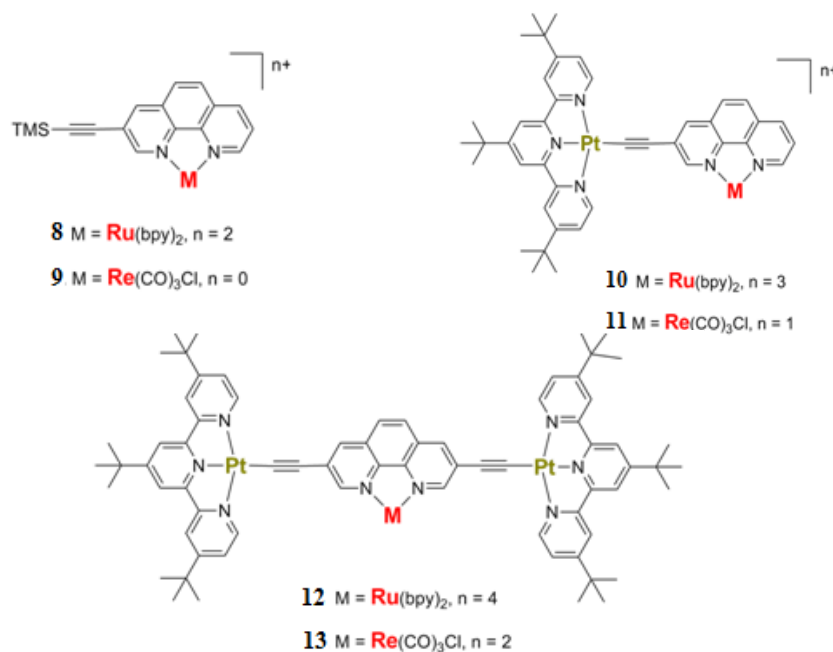


**Figure I.3.** Complexes bearing Pt(II), Ru(II) and Re(III).<sup>34</sup>

The absorption behaviour for all complexes shows that the bands associated with ligand-centered (LC) transitions are intense and located below 300 nm. The absorption band placed between 310 and 350 nm is assigned to acetylide  $\pi$ - $\pi^*$  transition. Lower energy bands observed in the 390-480 nm range arise from MLCT transitions where the metal-centered contribution is mixed with some ligand-to-ligand charge-transfer (LLCT) for Pt complexes.

The medium energy band placed between 310 and 350 nm for complexes **6** and **7** is stronger and red-shifted in **7** compared to **6** with a molar extinction coefficient of twice in the first ( $\epsilon = 6.85 \times 10^4 \text{ M}^{-1} \text{ cm}^{-1}$  vs  $3.64 \times 10^4 \text{ M}^{-1}$  compared to the latter). The  $^3\text{MLCT}$  band is more red-shifted in **7** (432 nm) than **6** (405 nm). On the other hand, the same band is more red-shifted in complexes **12** and **13** than **10** and **11**. The red shift in the diplatinum species **12** and **13** is due to the reduction of the energy gap between the HOMO and the LUMO and according to the Huckel molecular orbital theory,<sup>35</sup> the  $\pi$ -donor energy level of the ligand is raised in **12** and **13** compared to **10** and **11** and this will increase the energy level in  $d\pi(\text{Pt})$  orbital through  $p\pi$ - $d\pi$  overlap and as a result red shifting of the low energy band for the diplatinum species in comparison with that of the monometallic species is observed.<sup>36</sup> The MLCT absorption bands of the Pt complexes **6** and **7** is more blue-shifted than those for **8** (Ru) and **9** (Re). Similarly, the MLCT bands for the Pt-Ru complex **8** is more blue-shifted than that for Pt- or Ru-containing complexes **6-8**. Figure I.4 shows a comparison of the absorption spectra between **7** and **12** and **7** and **13** in ACN and at room temperature.

The emission lifetimes are in the sub microsecond range. The emission quantum yields are the lowest (0.3%) for the Re complex **8**, and the highest (6.6%) for the mixed-metal complex Pt-Ru-Pt **12**. Besides, the Ru complex **8** exhibits a higher emission quantum yield than that of the Re one (**9**). This is due to the more efficient intersystem crossing process populating the  $^3\text{MLCT}$  state of the Ru complex **8**.<sup>37</sup> Complexes **6** and **7** show maximum emissions between 530 and 560 nm. The dinuclear complex **7** exhibits a more red-shifted emission than that of the mono-platinum one **6**. This is due to the more extensive conjugation in **7** compared to **6**.



In the Pt-Ru and Pt-Ru-Pt complexes **10** and **12**, the luminescence arises from Ru center as the Pt centred emissions was quenched. This indicates a possibility of energy transfer from centred Pt  $^3\text{MLCT}$  excited state to the acceptor Ru one. Pt-Re complex **11** emits at  $\sim 600$  nm. The Pt-Re-Pt complex **13** exhibits a dual emission at 570 and 610 nm. Its emission lifetime is bi-exponential indicating 2 possible emissions from different triplet states. The energy transfer from the Pt unit to Re center is slower compared to that described for **10** and **12**, i.e from the Pt unit to the Ru one.

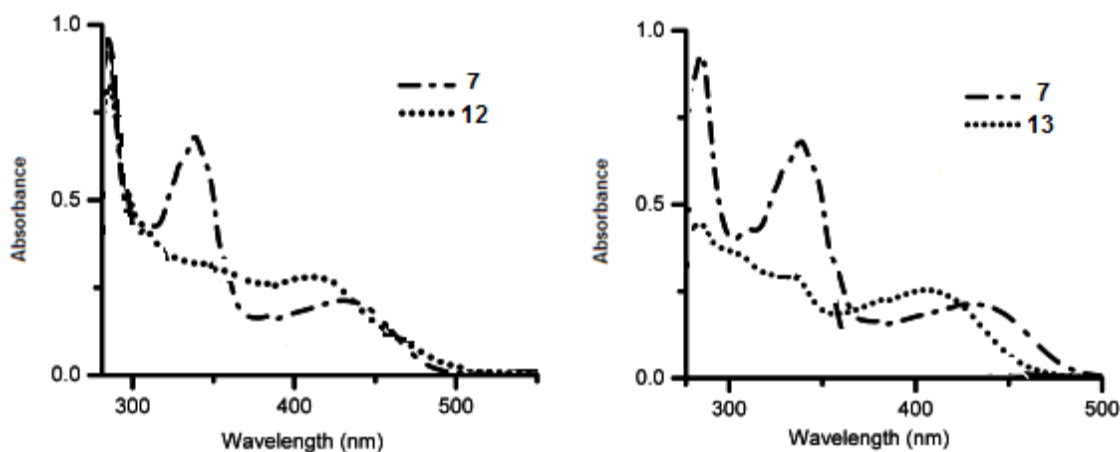


**Figure I.4.** Comparison of the absorption spectra of **7** and **12** (left) and **7** and **13** in ACN at room temperature.

In 2009, Ziessel and Castellano reported the synthesis and photophysics of mono- and tetranuclear Pt(II) polypyridyls when they are chelated to Fe(II) and Zn(II) metals.<sup>38</sup> For Pt(II) complex **14** in Figure I.5, the polypyridyls  $\pi\text{-}\pi^*$  transitions was observed between 250 and 350 nm. The CT (charge-transfer) band was found at  $\sim 430$  nm.

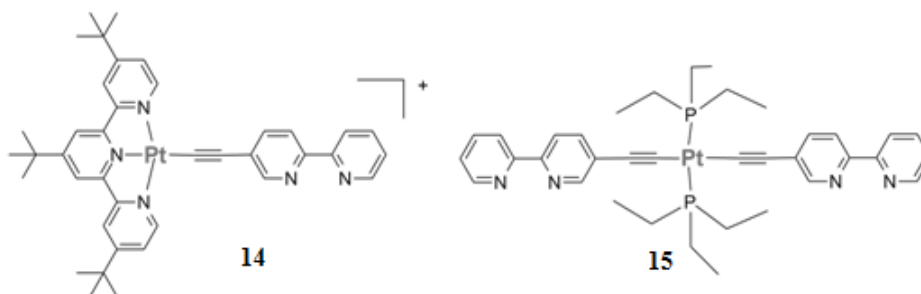


**Figure I.5.** Structures of the Polypyridyl Pt complexes reported by Ziessel and Castellano.<sup>38</sup>

The emission spectra of complex **14** in degassed  $\text{CH}_2\text{Cl}_2$  show a broad band at 575 nm with a 22% emission quantum yield and a lifetime of 5.8  $\mu\text{s}$ . The photoluminescence was quenched upon using  $\text{CH}_3\text{CN}$  instead of  $\text{CH}_2\text{Cl}_2$ . The photophysical properties of the Pt(II) complex bearing *trans* phosphines and bis(bipyridine)acetylide subunits, **15**, have been also studied.<sup>38</sup> The emission band exhibits a maximum at 520 nm with a shoulder at 555 nm. The emission lifetime is 26  $\mu\text{s}$ . The absence of charge-transfer band indicates that the emission arises from the ligand centered (LC) bipyridine-acetylide  $\pi\text{-}\pi^*$  band that might has less electronic communication with the Pt center.

Complex **14** has been titrated with  $\text{Fe}(\text{ClO}_4)_2$  and  $\text{Zn}(\text{ClO}_4)_2$  to afford complexes **16** and **17** (Figure I.6). The absorption and emission spectra were recorded each time upon addition of both metals and the titration was stopped when there were no more changes observed in the spectra. The absorption spectra show a new band at 542 nm upon the addition of Fe(II) through its chelation with bipyridine moiety along with 3 other bands at 332, 445 and 495 nm. The CT band of Pt(II) complex **14** is blue-shifted from 430 to 409 nm upon complexation. The emission band at 575 nm was quenched upon each addition of  $\text{Fe}(\text{ClO}_4)_2$  with the appearance of a residual peak 532 nm (Figure I.7 a).

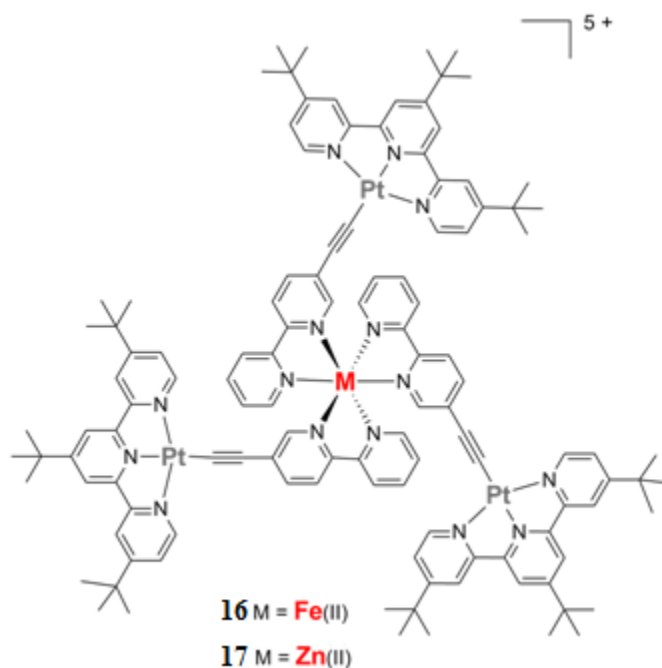


**Figure I.6.** Structures of the  $\text{Pt}_3\text{Fe}$  and  $\text{Pt}_3\text{Zn}$  complexes reported by Ziessel and Castellano.<sup>38</sup>

Addition of Zn(II) to the same complex **14** leads to a different results. The  $^3\text{MLCT}$  band is blue-shifted upon addition of Zn(II) compared to complex **14**. This shift maybe due to the Lewis acidity of Zn(II) that stabilizes the HOMO level.<sup>39</sup> The emission spectrum shows two emission bands, one is at 532 nm and the other band at 551 nm. The emission intensity increased upon addition of the metal, while the lower energy band decreased (Figure 1.7 b).

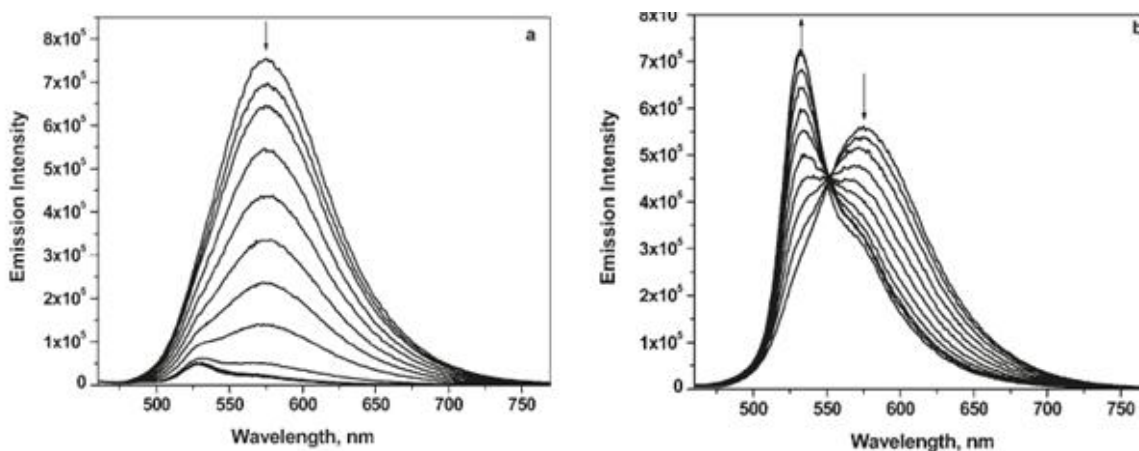


**Figure 1.7.** The changes in emission spectra of **14** upon addition of Fe(II) (a) and Zn(II) (b).<sup>38</sup>

The photophysical property investigations indicate that the absorption bands of complex **17** are more blue-shifted and its emission exhibits longer lifetimes and higher quantum yields compared to **16**. Furthermore, the emission has been quenched and increased upon the addition of  $\text{Fe}(\text{ClO}_4)_2$  and  $\text{Zn}(\text{ClO}_4)_2$  to Pt complex **14**, respectively.

In 1995, Raymond Ziessel and collaborators tested the charge transfer efficiency from the terminal Ru(II) donor to the acceptor Os(II) subunit with the absence of a Pt(II) center.<sup>40</sup> A year later, the same group synthesized triads in the form of Ru-Pt-Ru (**20**) and Os-Pt-Os (**21**), which are readily prepared in either the *cis*- or *trans*-configuration.<sup>41</sup>

These compounds are kinetically stable in solution and resistant to thermal- and light-induced isomerisation.

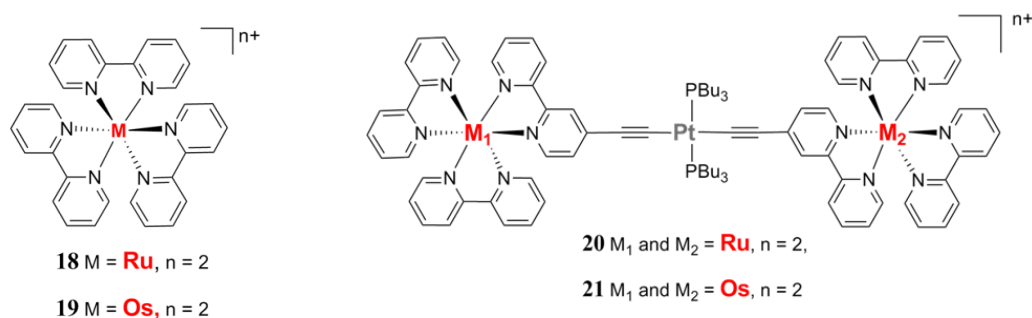


**Figure I.8.** Ru(II) or Os(II) containing Pt complexes.<sup>40</sup>

The absorption and emission bands of complex Ru-Pt-Ru **20** (Figure **1.8**) exhibit a small red-shift compared to those of the benchmark complex  $[\text{Ru}(\text{bpy})_3]^{2+}$  (**18**). This indicates that only minor spectral changes are induced by Pt(II) center. The other conclusion is that the Pt center does not quench the excited triplet <sup>3</sup>MLCT state of Ru sub-units. The same results have also been noted upon the use of Os(II) in complex Os-Pt-Os **21**, with also a 5 nm red shift in the latter compared to standard  $[\text{Os}(\text{bpy})_3]^{2+}$  (**19**).

### I.2.2 Ir containing complexes

In 2006, G. Williams and collaborators used palladium-catalysed Suzuki-type cross-coupling reaction to synthesize interesting complexes made of Ir(III) and Ru(II) (Figure **I.9**).<sup>42</sup>

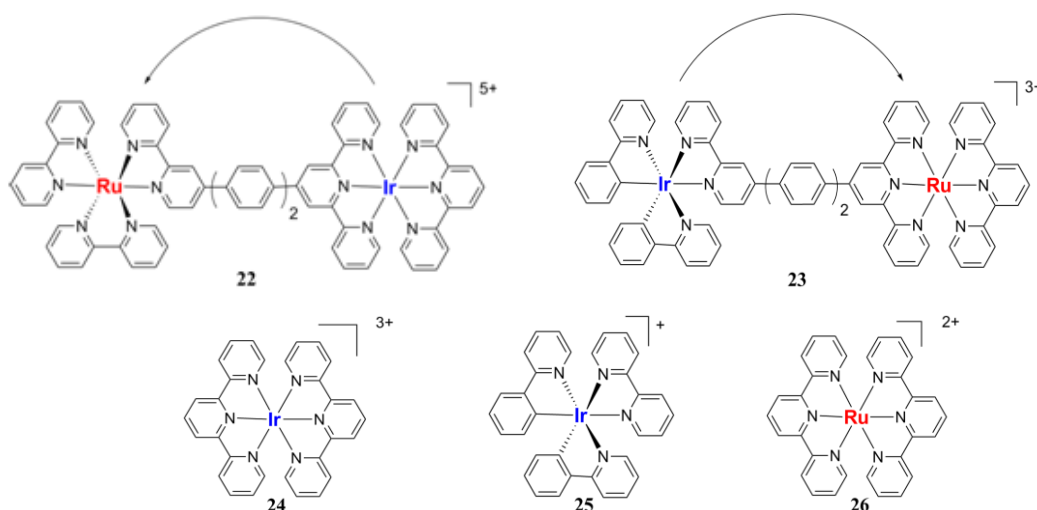


**Figure I.9.** The structures of **22-26** reported by Williams and illustration of the charge transfer process in **22** and **23**.<sup>42</sup>

The dimer complexes **22** and **23** show an absorption signature similar to the sum of individual metal complexes. This result indicates that the electronic communication between the fragments is minimal. The emission spectra for **22** shows the disappearance of the band associated with the Ir unit and the presence of Ru one. Moreover, both the Ru complex **18** and the dimer **22** shown in Figure **I.8** and **I.9** respectively, exhibit similar emission lifetimes of 1.6 and 1.3  $\mu\text{s}$ , respectively. The same result is noted for dimer **23**. These results indicate that there is an efficient charge transfer from Ir(III) fragment to Ru(II) unit.

Luisa De Cola and collaborators synthesized and characterized in detail the photophysics of a series of bimetallic Ir-Ru complexes that are separated by phenylene bridges ( $\text{ph}_n$ ).<sup>43</sup> The absorption spectra of  $[\text{Ir-ph}_n\text{-Ru}]^{3+}$  closely resembles the sum of the individual spectra of the mononuclear units of Ir and Ru containing species. This work also reports that the larger the number of phenylene bridges, the more red-shifted the emission is. Photo-induced electron transfer also occurs between the Ir(III) donor and Ru(II) acceptor.

In 1994, Serroni, Juris, Campagna and their coworkers investigated two tetranuclear bimetallic complexes containing an Ir(III) metal (Figure **I.10**).<sup>44</sup> These were obtained in ~70% yield from the reaction of  $[\text{Ir}(\text{ppy})_2\text{Cl}]_2$  with  $\text{M}(\text{dpp})_3^{2+}$  ( $\text{M} = \text{Ru}(\text{II}), \text{Os}(\text{II})$  and  $\text{dpp} = 2,3\text{-bis}(2\text{-pyridyl})\text{pyrazine}$ ) while refluxing in  $\text{CH}_2\text{Cl}_2$  for 2.5 h.

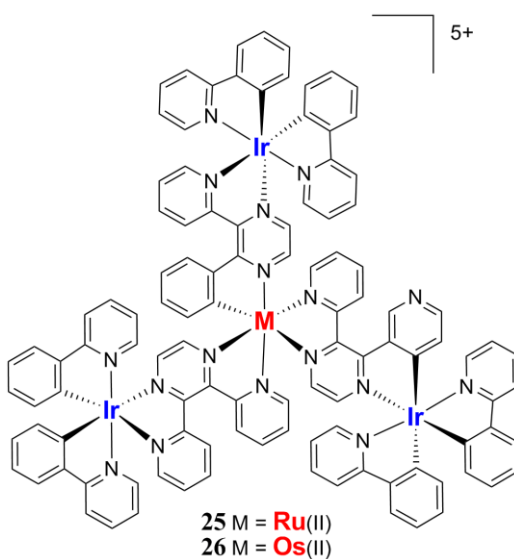


**Figure I.10.** Structure of the polymetallic complexes **25** and **26**.<sup>44</sup>

Both complexes exhibit strong  $^1\text{LC}$  absorption bands in the UV region and emission bands with maxima at 726 and 810 nm at 77K. These two bands are attributed to an emission arising from peripheral Ir(III) and Os(II) units, respectively. The emission quantum yields are low (less than 1% for both complexes).

For complex **25**, the central position is occupied by a  $\text{Ru}(\text{dpp})_3^{2+}$  unit. The absorption of a single photon by this chromophore results in the excitation being transferred to any one of the peripheral Ir fragments, which then emit.<sup>45</sup>

Conversely, a localised absorption at the Ir(III) antennas in **26** leads to a transfer of the excitation from them to the centre and the emission is always  $\text{Os}(\text{dpp})_3^{2+}$  based. These results are consistent with the known ordering of the emissive triplet state energy levels:  $\text{Ru}(\text{dpp})_3^{2+} > (\text{dpp})\text{Ir}(\text{ppy})_2^+ > \text{Os}(\text{dpp})_3^{2+}$ .<sup>45</sup> The direction of the charge transfer processes is illustrated at Figure **1.11**.

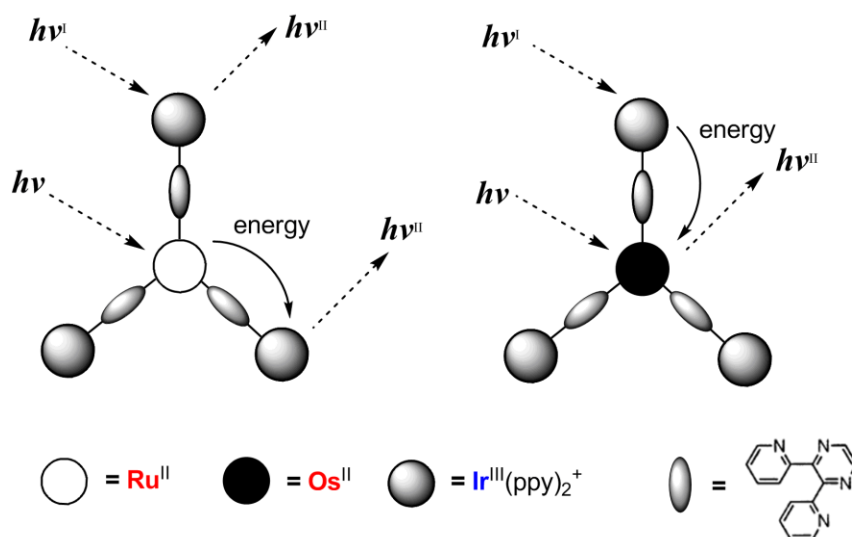


**Figure I.11.** Photo-induced energy transfer processes occurring in the Ru(II) and Os(II) based complexes.<sup>45</sup>

The construction of multiporphyrin with  $[\text{Ir}(\text{terpy})_2]^{3+}$  has been performed in 2000.<sup>46</sup> Free-base porphyrin ( $\text{PH}_2$ ) is the primary electron donor (D), Ir(III) is the first electron acceptor (**A1**) and Au(III) porphyrin ( $\text{Pau} = \text{A2}$ ) is the secondary electron acceptor (Figure **I.12**).

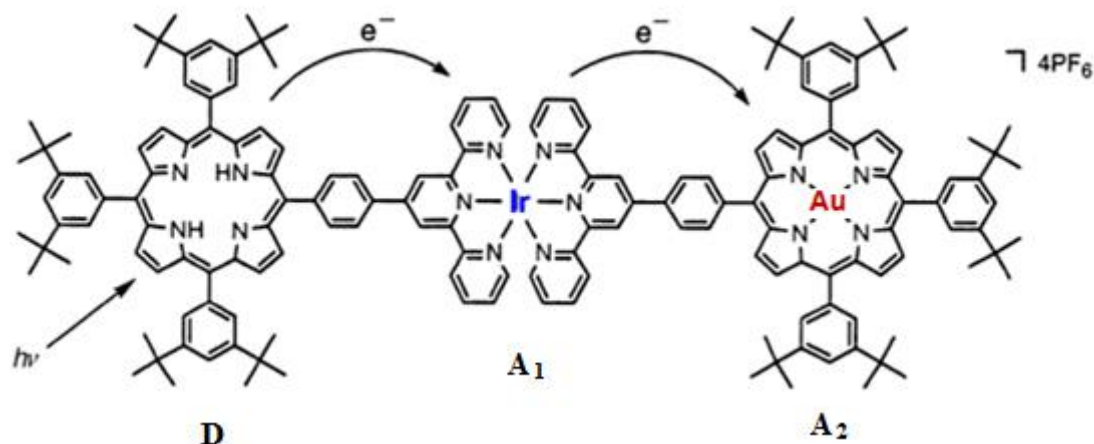


**Figure I.12.** Structure of complex  $\text{PH}_2(\text{D})\text{-Ir}(\text{A}_1)\text{-PAu}(\text{A}_2)$  (**27**) with the direction of the photo-induced charge transfer.<sup>46</sup>

The diads ( $\text{PH}_2\text{-terpy}$  and  $\text{terpy-PAu}$ ) has been synthesized via a Suzuki coupling reaction. From the diads and under harsh conditions over a short period of time, the synthesis of the Ir(III) complex occurs and triad **27** (Figure **1.12**) was formed. The triad has a linear arrangement with some flexibility and a good control over the geometry of the ensemble. From the absorption spectra, the triad spectrum is the same as that made from the sum of the individual components, indicating the absence of strong coupling between different structural units.

The luminescence intensity at 298K has been quenched in  $\text{CH}_3\text{CN}$  of  $\text{PH}_2\text{-[Ir]}$  and  $\text{PH}_2\text{-[Ir]-PAu}$  **27**, which is consistent with the fact that charge separated state are more stabilized in polar solvent. Time-resolved emission measurements indicate that the lifetime of the free base in its singlet excited state is reduced from 8.3 ns (when alone) to 30 ps in complex  $\text{PH}_2\text{-[Ir]}$  and  $\text{PH}_2\text{-[Ir]-PAu}$  **27**, while it is not the case at 77K, where quenching did not occur. The changes in the lifetimes at room temperature demonstrate the energy transfer from the free base  $\text{PH}_2$ .

### I.2.3 Ir and Pt complexes

There are very few examples of heteropolymetallic complexes of Pt/Ir nature. One of them has been studied by a group of G. Williams at the University of Durham in UK. Their paper in *Inorg. Chem.*, 2011,<sup>47</sup> described the synthesis and the photophysical properties of a rigid, polynuclear cyclometalated complex containing both Ir(III) and Pt(II) centers. The 4,6-di-(4-*tert*-butylphenyl)pyrimidine, **28** (Figure I.13) has been synthesized by Suzuki cross-coupling starting from 4,6-dichloropyrimidine and 2.6 equiv *tert*-butylbenzeneboronic acid. The *tert*-butyl group is used to increase solubility and prevent aggregation which could arise from the square-planar d<sup>8</sup> complexes.

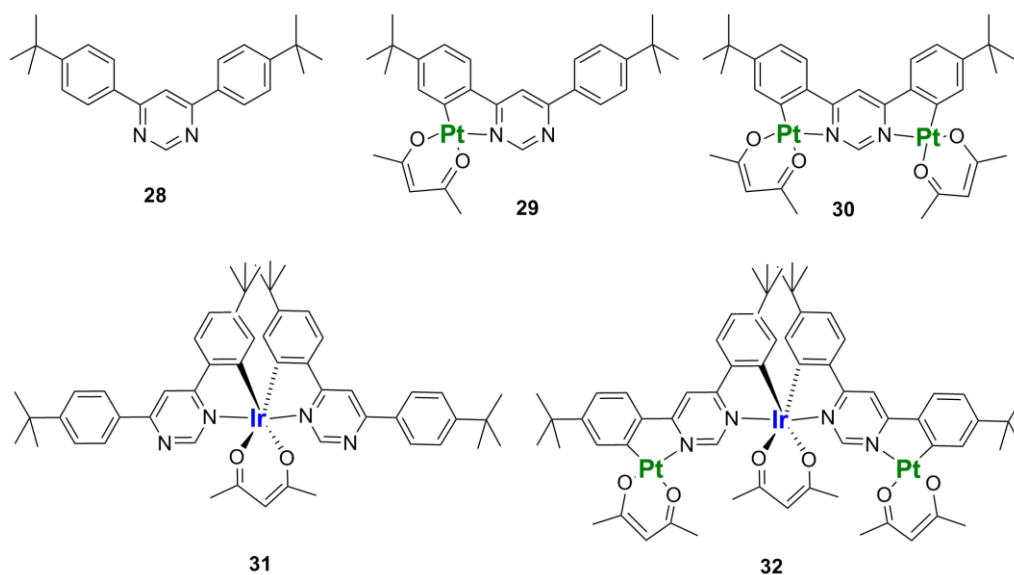


**Figure I.13.** Structures of Pt and Ir complexes.<sup>47</sup>

In Figure I.13, ligand **28** was complexed with iridium using 0.5 equiv. of IrCl<sub>3</sub>·H<sub>2</sub>O to form **31**. Upon using 1 or 2 equivalents of K<sub>2</sub>PtCl<sub>4</sub> in acetone, the mono-, Pt **29**, and the dinuclear Pt<sub>2</sub> **30** complexes have been formed, respectively. The trinuclear complex Pt<sub>2</sub>Ir **32** has been prepared by reacting the mononuclear Pt complex **29** with 0.5 equiv. of IrCl<sub>3</sub>·H<sub>2</sub>O.

The absorption spectrum shows that complex **29** exhibits an intense band between 250-260 nm, similar to those observed for ligand **28**, which is attributed to a ligand centered π-π\* transition. The Pt<sub>2</sub>Ir complex **32** is red and exhibits an absorption band that extends to 600 nm. The bands observed for **32** in the 370-500 nm range are as twice as intense as that for the Ir complex **31** (Figure I.14).



All complexes are highly luminescent. The emission spectrum (Figure I.15) shows that the introduction of metal ions induces a stabilization of the triplet states. The trend of the emission maxima is: Pt<sub>2</sub>Ir > Ir > Pt<sub>2</sub> > Pt at both 298 and 77K. At 298K, the emission band of complex Pt<sub>2</sub> 30 exhibits a shoulder, while for all the other complexes, the spectra are more structured showing some vibrational structures at lower energy sides than the  $\lambda_{\text{max}}$  of each. That behaviour is quite typical for complexes containing metals with a high degree of MLCT characters.

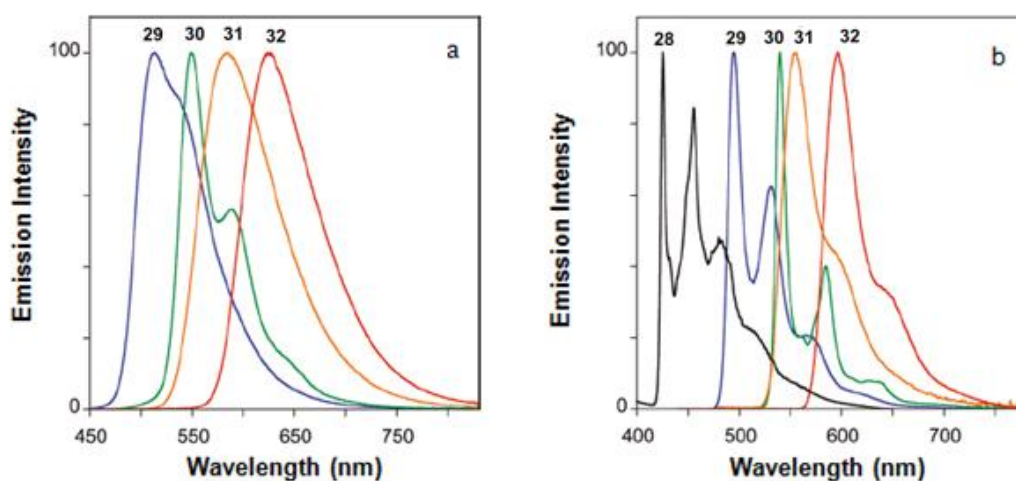


Figure I.14. Comparison of the absorption spectra of 28-32 in CH<sub>2</sub>Cl<sub>2</sub> at room temperature.<sup>47</sup>

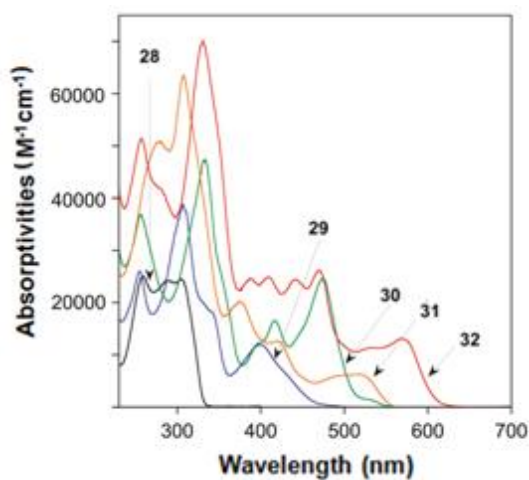


Figure I.15. Comparison of the emission spectra at 298K in CH<sub>2</sub>Cl<sub>2</sub> (a) and 77K in diethyl ether/isopentane/ ethanol (2:2:1 v/v) (b) of 28-32.<sup>47</sup>

The quantum yields for the complexes were between 31% (in Pt) and 54% (in Pt<sub>2</sub>). The lifetimes are in order of microseconds, a little less in complex **32** and a little more in Pt complexes (**29** and **30**).  $K_r$  is increased upon introduction of another Pt center to the Pt complex (**29**), despite the decrease of emission energy. Likewise, the presence of Pt center in the complex **32** enhances the  $K_r$  compared to Ir one. So generally the radiative triplet emission is increased by the introduction of another metal center(s).

The versatile structures of the 5 complexes give a new approach for tuning and optimizing the luminescence properties of the d-block metal complexes for future applications.

### **I.3 Organometallic polymers**

Prior to the early 1920's, chemists doubted the existence of molecules having molecular weights greater than a few thousand. This limiting view was challenged by Hermann Staudinger, a German chemist with experience in studying natural compounds such as rubber and cellulose. In contrast to the prevailing rationalization of these substances as aggregates of small molecules, Staudinger proposed they were made up of macromolecules composed of 10,000 or more atoms. He formulated a polymeric structure for rubber, based on a repeating isoprene unit (referred to as a monomer). For his contributions to chemistry, Staudinger received the 1953 Nobel Prize.

The insertion of a metal center into the polymeric chain could contribute to the delocalized  $\pi$ -electron system and often gives electronic interactions between the transition metal and the organic molecular framework leading to the possibility of optical transitions that do not occur in organic compounds. These transitions could be d-d electronic transitions, <sup>3</sup>MLCT, and ligand-to-metal-charge-transfer, as well as promoting intersystem crossing to generate triplet states. An interesting class of such organometallic conjugated polymers that includes Pt(II) and Ir(III) heavy metals has been synthesized and characterized photophysically in this study.

The characterization of a polymer requires several parameters which need to be specified. Among these methods, NMR which may occasionally determines the presence of the end group and consequently the Degree of Polymerization (PD). Other techniques such as wide angle and small

angle X-ray scattering, and small angle neutron scattering are used mainly to determine the crystalline structure of polymers. Thermal properties such as the glass transition temperature and melting point can be determined by differential scanning calorimetry and dynamic mechanical analysis. Gel Permeation Chromatography (GPC) is a strong tool used to determine the number average molecular weight ( $M_n$ ), weight average molecular weight ( $M_w$ ), and polydispersity (PD). Polymer molecular weight is important because it determines many physical properties.

Organometallic polymers have the properties of polymers and organometallic compounds. It has wide range of applications. In our studies we are hoping to synthesize polymers that could be suitable in photovoltaic or electroluminescent devices.

### I.3.1 Pt containing organometallic polymers

This section describes some examples of Pt-polymers. Starting with an interesting studies that have been made by Kirk Schanze and his collaborators in 2009.<sup>48</sup> They used different types of transition metals ( $Fe^{3+}$ ,  $Co^{2+}$ ,  $Zn^{2+}$ ,  $Ni^{2+}$ ,  $Cu^{2+}$  and  $Pd^{2+}$ ) chelated to bipyridyl monomeric and polymeric Pt acetylide moiety (Figure I.16)

Metal ion binding to bipyridine unit in the polymer induces a red-shift in the near-UV absorption band. This binding also results in phosphorescence quenching except with  $Zn^{+2}$ . The quenching varied between different metals, also between the monomer and the polymer.

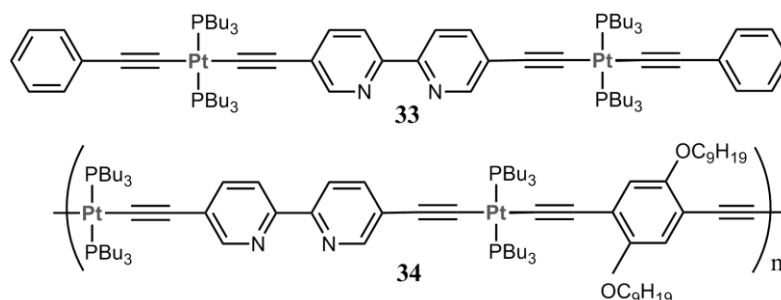


**Figure I.16:** Structures of the Pt complex **33** and polymer **34**.<sup>48</sup>

The photophysical studies (Table I.1) indicates that both the Pt complex **33** and Pt-containing polymeric **34** has the same band maximum of emission although it is slightly red-shifted in the polymer emission. The lower phosphorescence efficiency for the polymer might be due to the efficient non-radiative decay that results from the polymer aggregates or vibrational motion through the long molecular structure.

**Table I.1.** Photophysics of the Pt complex **33** and polymer **34**.<sup>48</sup>

Compound	$\lambda_{\text{abs}}/(\text{nm})$	$\lambda_{\text{em}}/(\text{nm})$	$\Phi\%$	$\tau(\mu\text{s})$
<b>33</b>	379	562, 610	12	85
<b>34</b>	396	565, 610	6.5	58

The analysis suggests that the difference in quenching efficiency for the metal ions arises in part from the variation in the stability constants and mainly from the difference in intrinsic quenching efficiency in the metal ion–bipyridine complex. These complexes were designed to be sensitive and selective sensors.

Jean Fréchet and collaborators synthesized using Stille conditions the Pt-containing conjugated polymers, **35a** and **35b** (Figure I.17).<sup>49</sup> The polymers exhibit a weak emission and a small stock shift suggesting that the emission arises from the singlet state. Optical and electronic properties have been studied to determine the effect of conjugation on the photovoltaic applications when compared to the monomers. The photovoltaic performance has power conversion efficiency as high as 1.3%.

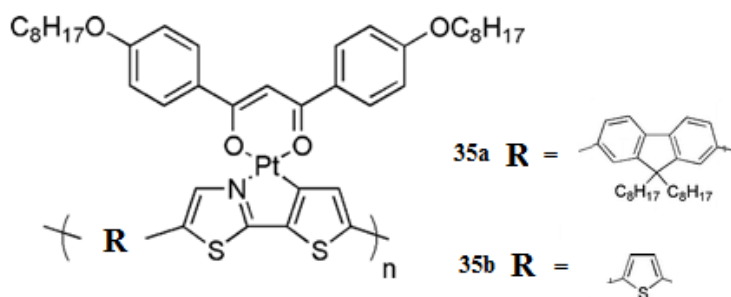


**Figure I.17.** General structure of cyclometalated Pt polymers **35a** and **35b**.<sup>49</sup>

Harvey *et al* synthesized and characterized photophysically 1-D nanometer sized oligomers build upon a metalloporphyrin and a rigid spacer (Figure I.18).<sup>50</sup> The polymers show good thermal stability with first weight lose at 300 and 280 ° C for **36a** and **36b** and they have a number of repetitive units equal to 9 and 3 respectively. All metal complexes and polymers are air-stable and exhibit good solubility in CH<sub>2</sub>Cl<sub>2</sub> and CHCl<sub>3</sub>.

The studies show that T<sub>1</sub> energy transfer occurred from the Pt(II) spacer (donor) to the Zn(II)Porphyrin (acceptor). Evidence of that is proved by the decrease in the emission lifetimes of the Pt spacer compared to the polymers with k<sub>ET</sub> rates ranging from 10<sup>4</sup> to 10<sup>6</sup> s<sup>-1</sup>. It is also interesting to note that the chromophore spacer topology bears some resemblance to the light harvesting devices in photosystems of some photosynthetic bacteria.

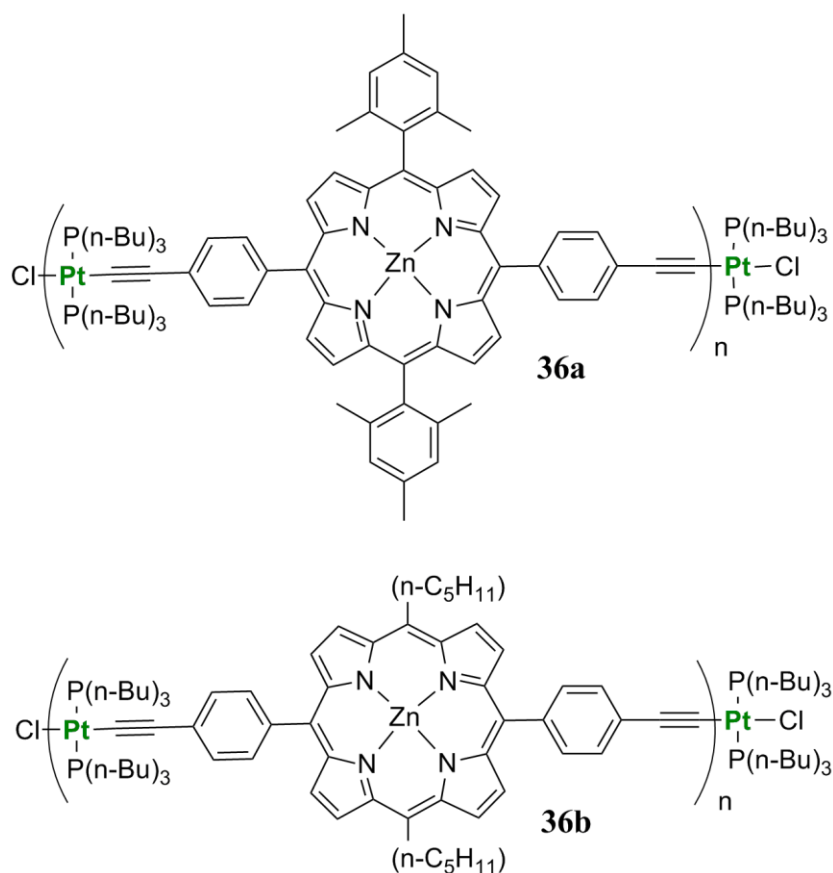


**Figure I.18.** General structure of polymers **36a** and **36b**.<sup>50</sup>

### 1.3.2 Ir containing organometallic polymers

Three versatile classes of Ir(III)-containing polymers can be defined regardless of whether the main chain is conjugated or not. Polymers with iridium centers as pendant groups,<sup>51</sup> with iridium centers anchored adjacent to the backbone via a chelating ligand<sup>52</sup> and with iridium centers directly incorporated into the polymer backbone via two chelating units (Figure I.19).<sup>53</sup> There are rare examples of polymers that fit into the latter category. This section discusses an example for each class.

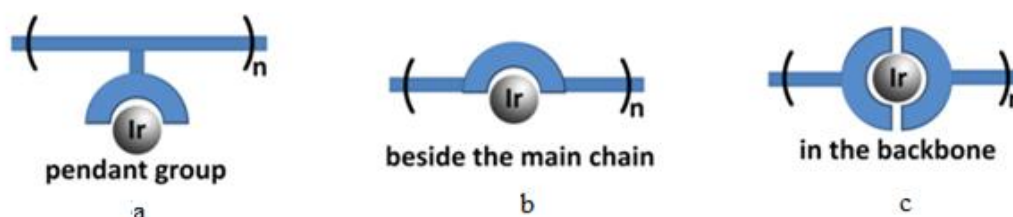


**Figure I.19.** Classes of Ir(III)-containing polymers.

A poly(styrene) with pendant Ir(III) dendronized complex attached to every repetitive unit is an example of the first class (pendant group).<sup>51f</sup> It was prepared by a free radical polymerization. Making dendrimers with pendant Ir(III) complexes (**37b**, Figure I.20) was found to improve thermal stability, solubility and emission quantum yields relative to the non-dendronized polymer.

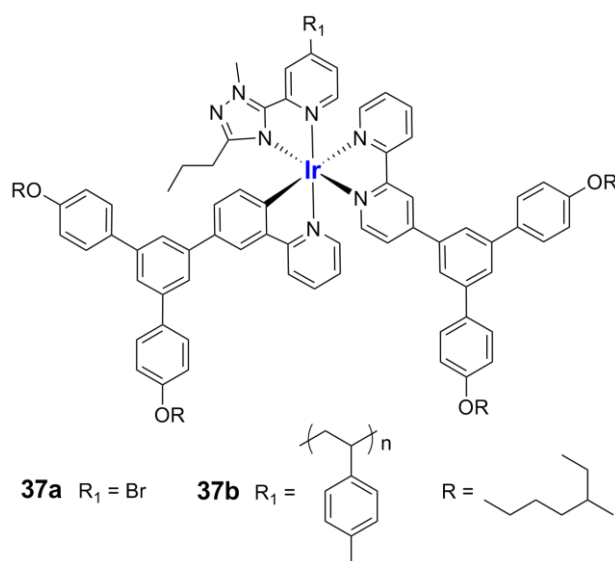


**Figure I.20.** General structure of polymers **36a** and **36b**.<sup>51f</sup>

Complex **37a** is emitting green light and exhibits a monoexponential decay of 1.6  $\mu$ s. In solution, the emission quantum yield is 61%. On the other hand, the dendritic Ir(III) polymer **37b** exhibits an emission with a biexponential decay (1.03 and 1.95  $\mu$ s), and an emission quantum yield of 92%. The biexponential decay indicates that the polymer has more than one emissive site in its structure. The presence of styrene pendant group decreases the quantum efficiency of **37b**. The emission quantum yield of the dendritic Ir(III) polymer **37b** is over than twice of the non-dendronized polymer, which had an emission quantum yield of 23%, and this demonstrates the positive effect on the quantum efficiency upon using the dendrimers. In the solid state, the quantum yield of **37b** has been decreased to 13% and this maybe be attributed to interchromophore interactions.

An OLED has been commercialized using the poly-dendrimers and showed a good performance with a quantum efficiency of 6.2%. Also, polymer **37b** showed high viscosity compared to the simple dendrimer which can be useful in inkjet printing applications.

Wang and collaborators synthesized by Suzuki polycondensation a series of red-light electrophosphorescent polyfluorenes (PFs) with varying content of a quinoline-based iridium complex (Figure **I.21**).<sup>51k</sup> To avoid the loss of triplet excitons, the triplet energy of the polymer must be higher than that of the triplet emitter. PF has a triplet energy in the sufficient range to host the iridium complexes.

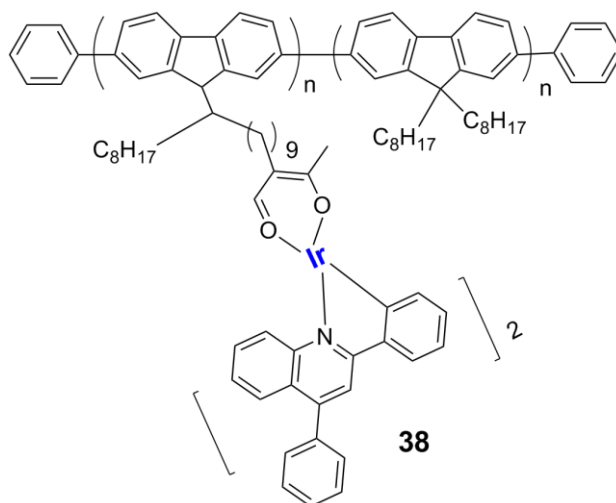


**Figure I.21.** General structure of Ir(III) polymer **38**.<sup>51k</sup>

Absorption band at 380 nm remains unchanged. The low-energy bands in the polymers showed an increase in intensity as the Ir content incorporated onto the PFs increased. PFs emission band is completely quenched at 450 nm aiming to charge transfer from it to the Ir phosphorescent unit.

Do-Hoon Hwang, Hong-Ku Shimin and collaborators synthesized an ancillary diketonated and a carbazole unit in the polymer main chain (Figure I.22)<sup>52d</sup>. It is an example of Ir(III) polymers being beside the main chain type. The structure of **39** disrupts the conjugation of the polymer chain, leading to a shorting of the conjugation length of the molecules and to a blue shift in the absorption maxima (compared to the homopolymer) at 357 nm. The study also shows that when the Ir(III) fraction is increased in the polymer chain, the 2 other absorption bands at 320 and 426 nm are also increased. The peak at 320 nm is due to the ancillary unit, while the one at 426 nm is for the Ir(III) complex.

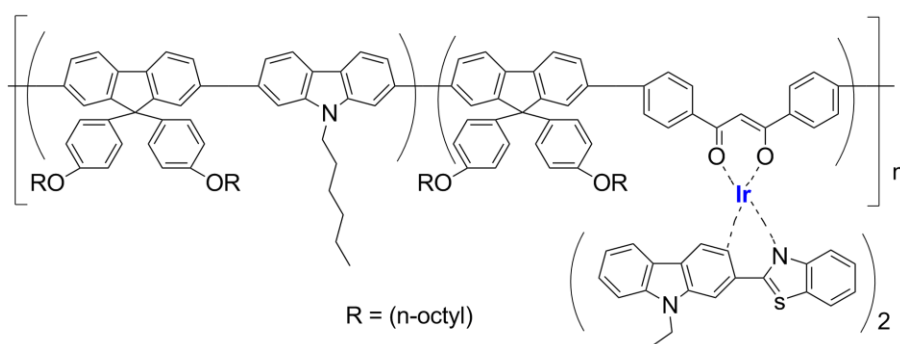


**Figure I.22.** Structure of the Ir(III)-containing polymer **39**.<sup>52d</sup>

The photoluminescence properties of polymer **39** have been investigated, and it exhibits 2 intense emission bands at 473 and 640 nm. The emission at 640 nm increased as the fraction of Ir units increased in the polymer chain. Photonic devices show a good performance. In particular, electroluminescent devices were fabricated and shown to emit white light composed of blue and red emission. This light was stable upon applying voltage to the device.

Polyfluorenes with charged iridium complexes in the main chain are demonstrated to have useful application in the flash memory device (Figure I.23).<sup>52a</sup> The polymer solution is spin-coated and sandwiched between aluminum and tin oxide electrodes. The device shows very good memory performance. The fluorene moieties act as an electron donor and iridium complex as an acceptor.



Wei Huang and collaborators studies the effect of temperature and solvent on the energy transfer PFs to charged iridium complexes.<sup>52e</sup> An efficient energy transfer occurred at low temperature and diluted THF. This study provides a good way to achieve high phosphorescent emission for conjugated polymers with low iridium content.

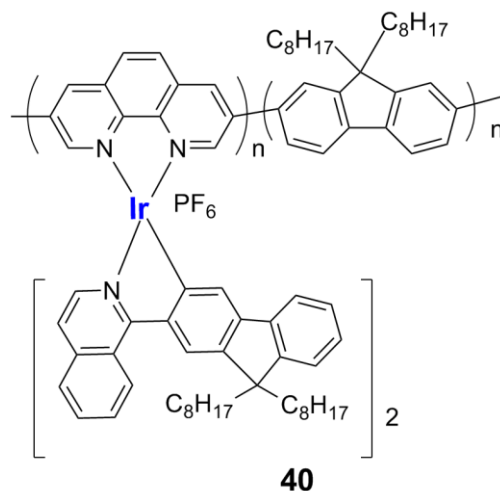
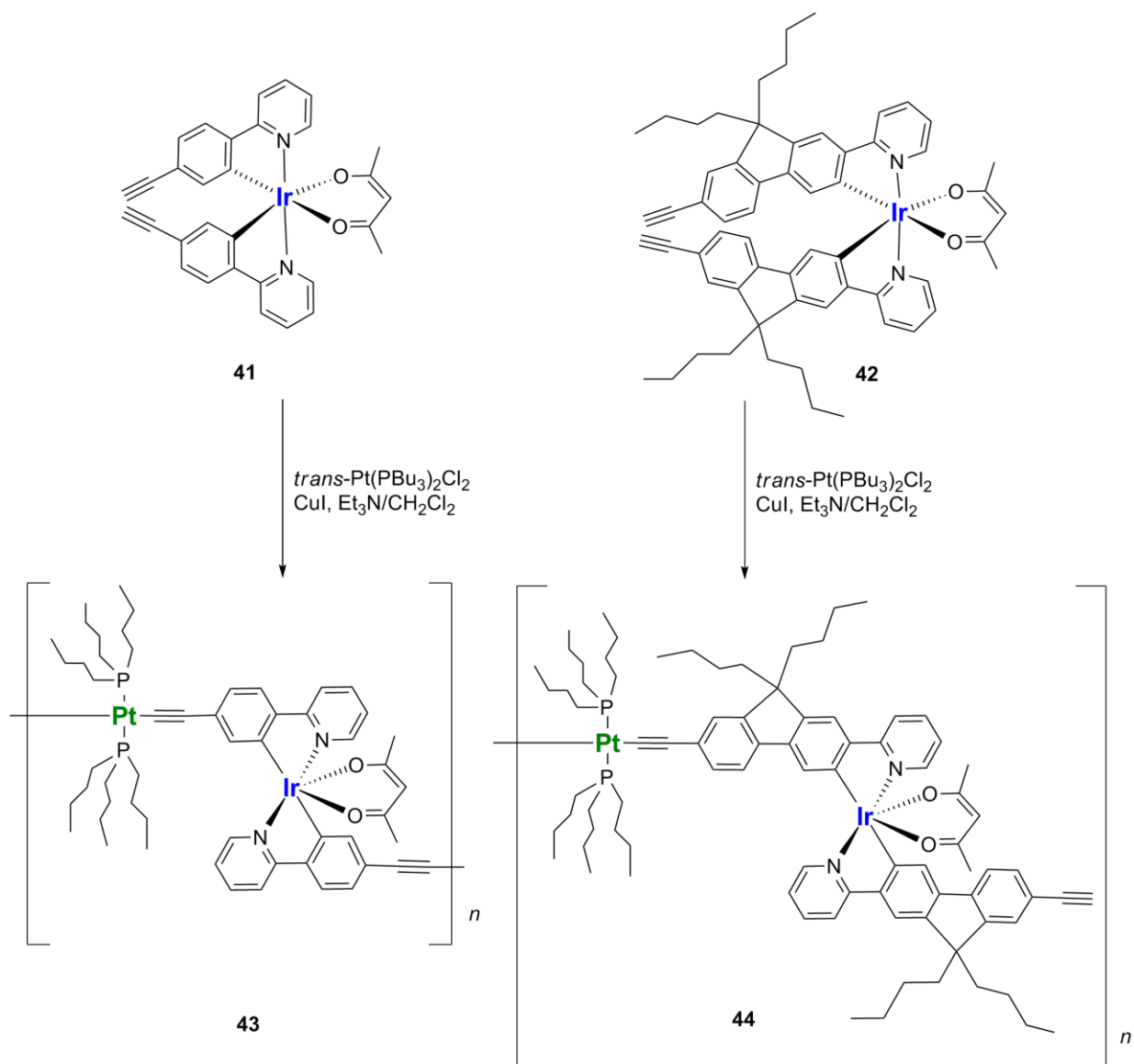


**Figure I.23.** Structure of charged Ir(III)-containing polymer **40**.<sup>52a</sup>

### I.3.3 Ir and Pt containing organometallic polymers

In 2010, the use of Ir(III) and Pt(II) heavy metals in order to obtain novel phosphorescent neutral oligometallayne polymers bearing both metal centers was made. The polymers studied are of Class(III) at which the iridium centers directly incorporated into the polymer backbone via two chelating units.<sup>53b</sup>

Starting by a selective Stille coupling reaction to form the bromo-substituted ppy-type ligand, the product then underwent complexation with Ir(III). The alkyne group had been installed on the resulting complex via a Sonogashira coupling reaction. After deprotection with a base under mild conditions, **41** and **42** were both obtained as orange solids in high yields (85%). Complexes **43** and **44** were synthesized via a reaction between **41** and **42** respectively with *trans*-Pt(PBu<sub>3</sub>)<sub>2</sub>Cl<sub>2</sub> in 1:1 ratio and in the presence of CuI and Et<sub>3</sub>N (Scheme I.2).



**Scheme I.2.** Synthesis of the mixed-metal Ir(III) and Pt(II) organometallic polymers.<sup>53b</sup>

Polymers **43** and **44** exhibit 2 major absorption bands. The intense one near 400 nm is attributed to a spin-allowed  $\pi$ - $\pi^*$  transition. The weak absorption bands at low energy results from MLCT bands. The emission bands of the polymers are more red-shifted than the monomers **41** and **42**. However, **42** exhibits a red-shifted emission compared to that of complex **41**. This is believed to be due to the presence of long alkyl chains in **42** that sterically force a polymer conformation to favour conjugation.

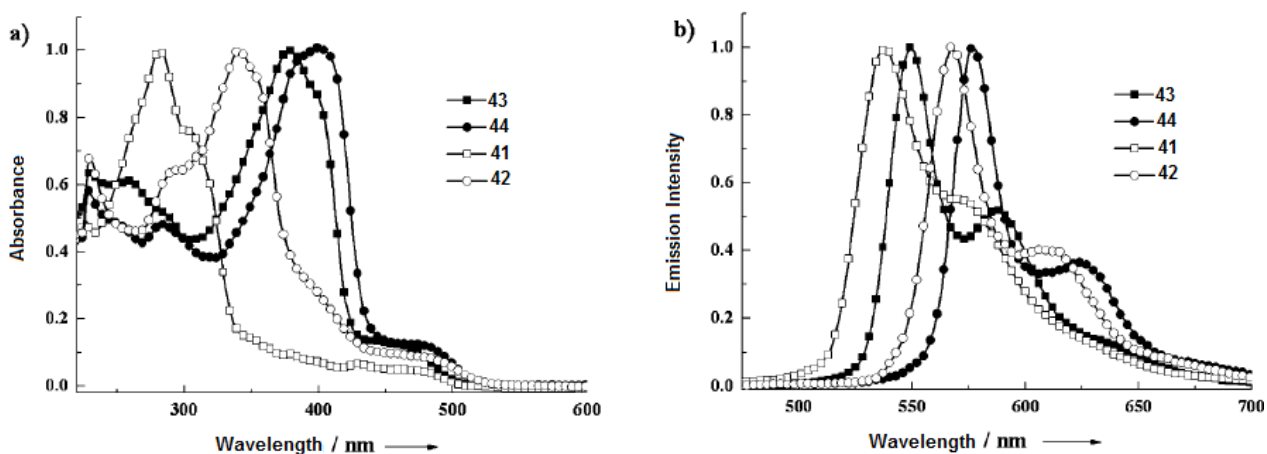


**Figure I.24.** Absorption and emission of the complexes **41**, **42**, **43** and **44** at 298K in  $\text{CH}_2\text{Cl}_2$ .<sup>53b</sup>

Upon light excitation at 400 nm, the emission spectra shows maxima at 549 and 577 nm for polymers **43** and **44**, respectively (Figure I.24). The two other shoulders that are present for both polymers at 588 and 625 nm originates from LC (ligand centered)  $^3\pi\text{-}\pi^*$  with minor  $^3\text{MLCT}$  transitions. The order of the red-shifting of the 4 complexes is **44** > **42** > **43** > **41**.

The emission quantum yields of the polymers is half that of the monomers. However, the emission lifetimes for polymers **43** and **44** are shorter at room temperature but longer at 77K compared to the corresponding monomers **41** and **42**.

The TD-DFT computations for one repetitive unit of **43** show that the electron density of the HOMO and the LUMO is localized in the Ir(III) metal. While for **44**, the highest contribution to HOMO is in the Pt(II) and for the LUMO is in the Ir(III) center. This means that the emissive properties of such polymers arise from the Ir building block.

## I.4 Theory:

The major aim of this thesis is to study the photophysical properties of monomeric and polymeric organometallic complexes containing Pt(II) and Ir(III) metals. In order to understand these photophysical results, we should consider some fundamental background in photophysics.

Photophysics and photochemistry are 2 different terms. Photophysics involves the absorption, transfer, movement, and emission of electromagnetic light and energy without chemical reactions. Conversely, photochemistry involves the interaction of electromagnetic energy that results in chemical reactions (i.e. bond breaking and bond formation).

Light is composed of particles known as photons, each of which has the energy of Planck's quantum,  $hc/\lambda$ ; where  $h$  is Planck's constant,  $c$  is velocity of light and  $\lambda$  is the wavelength of the radiation. Light has dualistic properties of both waves and particles.

Electronic absorption spectra arise from the absorption of light by a molecule at a particular wavelength. The energy of the absorbed radiation corresponds to the energy of a transition generally from the ground to an excited state. Selection rules for electronic spectroscopy only allow transitions between states of the same multiplicity (i.e. spin-allowed transition). Thus, excitation may occur from the ground state ( $S_0$ ) to the singlet excited states ( $S_1$ ) for diamagnetic compounds such as those dealt with in this work. Optical transmittance,  $T$ , is a measure of how much light that enters a sample is absorbed. If no light is absorbed then  $I = I_0$ . Low transmittance values indicate that a large part of the light has been absorbed.

$$T = I/I_0$$

The relaxation of the excited molecules (Figure **I.26**) back to the ground state may take place by:

- 1- Radiative decay such as emission of electromagnetic radiation.
- 2- Non-radiative decay in which thermal energy is lost.

- 3- Non-radiative intersystem crossing to a triplet state ( $T_1$  represents the lowest energy triplet state).

These processes compete with each others. Emission without change in multiplicity is called fluorescence, while phosphorescence refers to an emission with multiplicity changes. The latter is a spin-forbidden transition. Consequently, the fluorescence and phosphorescence exhibit fast and slow decays, respectively.

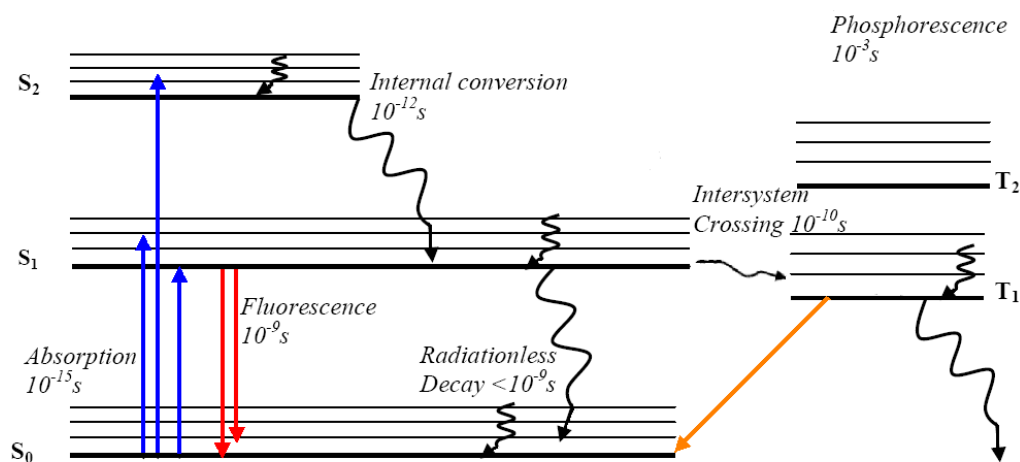


**Figure I.25.** Energy level diagram illustrating the radiative and the non-radiative processes.

The radiative and the non-radiative processes are represented by straight and wavy arrows, respectively. The wavelength of light emitted in phosphorescence will be longer (red-shifted) and lower in energy than the absorbed radiation. The fluorescence band is also red-shifted, but to a much smaller extent. The fluorescence spectrum exhibits a vibrational progression involving the ground state vibrational levels ( $v$ ), whereas the absorption one exhibits a progression build upon excited state vibronic levels ( $v'$ ).

However, phosphorescence occurs from the lowest vibrational level on the triplet excited state  $T_1$  to  $S_0$ . Again since phosphorescence involves a spin-forbidden transition, the emission lifetime of the excited state is often relatively long (nanoseconds to microseconds or longer). In contrast, the fluorescence lifetimes (typically between singlet states) are shorter and usually lie in the picosecond

to nanosecond. Luminescence is a general term that refers to the spontaneous emission of radiation from an electronically excited species and includes both the fluorescence and the phosphorescence.

The emission quantum yield,  $\Phi$ , measures the number of photons absorbed versus the number of photons emitted for an excited state. When calculating the sum of all quantum yields (radiative and non-radiative) of the singlet and of the triplet, we should obtain 1 (Equation 1):

$$\Phi_F + \Phi_P + \sum \Phi_{NR} = 1 \quad (1)$$

where  $\Phi_F$  is the fluorescence quantum yield,  $\Phi_P$  is the phosphorescence quantum yield and  $\sum \Phi_{NR}$  represents the sum of all quantum yields for all non-radiative processes.

Figure I.26 illustrates the energy diagram for all the constants used in the calculus,  $k_F$  is the radiative rate constant for fluorescence,  $k_P$  is the radiative rate constant for phosphorescence,  $k_{IC}$  is the radiative rate constant for internal conversion and  $k_{ISC}$  is the radiative rate constant for intersystem crossing.

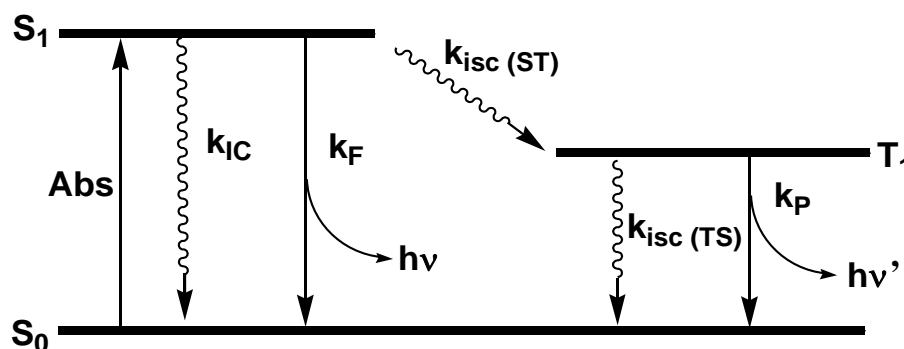


**Figure I.26.** Schematic representation of the various radiative and non-radiative rate constants transitions implied in the quantum yield and emission lifetime calculations.

It is possible to calculate the quantum yield using the ratio of fluorescence speed over the sum of the deactivation of the  $S_1$  state. Equation 2 allows for the calculation of the fluorescence quantum yield.

This calculus can further be simplified by multiplying the radiative fluorescence constant  $k_f$  with the fluorescence lifetime  $\tau_F$ (Equation 2).

$$\Phi_F = \frac{k_F}{k_F + k_{IC} + k_{ISC}} = k_F \tau_F \quad (2)$$

It is possible using Equation 3 to calculate the fluorescence lifetime of the singlet which is equal to the reciprocal of all singlet deactivation rate constants.

$$\tau_F = \frac{1}{k_F + k_{IC} + k_{ISC}} \quad (3)$$

For the phosphorescence quantum yield, it is important to consider the ratio of the phosphorescence over the sum of all the  $T_1$  state deactivation rate constants (Equation 4). As opposed to the fluorescence, in the phosphorescence calculations, we need to include the quantum yield of the singlet to triplet intersystem crossing  $\Phi_{ISC}$ . This quantum yield represents the probability of the  $T_1$  formation.

$$\Phi_P = \Phi_{ST} \times \frac{k_P}{k_P + k_{ISC}} = \Phi_{ISC} k_P \tau_P \quad (4)$$

$\Phi_{ISC}$  is defined by equation 5:

$$\Phi_{ISC} = \frac{k_{ISC}}{k_F + k_{IC} + k_{ISC}} = k_{ISC} \tau_F \quad (5)$$

For quantum yield measurements, one can use the comparative method. In this study, the following conditions were fulfilled:

- The standard must absorb and emit at the same wavelength range as the sample, otherwise the effect of the refractive index should be included, which was not needed in this work.
- The absorptivity of both the standard and the sample must be the same and below 0.05 absorbance at the wavelength of the excitation.
- The spectra should be corrected for instrumental response.

- The spectra should be converted into a linear scale of energy prior to extract the area under these. In this work, this scale was wavenumbers.

The luminescence lifetime is the average time that the molecule remains in its excited state before the photon is emitted. From a kinetic point of view, the lifetime can be defined by the rate of depopulation of the excited (singlet or triplet) states following an optical excitation from the ground state. Luminescence generally follows first order kinetics.

The triplet state lifetime is represented in Equation 6:

$$\tau_P = \frac{1}{k_P + k_{ISC}} \quad (6)$$

where  $k_P$  is the phosphorescence rate constant while  $k_{ISC}$  is the intersystem crossing rate constant.

The total decay rate is the sum of radiative ( $k_{\text{radiative}}$ ) and non-radiative ( $k_{\text{nonradiative}}$ ) rate constants (Equation 7):

$$k_{\text{total}} = k_{\text{radiative}} + k_{\text{non-radiative}} \quad (7)$$

A transfer of energy from the donor to the acceptor will occur when an energy acceptor molecule is placed at the proximity of an excited energy donor molecule. After energy transfer, the donor relaxes to its ground state and the acceptor is promoted to one of its excited states.

Radiative transfer occurs when the extra energy of the  $D^*$  is emitted in form of luminescence and this radiation is absorbed by the acceptor (A). This can be represented by the following equations:





The vibrational factor associated to the non-radiative relaxations refers to the internuclear distance. This process is best described using the Frank-Condon principle of the radiationless transitions. In order for the transition to be radiationless, the principle demands that the process be horizontal as well as vertical in a way that it is confined to a very small region of the potential energy curve or surface. This relation is between the different vibrational probability functions, where the overlap between the starting and finishing state vibrational probability function will determine the efficiency of the relaxation. The more overlap there is between the probability functions of the two states (ground state and excited state), the more efficient the relaxation (passage from one state to the other) will be (Figure I.27).<sup>54a</sup> This process is part of the internal conversion.

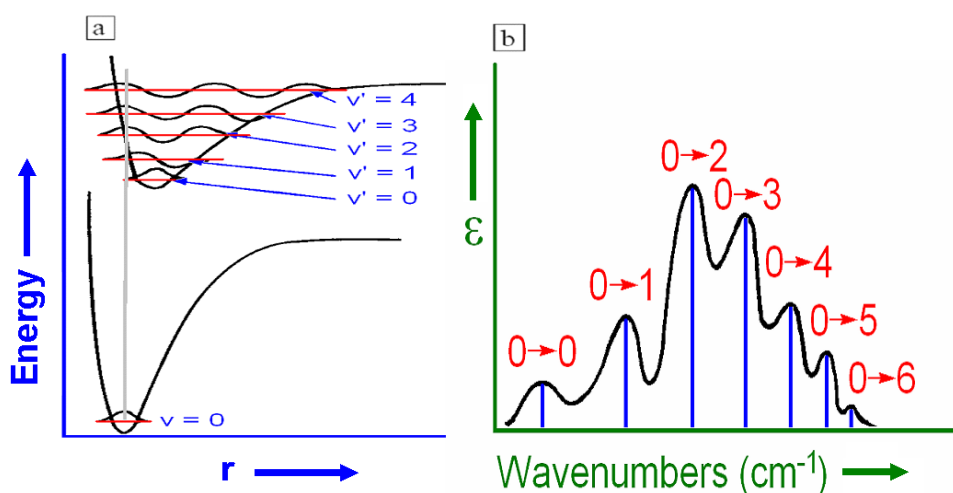


**Figure I.27.** (a) Potential energy diagram for a diatomic molecule illustrating the Franck-Condon excitation. (b) Intensity distribution among vibronic bands as determined by the Franck-Condon principle.<sup>54a</sup>

At room temperature, the ground state population is distributed within the higher vibrational levels than the fundamental level. The electrons in these levels move to higher levels, these higher level transitions are referred to as hot bands. The presence of metal-metal bonds in chromophore for instance or very low frequency vibrational modes, can allow of such phenomenon to be observed since the vibrational spacings are small ( $\sim 100\text{cm}^{-1}$ ) and can be easily be populated. In fact, the presence of these hot bands will depend on active mode vibrationnal frequency in the electronic transitions. The  $d(\sigma)^2 \rightarrow d(\sigma)^{2*}$  transition is of  $\nu(M_2)$  mode often coupled with this electronic

transition. This low frequency vibrational mode will lead to a significant contribution of the hot bands in the spectral representation of the  $d(\sigma)^2 \rightarrow d(\sigma)^{2*}$  transition (both absorption and emission).

In these metal-to-ligand-charge-transfer (MLCT) transitions, higher frequency active modes are also generally active such as  $\nu(\text{ML})$  ( $\sim 300\text{cm}^{-1}$ ) or intraligand stretching ( $>400\text{cm}^{-1}$ ). Due to the large vibrational spacing, it is possible that these levels are not thermally accessible. Hot bands are observed at room temperature. For low-frequency modes, the hot bands are removed by cooling the sample to 77 K (Figure I.28).<sup>54b</sup> Indeed at lower temperatures, the molecule does not have enough thermal energy for higher vibrational levels to be populated. The consequence upon cooling is the removal of the hot bands in the absorption spectra. Such property can be useful in order to confirm the presence of metal-metal bond for example, or other fragment exhibiting active vibrational modes.

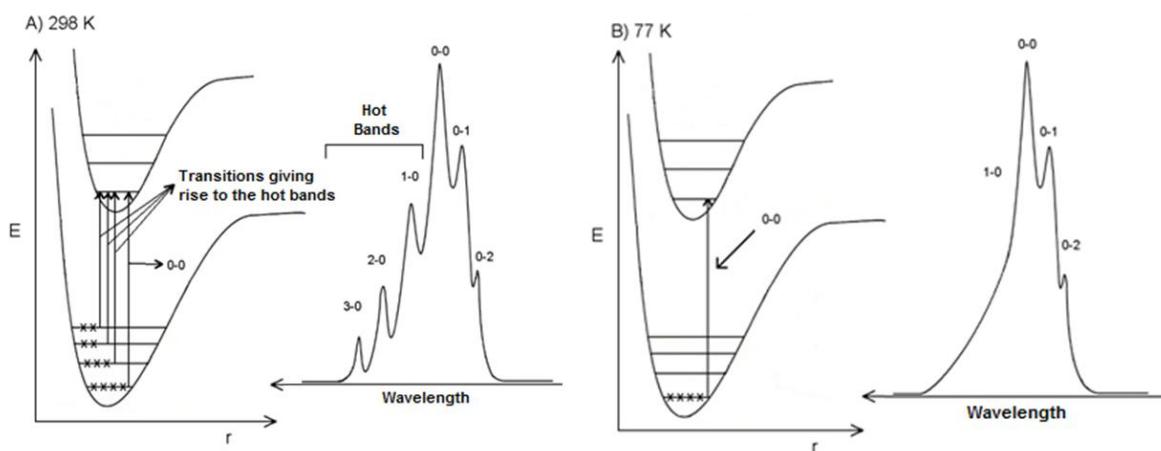
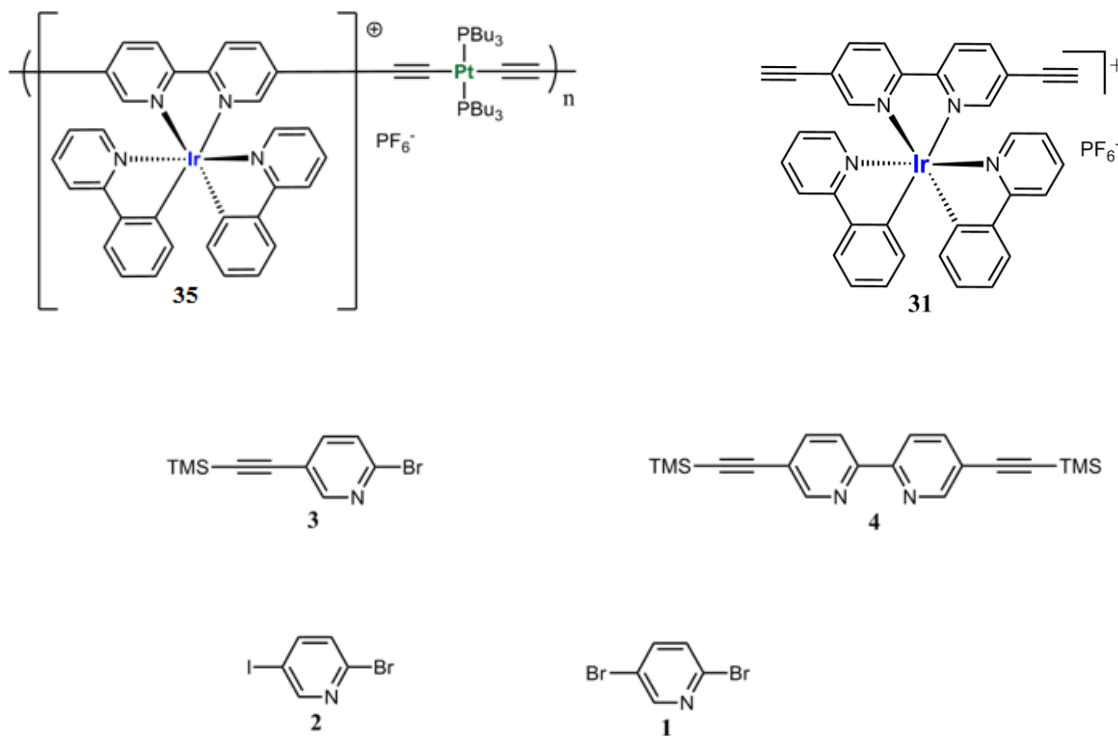


**Figure I.28.** 298K (A) and 77 K (B) absorption spectrum showing the removal of the hot bands.<sup>54b</sup>

## CHAPTER 1: SYNTHESIS

This chapter reports the synthesis of different Pt, Ir and Pt-Ir complexes and the target Pt-Ir polymer. The monomers are important to compare and consequently understand the physical and the photophysical behaviour of Pt-Ir polymer. The retrosynthesis of this polymer is outlined in Scheme 1.1.



**Scheme 1.1.** Retrosynthesis of Pt-Ir polymer (35).

### 1.1 Synthesis of the bipyridine ligands

The 2 ligands, 5,5'-diethynyl-2,2'-bipyridine **5** and 5-ethynyl-2,2'-bipyridine **10** are presented in Figure 1.1.

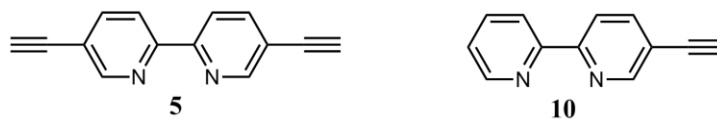
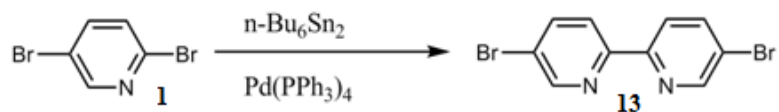


**Figure 1.1.** Structures of the target bipyridine ligands **5** and **10**.

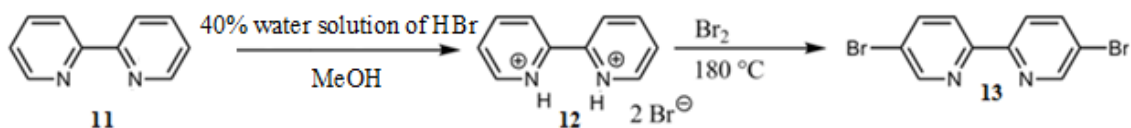
The synthesis of the 5,5'-diethynyl-2,2'-bipyridine (**5**) was first attempted from the 5,5'-dibromo-2,2'-bipyridine **13**. The later substrate was formed via a Stille-Kelley coupling reaction of 2,5-dibromopyridine **1** in the presence of a catalyst (Scheme **1.2**).<sup>55</sup> The reaction was followed by TLC and by GC/MS. After purification by column chromatography, impurities were detected in the aliphatic region of the <sup>1</sup>H NMR spectra, which were attributed to the butyl groups of n-Bu<sub>6</sub>Sn<sub>2</sub> and the desired product was difficult to isolate in a pure form.

Efforts were made to remove these impurities by preparing a 3 to 1 (by weight) solution of the target product and KF in hexanes and then adding it to a column filled with silica. The amount of impurities was partially removed but the end product was still not pure enough.



**Scheme 1.2.** Synthesis of 5,5'-dibromo-2,2'-bipyridine via a Stille-Kelley coupling reaction.

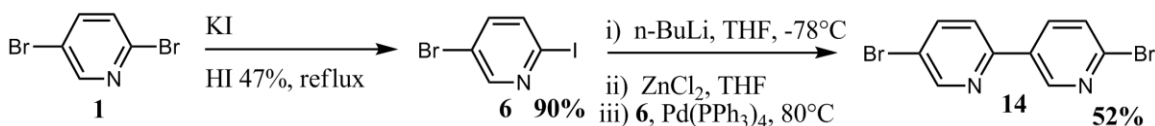
The second strategy was to synthesize the 5,5'-dibromo-2,2'-bipyridine **13** from the 2,2'-bipyridyl hydrobromide **12** (which is obtained from the bipyridine **11**) using Br<sub>2</sub> and high temperature (Scheme **1.3**). The yield was 40%, lower than what was reported (53%).<sup>56</sup> The use of a corrosive reagent like Br<sub>2</sub> and the long reaction time (4 days) were reasons to not pursue this method further.



**Scheme 1.3.** Synthesis of 5,5'-dibromo-2,2'-bipyridine (**13**) using Br<sub>2</sub>.<sup>56</sup>

Another synthetic plan is a halogen to halogen exchange reaction of 2,5-dibromopyridine **1** to form the 5-bromo-2-iodopyridine **6** with a 90% yield as shown in Scheme **1.4**. Compound **6** was then subjected to a Negishi Pd-catalyzed homocoupling reaction in order to obtain the 5,5'-dibromo-2,2'-bipyridine **13**.

Surprisingly, according to the  $^1\text{H}$  NMR spectrum, the resulting product was something else than **13**. The spectrum showed 6 peaks with different multiplicities in the aromatic region. This result did not correspond to the data reported for compound **13** and might correspond to 5,6'-dibromo-2,3'-bipyridine **14**.



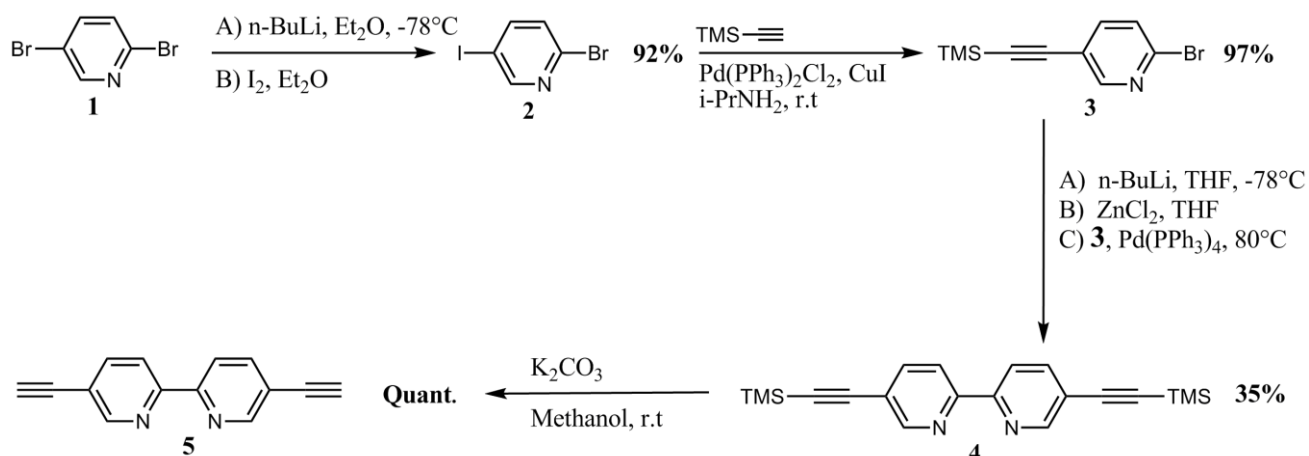
**Scheme 1.4.** A trial to obtain 5,5'-diethynyl-2,2'-bipyridine from 2,5 dibromopyridine **1**.

In order to understand where the lithiation occurs on the 5-bromo-2-iodopyridine **6** substrate,  $n\text{-BuLi}$  was added to a solution containing compound **6** in THF at  $-78^\circ\text{C}$  and prior to addition of a  $\text{ZnCl}_2$  solution in THF. Besides some impurities, 40% of deiodinated product, 19% of debrominated and the 18% of unreacted starting material were detected using GC/MS analysis.

The most efficient method to obtain the 5,5'-diethynyl-2,2'-bipyridine **5** is illustrated in Scheme **1.5**. The target bisethynylbipyridine ligand **5** was obtained from the 2,5-dibromopyridine **1** via a 4-step procedure.

2-Bromo-5-iodopyridine **2** was obtained via an iodine quench of the lithiated substrate formed by a metal-halogen exchange of the bromo substituent at the 5-position of the 2,5 dibromopyridine **1** in 92% yield.<sup>57</sup>

A Sonogashira cross-coupling reaction between 1 equiv. of **2** and 1 equiv. of commercially available TMS-acetylene was performed at room temperature with an excellent yield (97%). On the other hand, the desired end product **3** did not form when the reaction was carried out under reflux. Only the starting material was detected by GC/MS. A carbon-carbon coupling reaction between 2 acetylenic units to give bis-trimethylsilylbutadiyne was observed in this case as an undesired side product



**Scheme 1.5.** The formation of **5** starting from 2,5 dibromopyridine **1**.

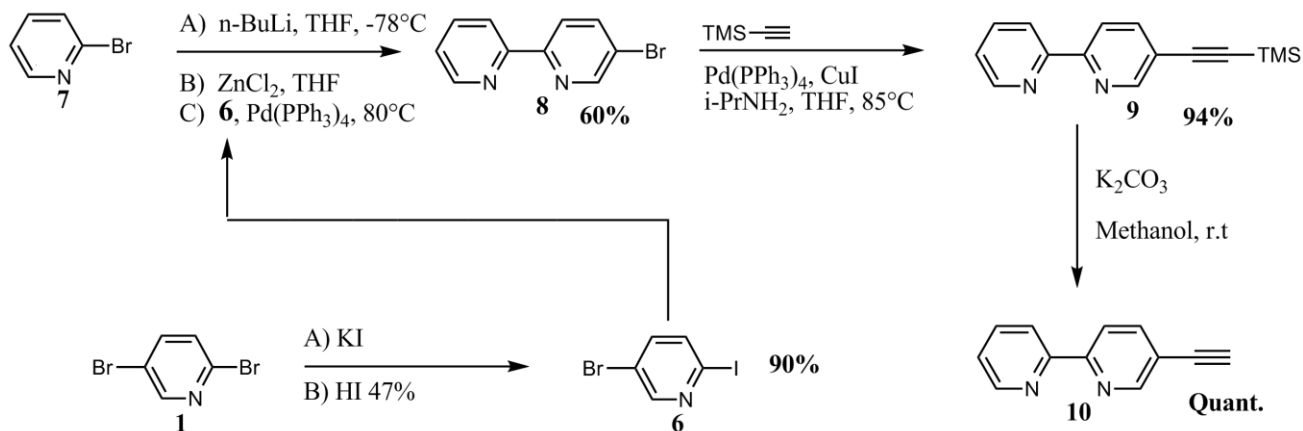
A Sonogashira reaction was followed by a palladium-catalyzed Negishi homocoupling reaction with **3** that led to the formation of product **4** with a maximum yield of 35%. The reaction was monitored by GC/MS and by observing the blue luminescence of the solution and in the TLC upon illumination with short wavelength UV-lamp.

A Negishi reaction has many advantages over other coupling reactions. It is selective and usually gives high yields. Also, less toxic compared to the Stille coupling reaction that uses stannane intermediates. On the other hand, there is no use of additives compared to the Suzuki reaction and considered the most reactive in Pd-catalyzed cross-coupling reaction.

After successfully obtaining product **4**, it was subjected to a 2 hours deprotection reaction of the TMS groups to afford target ligand **5** with a quantitative yield.

The synthesis of the second ligand, 5-ethynyl-2,2'-bipyridine **10**, is shown in Scheme **1.7** and was prepared via a 4 step procedure with a combined yield of ~51%.

From 2,5-dibromopyridine **1**, the bromide at the 2-position was exchanged with iodide using KI and aqueous solution of 47% HI. The reaction was kept away from direct contact with light using an aluminum foil. The reaction was completed in 4 days and was followed by GC/MS every day until a complete conversion of the starting material into the end product occurred.



**Scheme 1.6.** Synthesis of 5,5'-diethynyl-2,2'-bipyridine (**10**) from 2,5 dibromopyridine (**1**).

The next 3 steps use the same type of reactions as that for ligand **5** but in different ordering. Compound **6** (Scheme **1.6**) was cross coupled with the commercially available substrate **7** via a palladium-catalyzed Negishi reaction to obtain the 5-bromobipyridine **8** as a white solid in 60% yield. The end product of the previous reaction was subjected to a Sonogashira reaction to obtain **9** in an excellent yield (94%). The TMS group of compound **9** was removed using K<sub>2</sub>CO<sub>3</sub> and MeOH at room temperature.

## 1.2 Synthesis of Pt complexes and Pt-containing polymer

After obtaining ligands **5** and **10**, the next step is to coordinate these ligands with Pt(II). 3 types of Pt complexes (**16**, **20** and **22**) were synthesized (Figure **1.2**).

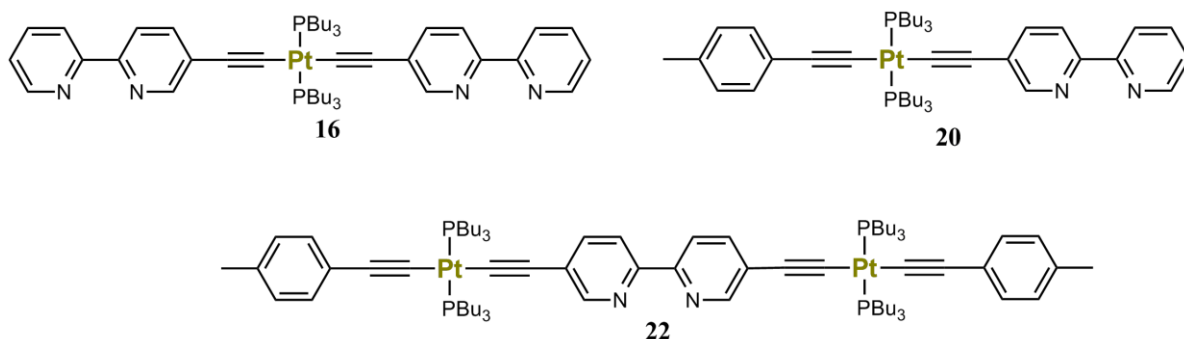
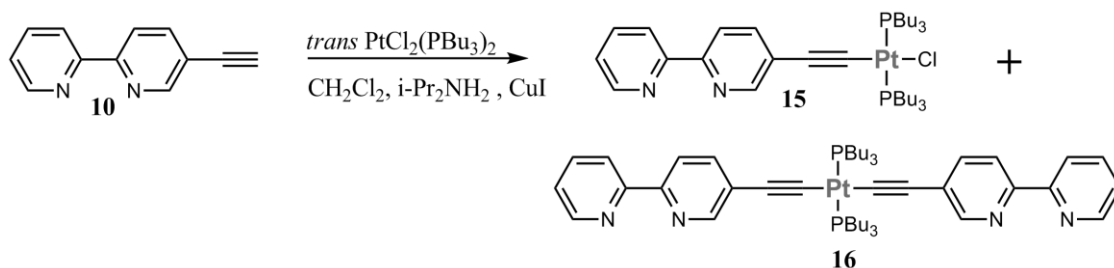


**Figure 1.2.** Structures of the Pt complexes **16**, **20** and **22**.

In order to synthesize these complexes, the first step is to prepare the *trans*-Pt(PBu<sub>3</sub>)<sub>2</sub>Cl<sub>2</sub> complex according to a procedure outlined in literature.<sup>58</sup> The yield was 73%.

The synthesis of complex **16** is outlined in Scheme 1.7. The resulting crude solution of this reaction contains 3 compounds: the excess *trans*-Pt(PBu<sub>3</sub>)<sub>2</sub>Cl<sub>2</sub>, compounds **15** and **16**. They were separated by column chromatography. The use of 10% EtOAc /hexanes as the mobile phase was inadequate to separate the excess *trans*-Pt(PBu<sub>3</sub>)<sub>2</sub>Cl<sub>2</sub> from compound **15**. The best solvent mixture was 50% dichloromethane/hexanes. The *trans*-Pt(PBu<sub>3</sub>)<sub>2</sub>Cl<sub>2</sub> was eluted first followed by compound **15**. However, complex **16** was easily separated using 30% EtOAc /hexanes. Silica gel was used in all columns.



**Scheme 1.7.** Synthesis of Pt complex **15** and **16**.



Both yields for compounds were optimized using different amount of *trans*-Pt(PBu<sub>3</sub>)<sub>2</sub>Cl<sub>2</sub>. Yields of both complexes can be seen in Table 1.1. The maximum yield for compound **15** was obtained upon using 9 equiv. of *trans*-Pt(PBu<sub>3</sub>)<sub>2</sub>Cl<sub>2</sub>, while for compound **16** it was obtained with only 3 equiv. This reaction is called the Hagihara coupling, named after Nobue Hagihara, a Japanese chemist. The Stille coupling could be another synthetic pathway to obtain such Pt complexes but it has not been tried as it is less environmentally friendly.

**Table 1.1.** Optimization of **15** and **16** yields upon using different equiv. of *trans* Pt(PBu<sub>3</sub>)<sub>2</sub>Cl<sub>2</sub>.

	<i>trans</i> -PtCl <sub>2</sub> (PBu <sub>3</sub> ) <sub>2</sub>	<b>15</b>	<b>16</b>
Reaction 1	3 Eq	7%	28%
Reaction 2	9 Eq	73%	13%

Products **15** and **16** exhibit slight differences in the <sup>1</sup>H NMR spectra. As seen in Figure 1.3 there is a small upfield shift in the aromatic peaks between 5 and 9 ppm of the biscoupled Pt complex **16** compared to **15**. The reason might be the electronegativity of the Cl atom that reduces the electron density around the molecule and therefore the nucleus of **15** was deshielded.

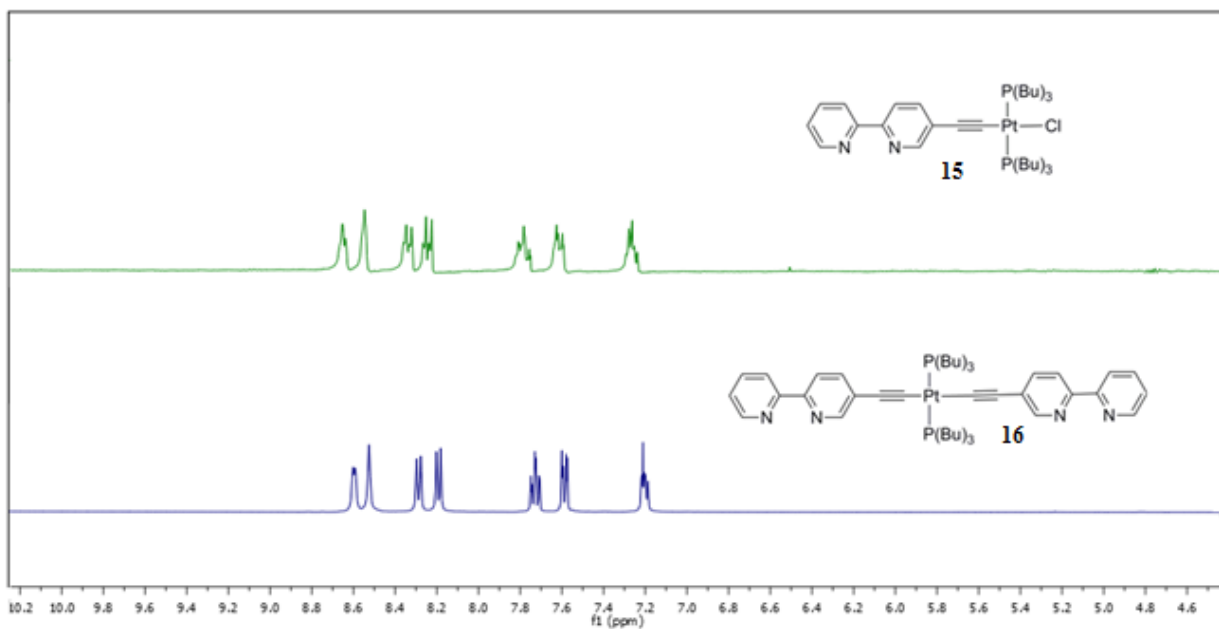
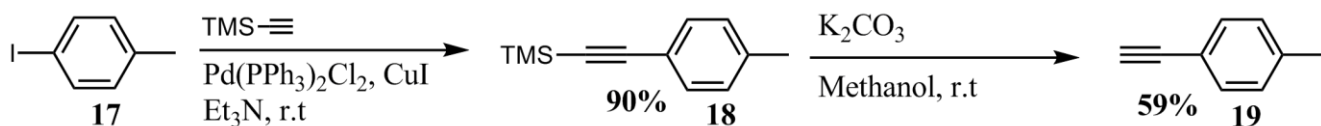


**Figure 1.3.** <sup>1</sup>H NMR spectra between **15** and **16** complexes in CDCl<sub>3</sub>.

After the separation and purification of complex **15**, it was capped with **19** to obtain complex **20**. 1-ethynyl-4-methylbenzene **19** was synthesized via a 2 step procedure starting from the commercially available 1-iodo-4-methylbenzene **17** as shown in Scheme 1.8. The choice of the tolyl group was motivated by the presence of the  $^1\text{H}$  NMR tag, aryl-CH $_3$ , hence rendering easier the monitoring of the end product.

Complex **20** was obtained from **15** at a room temperature using an excess of **19**. The end product was purified by column chromatography and the excess of **19** was easily eluted by 50% dichloromethane/hexanes (Scheme 1.9).

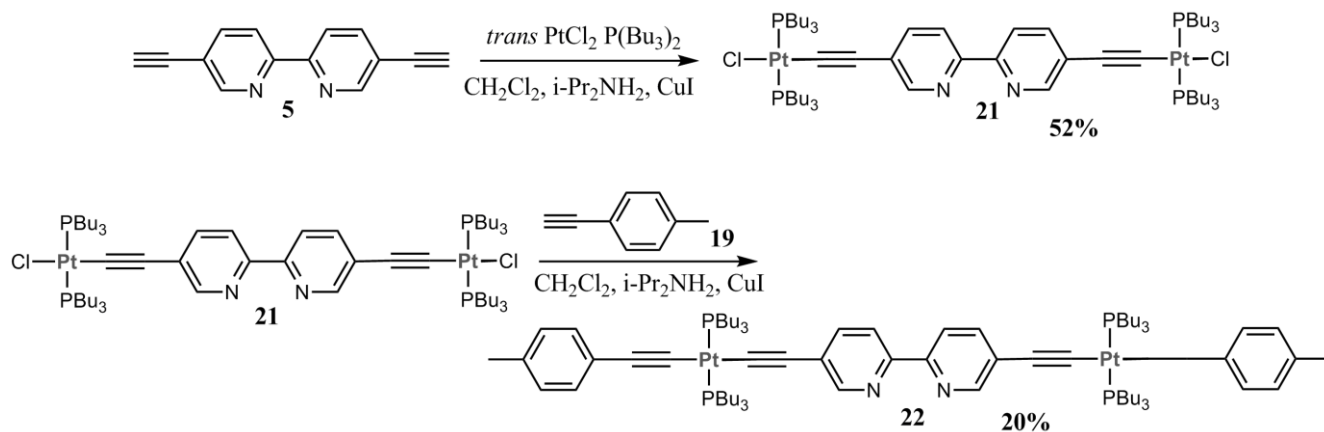


**Scheme 1.8.** Synthesis of 1-ethynyl-4-methylbenzene **19**.



**Scheme 1.9.** Synthesis of Pt complex **20**.

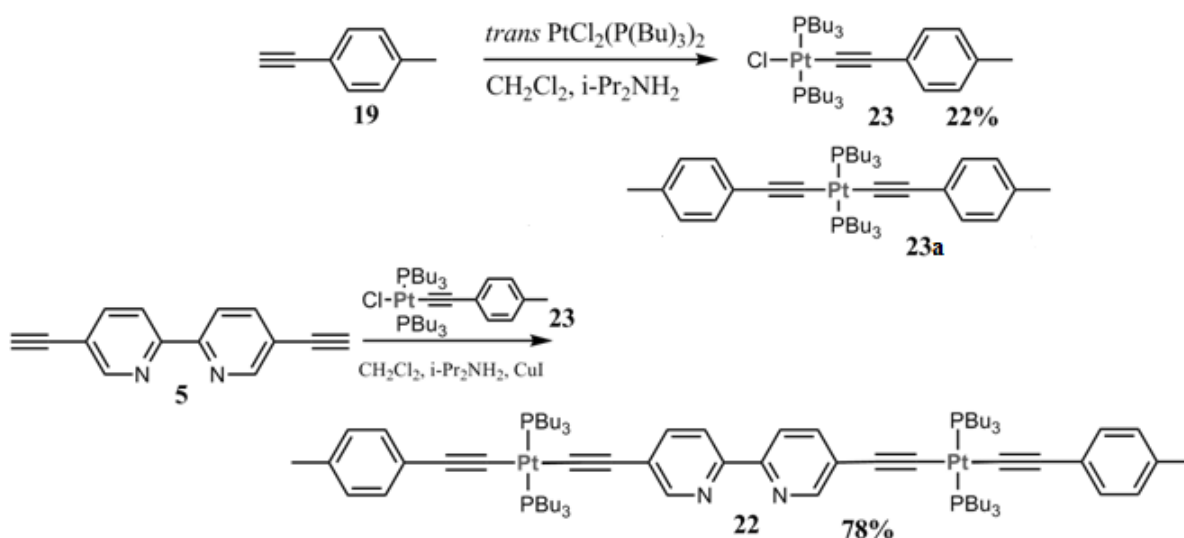
The synthesis of the complex **21** uses ligand **5** (Scheme 1.10) and 9 equiv. of *trans* Pt(PBu $_3$ ) $_2$ Cl $_2$  and the yield was 52%. The excess *trans*-Pt(PBu $_3$ ) $_2$ Cl $_2$  has been recuperated.



**Scheme 1.10.** The first method for the synthesis of complex **22**.

Complex **21** was capped with 2 equiv. of 1-ethynyl-4-methylbenzene **19** to obtain **22**. The reaction yield was low (20%). Due to difficulties to purify complex **21** and the lower yield for complex **22**, a second method has been attempted and ultimately replaced this method.

The second method to obtain **22** is to cap the ligand **5** with 2 equiv. of complex **23** (Scheme **1.11**). The later complex was obtained from **19** using an excess  $\text{trans-Pt}(\text{PBu}_3)_2\text{Cl}_2$ . Then, ligand **5** was capped with 2.5 equiv. of **23** leads to the formation of desired complex **22** with a very good yield (78%).



**Scheme 1.11.** Alternative synthesis of complex **22**.

Synthesis of polymer **24** started from ligand **5**. It has been synthesized from 1:1 coupling reaction of ligand **5** and *trans*-Pt(PBu<sub>3</sub>)<sub>2</sub>Cl<sub>2</sub>. The resulting polymer was brown and soluble in dichloromethane, CHCl<sub>3</sub> and THF. The GPC indicated that this polymer has a number of repetitive units equals to ~15. Its synthesis and GPC results are shown in Figure 1.5. Schanze and collaborators prepared and characterized by GPC a similar Pt-polymer (Figure 1.4),<sup>48</sup> with a PDI (polydispersity index) of 2, the same as our result, but their polymer was smaller *M<sub>n</sub>* of 7160 (number averaged molecular weight) compared to ours (*M<sub>n</sub>* = 12194).

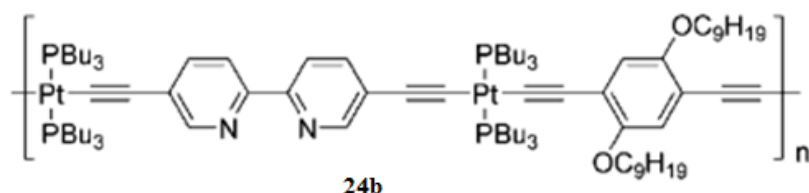


**Figure 1.4.** Structure of the polymer reported by Schanze and collaborators.<sup>48</sup>

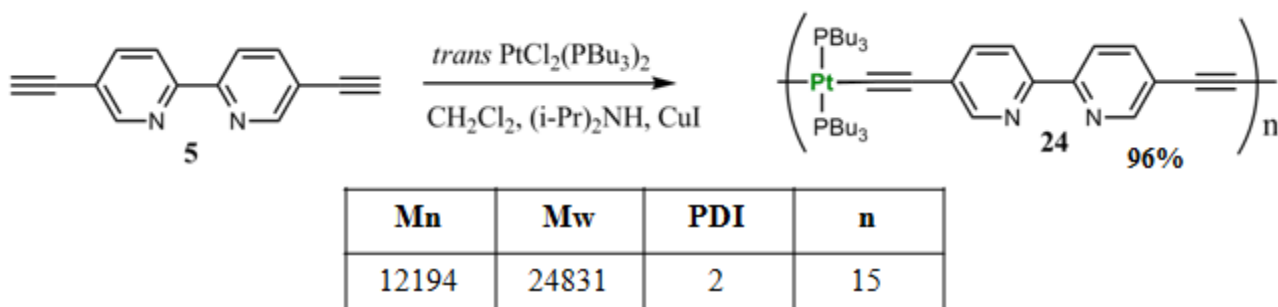
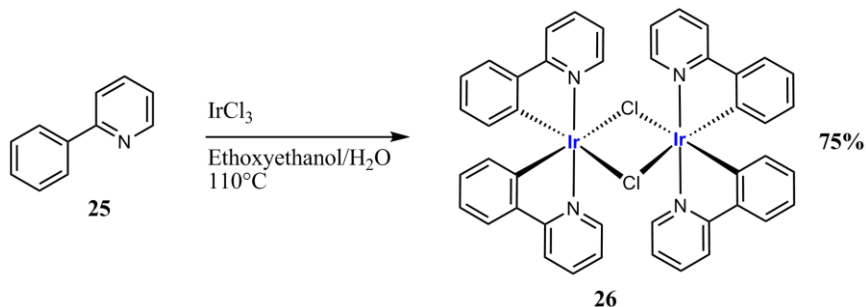


**Figure 1.5.** Synthesis and GPC results for polymer **24**.

### 1.3 Synthesis of Pt-Ir model complexes and Pt-Ir containing polymers

After the synthesis of ligands **5** and **10** and the 3 Pt complexes **16**, **20**, and **22**, the next step is to coordinate them with Ir complexes to form model compounds and polymers.

The precursor ( $[(ppy)_2IrCl]_2$ ) dimer is prepared from 2 equiv. of phenylpyridine (**25**) and 1 equiv. of  $IrCl_3$  in the presence of ethoxyethanol as solvent.<sup>59</sup> The reaction is shown in Scheme 1.12.



**Scheme 1.12.** Synthesis of the precursor  $[(ppy)_2IrCl]_2$  dimer.<sup>59</sup>

The cleavage of the Ir dimer with 5,5'-bis(trimethylsilyl)ethynyl-2,2'-bipyridine and 5,5'-diethynyl-2,2'-bipyridine in the presence of ethylene glycol as the solvent was first attempted. The reaction was carried out at high temperature (150 °C) for 20 hours. Addition of ether/water in a 1:1 ratio was made. The aqueous layer was separated and the metathesis with  $NH_4PF_6$  did not induce precipitation. The aqueous phase was extracted with dichloromethane, and the dichloromethane was evaporated and identified by  $^1H$  NMR. The spectra contained impurities in the aliphatic region. Moreover, the aromatic region did not contain the expected number of peaks corresponding to the end product. The product contained in the ether layer (obtained from evaporation), exhibited the same  $^1H$  NMR spectra. Gentle heating at 60 °C in dichloromethane/ $CH_3OH$  for 16 hours was performed. This method was applied to all ligands and all the Pt complexes as seen in Scheme 1.14. The complexation with the Ir dimer has been also attempted with complex **21** (Scheme 1.10) in order to obtain complex **29** (Figure 1.6), but the  $^1H$  NMR did not correspond to the required end product. Also, complexes **27** and **28** have been synthesized (Figure 1.6).

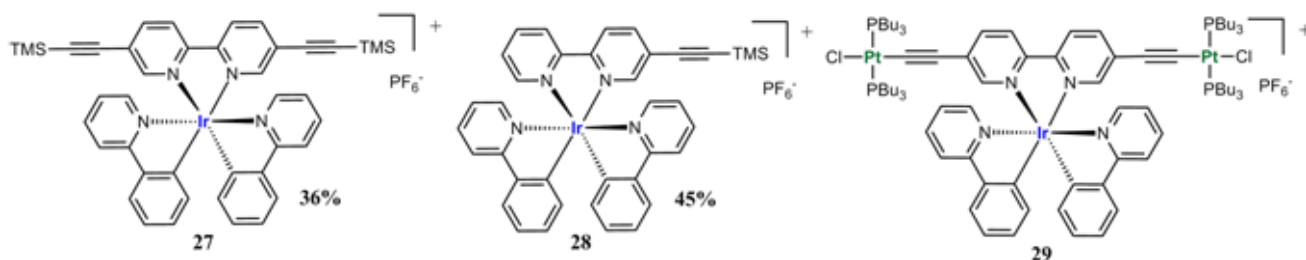
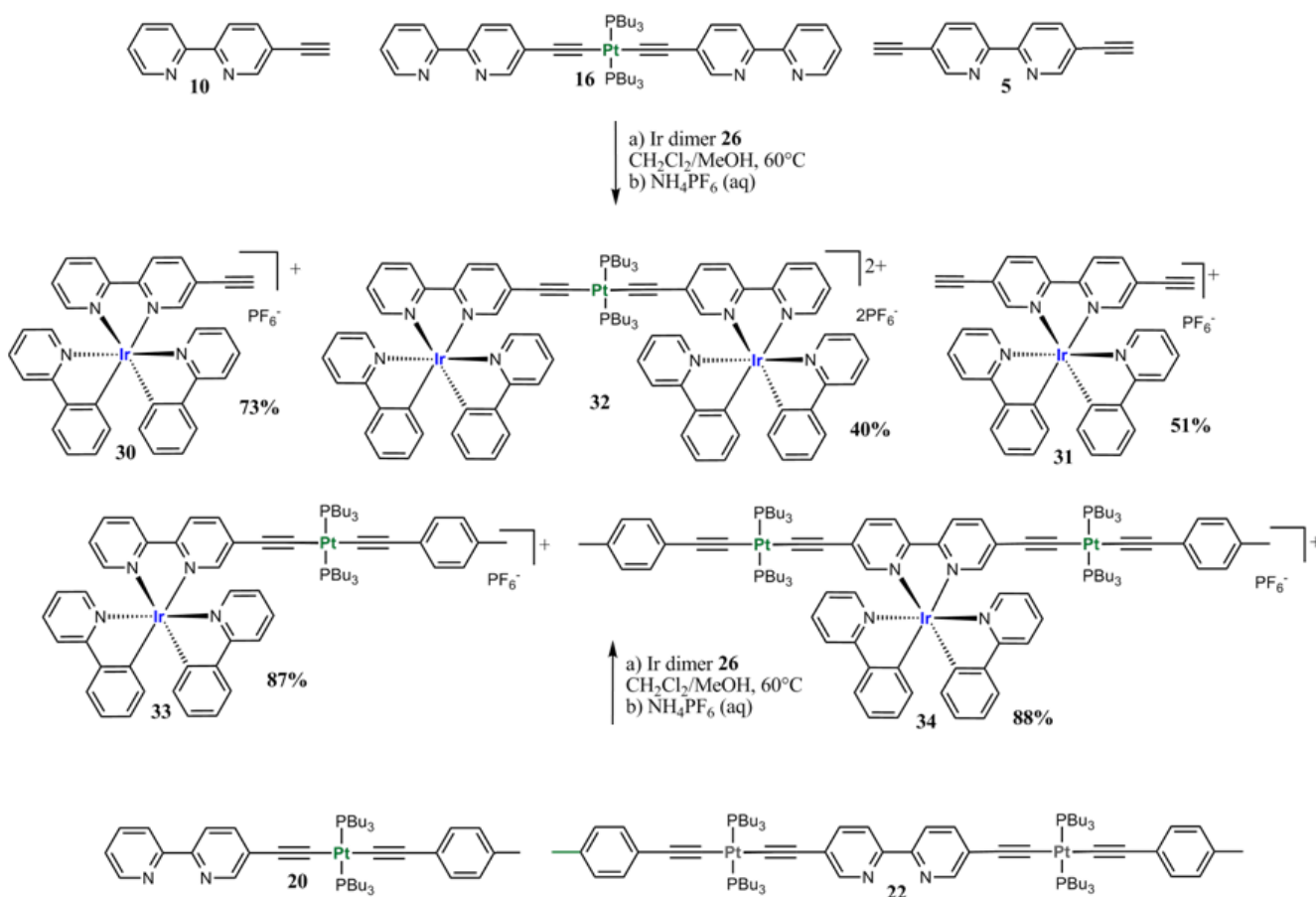


**Figure 1.6.** Structures of the Ir complexes **27** and **28** and Pt-Ir complex **29**.



**Scheme 1.13.** Synthesis scheme for complexes 30-34.

The mixed-metal Pt-Ir oligomer has been synthesized the same way as for complex 24. It consists in a 1:1 reaction of Ir complex 31 with *trans*-Pt(PBu<sub>3</sub>)<sub>2</sub>Cl<sub>2</sub> (Figure 1.7). The polyanionic oligomer precipitated but was partially soluble in CHCl<sub>3</sub>, soluble in THF and 2-MeTHF. It has a 9 repetitive units and a low polydispersity index of 1.12 according to the GPC data.

All oligomers have been characterized with <sup>1</sup>H and <sup>31</sup>P NMR and the GPC.

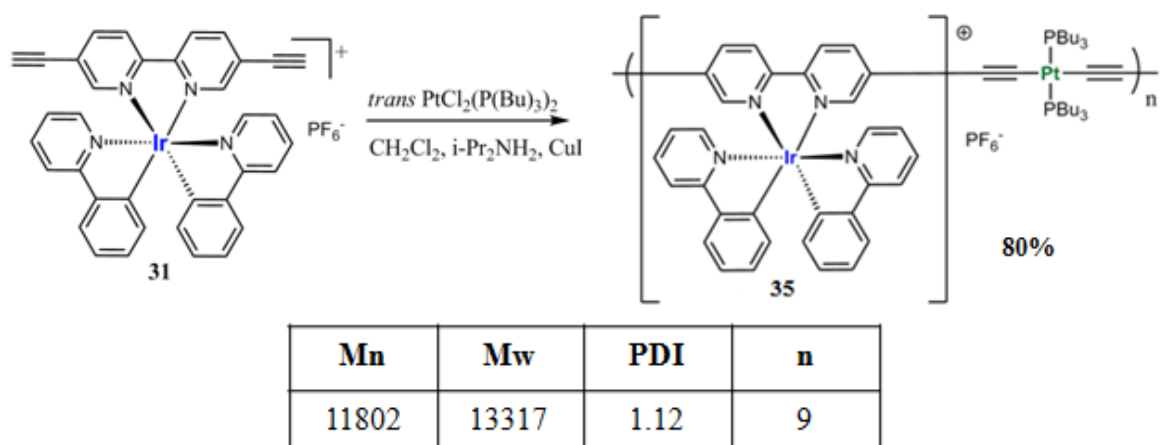


**Figure 1.7.** Synthesis and GPC results of Pt-Ir polymer **35**.

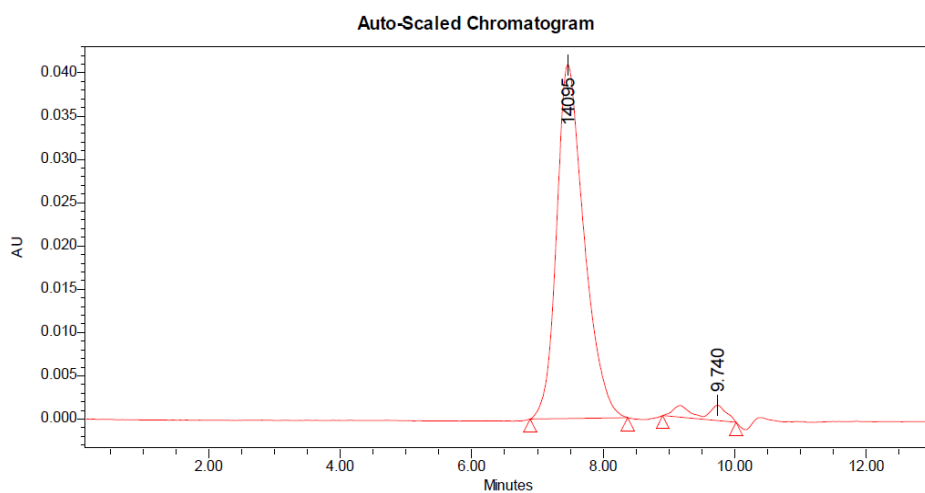


**Figure 1.8.** GPC trace of Pt-Ir oligomer **35**.

## CHAPTER 2: PHOTOPHYSICS AND DFT CALCULATIONS

After the successful preparation and purification of the model complexes and polymers, their photophysical properties were investigated.

Before discussing the photophysical properties of the complexes, some relevant remarks should be made. All samples were prepared in distilled and dried 2-methyltetrahydrofuran (2-MeTHF) for the complexes and HPLC grade acetonitrile (ACN) for the external reference  $[\text{Ru}(\text{bpy})_3](\text{PF}_6)_2$ . The absorption spectra were recorded at room temperature. Steady-state emission spectra were obtained by exciting at the lowest energy absorption maxima. A stock solution with absorbance of ca. 0.5 was prepared and then four dilutions were prepared with dilution factors of 40, 20, 13.3 and 10 to obtain solutions with absorbances of ca. 0.013, 0.025, 0.038 and 0.05, respectively. Then, the emission spectra were measured after the solutions were rigorously degassed with solvent-saturated nitrogen gas ( $\text{N}_2$ ) for 15 minutes prior to spectrum acquisition. A solution of  $[\text{Ru}(\text{bpy})_3](\text{PF}_6)_2$  in ACN ( $\Phi = 9.5\%$ ) was used as the external reference.<sup>60</sup> The experimental uncertainty in the emission quantum yields is conservatively estimated to be 10%. The emission lifetimes were measured on 2 instruments. The first was with a source of nitrogen laser, while the second with a pulsed NanoLED at 341 nm.

In order to get adapted with the instruments for absorption, emission and lifetime measurements, and to make sure that the methodology was correct, a known Ir complex,  $[(\text{ppy})_2\text{Ir}(\text{bpy})]\text{PF}_6$  (**36**), was first studied.<sup>61</sup> Its measurements have been repeated 3 times to make sure that the results were reproducible.

This chapter is divided into 6 sections. The first compares the photophysical properties of the three Ir complexes **36**, **30** and **31**. The second discusses the same properties but with the Pt complexes **16**, **20** and **22**. While the third one focuses on the Pt-Ir-containing complexes **32**, **33** and **34**. Sections 4 and 5 describe the photophysics of the mononuclear complexes and polymers, respectively. The last section deals with the computational studies of selected complexes (TDDFT calculations).



## 2.1 Photophysical Properties of Ir complexes

The absorption spectra of the Ir complexes **36**, **30**, **31** (Figure 2.1) exhibit similar features. The three complexes show intense  $\pi$ - $\pi^*$  high-energy ligand-centred ( $^1$ LC) bands which are attributed to both the phenylpyridines and the bipyridine. The other bands located between 300 and 350 nm are due to  $^1$ MLCT (metal-to-ligand charge transfer) transition from the spin allowed singlet state. The second more red-shifted band between 380 and 420 nm is assigned to spin forbidden  $^3$ MLCT transition.

For the Ir complexes, the absorption maxima is blue shifted compared to the Pt- and Pt-Ir-containing complexes. In Ir complex **31**, this band is observed at 250 nm with a higher molar absorptivity of  $4.2 \times 10^4 \text{ M}^{-1} \text{ cm}^{-1}$  compared to complexes **36** and **30**. The  $^1$ MLCT band for the Ir complex **36** is at 300 nm  $^{60}$  ( $\epsilon = 1.7 \times 10^4 \text{ M}^{-1} \text{ cm}^{-1}$ ) and is blue shifted by 25 nm compared to complex **30** and 15 nm compared to complex **31**. On the other hand, the  $^3$ MLCT band in **36** is red-shifted to 465 nm compared to **30** (450 nm) and **31** (370 nm).

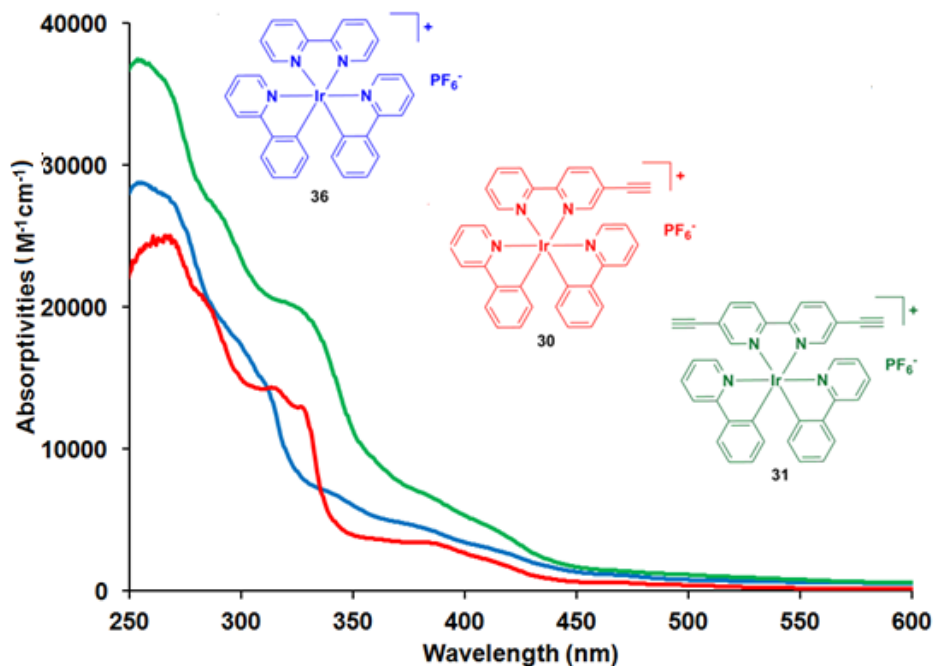


**Figure 2.1.** Absorption spectra of complexes **30**, **31** and **36** in 2-MeTHF at 298K.

The emission peaks at room temperature for the three complexes are broad and featureless (Figure 2.2). The Ir complex **31** exhibits a more red-shifted emission at 638 nm than the other two complexes. This is consistent with the longer extent of the conjugation (2 ethynyls) in complex **31**.

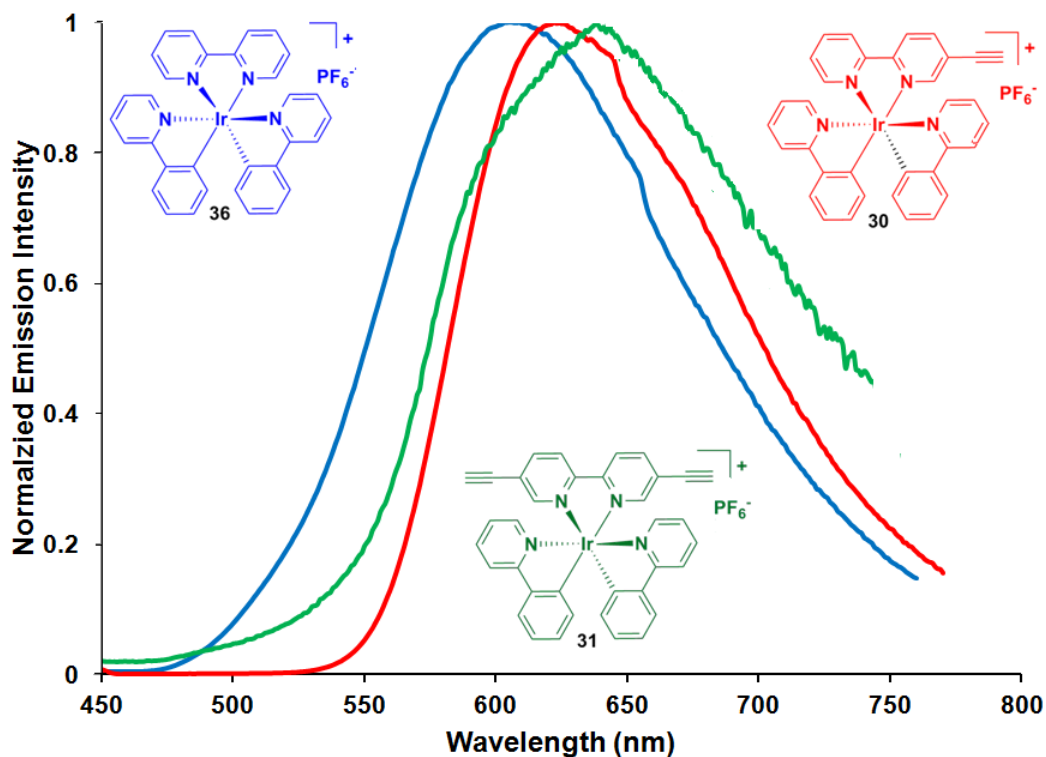


**Figure 2.2.** Emission spectra of **30**, **31** and **36** in 2-MeTHF at 298K.

The emission bands at 77K exhibit close maxima for complexes **36** and **30** at 532 and 536 nm, respectively. However, this emission is red-shifted for complex **31**. The emission band for complex **36** exhibits two maxima at 506 and 532 nm, while it is featureless for the other two complexes. These are of vibronic origin. Figure 2.3 exhibits the emission spectra for these three Ir-containing complexes at 77K.

The large Stokes shift (Table 2.1) at both temperatures (along with the emission lifetimes described below) indicates that the emission originates from the triplet state.

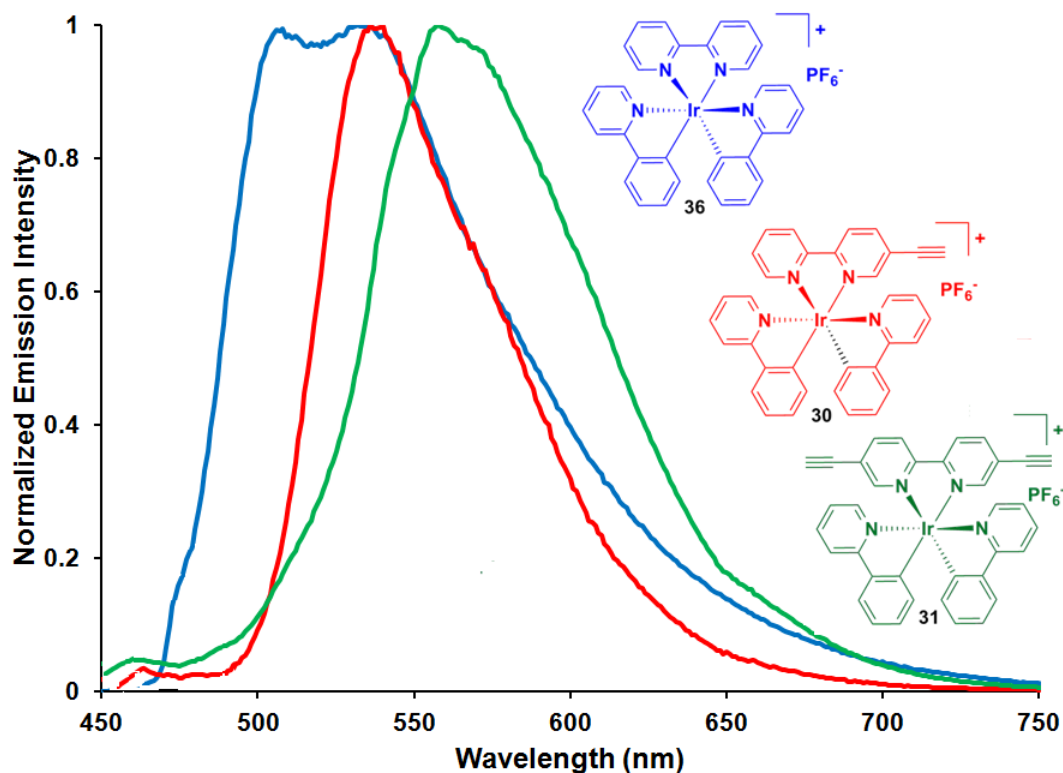


**Figure 2.3.** Emission spectra of **30**, **31** and **36** in 2-MeTHF at 77K.

The behaviour of complex **30** in 2-MeTHF is similar to that reported in dichloromethane by Castellano et *al* in 2010.<sup>62</sup> They reported an emission band at room temperature for such complex placed at 629 nm. They also reported comparable results for the quantum yield and emission lifetime (2.7% and 0.24 ns respectively).

On the other hand, the emission quantum yields for the three complexes compared to external reference ( $[\text{Ru}(\text{bpy})_3](\text{PF}_6)_2$ ,  $\Phi = 9.5\%$ ) increased insignificantly in complex **36** compared to complex **30** and higher in **30** compared to **31**. This result was consistent with the emission lifetime value which is longer for complex **36** (5.8  $\mu\text{s}$  at 77K and 0.55  $\mu\text{s}$  at 298K).

The non-radiative rate constant,  $k_{\text{nr}}$ , for complex **31** is significantly greater than that found for **36**. On the other hand, the radiative rate constant,  $k_{\text{r}}$ , remains within the same range, which is consistent with the fact that the molecular symmetry remained the same ( $C_2$ ,  $C_1$ ,  $C_2$ ). Noteworthy complex **30** exhibits the largest radiative rate constant among these 3 Ir complexes. This complex exhibits the lowest symmetry ( $C_1$ ).

**Table 2.1** Photophysical properties of Ir complexes.

Complex	Absorbance 298 K (nm) [Molar Absorptivities ( $\times 10^4 \text{ M}^{-1} \text{ cm}^{-1}$ )]	$\lambda_{\text{max}}$		Stokes shifts		$\Phi_e$ (%) <sup>a</sup>	$\tau_e$		$k_r$ ( $\times 10^5 \text{ s}^{-1}$ )	$k_{nr}$ ( $\times 10^5 \text{ s}^{-1}$ )
		77K (nm)	298K (nm)	77K ( $\text{cm}^{-1}$ )	298K ( $\text{cm}^{-1}$ )		77K ( $\mu\text{s}$ )	298K ( $\mu\text{s}$ )		
<b>30</b>	265 [2.3]; 310 [1.0]; 325 [0.9]; 380 [0.2]; 450 [0.1]	536	623	2620	5230	8.5	4.12	0.16	5.3	57.2
<b>31</b>	250 [4.2]; 280 [3.3]; 315 [2.3]; 370 [0.8]	558	638	9100	11350	1.6	2.65	0.09	1.8	109
<b>36</b>	255 [2.9]; 300 [1.7]; 355 [0.6]; 370 [0.4]; 465 [0.1]	532	607	2710	5030	8.9	5.82	0.55	1.6	16.6

<sup>a</sup>Measured in 2-MeTHF using  $\text{Ru}(\text{bpy})_3(\text{PF}_6)_2$   $\Phi = 9.5\%$  in ACN.

## 2.2 Photophysical properties of Pt complexes

The 3 Pt complexes **16**, **20**, **22** are characterized by the presence of strong 0-0 absorption band. Complex **22** exhibits an absorption band that is more red shifted compared to the other 2 complexes. This band is in the same range as for **20** and **16**. Complex **16** exhibits a higher molar absorptivities of  $6.0 \times 10^4 \text{ M}^{-1} \text{ cm}^{-1}$  compared to  $4.7 \times 10^4 \text{ M}^{-1} \text{ cm}^{-1}$  for **20**. The 0-0 transition peak for complex **22** is attributed to the presence of the CT-band of the Pt acetylide unit<sup>63</sup> which absorbs light intensely at 370 nm ( $\epsilon = 7.7 \times 10^4 \text{ M}^{-1} \text{ cm}^{-1}$ ).

The other characteristic band is the the  $\pi - \pi^*$  high-energy ligand-centred (<sup>1</sup>LC) one. It can be seen at 265 nm for complexes **20** and **22** with molar absorptivity equal to  $4.1 \times 10^4 \text{ M}^{-1} \text{ cm}^{-1}$  of the later. This band is blue shifted at 250 nm for complex **16**.

Schanze and his co-workers characterized photophysically Pt complex **37** (Figure 2.4).<sup>48</sup> The complex has a similar structure of complex **22** with the exception of the aryl-CH<sub>3</sub> tag groups. Complex **37** exhibits a narrow absorption band and a maximum absorption at 379 nm with a molar absorptivity of  $\sim 9 \times 10^4 \text{ M}^{-1} \text{ cm}^{-1}$  which is comparable to our results for complex **22**.

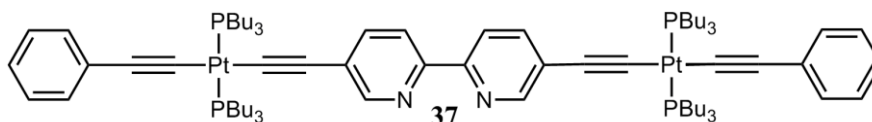


**Figure 2.4.** Structure of complex **37** characterized photophysically by Schanze et al.<sup>48</sup>

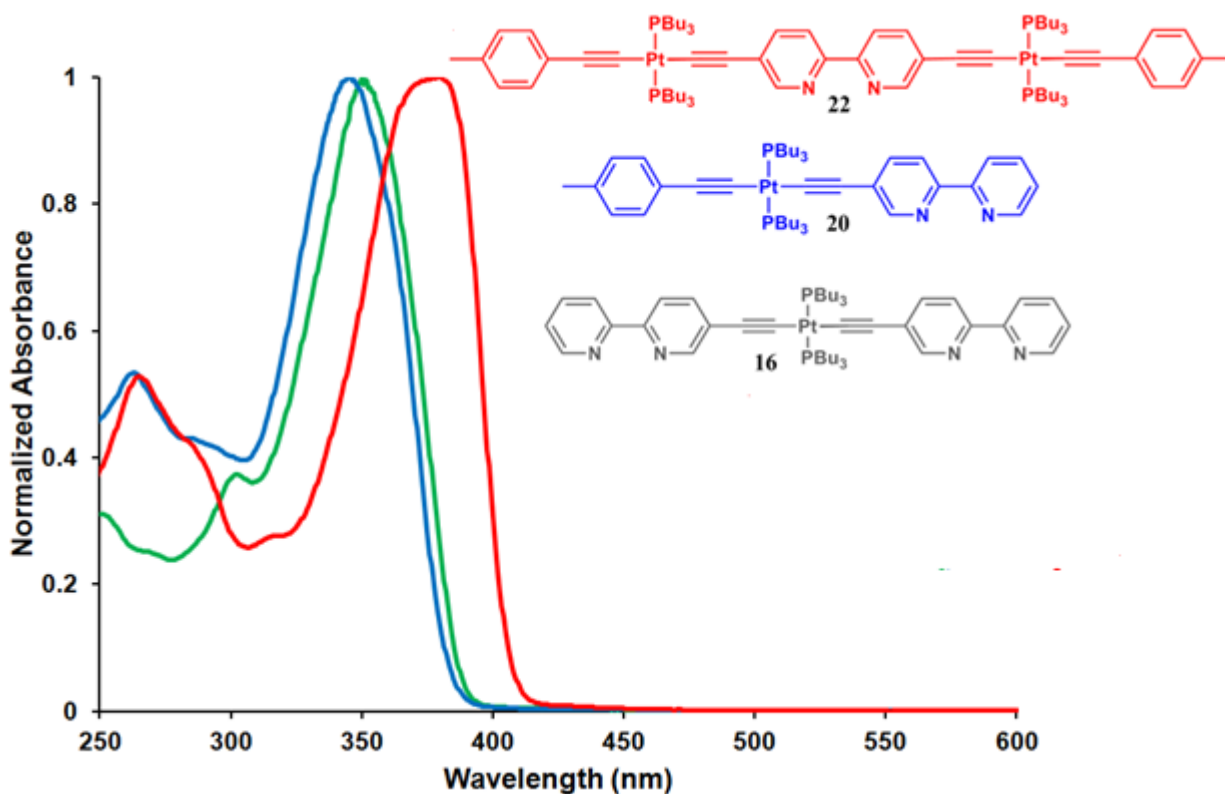


**Figure 2.5.** Absorption spectra of complexes **16**, **20** and **22** in 2-MeTHF at 298 K.

The 3 Pt-complex emission spectra are characterized by a shoulder in addition to their maximum emission bands. The emission peaks for complexes **16** and **20** are the same. Both emits at 516 and 519 nm, respectively, and with a shoulder at 549 nm for both.

On the other hand, Pt-complex **22** shows a bathochromic shift compared to the other Pt-complexes due to a more extensive conjugation for such complex (**22**) owing to the presence of 4 aryl rings. The complex emits at 561 nm with shoulder at 600 nm. The value difference between the emission maximum and the shoulder shows that the stretching frequency is attributed to the aromatic moiety ( $\sim 1100 \pm 50 \text{ cm}^{-1}$ ). Compound **37** exhibits a similar feature compared to **22** with a maximum at 562 nm and a shoulder at 610 nm.

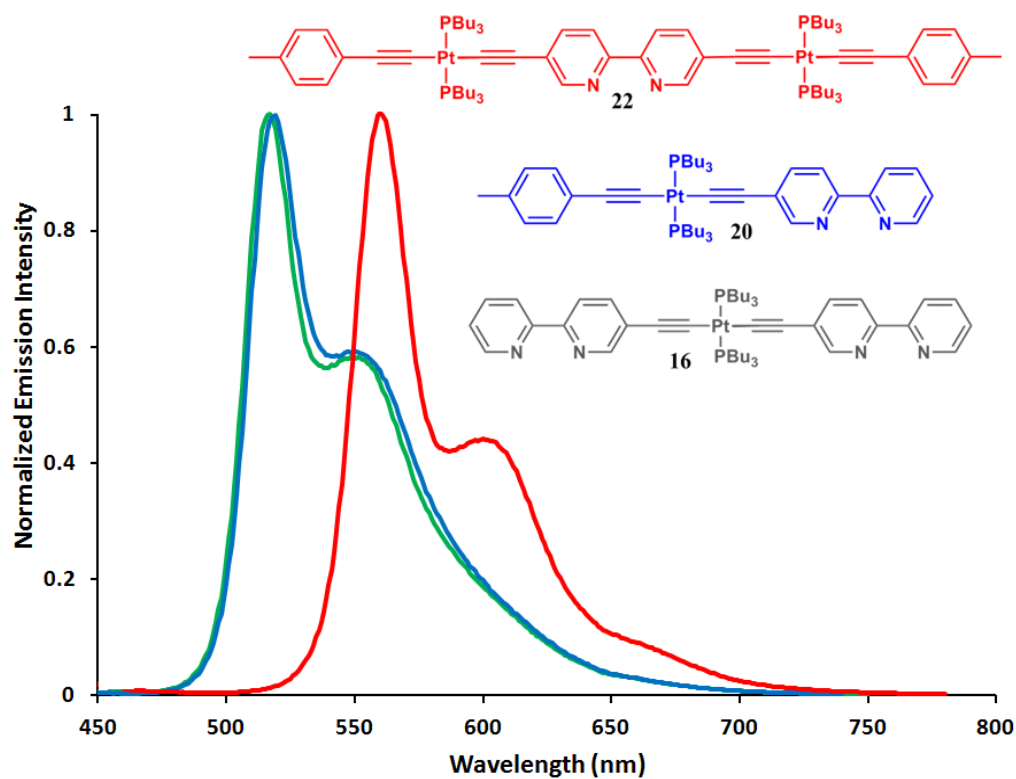


**Figure 2.6.** Emission spectra of **16**, **20** and **22** in 2-MeTHF at 298K.

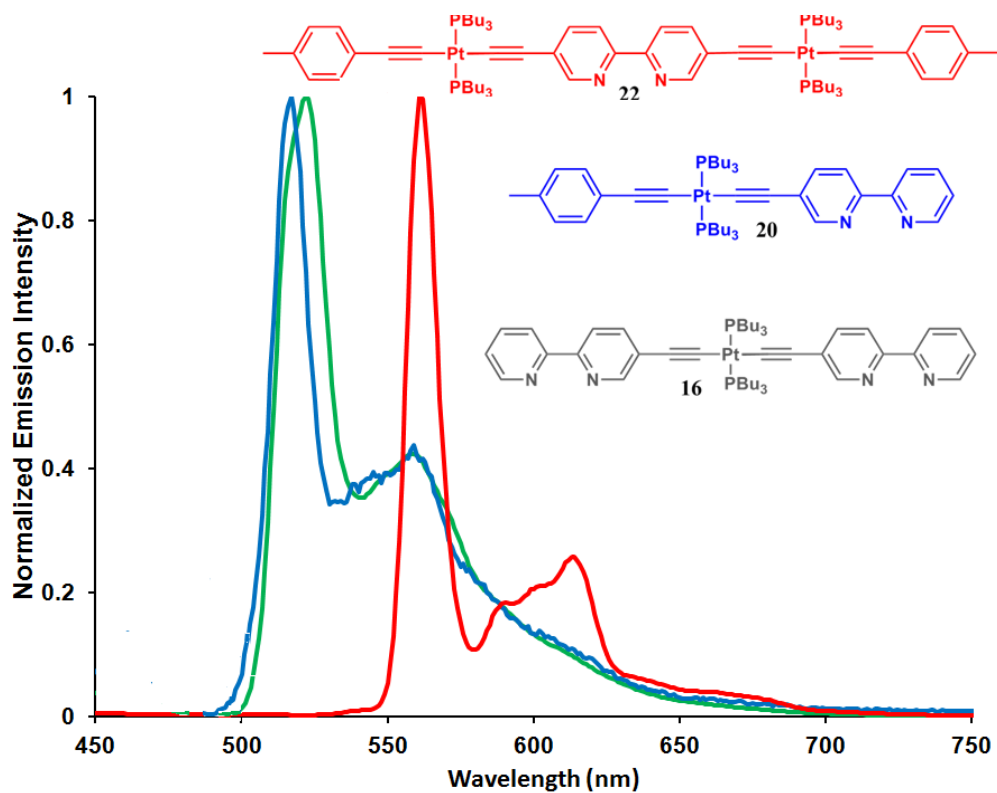


**Figure 2.7.** Emission spectra of **16**, **20** and **22** in 2-MeTHF at 77K.

The emissions at 77K are similar to those at 298K. Complex **16** is slightly red-shifted by 5 nm compared to complex **20**. Complexes **20** and **22** exhibit almost identical emission maxima at both temperatures but it is slightly red-shifted for complex **16** at 77K than 298K.

**Table 2.2.** The calculation of the energy difference between the peak and shoulder positions in the emission spectra of **16**, **20** and **22** in 2-MeTHF at 298 K.

Pt-complex	Wavelength 1 (nm)	Wavelength 2 (nm)	$\Delta E(\text{cm}^{-1})$
<b>16</b>	522	549	1165
<b>20</b>	517	549	1053
<b>22</b>	561	600	1159

The Pt-containing complexes exhibit larger quantum yields and longer emission lifetimes compared to the Ir ones. The emission quantum yields are in the 12.5-14.4 % range. The emission lifetimes at room temperature for **16**, **20** and **22** are very similar, from 150  $\mu\text{s}$  for **16** to 155  $\mu\text{s}$  for **20**. Furthermore, at 77K, the emission lifetimes range in a small window from 33.8 for **16** to 39.2  $\mu\text{s}$  for **22**.

Compound **37** shows a similar a quantum yield at room temperature compared to that for **22**. However, the lifetime was almost double for **37**. The lifetime measurements for compound **22** has been repeated twice in order to reproduce and confirm the results. Table **2.3** shows some of the photophysical properties of complex **37**,<sup>48</sup> while Table **2.4** for Pt-containing complexes.

**Table 2.3.** Photophysical properties for complex **37**.<sup>48</sup>

Compound	$\lambda_{\text{abs}}/(\text{nm})$	$\lambda_{\text{em}}/(\text{nm})$	$\Phi\%$	$\tau(\mu\text{s})$
Pt <sub>2</sub> BPyPh <sub>2</sub>	379	562, 610	12	85

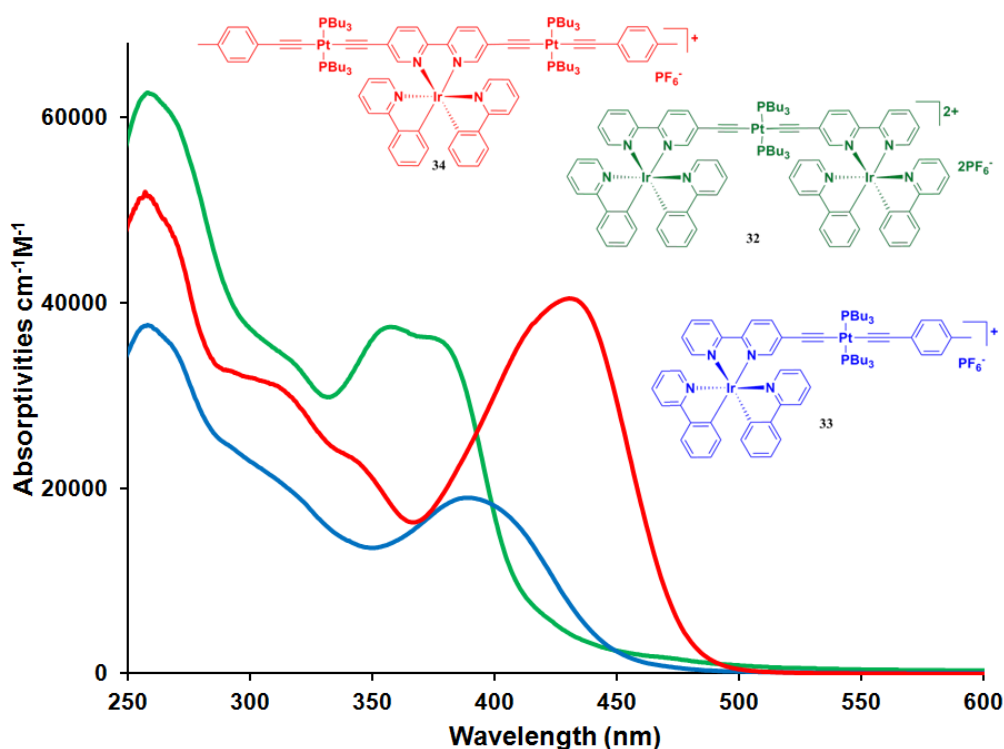
**Table 2.4.** Photophysical properties of complexes **16**, **20** and **22**.

Complex	Absorbance 298 K (nm) [Molar Absorptivities ( $\times 10^4 \text{ M}^{-1} \text{ cm}^{-1}$ )]	$\lambda_{\text{max}}$		Stokes shifts		$\Phi_e$ (%) <sup>a</sup>	$\tau_e$		$k_r$ ( $\times 10^5 \text{ s}^{-1}$ )	$k_{nr}$ ( $\times 10^5 \text{ s}^{-1}$ )
		77K (nm)	298K (nm)	77K ( $\text{cm}^{-1}$ )	298K ( $\text{cm}^{-1}$ )		77K ( $\mu\text{s}$ )	298K ( $\mu\text{s}$ )		
16	250 [1.8]; 265 [1.4]; 300 [2.1]; 350 [6.0]	522	516	9414	9192	14.4	150	33.8	0.02	0.3
20	240 [1.7]; 260 [2.4]; 280 [2.0]; 345 [4.7]	517	519	9640	9720	12.5	155	33.6	0.04	0.3
22	265 [4.1]; 280 [3.5]; 305 [2.0]; 370 [7.7]	561	561	9200	9200	13.7	153	39.2	0.04	0.3

<sup>a</sup>Measured in 2-MeTHF using  $\text{Ru}(\text{bpy})_3(\text{PF}_6)_2$   $\Phi = 9.5\%$  in ACN.

### 2.3 Photophysical properties of the Pt-Ir-containing complexes

After the photophysical characterization of the Ir and Pt-complexes, the mixed-metal Pt-Ir targets were also studied. Figure 2.8 shows the absorption spectra of the 3 Pt-Ir-containing complexes. Complex **34** exhibits a <sup>3</sup>MLCT band that is red-shifted compared to that for complex **32** and **33**. While this band is blue-shifted to 350 nm for complex **32** with respect to the other complexes and shows a shoulder at 370 nm. Complexes **32** and **33** exhibit the same absorptivity ( $\epsilon = 4 \times 10^4 \text{ M}^{-1} \text{ cm}^{-1}$ ) at the 0-0 peak of the <sup>3</sup>MLCT band.

**Figure 2.8.** Absorption spectra of Pt-Ir-containing complexes in 2-Me-THF at 298 K.



All complexes exhibit a moderately structured emission band at room temperature (Figure 2.9). For complexes **32** and **33**, the peak maxima and shoulders are respectively placed at 566 and 595 nm, and 572 and 611 nm. For complex **34**, these features appear at 623 and 670 nm clearly showing a red-shift, again consistent with the extension of the conjugation.

The emission bands measured at 77K for all the Pt-Ir-containing complexes also exhibit vibronic structure. Both complexes **33** and **34** have a similar emission maximum at 549 nm (Figure 2.10).

The photophysical parameters for Pt-Ir-containing complexes are placed in Table 2.5. The Stoke shifts along with the long emission lifetimes (microseconds) indicate that these emissions arise from the triplet state (phosphorescence). The quantum yield for complex **33** is twice as large compared to complex **34**, which are respectively 8.3 and 4.0%.

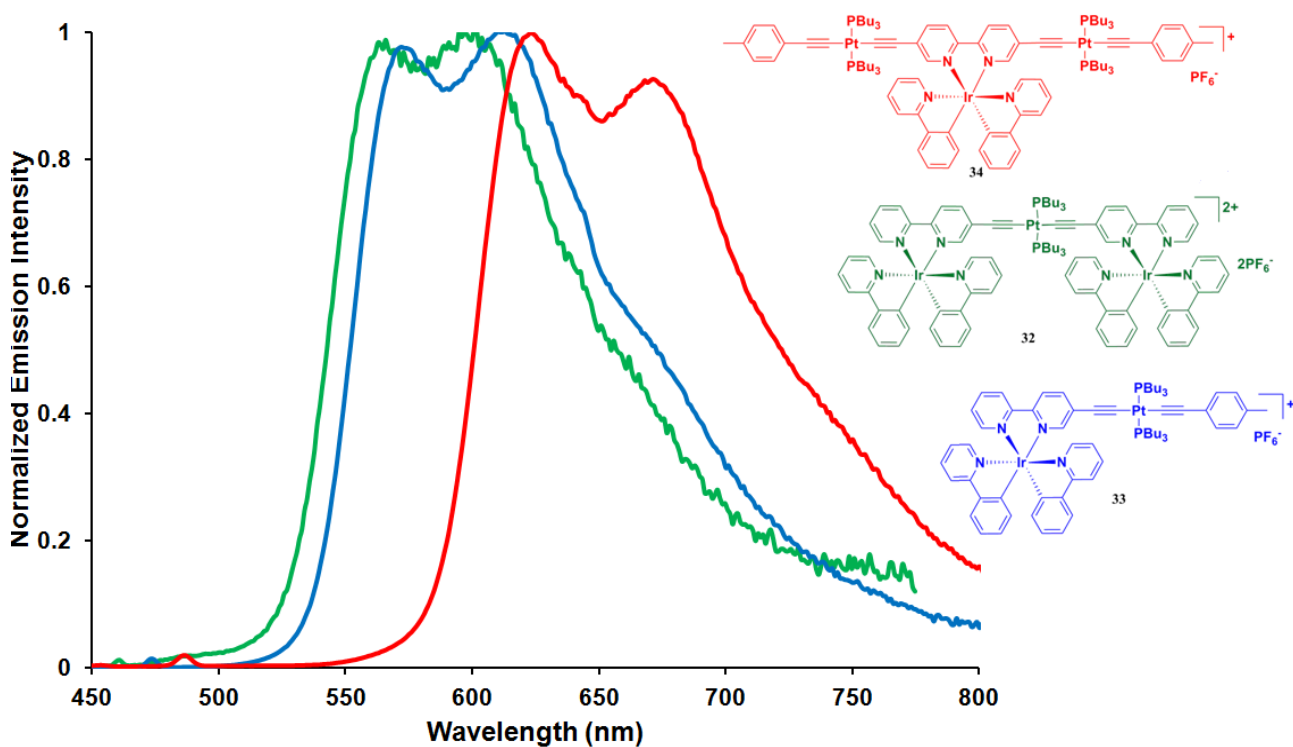


**Figure 2.9.** Emission spectra of compounds **32-34** in 2-MeTHF at 298K.

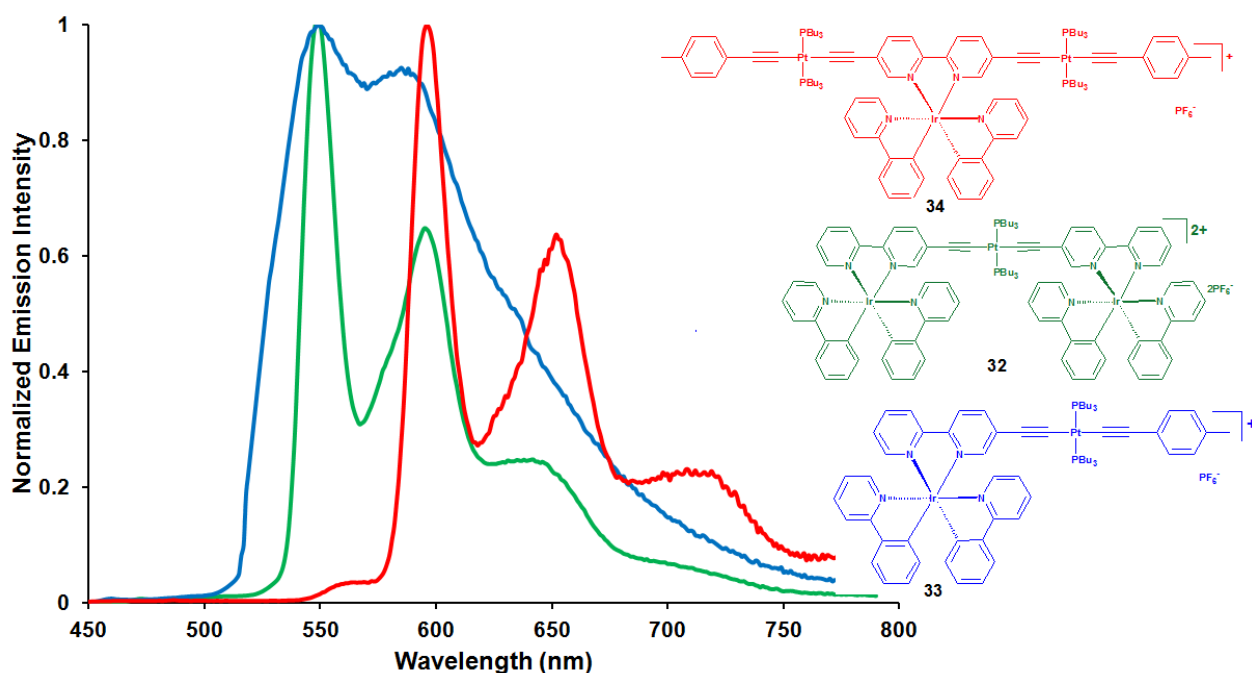


**Figure 2.10.** Emission spectra of compounds **32-34** in 2-MeTHF at 77K.

The emission lifetimes are again in order of microsecond time scale, with a larger value of 2.9 for complex **32** and a lower value of 0.73 for complex **33** at 298K. The nonradiative rate constant is maximum for complex **33**,  $12.7 \times 10^5 \text{ s}^{-1}$ , and minimum for complex **32**. The emission quantum yields and the radiative and non radiative constants for complex **32** present interesting photophysical properties.

**Table 2.5.** Photophysical properties of the Pt-Ir-containing complexes.

Complex	Absorbance 298 K (nm)	$\lambda_{\text{max}}$		Stokes shifts		$\Phi_e$ (%) <sup>a</sup>	$\tau_e$		$k_r$ ( $\times 10^5 \text{ s}^{-1}$ )	$k_{\text{nr}}$ ( $\times 10^5 \text{ s}^{-1}$ )
	[Molar Absorptivities ( $\times 10^4 \text{ M}^{-1} \text{ cm}^{-1}$ )]	77K (nm)	298K (nm)	77K ( $\text{cm}^{-1}$ )	298K ( $\text{cm}^{-1}$ )		77K ( $\mu\text{s}$ )	298K ( $\mu\text{s}$ )		
<b>32</b>	260 [6.8]; 300 [4.1]; 350 [4.0]; 370 [4.0]; 460 [0.2]	547	595	3460	4930	31.9	11.0	2.90	0.9	2.6
<b>33</b>	260 [3.6]; 295 [2.00]; 390 [1.9]; 450 [0.2]	549	611	4007	5856	8.3	3.44	0.72	1.2	12.7
<b>34</b>	260 [4.9]; 310 [2.7]; 345 [1.9]; 425 [4.0]	549	623	5310	7480	4.0	4.66	1.33	0.3	7.2

<sup>a</sup>Measured in 2-MeTHF using  $\text{Ru}(\text{bpy})_3(\text{PF}_6)_2$   $\Phi = 9.5\%$  in ACN.

## 2.4 Comparison of the photophysical properties of Pt, Ir and Pt-Ir complexes

This section presents comparison of the Pt (**16** and **20**) and Ir complexes (**30** and **36**) with those for the Pt-Ir complexes (**32** and **33**). It will be shown that the Pt-Ir-containing complexes exhibit hybrid excited states.

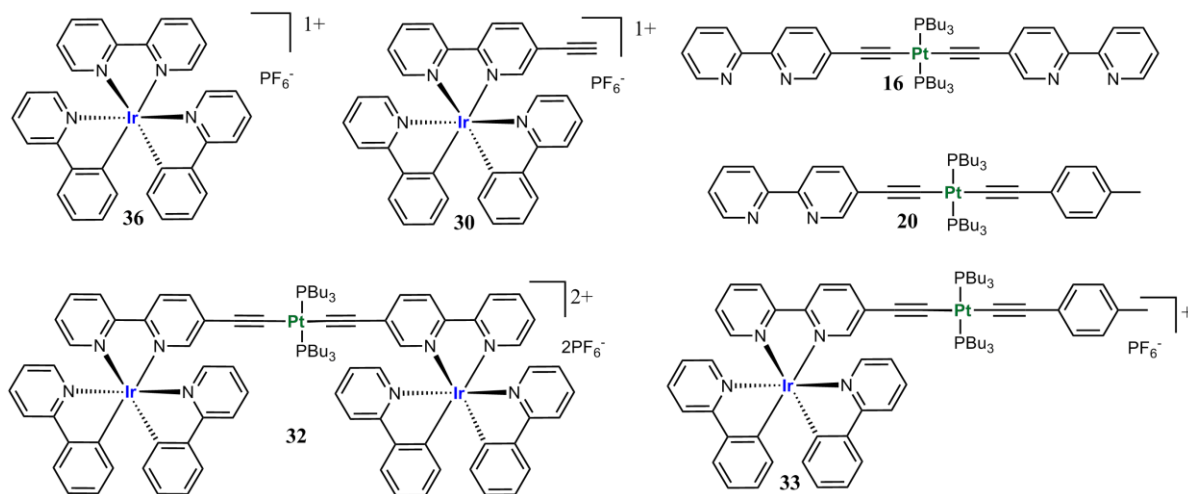


**Figure 2.11.** Structures of the complexes described in this section.

Figure 2.12 compares the absorption spectra for the 6 complexes placed in Figure 2.11 for convenience. The 2 Ir complexes, **30** and **36**, show very similar absorption pattern and has previously been discussed in section 3.1. Upon comparing these complexes with the 2 Pt complexes, **16** and **20**, we observe that the intensities (i.e. absorptivity) of the LC and MLCT bands are very different.

The  $\pi$ - $\pi^*$  high-energy ligand-centred ( $^1\text{LC}$ ) at 250 nm is more intense for the Ir complexes than for the Pt ones. Indeed, this band is stronger for the Ir complexes and exhibits molar coefficients of  $2.9 \times 10^4$  and  $2.3 \times 10^4 \text{ M}^{-1}\text{cm}^{-1}$  for **36** and **30** respectively, while reaching  $1.8 \times 10^4 \text{ M}^{-1}\text{cm}^{-1}$  for the 2 Pt complexes.

The  $^1\text{MLCT}$  band for Pt complexes is very intense with a maximum absorption at 350 nm. However, the analogous band is red-shifted (around 400 nm) and weaker for the Ir complexes (Figure 2.12).

The absorption data for the Pt-Ir-containing complexes exhibit intermediate properties between those for the Pt and Ir complexes. The absorption intensity of the  $\pi$ - $\pi^*$  ligand-centred ( $^1\text{LC}$ ) band at 250

nm for complex **33** is closer in magnitude to those of the Ir complexes. Upon an addition of an Ir center to the structure (complex **32**), the intensity of this band is increased to  $6.8 \times 10^4 \text{ M}^{-1}\text{cm}^{-1}$ .

The  $^1\text{MLCT}$  band for the Pt-Ir-containing complexes have increased compared to those for the Ir complexes. Complex **32** has a molar coefficient twice as large compared to **33**, and the latter complex has a molar coefficient 5 times more than that for complex **36** and 10 times more than that for complex **30** at 370 and 380 nm. This band is more red-shifted for the Pt-Ir complexes than those for the Pt-ones.

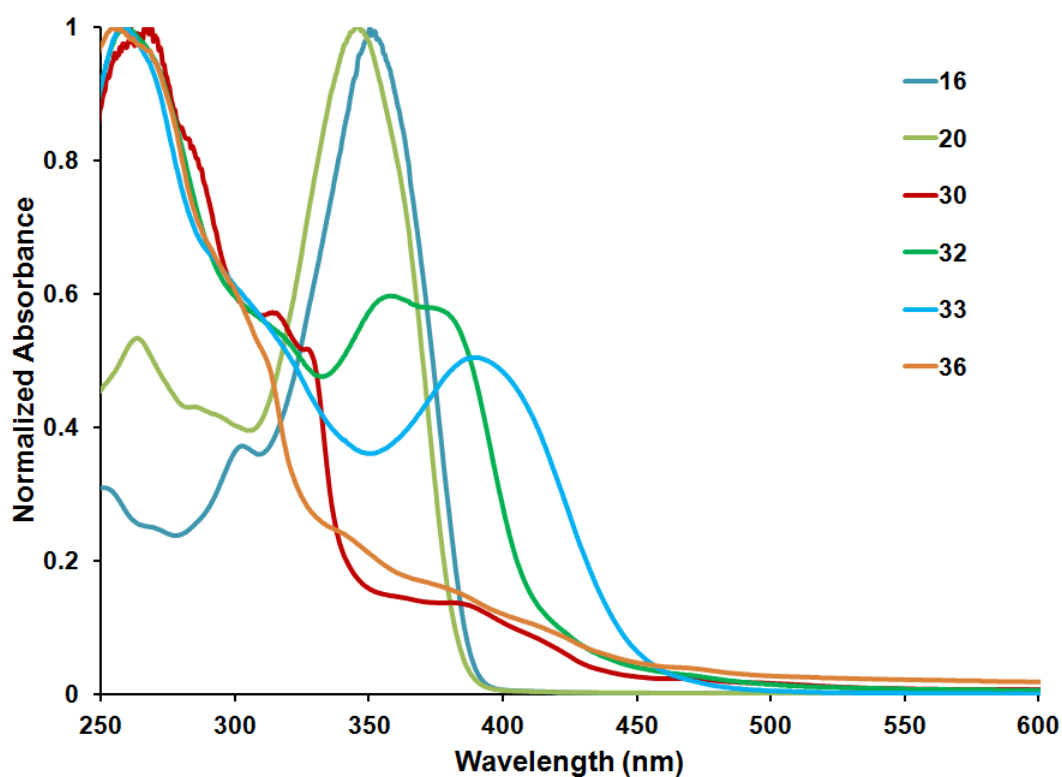


**Figure 2.12.** Absorption spectra of **16**, **20**, **30**, **32**, **33**, and **36** in 2-MeTHF at 298K.

The emission spectra for **16**, **20**, **30**, **32**, **33**, and **36** in 2-MeTHF at 298K are shown in Figure 2.12. The 2 Pt-complexes bands almost superimpose and have a shoulder at lower energy. The most red-shifted bands are those for the Ir complexes, **30** and **36**. The Pt-Ir complexes **32** and **33** exhibit a moderate vibronic progression. The emission maxima for these complexes lies between those for the Pt and Ir complexes, being at 595 nm for complex **32** and 611 nm for complex **33**. The Stokes shifts

at room temperature and 77K indicate that the emission occurs from the triplet state (i.e. phosphorescence).

The comparison slightly differs at 77K (Figure 2.14). The emission maxima blue shift by ~70 and 80 nm going from 298K and 77K for Ir complexes. No difference is noted for the Pt complexes. For the Pt-Ir complexes, the temperature-induced blue shift is only ~50 to 60 nm, which is an intermediate value between those observed for the Ir and Pt complexes.

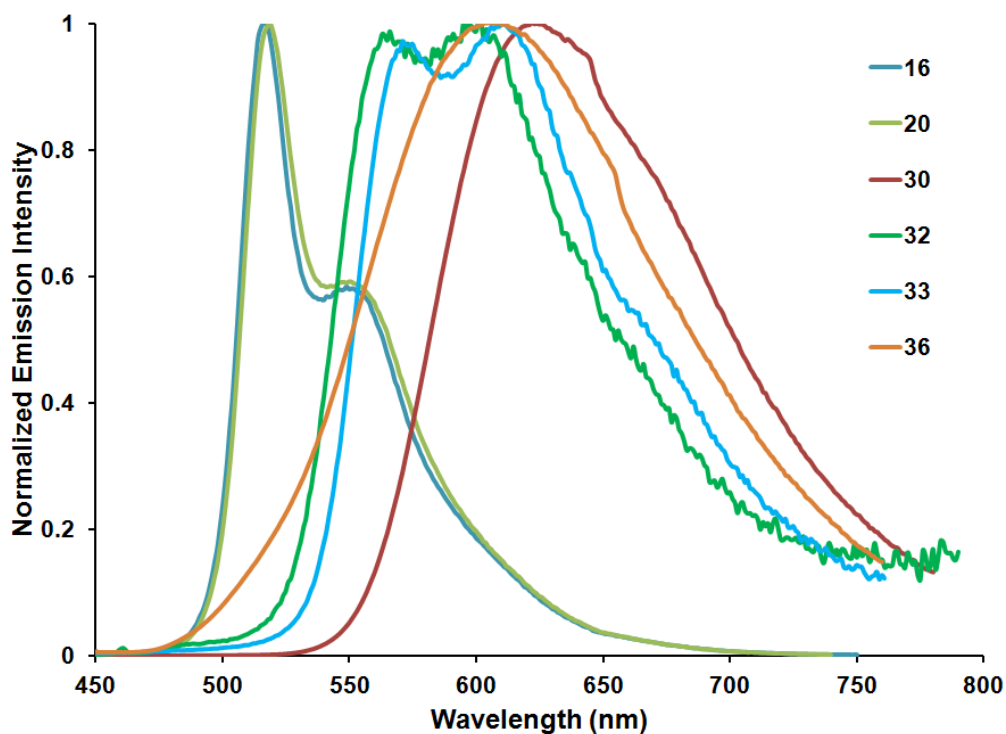


**Figure 2.13.** Emission spectra of **16**, **20**, **30**, **32**, **33**, and **36** in 2-MeTHF at 298K.

These investigated complexes exhibit emission quantum yields ranging between 8 and 15%, except complex **32**, which exhibits the highest value at 32%.

Noteworthy, the emission lifetimes for the Pt-Ir-containing complexes at room temperature also corroborate the fact that these complexes exhibit hybrid properties between those for the Pt and Ir complexes. The nonradiative rate constant is the highest for complex **30**, while the highest radiative one is noted for complex **16**.

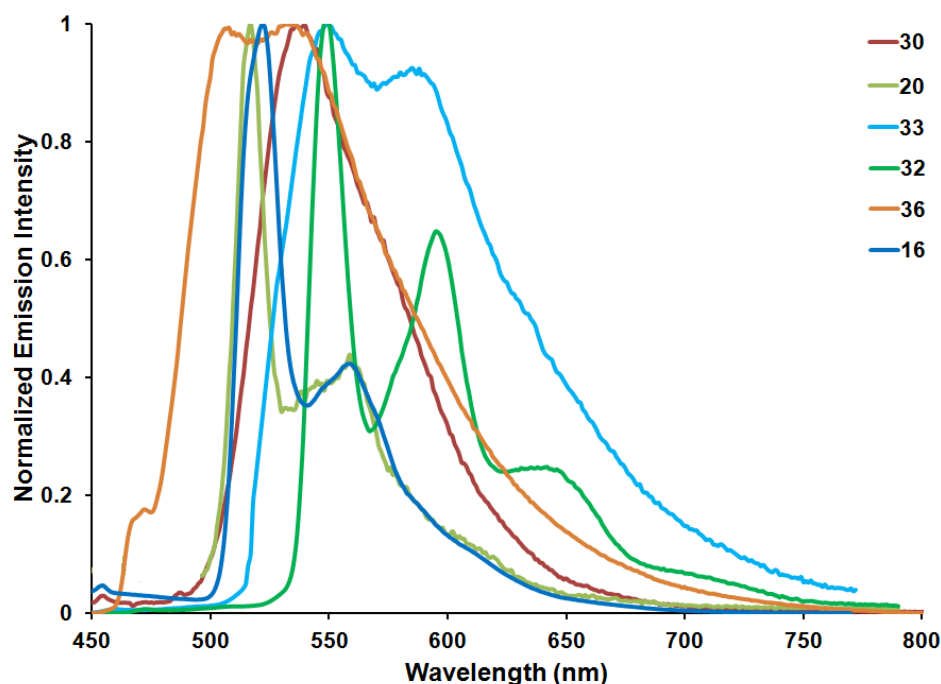


**Figure 2.14.** Emission spectra of **16**, **20**, **30**, **32**, **33**, and **36** in 2-MeTHF at 77K.

To conclude this section, the incorporation of a Pt moiety to the Ir complexes creates heterometallic complexes that possess hybrid photophysical behaviour and a blue shift of the emission bands compared to Ir complex **30** is observed. The emission lifetimes were significantly longer for the hybrids while emission quantum yields and molar absorptivities for the Pt-Ir-containing complex **32** are remarkably increased (Table 2.6)

**Table 2.6.** Photophysical properties of compounds **16**, **20**, **30**, **32**, **33**, and **36**:

Complex	Absorbance 298 K (nm)	$\lambda_{\max}$		Stokes shifts		$\Phi_e$ (%) <sup>a</sup>	$\tau_e$		$k_r$ ( $\times 10^5 s^{-1}$ )	$k_{nr}$ ( $\times 10^5 s^{-1}$ )
	[Molar Absorptivities ( $\times 10^4 M^{-1} cm^{-1}$ )]	77K (nm)	298K (nm)	77K ( $cm^{-1}$ )	298K ( $cm^{-1}$ )		77K ( $\mu s$ )	298K ( $\mu s$ )		
<b>16</b>	250 [1.8]; 265 [1.4]; 300 [2.1]; 350 [6.0]	522	516	9414	9192	14.4	150	33.8	0.02	0.3
<b>20</b>	240 [1.7]; 260 [2.4]; 280 [2.0]; 345 [4.7]	517	519	9640	9720	12.5	155	33.6	0.04	0.3
<b>30</b>	265 [2.3]; 310 [1.0]; 325 [0.9]; 380 [0.2]; 450 [0.1]	536	623	2620	5230	8.5	4.12	0.16	5.3	57.2
<b>32</b>	260 [6.8]; 300 [4.1]; 350 [4.0]; 370 [4.0]; 460 [0.2]	547	595	3460	4930	31.9	11.0	2.90	0.9	2.6
<b>33</b>	260 [3.6]; 295 [2.00]; 390 [1.9]; 450 [0.2]	549	611	4007	5856	8.3	3.44	0.72	1.2	12.7
<b>36</b>	255 [2.9]; 300 [1.7]; 355 [0.6]; 370 [0.4]; 465 [0.1]	532	607	2710	5030	8.9	5.82	0.55	1.6	16.6

<sup>a</sup>Measured in 2-MeTHF using  $Ru(bpy)_3(PF_6)_2$   $\Phi = 9.5\%$  in ACN.

## 2.5 Comparison of the photophysical Properties of monomers (31, 22, 34, ) and polymers (24 and 35)

This section focuses on the comparison of the photophysical between the Ir complex **31**, the Pt complex **22**, the Pt-Ir complex **34**, the Pt polymer **24** and the Pt-Ir polymer **35**.

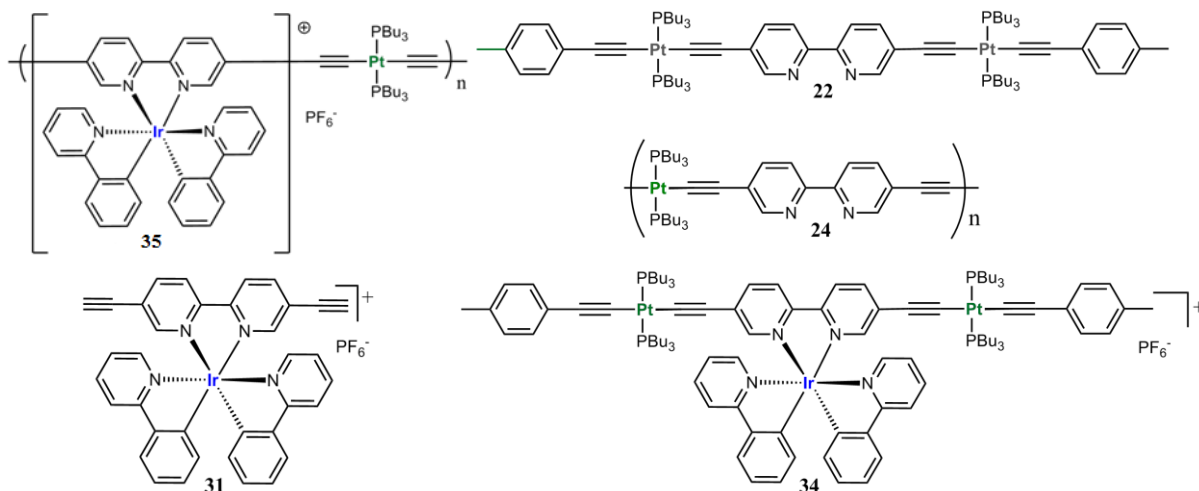


**Figure 2.15.** Structure of the complexes described in this section.

Complexes **31**, **22** and **34** exhibit a high-energy ligand-centred  $\pi$ - $\pi^*$  ( $^1$ LC) band at 250 nm with absorptivities ranging from  $4.1 \times 10^4$  to  $4.9 \times 10^4 \text{ M}^{-1}\text{cm}^{-1}$ . This band is red-shifted and featureless for Ir complex **31**. The  $^1$ MLCT band for complexes **31** and **22** are found at 370 nm. The absorptivities differ ( $7.7 \times 10^4$  and  $0.8 \times 10^4 \text{ M}^{-1}\text{cm}^{-1}$  for complexes **22** and **31**, respectively). Complex **31** exhibits an absorption maximum at 250 nm whereas it is seen 370 nm and 260 nm for complexes **31** and **34** respectively.

Concurrently, complex **22** and polymer **24** exhibit similar absorption features (Figure 2.16). The  $^3$ MLCT band is red-shifted by 20 nm for polymer **24** (390 nm), which is consistent with the extension of the conjugation compared to the model complex **22**.

The Pt-Ir-containing polymer **35** also exhibits similar absorption features to the Pt-Ir model complex **34**, but with some minor differences. The 0-0 peak is red-shifted by 10 nm for polymer **35** compared to model **34** due to the more extensive conjugation for the polymer. Generally, polymers exhibit lower absorptivities compared to the mononuclear complexes.

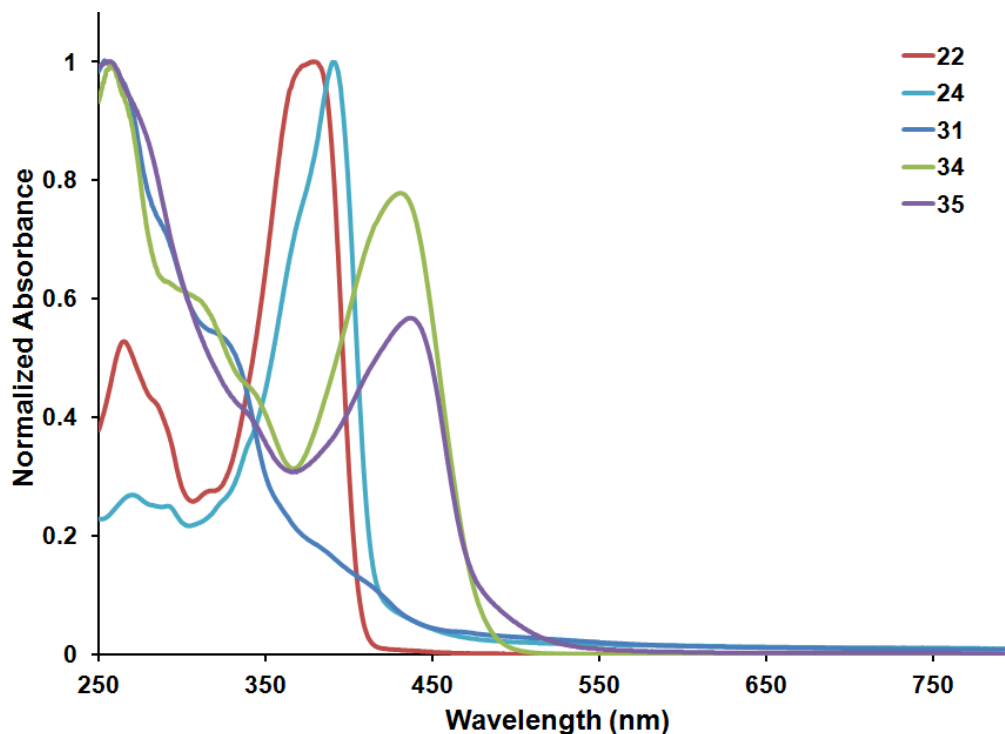


**Figure 2.16.** Comparison of the absorption spectra of **22**, **24**, **31**, **34** and **35** in 2-MeTHF at 298 K.

The emission spectra for the Ir complex **31** at room temperature is red-shifted to 638 nm compared to the other mononuclear complexes and polymers. The resulting emission at room temperature for Pt-Ir-containing complexes **35** and **34** is red-shifted and moderately structured compared to Pt-containing complexes **22** and **24**. Both Pt-mononuclear complex **22** and Pt polymer **24** have the same emission features and their emission maximum is the same at 561 nm. As mentioned in Section 3.2, all Pt-containing complexes exhibit a moderately structure a vibronic progression which can also be seen for polymer **24**. The only slight difference is that the shoulder of Pt-polymer emission (**24**) is red-shifted compared to that for model **22** and it is higher in intensity. The emission band of the Pt-Ir-containing polymer is blue-shifted by 6 nm (617 nm) compared to the Pt-Ir complex **34**.



These 5 complexes and polymers exhibit a similar range of emission at 77K (Figure 2.18). These values range from 549 nm for the Pt-Ir complex **34** and 563 nm for the Pt-Ir polymer **35**. The emission band of the Ir-containing compounds is significantly blue-shifted at 77 K, whereas those for the Pt-containing ones are not. Figure 2.17 shows the emission traces at room temperature for the 5 complexes and polymers. The spectral features of the mixed-metal Pt-Ir-containing compounds (**34** and **35**) best describe the behaviour of the formation of a hybrid emissive excited state, which is composed of features from both Ir- and Pt-containing chromophores.

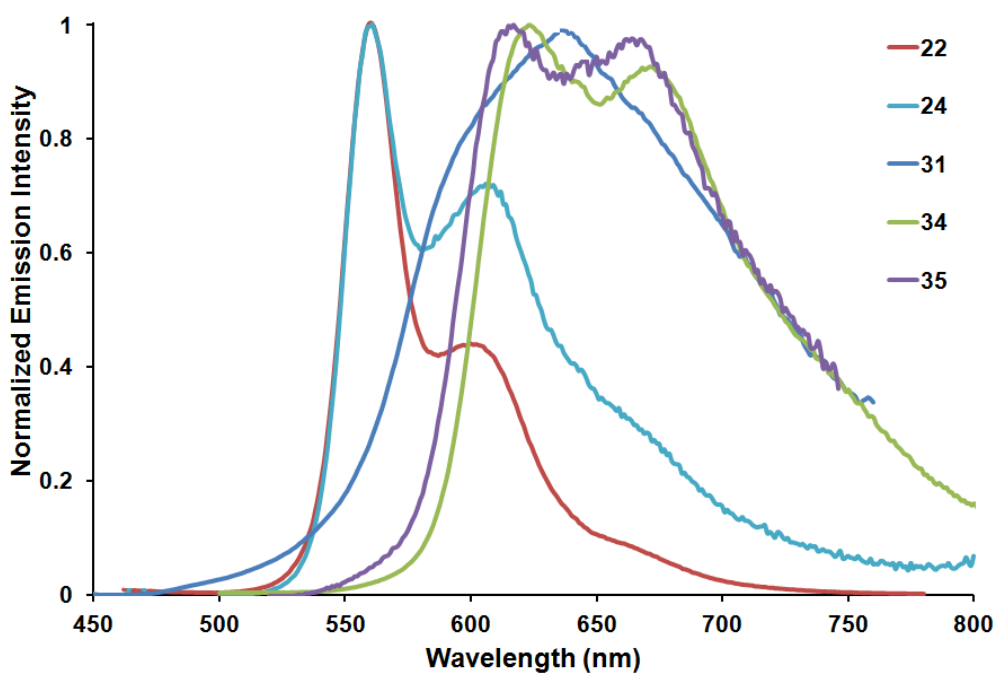


**Figure 2.17.** Comparison of the emission spectra of **22**, **24**, **31**, **34** and **35** in 2-MeTHF at 298K.

The hybrid behaviour has also been confirmed through the emission quantum yields and lifetimes (Table 2.7). For the Ir complex **31** and Pt complex **22**, the values of the emission quantum yields and lifetimes exhibit 2 extremes, low for the Ir complex and high for the Pt one, whereas these values lie in between the ones for Ir and the Pt complexes for the Pt-Ir-containing complex **34**.

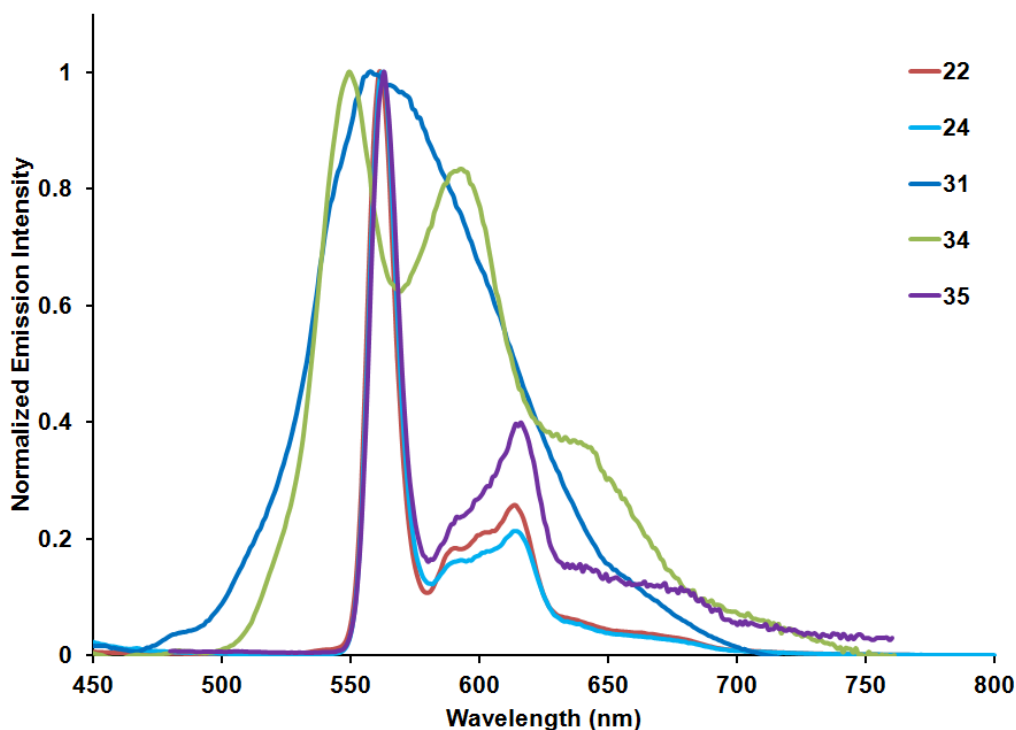


**Figure 2.18.** Comparison of the emission spectra of **22**, **24**, **31**, **34** and **35** in 2-MeTHF at 77K.

The emission quantum yields and lifetimes are slightly lower for polymers **24** and **35** compared to their monomers (**22** and **34**). This is simply due to an increase in non-radiative rate constants ( $k_{nr}$ ) as a result of the larger mass of the chromophore and the addition of flexible groups (such as the *n*-butyls) as a source of non-radiative pathways for deactivation of the emissive excited states (vibration and rotation). However, the decrease in  $k_{nr}$  for **35** compared to **34** is very modest, making **35** an attractive as a material in display applications. This phenomenon may be due to the relative rigidity of the polymer backbone.

**Table 2.7.** Photophysical properties of **22**, **24**, **31**, **34** and **35**.

Complex	Absorbance 298 K (nm)	$\lambda_{max}$		Stokes shifts		$\Phi_e$ (%) <sup>a</sup>	$\tau_e$		$k_r$ ( $\times 10^5 s^{-1}$ )	$k_{nr}$ ( $\times 10^5 s^{-1}$ )
	[Molar Absorptivities ( $\times 10^4 M^{-1} cm^{-1}$ )]	77K (nm)	298K (nm)	77K ( $cm^{-1}$ )	298K ( $cm^{-1}$ )		77K ( $\mu s$ )	298K ( $\mu s$ )		
<b>22</b>	265 [4.1]; 280 [3.5]; 305 [2.0]; 370 [7.7]	561	561	9200	9200	13.7	153	39.2	0.04	0.3
<b>24</b>	253 [0.4]; 270 [0.3]; 295 [0.3]; 390 [1.2]	562	561	7850	7820	12.8	70	9.2	0.14	0.95
<b>31</b>	250 [4.2]; 280 [3.3]; 315 [2.3]; 370 [0.8]	558	638	9100	11350	1.6	2.65	0.09	1.8	109
<b>34</b>	260 [4.9]; 310 [2.7]; 345 [1.9]; 425 [4.0]	549	623	5310	7480	4.0	4.66	1.33	0.3	7.2
<b>35</b>	250 [0.3]; 280 [0.2]; 340 [0.1]; 435 [0.2]	563	617	5230	6780	2.6	5.67	1.22	0.21	8.0

<sup>a</sup>Measured in 2-MeTHF using Ru(bpy)<sub>3</sub>(PF<sub>6</sub>)<sub>2</sub>  $\Phi = 9.5\%$  in ACN.

Polymer **24** exhibits a very similar absorption maximum (565 nm) compared to that studied by Schanze and his coworkers.<sup>48</sup> He reported the polymer shown in Figure **2.19**. The reported emission quantum yield and lifetime for this polymer is 6.5% and 58  $\mu\text{s}$ , respectively, compared to 12.8% and 9.2  $\mu\text{s}$  for our polymer **24**. He tentatively explained the lower phosphorescence efficiency for the polymer to be due to efficient non-radiative decay resulting from the polymer aggregates.

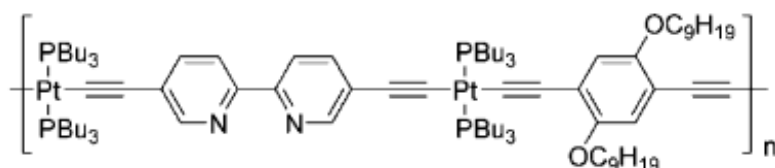


**Figure 2.19.** Structure of the Pt-containing polymer studied by Schanze *et al.*<sup>48</sup>

**Table 2.8.** Photophysical properties of all complexes and polymers investigated in this chapter.

Complex	Absorbance 298 K (nm) [Molar Absorptivities ( $\times 10^4 \text{ M}^{-1} \text{ cm}^{-1}$ )]	$\lambda_{\text{max}}$		Stokes shifts		$\Phi_e$ (%) <sup>a</sup>	$\tau_e$		$k_r$ ( $\times 10^5 \text{ s}^{-1}$ )	$k_{\text{nr}}$ ( $\times 10^5 \text{ s}^{-1}$ )
		77K (nm)	298K (nm)	77K ( $\text{cm}^{-1}$ )	298K ( $\text{cm}^{-1}$ )		77K ( $\mu\text{s}$ )	298K ( $\mu\text{s}$ )		
<b>16</b>	250 [1.8]; 265 [1.4]; 300 [2.1]; 350 [6.0]	522	516	9414	9192	14.4	150	33.8	0.02	0.3
<b>20</b>	240 [1.7]; 260 [2.4]; 280 [2.0]; 345 [4.7]	517	519	9640	9720	12.5	155	33.6	0.04	0.3
<b>22</b>	265 [4.1]; 280 [3.5]; 305 [2.0]; 370 [7.7]	561	561	9200	9200	13.7	153	39.2	0.04	0.3
<b>24</b>	253 [0.4]; 270 [0.3]; 295 [0.3]; 390 [1.2]	562	561	7850	7820	12.8	70	9.2	0.14	0.95
<b>30</b>	265 [2.3]; 310 [1.0]; 325 [0.9]; 380 [0.2]; 450 [0.1]	536	623	2620	5230	8.5	4.12	0.16	5.3	57.2
<b>31</b>	250 [4.2]; 280 [3.3]; 315 [2.3]; 370 [0.8]	558	638	9100	11350	1.6	2.65	0.09	1.8	109
<b>32</b>	260 [6.8]; 300 [4.1]; 350 [4.0]; 370 [4.0]; 460 [0.2]	547	595	3460	4930	31.9	11.0	2.90	0.9	2.6
<b>33</b>	260 [3.6]; 295 [2.00]; 390 [1.9]; 450 [0.2]	549	611	4007	5856	8.3	3.44	0.72	1.2	12.7
<b>34</b>	260 [4.9]; 310 [2.7]; 345 [1.9]; 425 [4.0]	549	623	5310	7480	4.0	4.66	1.33	0.3	7.2
<b>35</b>	250 [0.3]; 280 [0.2]; 340 [0.1]; 435 [0.2]	563	617	5230	6780	2.6	5.67	1.22	0.21	8.0
<b>36</b>	255 [2.9]; 300 [1.7]; 355 [0.6]; 370 [0.4]; 465 [0.1]	532	607	2710	5030	8.9	5.82	0.55	1.6	16.6

<sup>a</sup>Measured in 2-MeTHF using  $\text{Ru}(\text{bpy})_3(\text{PF}_6)_2$   $\Phi = 9.5\%$  in ACN.

Notably, each class of complexes that incorporate platinum(II) acetylide and cationic heteroleptic iridium(III) complexes have independently attracted considerable interest as luminophores in a myriad of applications.

The photophysical properties of the new charged complexes I reported during my M.Sc. work is reminiscent of both Pt and Ir containing moieties through the generation of Pt - Ir charge transfer excited state. The emission behavior and lifetimes provide an expected evidence for a hybrid excited states comprising features from both chromophores. The quantum yields are low, except for the trimer **32**, it was relatively high.

Another interesting characteristic is that the photophysical parameters,  $\Phi_e$  and  $\tau_e$ , for the polymer do not change significantly compared to the model Pt-Ir-Pt complex, **34**. This property is interesting because it permits one to take advantage of the good emission quantum yields and at the same time retain the processability of these materials.

In 2010, the use of both metals, Pt and Ir, in order to obtain novel phosphorescent neutral monomers and polymers was made.<sup>53b</sup> The inherent nature of these materials renders the fabrication of simple solution-processed doped phosphorescent organic light-emitting diodes (PHOLEDs) feasible by effectively blocking the closepacking of the host molecules. They reported that such a synergistic effect of these 2 metals is also important in affording decent device performance for the solution-processed PHOLEDs.

Therefore, we hope that our materials could have a positive impact for the design of photonic materials such as PLEDs (Polymer Light Emitting Diodes) and LEECs (Light Emitting Electrochemical Cells), which we are currently investigating. One of the future works that we aim to investigate will be directed to finding polymers with more repetitive units and see if this will have different photophysical properties or not when compared to the complexes that have been studied throughout my thesis.

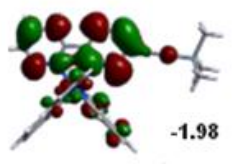
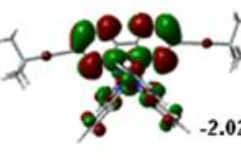
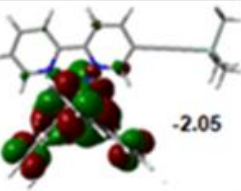
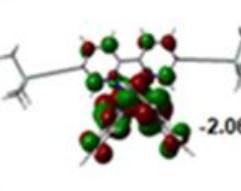
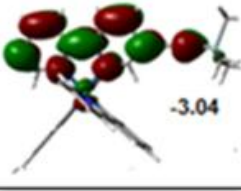
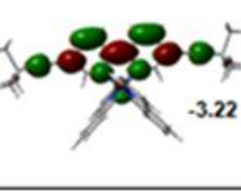
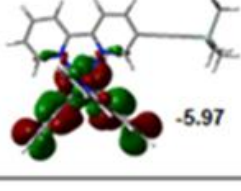
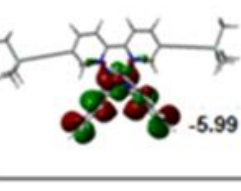
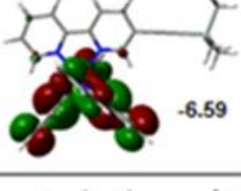
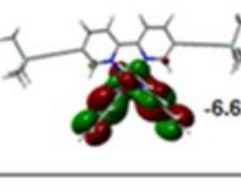
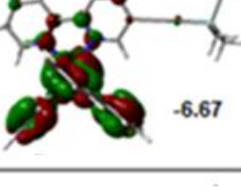
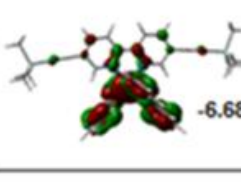
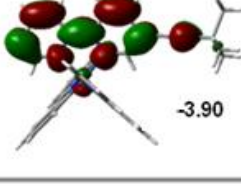
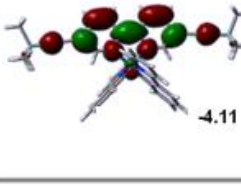
## 2.6 DFT Calculations

In this section, DFT and TDDFT computations were used to address the nature of the low-lying excited states of the Pt-Ir polymer **35**. Model Ir, Pt and Pt-Ir complexes were studied for comparison purposes. All the calculations have been performed by Dr. Daniel Fortin and then I extracted the new data and provided an interpretation afterward.

The frontier MOs for Ir complexes **28** and **27** have been computed by means of DFT computations and are presented in Figure **2.20**. The HOMO in these two Ir complexes exhibit the largest atomic contribution on the metal (mainly  $d_{x^2-y^2}$ ) and the phenylpyridine  $\pi$ -system in a conjugated manner. The LUMO exhibits atomic contribution located on the bipyridine  $\pi$ -system and extending to the ethenyl group. Some weak atomic contributions of the metal ( $d_{xz}$ ) are also computed. The LUMO+1, HOMO, HOMO-1 and HOMO-2 are quasi-degenerate and located on the Ir metal and the phenylpyridine  $\pi$ -system.

For Ir complex **28**, the DFT analysis predicts that the intense low energy  $S_0 \rightarrow S_1$  absorptions arise from HOMO-1  $\rightarrow$  LUMO and HOMO  $\rightarrow$  LUMO+1 transitions, which are consistent with the mixed  $^1\text{MLCT}/^1\text{LLCT}$  assignment for the emissive excited state, while for complex **27**, it stems from a mixture of HOMO  $\rightarrow$  LUMO+1 and HOMO-3  $\rightarrow$  LUMO.

Furthermore, this DFT MO analysis was extended to the triplet state, notably for the elucidation of the nature of the HSOMO (highest semi-occupied molecular orbital). It resembles that of the LUMO for both complexes (Figure **2.20**), indicating that the nature of the  $S_1$  and  $T_1$  states are the same.

MO	Image+Orbital Energy (eV)	
	28	27
LUMO+2	 -1.98	 -2.02
LUMO+1	 -2.05	 -2.06
LUMO	 -3.04	 -3.22
HOMO	 -5.97	 -5.99
HOMO -1	 -6.59	 -6.62
HOMO -2	 -6.67	 -6.68
HSOMO	 -3.90	 -4.11

**Figure 2.20.** Representations of the frontier MOs **27** and **28** along with calculated energies (eV) for each.

The 25 lowest energy transitions have been computed for both Ir complexes **27** and **28** (Table 2.9 and 3.10). From this TD-DFT analysis we can generate the calculated absorption spectrum (Figure 2.21 and 3.22). These appear as the form of bars for the 0-0 transitions by assigning 1000 cm<sup>-1</sup> for each bar. For Ir complex **28**, resemblance in the wavelength shift between the calculated and the experimental spectra is noted for the 2 main transitions, <sup>1</sup>LC and <sup>1</sup>MLCT. However, for Ir complex **27**, and as expected from the DFT calculations, the comparison of the 0-0 transition with the experimental data indicates that these calculated peaks are red-shifted compared to the observed bands.

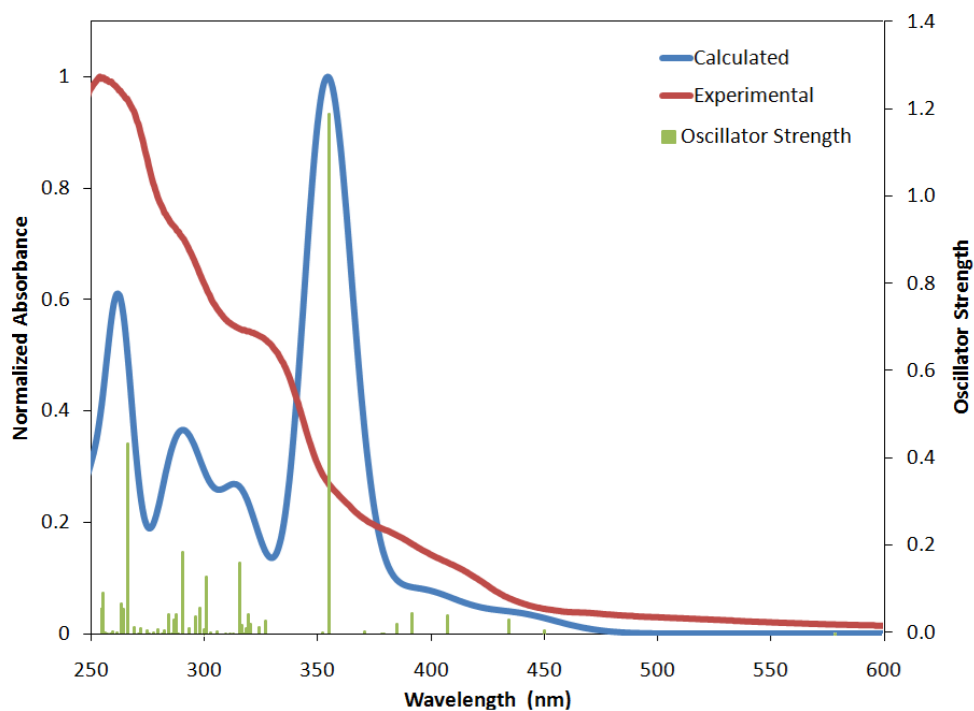
The calculated maximum emission (from the difference between the total energies of optimized geometries in the ground and triplet states) for **28** is 574 nm and for **27** is 605 nm. These values are red-shifted compared to the experimental results at 536 nm 558 nm for both complexes, respectively.

**Table 2.9.** Energy and composition of TD-DFT calculated transitions of **28**.

No.	Energy (cm <sup>-1</sup> )	Wavelength (nm)	Oscillator Strength	Symmetry	Major contributions
1	18155.6656	550.7922552	0.0002	Singlet-A	HOMO->LUMO (98%)
2	23140.2064	432.1482629	0.0012	Singlet-A	H-2->LUMO (94%)
3	24080.65536	415.27109	0.0451	Singlet-A	H-1->LUMO (92%)
4	25446.968	392.9741256	0.0489	Singlet-A	HOMO->L+1 (96%)
5	25633.28336	390.1177957	0.0468	Singlet-A	H-3->LUMO (87%)
6	26384.99728	379.0032606	0.0033	Singlet-A	HOMO->L+2 (-12%), HOMO->L+3 (83%)
7	26810.0544	372.9943942	0.002	Singlet-A	HOMO->L+2 (82%), HOMO->L+3 (12%)
8	27318.1872	366.0565003	0.0028	Singlet-A	H-4->LUMO (91%)
9	28289.28544	353.4907243	0.0085	Singlet-A	H-5->LUMO (96%)
10	28725.6344	348.1211193	0.0064	Singlet-A	HOMO->L+4 (98%)
11	30646.86032	326.2976989	0.1022	Singlet-A	H-2->L+1 (73%)
12	30847.69376	324.1733427	0.4761	Singlet-A	H-6->LUMO (77%), H-2->L+2 (13%) H-3->L+1 (16%), H-2->L+3 (14%), H-1->L+1 (61%)
13	30988.0352	322.7051969	0.013	Singlet-A	
14	31387.2824	318.6003768	0.0214	Singlet-A	HOMO->L+5 (93%)
15	31646.99472	315.9857702	0.0083	Singlet-A	H-2->L+3 (-23%), HOMO->L+6 (59%) H-2->L+1 (-13%), H-2->L+2 (-11%), H-1->L+3 (47%)
16	31741.36224	315.04634	0.0131	Singlet-A	H-2->L+3 (32%), H-1->L+1 (-18%), HOMO->L+6 (22%)
17	31969.61872	312.7969741	0.0405	Singlet-A	
18	32133.3504	311.2031542	0.2533	Singlet-A	H-2->L+2 (61%), H-1->L+3 (16%)
19	32482.59088	307.8572161	0.008	Singlet-A	H-1->L+2 (68%)
20	32914.90704	303.8137093	0.0012	Singlet-A	H-7->LUMO (94%)
21	33127.83888	301.8609224	0.0092	Singlet-A	H-3->L+1 (58%), H-2->L+3 (-10%)
22	33502.08272	298.4889054	0.1298	Singlet-A	H-3->L+3 (68%), H-1->L+3 (-14%)
23	33936.81856	294.6652168	0.0134	Singlet-A	H-3->L+2 (31%), H-2->L+4 (49%)
24	34156.20288	292.7725905	0.0587	Singlet-A	H-3->L+4 (13%), H-1->L+4 (71%)
25	34328.00016	291.3073862	0.0501	Singlet-A	H-3->L+2 (40%), H-2->L+4 (-30%)

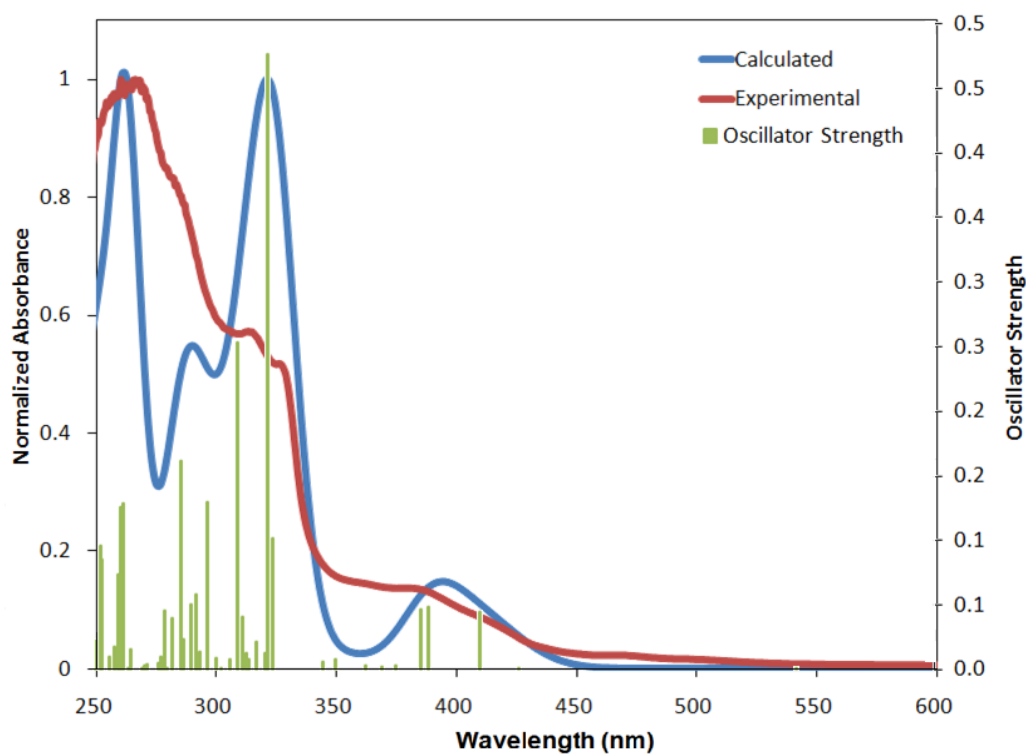
**Table 2.10.** Energy and composition of TD-DFT calculated transitions of **27**.

No.	Energy (cm <sup>-1</sup> )	Wavelength (nm)	Oscillator Strength	Symmetry	Major contributions
1	17091.0064	585.1030516	0.0001	Singlet-A	HOMO->LUMO (99%)
2	22134.42608	451.7849238	0.0086	Singlet-A	H-2->LUMO (94%)
3	22920.01552	436.2998791	0.0331	Singlet-A	H-1->LUMO (94%)
4	24500.06656	408.1621564	0.0435	Singlet-A	H-3->LUMO (91%)
5	25517.13872	391.8934685	0.0484	Singlet-A	HOMO->L+1 (86%), HOMO->L+2 (11%)
6	26002.68784	384.5756278	0.0235	Singlet-A	H-4->LUMO (86%)
7	26414.84	378.5750737	0.0008	Singlet-A	HOMO->L+3 (96%)
8	26473.71888	377.7331037	0.0029	Singlet-A	HOMO->L+1 (-11%), HOMO->L+2 (82%)
9	27039.924	369.8235247	0.0067	Singlet-A	H-5->LUMO (96%)
10	28253.7968	353.9347321	1.1939	Singlet-A	H-6->LUMO (90%)
11	28486.89264	351.0386382	0.0051	Singlet-A	HOMO->L+4 (98%)
12	30746.0672	325.2448495	0.0316	Singlet-A	H-2->L+1 (68%), H-2->L+2 (12%) H-3->L+1 (15%), H-2->L+3 (-14%), H-1->L+1 (60%)
13	31063.04528	321.9259384	0.016	Singlet-A	H-2->L+2 (-11%), HOMO->L+6 (77%)
14	31434.06288	318.1262326	0.023	Singlet-A	H-2->L+1 (-20%), H-2->L+2 (48%), HOMO->L+6 (18%)
15	31502.62048	317.4339102	0.0458	Singlet-A	H-8->LUMO (35%), H-2->L+3 (21%), HOMO->L+7 (29%)
16	31670.38496	315.7523981	0.0132	Singlet-A	H-8->LUMO (58%), H-2->L+3 (-16%), HOMO->L+7 (-15%)
17	31730.87696	315.1504452	0.0032	Singlet-A	H-2->L+3 (-10%), H-1->L+1 (-15%), H-1->L+2 (23%), HOMO->L+5 (-10%), HOMO->L+7 (29%)
18	31855.0872	313.9216018	0.0211	Singlet-A	H-2->L+2 (21%), H-1->L+3 (61%)
19	31940.58256	313.0813278	0.1654	Singlet-A	H-2->L+3 (11%), H-1->L+2 (38%), HOMO->L+5 (-18%), HOMO->L+7 (-16%)
20	32290.6296	309.6873652	0.002	Singlet-A	H-1->L+2 (22%), HOMO->L+5 (64%)
21	32399.5152	308.6465936	0.0016	Singlet-A	H-9->LUMO (94%)
22	32585.83056	306.881851	0.0008	Singlet-A	H-7->LUMO (28%), H-3->L+1 (42%)
23	32978.62528	303.2267087	0.0071	Singlet-A	H-7->LUMO (56%), H-3->L+1 (-22%)
24	33317.38048	300.1436444	0.0042	Singlet-A	H-3->L+3 (74%), H-1->L+3 (-15%)
25	33506.92208	298.4457951	0.1324	Singlet-A	



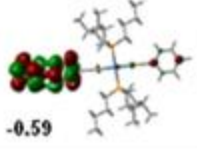
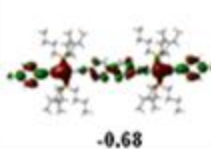
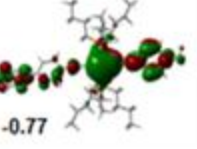
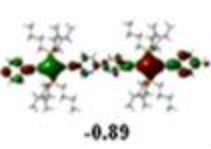
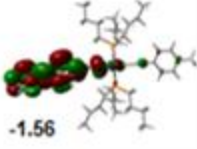
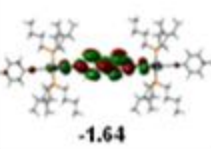
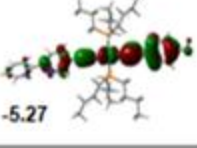
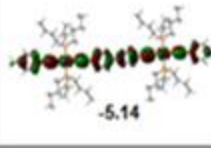
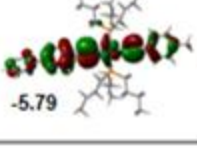
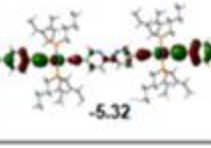
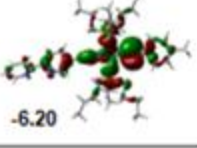
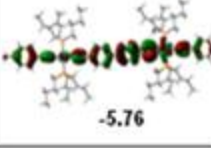
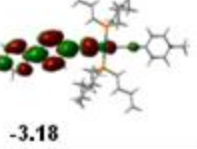
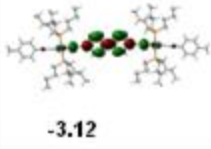
**Figure 2.21.** Calculated (blue) and experimental (red) absorption spectra for **28**. The calculated spectrum appears as a form of bars for the 0-0 transitions by assigning 1000 cm<sup>-1</sup> for each bar.





**Figure 2.22.** Calculated (blue) and experimental (red) absorption spectra for **27**. The calculated spectrum appears as a form of bars for the 0-0 transitions by assigning  $1000\text{ cm}^{-1}$  for each bar.

The frontier MOs for Pt complexes **20** and **22** have been computed as well (Figure 2.23). The HOMO for complex **20** is located on the (ethynyltolyl)platinum(II) and partially extended to the bipyridine, while for complex **22** on the bis(ethynyltolyl)platinum(II) and the bipyridine, consistent with the presence of conjugation. The LUMO is localized on the bipyridines  $\pi$ -system for both complexes, predicting the HOMO $\rightarrow$ LUMO transition will generate charge transfer excited states, namely Pt/ $\pi$ -bipyridine $\rightarrow$  bipyridine for metal-to-ligand-charge transfer ( $^1\text{MLCT}$ ).

MO	Image+Orbital Energy (eV)	
	20	22
LUMO+2	 -0.59	 -0.68
LUMO+1	 -0.77	 -0.89
LUMO	 -1.56	 -1.64
HOMO	 -5.27	 -5.14
HOMO -1	 -5.79	 -5.32
HOMO -2	 -6.20	 -5.76
HSOMO	 -3.18	 -3.12

**Figure 2.23.** Representations of the frontier MOs of **20** and **22** along with calculated energies (eV) for each.

Lowest energy transitions were computed for both Pt complexes **20** and **22** (Table 2.11 and 2.12) From this TD-DFT we can generate the calculated absorption spectrum (Figure 2.24 and 2.25).

Based on the calculated oscillator strength (f), the HOMO→LUMO for the 2 Pt-complexes **20** and **22** should be an intense transition. Other important transitions should be HOMO-2→LUMO and HOMO-1→LUMO+1 for complex **20** and HOMO-4→LUMO and HOMO-2→LUMO for complex **22**. From Figure 2.24, we can see that for complex **20** HOMO-2, HOMO and LUMO+1 are quasi-degenerate, while they are HOMO-2, HOMO and LUMO+2 for complex **22**.

**Table 2.11.** Energy and composition of TD-DFT calculated transitions of **20**.

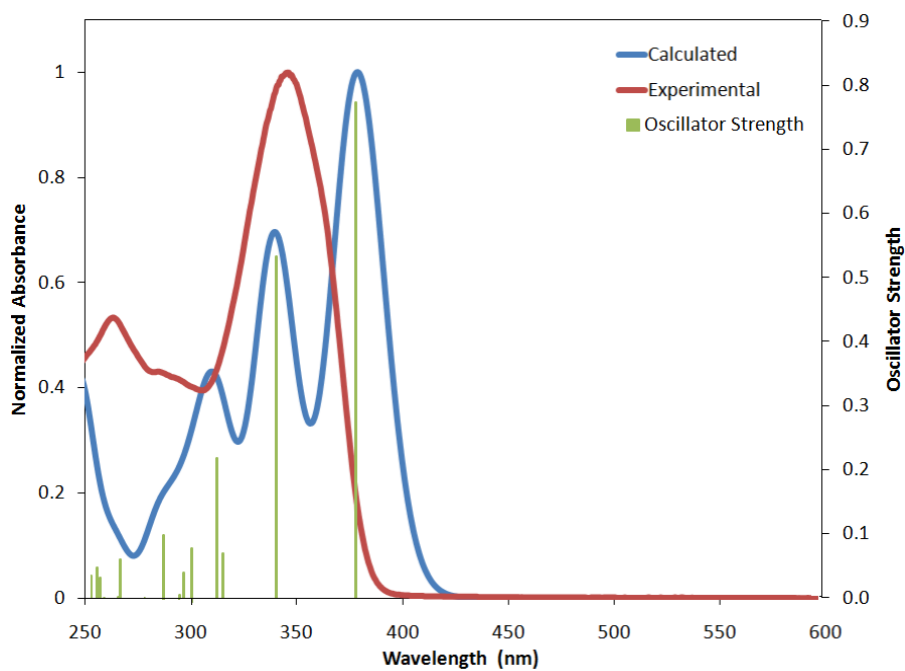
No.	Energy (cm <sup>-1</sup> )	Wavelength (nm)	Oscillator Strength	Symmetry	Major contributions
1	26405.16128	378.7138391	0.7792	Singlet-A	HOMO->LUMO (93%)
2	29447.5056	339.5873367	0.5392	Singlet-A	H-3->LUMO (-18%), H-1->LUMO (72%)
3	31863.95936	313.8341939	0.075	Singlet-A	H-5->LUMO (-28%), H-3->LUMO (47%), H-1->LUMO (13%)
4	32189.00304	310.6651047	0.2248	Singlet-A	HOMO->L+1 (86%)
5	33406.10208	299.3465079	0.0839	Singlet-A	H-5->LUMO (-13%), H-2->LUMO (54%), H-2->L+1 (-11%), H-1->L+1 (11%)
6	33882.77904	295.1351773	0.0452	Singlet-A	H-6->LUMO (15%), H-5->LUMO (42%), H-3->LUMO (15%), H-2->LUMO (12%)
7	34093.2912	293.312838	0.0112	Singlet-A	H-4->LUMO (95%)
8	34481.24656	290.012717	0.0038	Singlet-A	HOMO->L+2 (77%), HOMO->L+3 (-12%)
9	35143.43232	284.5481884	0.1041	Singlet-A	H-2->LUMO (-18%), H-1->L+1 (62%)
10	35904.0184	278.5203564	0.0019	Singlet-A	H-6->LUMO (57%)
11	36275.84256	275.6655475	0.006	Singlet-A	HOMO->L+2 (13%), HOMO->L+3 (77%)
12	36441.99392	274.4086951	0.0004	Singlet-A	HOMO->L+6 (93%)
13	36933.18896	270.7591811	0.0067	Singlet-A	H-3->L+2 (-10%), H-1->L+2 (38%), H-1->L+3 (-17%)
14	37855.08704	264.1652888	0.0668	Singlet-A	H-2->L+1 (61%)
15	38027.69088	262.9662693	0.0071	Singlet-A	H-7->L+1 (10%), HOMO->L+4 (54%), HOMO->L+5 (-22%)
16	38637.45024	258.8162505	0.0015	Singlet-A	H-5->L+2 (46%), H-3->L+2 (-12%)
17	38993.94976	256.4500406	0.0061	Singlet-A	H-3->L+3 (-14%), H-1->L+2 (31%), H-1->L+3 (14%)
18	39388.3576	253.8821268	0.0384	Singlet-A	H-4->L+1 (90%)
19	39503.69568	253.1408727	0.053	Singlet-A	HOMO->L+4 (24%), HOMO->L+5 (54%)
20	39975.53328	250.1530106	0.0409	Singlet-A	H-1->L+3 (40%)
21	40258.63584	248.3939108	0.0385	Singlet-A	H-8->LUMO (32%), H-3->L+1 (20%), H-1->L+6 (27%)
22	40301.38352	248.1304394	0.0172	Singlet-A	H-8->LUMO (-19%), H-1->L+6 (47%)
23	40461.0824	247.1510747	0.0191	Singlet-A	H-9->LUMO (81%)
24	40829.68032	244.9198701	0.1707	Singlet-A	H-8->LUMO (-14%), H-3->L+1 (39%)
25	41277.32112	242.2637838	0.0046	Singlet-A	H-4->L+6 (87%)

**Table 2.12.** Energy and composition of TD-DFT calculated transitions of **22**.

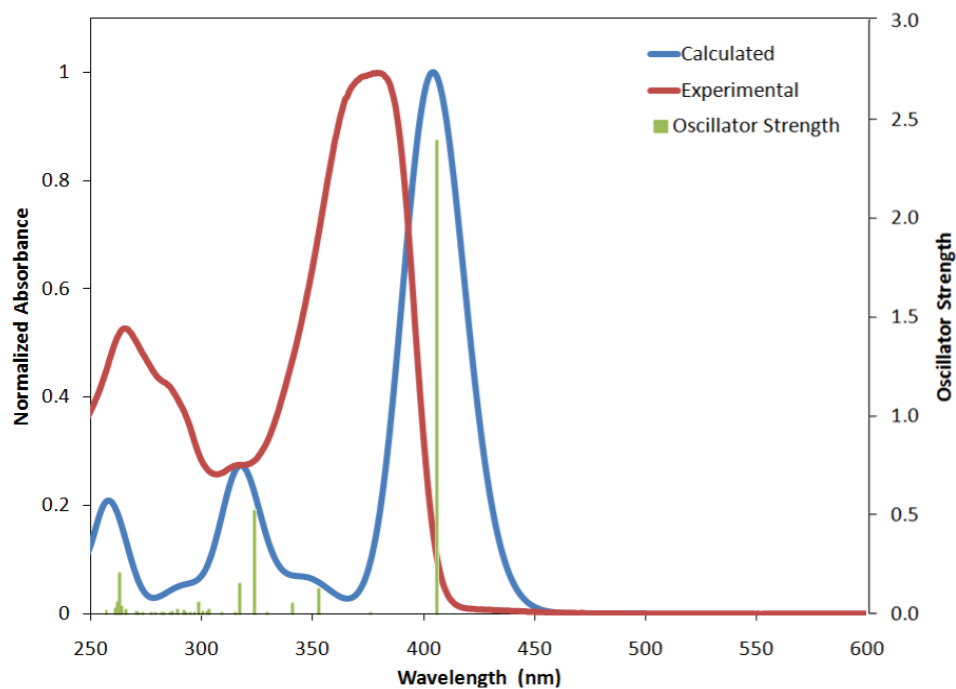
No.	Energy (cm <sup>-1</sup> )	Wavelength (nm)	Oscillator Strength	Symmetry	Major contributions
1	24739.61488	404.2100109	2.3939	Singlet-A	HOMO->LUMO (95%)
2	26818.12	372.8822155	0.0025	Singlet-A	H-1->LUMO (93%)
3	28618.36192	349.4260094	0.1256	Singlet-A	H-6->LUMO (-10%), H-3->LUMO (32%), H-2->LUMO (42%)
4	29643.49968	337.3420854	0.0526	Singlet-A	H-4->LUMO (-14%), H-3->LUMO (44%), H-2->LUMO (-21%)
5	30773.49024	324.9550156	0.0044	Singlet-A	H-1->L+2 (10%), HOMO->L+1 (80%)
6	31374.37744	318.731424	0.5195	Singlet-A	H-4->LUMO (36%), H-2->LUMO (-21%), H-1->L+1 (13%), HOMO->L+2 (10%)
7	32031.72384	312.1905037	0.1529	Singlet-A	H-2->LUMO (10%), H-1->L+1 (39%), HOMO->L+2 (28%)
8	32221.26544	310.354043	0.0056	Singlet-A	H-10->LUMO (14%), H-6->LUMO (33%), H-4->LUMO (13%)
9	32937.49072	303.6053986	0.0053	Singlet-A	H-9->LUMO (-19%), H-5->LUMO (36%)
10	33522.24672	298.3093611	0.0193	Singlet-A	H-1->L+1 (-15%), HOMO->L+2 (23%), HOMO->L+3 (49%)
11	33646.45696	297.2081135	0.0115	Singlet-A	H-8->LUMO (68%), H-7->LUMO (-24%)
12	33886.81184	295.1000539	0.0085	Singlet-A	H-8->LUMO (23%), H-7->LUMO (60%)
13	34176.36688	292.5998552	0.0577	Singlet-A	H-2->L+1 (-10%), H-1->L+1 (13%), HOMO->L+2 (-19%), HOMO->L+3 (31%)
14	34323.96736	291.3416126	0.0037	Singlet-A	H-11->LUMO (14%), H-9->LUMO (31%), H-6->LUMO (10%), H-5->LUMO (27%)
15	34583.67968	289.1537307	0.0039	Singlet-A	H-10->LUMO (27%), H-1->L+2 (-16%)
16	34790.15904	287.4376052	0.0027	Singlet-A	H-10->LUMO (27%), H-6->LUMO (-12%), H-1->L+2 (18%)
17	35010.34992	285.6298215	0.014	Singlet-A	H-2->L+1 (12%), H-1->L+3 (16%), HOMO->L+4 (29%)
18	35366.04288	282.7571078	0.0223	Singlet-A	H-1->L+2 (30%), HOMO->L+4 (-21%)
19	35557.1976	281.2370118	0.0106	Singlet-A	H-3->L+1 (34%), H-3->L+2 (-23%)
20	35726.5752	279.9036836	0.0008	Singlet-A	H-11->LUMO (49%), H-9->LUMO (-18%)
21	36130.66176	276.7732312	0.0012	Singlet-A	H-1->L+3 (-16%), H-1->L+10 (-13%), HOMO->L+10 (33%)
22	36165.34384	276.5078094	0.0002	Singlet-A	H-1->L+9 (15%), H-1->L+10 (11%), HOMO->L+9 (27%), HOMO->L+10 (-23%)
23	36219.38336	276.0952582	0.002	Singlet-A	H-1->L+3 (37%), H-1->L+9 (12%), HOMO->L+4 (-14%)
24	36638.79456	272.9347436	0.0004	Singlet-A	H-4->L+1 (-21%), H-2->L+1 (36%)
25	36842.04768	271.4289957	0.0016	Singlet-A	H-3->L+3 (11%), H-2->L+3 (23%)

The calculated absorption spectra for **20** and **22** (Figure 2.24 and 2.25) generated from the TD-DFT show that the 0-0 transition is significantly red shifted for the calculated results compared to the experimental one. TD-DFT calculations also indicate that the intense low energy absorption band in **20**, which result from a HOMO→LUMO transition, characterized as a mixed <sup>1</sup>MLCT/<sup>1</sup>LLCT transition.

The HSOMO resembles the LUMO for both Pt-complexes predicting that the nature of the singlet and the triplet states are the same. The predicted emissions for both complexes fit relatively well with the observed values. This similarity supports the assignment for the triplet emissive state as being Pt/ $\pi$ -bipyridine→ bipyridine for (<sup>1</sup>MLCT). The calculated maximum emission for **20** is 510 nm and for **22** is 568 nm.

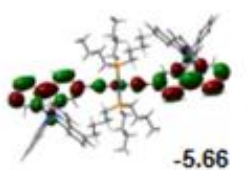
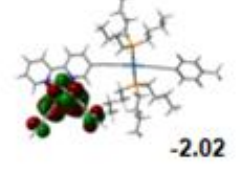
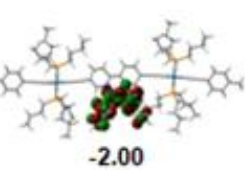
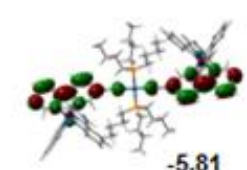
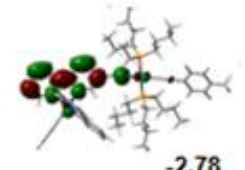
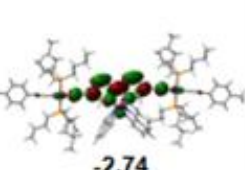
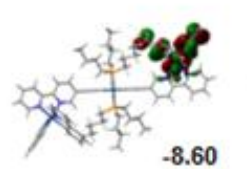
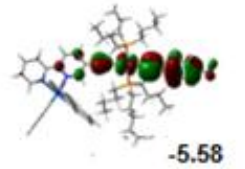
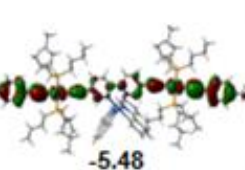
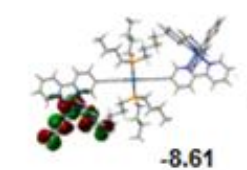
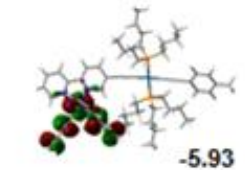
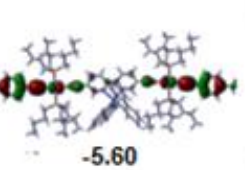
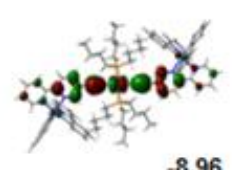
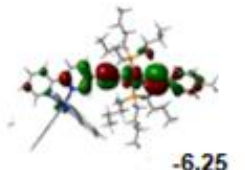
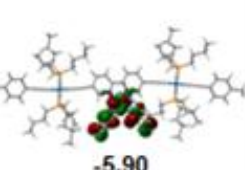
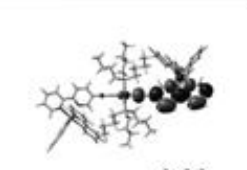
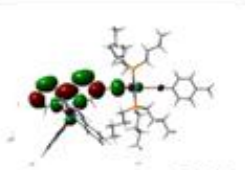
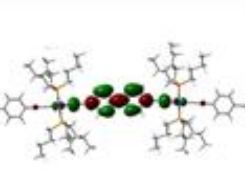


**Figure 2.24.** Calculated (blue) and experimental (red) absorption spectra for **20**. The calculated spectrum appears as a form of bars for the 0-0 transitions by assigning  $1000\text{ cm}^{-1}$  for each bar.



**Figure 2.25.** Calculated (blue) and experimental (red) absorption spectra for **22**. The calculated spectrum appears as a form of bars for the 0-0 transitions by assigning  $1000\text{ cm}^{-1}$  for each bar.

Computations for Pt-Ir containing complexes (**32**, **33** and **34**) have been performed as well and the MOs from HOMO-2 to LUMO+1 in addition to HSOMO are shown in Figure 2.26.

MO	Image+Orbital Energy (eV)		
	32	33	34
LUMO+1	 -5.66	 -2.02	 -2.00
LUMO	 -5.81	 -2.78	 -2.74
HOMO	 -8.60	 -5.58	 -5.48
HOMO -1	 -8.61	 -5.93	 -5.60
HOMO -2	 -8.96	 -6.25	 -5.90
HSOMO	 -6.82	 -3.87	 -3.12

**Figure 2.26.** Representations of the frontier MOs of **32**, **33** and **34** along with calculated energies (eV) for each.

The HOMO in the Pt-Ir complex **32** exhibits the largest atomic contributions on the metal (mainly  $d_{x^2-y^2}$ ) and the phenylpyridine  $\pi$ -system. The LUMO exhibits atomic contributions located on the bipyridines  $\pi$ -system and extending to the ethynyl group.

However, the HOMO is localized on the ethynyltolylplatinum(II) and the LUMO on the bipyridine  $\pi$ -systems for complex **33**. For complex **34**, The HOMO and HOMO-1 do exhibit the largest electronic density onto both  $\pi$ -systems of bis(ethynyltolyl)platinum(II). The LUMO is strongly concentrated onto the central bis(ethynyl)-bipyridine residue. Both complexes show similar HOMO and LUMO localization as Pt complexes **20** and **22** respectively. The LUMO and LUMO+1, HOMO-1 and HOMO for complex **32**, HOMO-1 and LUMO+1 for complex **33** and finally HOMO-2 and LUMO+1 for complex **34**, are degenerate (i.e. same energy).

**Table 2.13.** Energy and composition of TD-DFT calculated transitions of **32**.

No.	Energy ( $\text{cm}^{-1}$ )	Wavelength (nm)	Oscillator Strength	Symmetry	Major contributions
1	17574.9424	568.9919075	0.0002	Singlet-A	HOMO->LUMO (62%), HOMO->L+1 (-36%)
2	17612.04416	567.7932618	0.0001	Singlet-A	H-1->LUMO (64%), H-1->L+1 (34%)
3	21617.42112	462.5898688	0.0175	Singlet-A	HOMO->LUMO (37%), HOMO->L+1 (61%)
4	21713.40176	460.5450639	0.001	Singlet-A	H-1->LUMO (-35%), H-1->L+1 (63%)
5	22036.83232	453.7857281	0.9277	Singlet-A	H-2->LUMO (87%)
6	22926.468	436.1770858	0.0053	Singlet-A	H-5->LUMO (48%), H-5->L+1 (-18%) H-6->LUMO (45%), H-6->L+1 (15%), H-5->L+1 (-12%)
7	23167.62944	431.6367381	0.0748	Singlet-A	H-3->LUMO (61%), H-3->L+1 (-27%)
8	23549.93888	424.6295522	0.0112	Singlet-A	H-4->LUMO (63%), H-4->L+1 (26%)
9	23674.95568	422.3872743	0.0163	Singlet-A	H-2->L+1 (68%)
10	24168.5704	413.7605094	0.0596	Singlet-A	H-9->LUMO (-10%), H-8->LUMO (-12%), H-7->LUMO (44%)
11	24692.8344	404.9757852	0.1381	Singlet-A	HOMO->L+2 (49%), HOMO->L+3 (22%), HOMO->L+4 (15%)
12	24745.2608	404.1177857	0.0352	Singlet-A	H-1->L+2 (-14%), H-1->L+3 (66%), H-1->L+4 (-14%)
13	24806.55936	403.1191853	0.0343	Singlet-A	H-9->LUMO (52%), H-8->L+1 (-24%)
14	25323.56432	394.8891188	0.021	Singlet-A	H-9->L+1 (-13%), H-8->LUMO (41%), H-7->LUMO (13%), H-7->L+1 (-11%)
15	25392.12192	393.8229358	0.0862	Singlet-A	HOMO->L+2 (-15%), HOMO->L+4 (16%), HOMO->L+5 (37%)
16	25813.9528	387.3873977	0.0066	Singlet-A	H-1->L+6 (72%)
17	25843.79552	386.9400682	0.0044	Singlet-A	H-1->L+4 (33%), H-1->L+5 (-19%), H-1->L+6 (-23%)
18	25878.4776	386.4214949	0.0085	Singlet-A	HOMO->L+7 (77%)
19	25990.58944	384.7546445	0.0026	Singlet-A	H-10->LUMO (18%), H-9->L+1 (-12%), H-7->L+1 (20%), HOMO->L+7 (11%)
20	26066.40608	383.6355487	0.0114	Singlet-A	H-12->L+1 (-11%), H-11->LUMO (50%), H-10->L+1 (-14%), H-6->LUMO (-10%)
21	26457.58768	377.9634077	0.0219	Singlet-A	H-12->LUMO (17%), H-11->L+1 (-13%), H-10->LUMO (13%), H-3->LUMO (11%), H-3->L+1 (29%)
22	26506.78784	377.2618569	0.0047	Singlet-A	H-12->LUMO (-15%), H-3->LUMO (18%), H-3->L+1 (38%)
23	26570.50608	376.3571522	0.0005	Singlet-A	H-4->LUMO (-29%), H-4->L+1 (69%)
24	26736.65744	374.0183313	0.0005	Singlet-A	H-13->LUMO (98%)
25	27203.65568	367.5976537	0.002	Singlet-A	

**Table 2.14.** Energy and composition of TD-DFT calculated transitions of **33**.

No.	Energy (cm <sup>-1</sup> )	Wavelength (nm)	Oscillator Strength	Symmetry	Major contributions
1	19829.2776	504.3048063	0.2067	Singlet-A	H-1->LUMO (-45%), HOMO->LUMO (53%)
2	19920.41888	501.9974761	0.195	Singlet-A	H-1->LUMO (53%), HOMO->LUMO (44%)
3	24293.5872	411.6312637	0.2684	Singlet-A	H-4->LUMO (-10%), H-2->LUMO (74%) H-6->LUMO (36%), H-5->LUMO (-27%), H-4->LUMO (-12%)
4	24823.49712	402.8441259	0.0797	Singlet-A	H-1->L+1 (97%)
5	25314.69216	395.0275175	0.0431	Singlet-A	H-4->LUMO (13%), H-3->LUMO (64%)
6	25860.73328	386.6866377	0.0488	Singlet-A	H-1->L+2 (89%)
7	26235.78368	381.1588067	0.0049	Singlet-A	HOMO->L+1 (92%)
8	26274.49856	380.5971778	0.0034	Singlet-A	H-5->LUMO (57%), H-4->LUMO (-15%), H-2->LUMO (-10%)
9	26725.3656	374.1763593	0.0134	Singlet-A	H-6->LUMO (51%), H-4->LUMO (23%)
10	27011.6944	370.2100228	0.0079	Singlet-A	HOMO->L+2 (89%)
11	27160.10144	368.1871374	0.0046	Singlet-A	H-8->LUMO (74%)
12	27319.80032	366.0348862	0.0291	Singlet-A	HOMO->L+3 (85%)
13	27799.70352	359.7160665	0.1843	Singlet-A	H-1->L+3 (86%)
14	28096.5176	355.9159944	0.0107	Singlet-A	H-7->LUMO (54%), H-4->LUMO (-16%), H-1->L+3 (-11%)
15	28408.65632	352.0053848	0.2549	Singlet-A	H-9->LUMO (94%)
16	29320.87568	341.053934	0.0204	Singlet-A	HOMO->L+4 (80%)
17	29830.6216	335.2260015	0.0047	Singlet-A	H-1->L+4 (90%)
18	30009.67792	333.2258356	0.0131	Singlet-A	H-10->LUMO (91%)
19	30249.22624	330.5869684	0.0111	Singlet-A	H-6->L+1 (27%), H-5->L+1 (-11%), H-4->L+1 (-21%), H-2->L+1 (16%)
20	30313.75104	329.8832925	0.0307	Singlet-A	H-8->L+1 (15%), H-6->L+2 (-10%), H-3->L+1 (41%)
21	30778.3296	324.903922	0.0052	Singlet-A	H-2->L+1 (63%)
22	31276.78368	319.72597	0.0045	Singlet-A	H-1->L+5 (84%)
23	31368.73152	318.7887911	0.0142	Singlet-A	HOMO->L+5 (68%), HOMO->L+7 (-15%)
24	31418.73824	318.2814002	0.1645	Singlet-A	H-1->L+6 (60%)
25	31454.22688	317.9222951	0.0037	Singlet-A	

**Table 2.15.** Energy and composition of TD-DFT calculated transitions of **34**.

No.	Energy (cm <sup>-1</sup> )	Wavelength (nm)	Oscillator Strength	Symmetry	Major contributions
1	19370.34496	516.2530673	1.3322	Singlet-A	HOMO->LUMO (97%)
2	20165.61312	495.8936751	0.0125	Singlet-A	H-2->LUMO (88%)
3	20664.0672	483.931837	0.0039	Singlet-A	H-1->LUMO (88%)
4	24045.16672	415.8839952	0.3533	Singlet-A	H-3->LUMO (83%)
5	24940.44832	400.955102	0.0471	Singlet-A	H-7->LUMO (40%), H-4->LUMO (39%) H-10->LUMO (-15%), H-7->LUMO (-12%), H-5->LUMO (-11%), H-4->LUMO (33%), H-2->L+1 (-19%)
6	25242.10176	396.1635245	0.019	Singlet-A	H-2->L+1 (67%)
7	25274.36416	395.6578269	0.0334	Singlet-A	HOMO->L+1 (87%)
8	25671.19168	389.5417137	0.0119	Singlet-A	H-6->LUMO (55%), H-2->L+2 (-26%)
9	25942.19584	385.472381	0.0351	Singlet-A	H-6->LUMO (18%), H-2->L+2 (42%), HOMO->L+2 (31%)
10	26112.38	382.9601132	0.0113	Singlet-A	H-2->L+2 (-27%), HOMO->L+2 (57%)
11	26375.31856	379.1423401	0.005	Singlet-A	H-7->LUMO (-18%), H-5->LUMO (68%)
12	26647.93584	375.2635874	0.4012	Singlet-A	H-1->L+1 (90%)
13	26963.3008	370.8744739	0.0003	Singlet-A	H-11->LUMO (12%), H-9->LUMO (34%), H-8->LUMO (33%)
14	27315.76752	366.0889262	0.0042	Singlet-A	H-12->LUMO (13%), H-9->LUMO (-11%), H-8->LUMO (59%)
15	27345.61024	365.6894073	0.005	Singlet-A	H-12->LUMO (18%), H-10->LUMO (22%), H-9->LUMO (37%)
16	27443.204	364.3889394	0.0117	Singlet-A	H-1->L+2 (34%), HOMO->L+3 (58%)
17	27536.76496	363.1508645	0.2044	Singlet-A	H-12->LUMO (-13%), H-10->LUMO (41%), H-9->LUMO (-10%)
18	27559.34864	362.8532782	0.005	Singlet-A	H-1->L+2 (62%), HOMO->L+3 (-33%)
19	27676.29984	361.3199762	0.0831	Singlet-A	H-12->LUMO (29%), H-11->LUMO (54%)
20	27888.42512	358.5716998	0.0989	Singlet-A	H-2->L+3 (54%), H-1->L+3 (36%)
21	28491.732	350.9790138	0.0084	Singlet-A	H-2->L+3 (-41%), H-1->L+3 (45%)
22	28732.08688	348.0429403	0.0071	Singlet-A	H-14->LUMO (48%), H-13->LUMO (-38%)
23	29597.52576	337.8660798	0.0131	Singlet-A	H-14->LUMO (46%), H-13->LUMO (40%)
24	29666.88992	337.0761151	0.0129	Singlet-A	H-7->L+1 (36%), H-3->L+1 (-33%)
25	30043.55344	332.8501078	0.0262	Singlet-A	



From the DFT computations of the Ir complex **27** and Pt complex **22**, we can see that the HOMO is very similar to that described for the Pt-containing unit of **22** and the LUMO is essentially identical to that located on the Ir fragment of compound **27**. Consequently, these calculations corroborate that the excited state is a hybrid between the two chromophores as deduced spectroscopically, best describing a charge transfer behavior from Pt→Ir.

Figures 3.27, 3.28 and 3.29, show calculated and experimental absorption spectra for complexes **32**, **33** and **34**. The 3 complexes demonstrate that the 0-0 transition is red shifted in the calculated results compared to the experimental one. These figures have been generated from the TD-DFT lowest energy transitions shown in Table 2.13, 2.14 and 2.15.

TD-DFT calculations indicate that the intense low energy absorption band for the 3 complexes, that result from a HOMO→LUMO transition, characterized by being of  $^1\text{MLCT}$  nature.

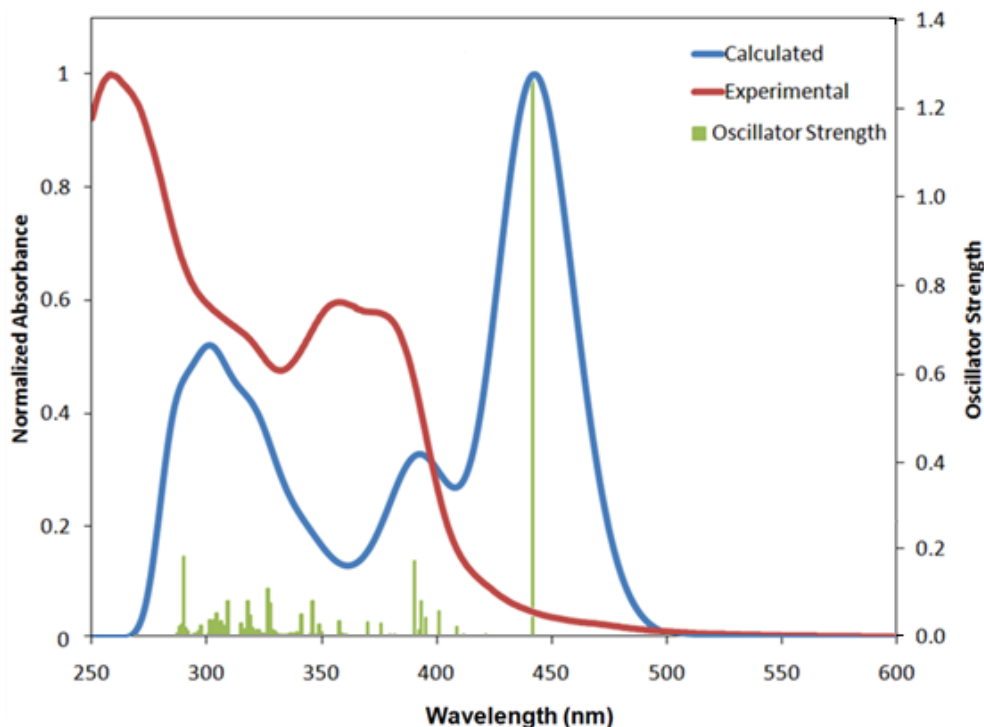


**Figure 2.27.** Calculated (blue) and experimental (red) absorption spectra for **32**. The calculated spectrum appears as a form of bars for the 0-0 transitions by assigning  $1000\text{ cm}^{-1}$  for each bar.

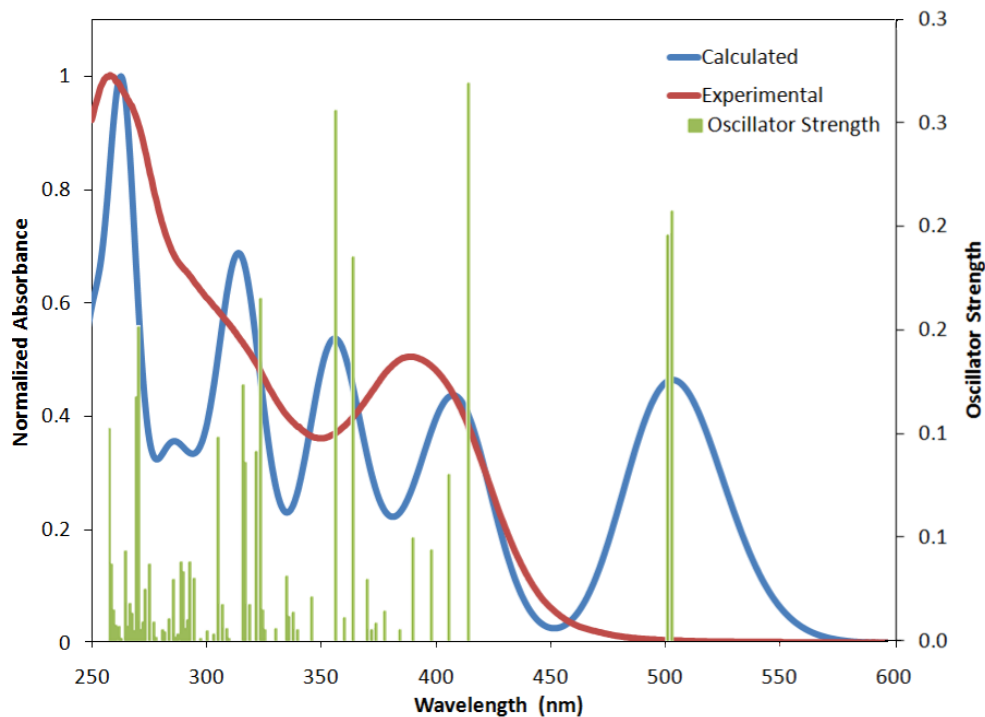


**Figure 2.28.** Calculated (blue) and experimental (red) absorption spectra for **33**. The calculated spectrum appears as a form of bars for the 0-0 transitions by assigning  $1000\text{ cm}^{-1}$  for each bar.

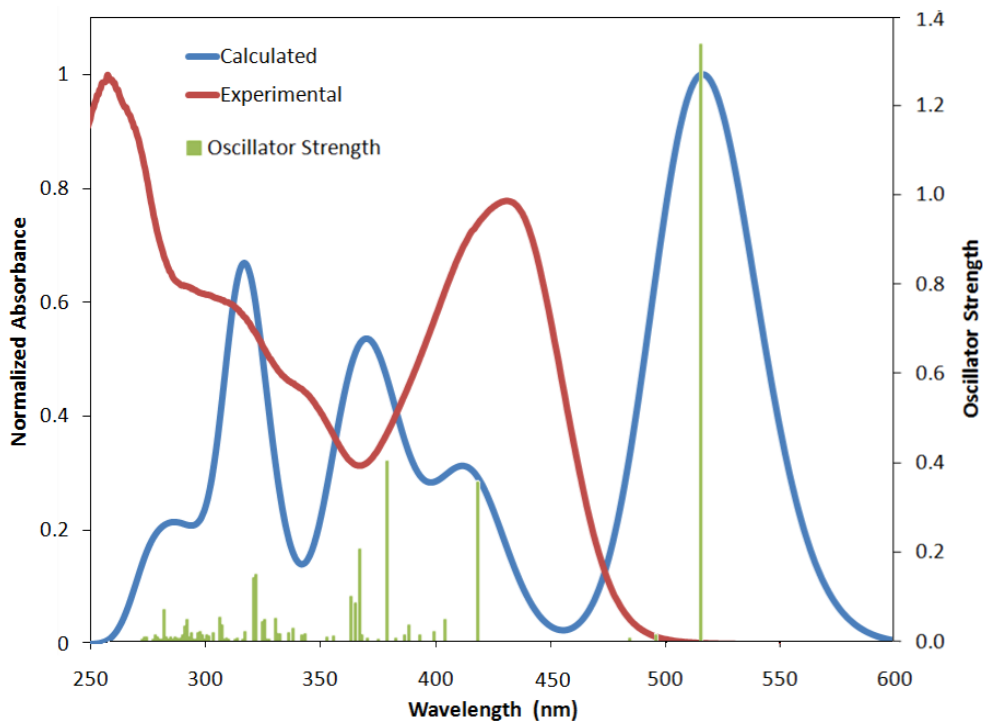


**Figure 2.29.** Calculated (blue) and experimental (red) absorption spectra for **34**. The calculated spectrum appears as a form of bars for the 0-0 transitions by assigning  $1000\text{ cm}^{-1}$  for each bar.

The calculated maximum emission for **32** is 554 nm while for complex **33** is 601 nm. The values for the complex **32** is blue-shifted by 57 nm at 611 nm, while it is red shifted for complex **33** by only 6 nm (595 nm) compared to the experimental results. For Pt-Ir complex **34**, it shows a calculated emission at 650 nm while the experimental at 623 nm.

The HSOMO resembles the LUMO and can be seen at Figure **2.31**. for the 3 Pt-Ir containing complexes suggesting that the nature of the first singlet and triplet excited states are of the same nature.

The interesting feature of the Pt-Ir polymer is compared to other Pt-containing polymers generally encountered is the incorporation of a luminescent cationic iridium acceptor moiety. Its presence permits CT transitions between the Pt and Ir units. Indeed, spectroscopic evidence indicates the presence of a hybrid excited state, which is corroborated by DFT and TDDFT calculations.

## General conclusion

Herein, I reported charged Pt-Ir-containing monomers and polymers. As a first step towards the construction of the polymeric complexes, a covalent bond of an Ir(III) fragment into the bis(ethynyl)bipyridine has been achieved, then by adding the *trans*-Pt(PBu<sub>3</sub>)<sub>2</sub>Cl<sub>2</sub> unit, the new polymeric complex containing both metals was obtained.

In order to understand the photophysical behaviour of the polymer, monomers have been synthesized first and characterized photophysically. This charged configuration with both metals is strongly luminescent and helped to keep the conjugation between them high in order to enable the charge transfer behaviour and even tailor a hybrid excited state of the two moieties. Such hybrid excited state between Pt and Ir center is totally new.

The new type of conjugated Pt-Ir polymer was characterized and investigated for its unique photophysical properties. The distinguishing feature compared to other [Pt]-containing polymers generally encountered is the incorporation of a luminescent cationic iridium acceptor moiety. Its presence permits CT transitions between the Pt and Ir units. Indeed, spectroscopic evidence indicates the presence of a hybrid excited state, which is corroborated by DFT and TDDFT calculations. These materials could therefore have a positive impact for the design of photonic materials such as PLEDs (Polymer Light Emitting Diodes) and LEECs (Light Emitting Electrochemical Cells).

Future work revealed an unprecedented triplet energy transfer from the terminal iridiums to the central Ir subunit upon studying the photophysical and the electrochemical properties of the pentanuclear complex **36** (Figure 2.30). This work has been accepted in the journal of *Chem. Commun.*<sup>64</sup>

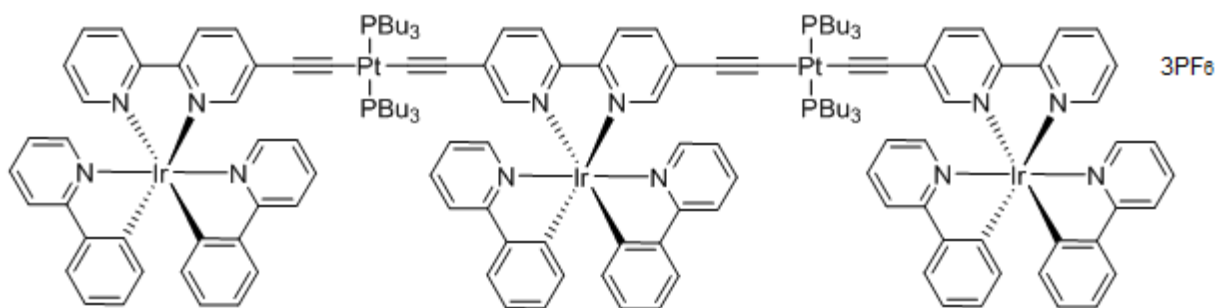


Figure 2.30. Pentanuclear complex **36**.<sup>64</sup>

Another future project that will describe the synthesis, photophysical and electrochemical characterization as well as theoretical investigation of a new series of fluorinated complexes, **37**, **38**, **39** and **40** (Figure 2.31) is under preparation. The photophysical and electrochemical properties of these complexes will be compared to the non-fluorinated model systems, that have been investigated throughout my thesis.

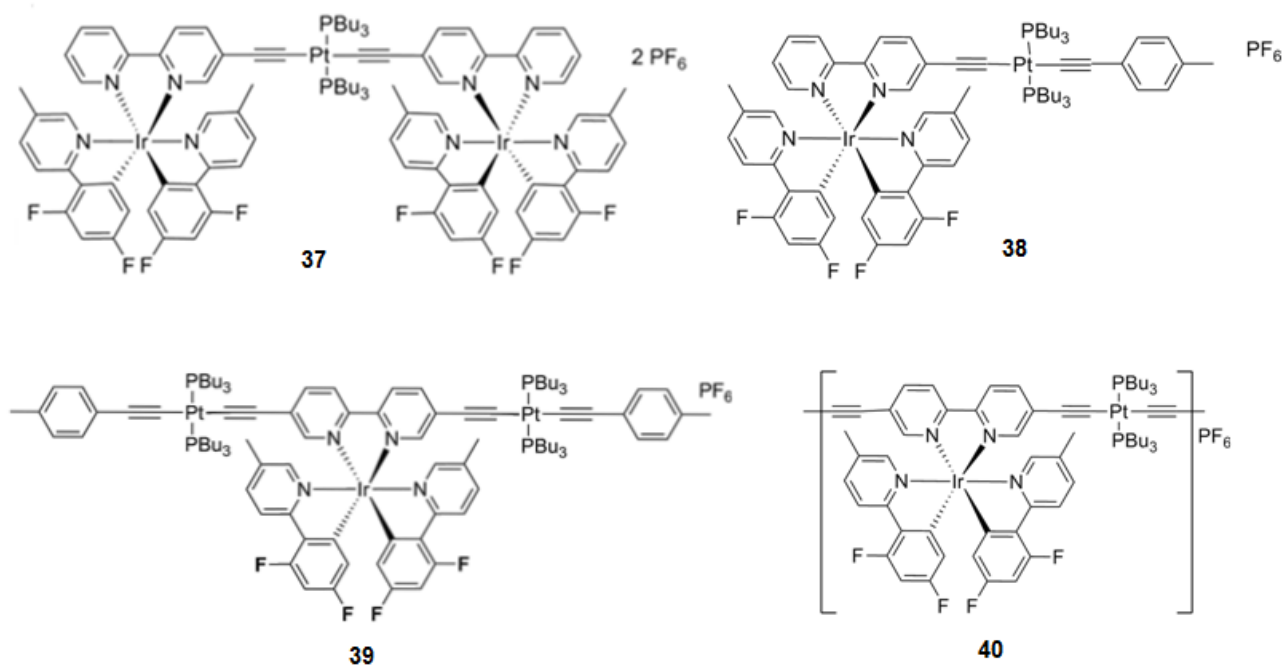


Figure 2.31. New series of fluorinated complexes **37**, **38**, **39** and **40**.

## References:

- 1- U. Mitschke and P. Bauerle, *J. Mater. Chem.*, **2000**, *10*, 1471.
- 2- T.A. Yourre, L.I. Rudaya, N.V. Klimova and V.V. Shamanin, *Semiconductors*, **2003**, *37*, 807.
- 3- a) B. Xu and T. Swager, *J.Am.Chem. Soc.*, **1987**, *115*, 1159. b) S.R. Marder, B.K. Kippelen, A.K.Y. Jen and N. Peyghambarian, *Nature*, **1997**, *388*, 845.
- 4- *Metal-carbon bonds in enzymes and cofactors. Metal Ions in Life Sciences*. Astrid Sigel, Helmut Sigel and Roland K.O. Sigel, Royal Society of Chemistry, **2009**.
- 5- *Synthetic Models for Bioorganometallic Reaction Centers*, G. Jaouen; Wiley-VCH: Weinheim, **2005**.
- 6- W.C. Zeise, *Pogg. Ann.*, **1827**, *9*, 632; **1831**, *21*, 497.
- 7- R. Bunsen, *Liebigs Ann. Chem.*, **1837**, *24*, 471.
- 8- E. Frankland, *Liebigs Ann. Chem.*, **1849**, *71*, 171.
- 9- E. Frankland, *Phil. Trans.*, **1852**, *142*, 417.
- 10- C. Lowig, *Liebigs Ann. Chem.*, **1853**, *88*, 318.
- 11- W. Hallwachs and A. Schfarik, *Liebigs Ann. Chem.*, **1859**, *109*, 207.
- 12- a) C. Friedal and J.M. Crafts, *Liebigs Ann. Chem.*, **1863**, *127*, 28. b) C. Friedal and J.M. Crafts, *Liebigs Ann. Chem.*, **1865**, *136*, 203.
- 13- M.P Schutzenberger, *Liebigs Ann. Chem.*, **1868**, *15*, 100.
- 14- L. Mond and C. Langler, *J. Chem. Soc.*, **1891**, *59*, 1090.
- 15- V. Grignard, *C.R. Acad. Sci.*, **1900**, *130*, 1322.
- 16- W. Schlenk and J. Holtz, *Chem. Ber.*, **1917**, *50*, 262.
- 17- a) T. J. Kealy and P.L. Pauson, *Nature*, **1951**, *168*, 1039. b) S.A. Miller, J.A. Tebboth and J.F. Tremaine, *J. Chem. Soc.*, **1952**, 623.
- 18- E.O. Fischer and A. Maasbol, *Angew. Chem. Int. Ed. Engl.*, **1964**, *3*, 580.
- 19- E.O. Fischer, G. Kreis, C.G. Kreiter, J. Muller, G. Huttner and H. Lorenz, *Angew. Chem. Int. Ed. Engl.*, **1973**, *12*, 564.
- 20- P.G. Lenhart and Crowfoot-Hodgkin, *Nature*, **1961**, *192*, 937.
- 21- T. Ando (Translator), *Serendipity*, Kagaku Dojin, Kyoto, **1993**.
- 22- a) M. Maestri, V. Balzani, C. Deuschel-Cornioley and A. Von Zelewsky, *Adv. Photochem.*, **1992**, *17*, 1. b) R. J. Watts, *Comments Inorg. Chem.*, **1991**, *11*, 303.

- 23- B. Martin and G. M. Waind, *J. Chem. Soc.*, **1958**, 4282.
- 24- B. Chiswell and S. E. Livingstone, *J. Inorg. Nucl. Chem.*, **1964**, 26, 47.
- 25- M. A. Baldo, M. E. Thompson and S. R. Forrest, *Nature*, **2000**, 403, 75.
- 26- <http://en.wikipedia.org/wiki/Iridium>
- 27- <http://en.wikipedia.org/wiki/Platinum>
- 28- a) F. Matsumoto, N. Matsumi, Y. Chujo, *Polym. Bull.*, **2002**, 48, 11; b) L. Liu, W.-H. Ai, M.-J. Li, S.-Z. Liu, C.-M. Zhang, H.-X. Yan, Z.-L. Du, W.-Y. Wong, *Chem. Mater.*, **2007**, 19, 1704.
- 29- a) J. Lewis, P. R. Raithby, W.-Y. Wong, *J. Organomet. Chem.*, **1998**, 556, 219; b) W.-Y. Wong, G.-L. Lu, K.-H. Choi, J.-X. Shi, *Macromolecules*, **2002**, 25, 3506; c) M. S. Khan, M. R. A. Al-Mandhary, M. K. Al-Suti, B. Ahrens, M. F. Mahon, L. Male, P. R. Raithby, C. E. Boothby, A. Kohler, *Dalton Trans.*, **2003**, 74; d) W.-Y. Wong, K.-H. Choi, G.-L. Lu, J.-X. Shi, *Macromol. Rapid Commun.*, **2001**, 22, 461; e) C.-L. Ho, W.-Y. Wong, *Chin. J. Polym. Sci.*, **2009**, 27, 455; f) W.-Y. Wong, L. Liu, S.-Y. Poon, K.-H. Choi, K.-W. Cheah, J.-X. Shi, *Macromolecules*, **2004**, 37, 4496; g) L. Liu, W.-Y. Wong, J.-X. Shi, K.-W. Cheah, *J. Polym. Sci. Part A: Polym. Chem.*, **2006**, 44, 5588; h) L. Liu, W.-Y. Wong, J.-X. Shi, K.-W. Cheah, T.-H. Lee, L. M. Leung, *J. Organomet. Chem.*, **2006**, 691, 4028.
- 30- W.-Y. Wong, P.D. Harvey, *Macromol. Rapid Commun.*, **2010**, 31, 671.
- 31- A. M. Soliman, D. Fortin, E. Zysman-Colman and P. D. Harvey, *Macromol. Rapid Commun.*, **2012**, 33, 522.
- 32- a) A. B. Tamayo, S. Garon, T. Sajoto, P. I. Djurovich, I. M. Tsyba, R. Bau, and M. E. Thompson, *Inorg. Chem.*, **2005**, 44, 8723; b) Z. Liu, Z. Bian, F. Hao, D. Nie, F. Ding, Z. Chen, *Organic Electronics*, **2009**, 10, 247; c) W.-S. Huang, C.-W. Lin, J. T. Lin, J.-H. Huang, C.-W. Chu, Y.-H. Wu, *Organic Electronics*, **2009**, 10, 549; d) J. Seo, Y. Kim, Y. Ha., *Thin Solid Films*, **2009**, 517, 1807.
- 33- R. Ziessel, S. Diring and P. Retailleau, *Dalton Trans.*, **2006**, 3285.
- 34- Y. Fan, L.-Y. Zhang, F.-R. Dai, L.-X. Shi, and Z.-N. Chen. *Inorg. Chem.*, **2008**, 47, 2811.
- 35- R. Hoffmann, *Tetrahedron*, **1966**, 22, 521.
- 36- a) V. W.-W. Yam, V. C.-Y. Lau, K.-K. Cheung, *Organometallics*, **1996**, 15, 174; b) V. W.-W. Yam, K. M.-C. Wong, N. Zhu, *Angew. Chem., Int. Ed.*, **2003**, 42, 1400.
- 37- N. M. Shavaleev, Z. R. Bell, T. L. Easun, R. Rutkaite, L. Swanson, M. D. Ward, *Dalton Trans.*, **2004**, 3678; (b) D. R. Striplin, G. A. Crosby, *Coord. Chem. Rev.*, **2001**, 211, 163; (c) K. S. Schanze, D. B. MacQueen, T. A. Perkins, L. A. Cabana, *Coord. Chem. Rev.*, **1993**, 122, 63; (d) A. Juris, V.

Balzani, F. Barigelletti, S. Campagna, P. Belser, A. V. Zelewsky, *Coord. Chem. Rev.*, **1988**, *84*, 85; (e) V. W.-W. Yam, V. C.-Y. Lau, K.-K. Cheung, *Organometallics*, **1996**, *15*, 1740.

38- M.L. Muro, S. Diring, X. Wang, R. Ziessel and F.N. Castellano. *Inorg. Chem.*, **2009**, *48*, 11533.

39- a) K. M.-C. Wong, W.-S. Tang, X.-X. Lu, N. Zhu, V. W.-W. Yam, *Inorg. Chem.*, **2005**, *44*, 1492; b) M. L. Muro, S. Diring, X. Wang, R. Ziessel, F. N. Castellano, *Inorg. Chem.*, **2008**, *47*, 6796; c) V. W.-W. Yam, C.-K. Hui, S.-Y. Yu, N. Zhu, *Inorg. Chem.*, **2004**, *43*, 812; d) W. Lu, M. C. W. Chan, N. Zhu, C. M. Che, Z. He, K. M.-C. Wong, *Chem. Eur. J.*, **2003**, *9*, 6155 (e) X. Han, L.-Z. Wu, G. Si, J. Pan, Q.-Z. Yang, L.-P. Zhang, C.-H. Tung, *Chem. Eur. J.*, **2007**, *13*, 1231.

40- V. Grosshenny, A. Harriman and R. Ziessel, *Angew. Chem. Int. Ed. Engl.*, **1995**, *34*, 1100.

41- a) A. Harriman, M. Hissler, R. Ziessel, A. De Cian and J. Fisher, *J. Chem. Soc. Dalton Trans.*, **1995**, 4067; b) V. Grosshenny, A. Harriman, M. Hissler and R. Ziessel, *J. Chem. Soc. Faraday Trans.*, **1996**, *92*, 2223.

42- K.J. Arm and J.A.G. Williams, *Dalton Trans.*, **2006**, 2172.

43- S. Welter, F. Lafalet, E. Cecchetto, F. Vergeer, and L. De Cola, *ChemPhysChem.*, **2005**, *6*, 2417.

44- S. Serroni, A. Juris, S. Campagna, M. Venturi, G. Denti, V. Balzani, *J. Am. Chem. Soc.*, **1994**, *116*, 9086.

45- I. M. Dixon, J.-P. Collin, J.-P. Sauvage, L. Flamigni, S. Encinas and F. Barigelletti, *Chem. Soc. Rev.*, **2000**, *29*, 385.

46- I. M. Dixon, J.-P. Collin, J.-P. Sauvage, F. Barigelletti and L. Flamigni, *Angew. Chem., Int. Ed.*, **2000**, *39*, 1292.

47- V.N. Kozhevnikov, M.C. Durrant and J.A.G. Williams, *Inorg. Chem.*, **2011**, *50*, 6304.

48- K. Ogawa, F. Guo and K. S. Schanze. *J. Photochem. Photobiol. A: Chemistry*, **2009**, *207*, 79.

49- T. A. Clem, D. F. J. Kavulak, E. J. Westling and J. M. J. Fréchet, *Chem. Mater.*, **2010**, *22*, 1977.

50- L. Liu, D. Fortin and P. D. Harvey, *Inorg. Chem.*, **2009**, *48*, 5891.

51- a) J. Deng, Y. Liu, Y. Wang, H. Tan, Z. Zhang, G. Lei, J. Yu, M. Zhu, W. Zhu, Y. Cao, *Eur. Polym. J.*, **2011**, *47*, 1836; b) F. Dumur, Y. Guillaneuf, A. Guerlin, G. Wantz, D. Bertin, F. Miomandre, G. Clavier, D. Gigmes, C. R. Mayer, *Macromol. Chem. Phys.*, **2011**, *212*, 1616; c) Z. Ma, J. Ding, Y. Cheng, Z. Xie, L. Wang, X. Jing, F. Wang, *Polymer*, **2011**, *52*, 2189; d) M. Goikhman, I. Podeshvo, N. Loretsyan, T. Anan'eva, R. Smyslov, T. Nekrasova, M. Smirnov, E. Popova, A. Yakimanskii, *Polym. Sci. Ser. B Polym. Chem.*, **2011**, *53*, 89; e) J. P. Gunning, J. W. Levell, M. F. Wyatt, P. L. Burn, J. Robertson, I. D. W. Samuel, *Polym. Chem.*, **2010**, *1*, 730; f) W.-Y. Lai, J. W. Levell, A. C. Jackson, S.-C. Lo, P. V. Bernhardt, I. D. W. Samuel, P. L. Burn,



*Macromolecules*, **2010**, *43*, 6986; g) J. Vicente, J. Gil-Rubio, G. Zhou, H. J. Bolink, J. Arias-Pardilla, *J. Polym. Sci. Part A: Polym. Chem.*, **2010**, *48*, 3744; h) N. B. Sankaran, A. Z. Rys, R. Nassif, M. K. Nayak, K. Metera, B. Chen, H. S. Bazzi, H. F. Sleiman, *Macromolecules*, **2010**, *43*, 5530; i) C. Ulbricht, C. R. Becer, A. Winter, U. S. Schubert, *Macromol. Rapid Commun.*, **2010**, *31*, 827; j) T. Fei, G. Cheng, D. Hu, W. Dong, P. Lu, Y. Ma, *J. Polym. Sci., Part A: Polym. Chem.*, **2010**, *48*, 1859; k) Z. Ma, J. Ding, B. Zhang, C. Mei, Y. Cheng, Z. Xie, L. Wang, X. Jing, F. Wang, *Adv. Funct. Mater.*, **2010**, *20*, 138.

52- a) S.-J. Liu, Z.-H. Lin, Q. Zhao, Y. Ma, H.-F. Shi, M.-D. Yi, Q.-D. Ling, Q.-L. Fan, C.-X. Zhu, E.-T. Kang, W. Huang, *Adv. Funct. Mater.*, **2011**, *21*, 979; b) S. Albert-Seifried, J. M. Hodgkiss, F. D. R. Laquai, H. A. Bronstein, C. K. Williams, R. H. Friend, *Phys. Rev. Lett.*, **2010**, *105*, 195501; c) H.-F. Shi, S.-J. Liu, H.-B. Sun, W.-J. Xu, Z.-F. An, J. Chen, S. Sun, X.-M. Lu, Q. Zhao, W. Huang, *Chem. Eur. J.*, **2010**, *16*, 12158; d) M.-J. Park, J. Kwak, J. Lee, I. H. Jung, H. Kong, C. Lee, D.-H. Hwang, H.-K. Shim, *Macromolecules*, **2010**, *43*, 1379; e) S.-J. Liu, W.-J. Xu, T.-C. Ma, Q. Zhao, Q.-L. Fan, Q.-D. Ling, W. Huang, *Macromol. Rapid Commun.*, **2010**, *31*, 629.

53- a) W.-S. Huang, Y.-H. Wu, H.-C. Lin, J. T. Lin, *Polym. Chem.*, **2010**, *1*, 494; b) G. Zhou, Y. He, B. Yao, J. Dang, W.-Y. Wong, Z. Xie, X. Zhao, L. Wang, *Chem. Asian J.*, **2010**, *5*, 2405.

54- a) *Electronic Aspects of Organic Photochemistry*, J. Michl, V. Bonacic-Koutechy, Wiley, New York, **1990**; b) *Vibrational states*, S. Califano, Wiley, New York, **1976**.

55- S.-J. Liu, Q. Zhao, R.-F. Chen, Y. Deng, Q.-L. Fan, F.-Y. Li, L.-H. Wang, C.-H. Huang, and W. Huang, *Chem. Eur. J.*, **2006**, *12*, 4351.

56- A. B. Zdravkov and N. N. Khimich, *Russ. J. Org. Chem.*, **2006**, *42*, 1200.

57- U. Lehmann and A. D. Schlüter, *Eur. J. Org. Chem.*, **2000**, *2000*, 3483.

58- G. B. Kauffman, L. A. Teter and J. E. Huheey, in *Inorg. Synth.*, John Wiley & Sons, Inc., **2007**, 245.

59- M. Nonoyama, *Bull. Chem. Soc. Jpn.*, **1974**, *47*, 767.

60- H. Ishida, S. Tobita, Y. Hasegawa, R. Katoh and K. Nozaki, *Coord. Chem. Rev.*, **2010**, *254*, 2449

61- S. Ladouceur, D. Fortin and E. Zysman-Colman, *Inorg. Chem.*, **2010**, *49*, 5625.

62- A. A. Rachford, R. Ziessel, T. Bura, P. Retailleau and F. N. Castellano, *Inorg. Chem.*, **2010**, *49*, 3730.

63- (a) K. Gagnon, S. Mohammed Aly, A. Brisach-Wittmeyer, D. Bellows, J.-F. Bérubé, L. Caron, A. S. Abd-El-Aziz, D. Fortin and P. D. Harvey, *Organometallics*, **2008**, *27*, 2201; (b) J. E. Rogers, T. M. Cooper, P. A. Fleitz, D. J. Glass and D. G. McLean, *J. Phys. Chem. A*, **2002**, *106*, 10108.

64- A. M. Soliman, D. Fortin, E. Zysman-Colman and P. D. Harvey, *Chem. Commun.*, **2012**, 48, 6271.

**Experimental section:**

## General Procedures:

Commercial chemicals were used as supplied. All experiments were carried out with freshly distilled anhydrous solvents obtained from a Pure Solv<sup>TM</sup> solvent purification system from Innovative Technologies except where specifically mentioned. *N,N,N*-Triethylamine (Et<sub>3</sub>N), *N,N*-diisopropylamine (*i*-Pr<sub>2</sub>NH) were distilled over CaH<sub>2</sub> under a nitrogen atmosphere. All reagents wherein the synthesis is not explicitly described in the SI were purchased and used without further purification. Flash column chromatography was performed using silica gel (Silia-P from Silicycle, 60 Å, 40-63 µm). Analytical thin layer chromatography (TLC) was performed with silica plates with aluminum backings (250 µm with indicator F-254). Compounds were visualized under UV light. <sup>1</sup>H and <sup>13</sup>C NMR spectra were recorded on a Bruker Avance spectrometer at 400 MHz and 100 MHz, respectively or a Bruker Avance spectrometer at 300 MHz and 75MHz, respectively. <sup>31</sup>P NMR spectra was recorded on a Bruker Avance spectrometer at 121 MHz. Deuterated chloroform (CDCl<sub>3</sub>) was used as the solvent of record. Melting points (Mp's) were recorded using open end capillaries on a Meltemp melting point apparatus and are uncorrected. GC-MS samples were separated on a Shimadzu QP 2010 Plus equipped with a HP5-MS 30 m x 0.25 mm ID x 0.25 µm film thickness column. High resolution mass spectra were recorded on either a VG Micromass ZAB-2F or a Waters Synapt MS G1 (ES-Q-TOF) at the Université de Sherbrooke. GPC (Gel Permeation Chromatography) instrument, equipped with a Waters 410 differential refractometer detector and a Waters 996 photodiode array detector, was also utilized to measure the M<sub>n</sub>, M<sub>w</sub> (number and weight-average molecular weight) and the polydispersity index (PDI) using polystyrene (PS) standards. The GPC measurements were conducted at 35 °C using one column (Waters Styragel HR4E, 7.8 mm x 300 mm, 5 µm beads) and THF eluent (flow rate: 1.0 mL min<sup>-1</sup>).

### ***trans*-Dichloro-bis(tri-*n*-butylphosphine)platinum(II):<sup>1</sup>**



In A dry flask charged with PtCl<sub>2</sub> (1.00 g, 3.76 mmol, 1.0 equiv.), DCM (150 mL) was added and the solution was purged with N<sub>2</sub> for 30 min. The reaction vessel was sealed tightly and transferred to the glove box to which a solution PBu<sub>3</sub> (2.2 ml, 8.6 mmol, 2.3 equiv.) was added to the flask by a

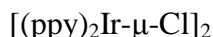
syringe. After stirring 5 minutes, the entire  $\text{PtCl}_2$  solid was solubilised and the reaction left overnight. On the second day, DCM was evaporated to obtain a yellow oily liquid. This liquid was heated to  $160\text{ }^\circ\text{C}$  to obtain the *trans* form. The *trans* product was separated from the remained *cis* conformer by using 30% DCM/hexanes as an eluent and the *cis* conformer was recuperated and re-heated again to yield 1.82 g (73%) of a yellow solid of the *trans* conformer.

### Copper(I) iodide recrystallisation:<sup>2</sup>

#### CuI

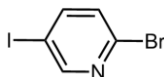
To a solution of KI (135 g, 813 mmol, 12.0 equiv.) and commercial CuI (13.2 g, 69.3 mmol, 1.0 equiv.) in water (100 mL) was added activated charcoal (6 g). The mixture was stirred vigorously for 0.5 h. The mixture was then filtered through a Celite plug and washed with water (10 mL). The solution was then diluted with water (400 mL) and cooled at  $0\text{ }^\circ\text{C}$ . A white solid started to precipitate. The white precipitate was then filtered under a constant  $\text{N}_2$  flow. The solid was then washed with water (2 x 100 mL), acetone (2 x 80 mL) and  $\text{Et}_2\text{O}$  (2 x 80 mL). The white solid was then dried under vacuum to yield 10.8 g (82%).

### Bis(chloro-diphenylpyridine), bis-iridium(III) dimer (26):<sup>3</sup>



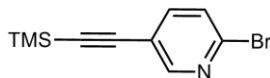
In A flask charged with anhydrous  $\text{IrCl}_3$  (0.86 g, 2.90 mmol, 1.00 equiv.) and phenylpyridine (**25**) (9.0 g, 5.8 mmol, 2.0 equiv.), ethoxyethanol (10 mL) was added and the reaction was stirred at room temperature for 20 h. The yellow precipitate was filtered and dried under vacuum overnight to yield 0.52 g (76%) of yellow solid.

### 2-Bromo-5-iodopyridine (2):<sup>4</sup>



To a mixture of 2,5-dibromopyridine (**1**) (10.0 g, 42.2 mmol, 1.00 equiv.) in Et<sub>2</sub>O (500 mL) at -78 °C was added *n*-BuLi 2.2 M solution in hexanes (21.1 ml, 46.4 mmol 1.10 equiv.) over 25 min. The peach lithiate was stirred for 10 min at -78 °C. A solution of iodine (11.8 g, 46.4 mmol, 1.10 equiv.) in Et<sub>2</sub>O (200 mL) was canulated in over 30 min. During the iodine addition, the solution first turns mauve then at the end of the addition, a light tan colour was obtained. The mixture was stirred at room temperature for 18 h. The reaction was followed by GCMS, then was quenched with saturated NaHSO<sub>3(aq)</sub>. The phases were separated and the organic layer was further washed with saturated NaHSO<sub>3(aq)</sub> (2x) and then neutralized with NaHCO<sub>3(aq)</sub>. The aqueous layer combined and extracted with Et<sub>2</sub>O until no more product was observed by TLC. The organic phase was dried over MgSO<sub>4</sub> and concentrated under reduced pressure. The residue was purified by flash chromatography (10% EtOAc/hexanes on silica gel) to yield 11.0 g of white solid (Yield: 93%). **Rf**: 0.38 (10% EtOAc/hexanes on silica). **Mp**: 118-120°C. (**Litt.**: 124-126°C).<sup>5</sup> **<sup>1</sup>H NMR (300 MHz, CDCl<sub>3</sub>) δ (ppm)**: 8.57 (d, *J* = 2.4 Hz, 1H), 7.79 (dd, *J* = 2.4 Hz, 8.4 Hz, 1H), 7.26 (dd, *J* = 0.6 Hz, 8.1 Hz, 1H). **<sup>13</sup>C NMR (75 MHz, CDCl<sub>3</sub>) δ (ppm)**: 156.0, 146.4, 141.3, 129.8, 91.5. **LR-MS (EI, 70eV) (*m/z*)**: 283, 285 (M<sup>+</sup>); **HR-MS (EI, 70eV): Calculated** (C<sub>5</sub>H<sub>3</sub>BrIN): 282.8494 (C<sub>5</sub>H<sub>3</sub>BrIN) **Found**: 282.8499. The <sup>1</sup>H and <sup>13</sup>C NMR spectrum correspond to that found in the literature.<sup>5</sup>

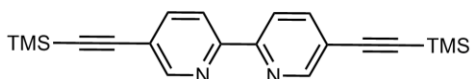
### 2-Bromo-5-((trimethylsilyl)ethynyl)pyridine (**3**):<sup>6</sup>



To a solution of PdCl<sub>2</sub>(PPh<sub>3</sub>)<sub>2</sub> (298 mg, 0.42 mmol, 0.03 equiv.), CuI (161 mg, 0.85 mmol, 0.06 equiv.), 2-bromo-5-iodopyridine (**2**) (4.00 g, 14.1 mmol, 1.00 equiv.) in *i*-Pr<sub>2</sub>NH (120 mL). The solution was degassed and then (TMSA) was added (1.99 ml, 14.1 mmol, 1.00 equiv.). The solution was stirred for 8 h at room temperature under N<sub>2</sub>. The reaction was followed by GC-MS. The solution was diluted with ether and then treated with 0.1 N HCl<sub>aq</sub> until the aqueous layer was at pH = 1. The aqueous solutions were extracted multiple times with ether. The organic phase was dried over MgSO<sub>4</sub>, filtered on a Celite ® plug and concentrated under reduced pressure to obtain the crude product. The product was purified by flash chromatography (10% EtOAc/hexanes on silica gel) to yield 3.45 g of brown solid (Yield: 97%). **Rf**: 0.82 (10% EtOAc/hexanes). **Mp**: 66.0-67.3°C. (**Litt.**:

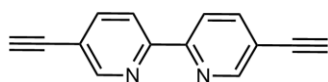
71-71.9°C). <sup>1</sup>H NMR (400 MHz, CDCl<sub>3</sub>) δ (ppm): 8.43 (dd, *J* = 2.4, 0.7, 1H), 7.58 (dd, *J* = 8.2, 2.4, 1H), 7.43 (dd, *J* = 8.2, 0.8, 1H), 0.26 (s, 9H). <sup>13</sup>C NMR (101 MHz, CDCl<sub>3</sub>) δ (ppm): 153.0, 141.5, 141.2, 127.8, 119.4, 100.3, 100.2, 0.0. LR-MS (EI, 70eV) (*m/z*): 253 (M<sup>+</sup>), 240. HR-MS (EI, 70eV): Calculated (C<sub>10</sub>H<sub>12</sub>BrNSi): 252.9922 Found: 252.9922. The <sup>13</sup>C and <sup>1</sup>H NMR spectrum corresponds to that found in the literature.<sup>8</sup>

#### 5,5'-Bis((trimethylsilyl)ethynyl)-2,2'-bipyridine (4):



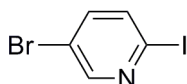
To a degassed solution of 5-Bromo-2-((trimethylsilyl)ethynyl)pyridine (**3**) (1.50 g, 5.93 mmol, 1.00 equiv.) in THF (12 ml) at -78 °C was added *n*-BuLi 2.2 M solution in hexanes (3.50 ml, 7.70 mmol, 1.30 equiv.) over 15 minutes. The mixture was stirred for 20 min at -78 °C then a solution of ZnCl<sub>2</sub> (1.05 g, 7.70 mmol, 1.30 equiv.) in THF (10 mL) was added in over 40 min. The mixture was stirred at room temperature for 2 h. The zincate solution was added into a mixture of 5-Bromo-2-((trimethylsilyl)ethynyl)pyridine (**3**) (1.50 g, 5.93 mmol, 1.00 equiv.) and Pd(PPh<sub>3</sub>)<sub>4</sub> (343 mg, 0.30 mmol, 5.0 mol%) in THF (12 ml). The reaction mixture was heated to reflux for 24 h. The reaction was followed by GC-MS. It was added to an aqueous solution of EDTA:NaHCO<sub>3</sub> (sat.) (1:1, 15 mL) then stirred for 2 h at room temperature. To the mixture was added DCM and then the phases were separated. The organic phase was further washed with an aqueous solution of EDTA:NaHCO<sub>3</sub> (sat.) (1:1, 2 x 15 mL). The organic phase was dried over MgSO<sub>4</sub> and concentrated under reduced pressure. The residue was purified by flash chromatography (DCM on silica gel) to yield 0.71 g of light brown solid (Yield: 35%). **R<sub>f</sub>**: 0.15 (DCM). **Mp**: 165.7-168°C. <sup>1</sup>H NMR (300 MHz, CDCl<sub>3</sub>) δ (ppm): 8.72 (d, *J* = 1.7 Hz, 2H), 8.35 (d, *J* = 8.3 Hz, 2H), 7.86 (dd, *J* = 8.2, 2.1 Hz, 2H), 0.28 (s, 18H). <sup>13</sup>C NMR (101 MHz, CDCl<sub>3</sub>) δ (ppm): 154.3, 152.2, 139.9, 120.6, 120.5, 101.9, 99.6, 0.0. LR-MS (EI, 70eV) (*m/z*): 348 (M<sup>+</sup>), 333. HR-MS (EI, 70eV): Calculated (C<sub>20</sub>H<sub>24</sub>N<sub>2</sub>Si<sub>2</sub>): 348.1478 Found: 348.1479. The <sup>13</sup>C and <sup>1</sup>H NMR spectrum corresponds to that found in the literature.<sup>9</sup>

#### 5,5'-Diethynyl-2,2'-bipyridine (5):



To a solution of the protected 5,5'-bis((trimethylsilyl)ethynyl)-2,2'-bipyridine (**4**) (200 mg, 0.57 mmol, 1.00 equiv.) in MeOH (10 mL) was added  $K_2CO_3$  (364 mg, 2.64 mmol, 4.60 equiv.). The reaction was stirred for 2 h at room temperature and followed by GC-MS. The reaction was poured into a solution of  $H_2O/Et_2O$  (1:1), the layers were separated and the organic phase was washed with  $H_2O$  (twice). The combined aqueous fractions were extracted with  $Et_2O$  (three times). The organic phase were combined and dried over  $MgSO_4$ , the organic phase was filtered and then concentrated under reduced pressure to yield 116 mg of light brown solid (Yield: 99 %). **Mp**: 178 °C dec. (**Litt** : 130 °C dec).  **$^1H$  NMR (400 MHz,  $CDCl_3$ )  $\delta$  (ppm)**: 8.70 (dd,  $J = 2.0, 0.7$ , 2H), 8.32 (dd,  $J = 8.2, 0.8$ , 2H), 7.83 (dd,  $J = 8.2, 2.1$ , 2H), 3.24 (s, 2H).  **$^{13}C$  NMR (101 MHz,  $CDCl_3$ )  $\delta$  (ppm)**: 154.8, 152.5, 140.3, 120.8, 119.7, 81.9, 80.8. **LR-MS (EI, 70eV) ( $m/z$ )**: 204 ( $M^+$ ), 102. **HR-MS (EI, 70eV): Calculated** ( $C_{14}H_8N_2$ ): 204.0687 **Found**: 204.0688. The  $^{13}C$  and  $^1H$  NMR spectrum corresponds to that found in the literature.<sup>10</sup>

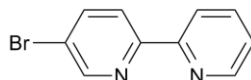
### 5-Bromo-2-iodopyridine (**6**):<sup>11</sup>



To a mixture of 2,5-dibromopyridine (**1**) (4.00 g, 16.88 mmol, 1.00 equiv.) and KI (8.41 g, 50.63 mmol, 3.00 equiv.) was added HI (48 % wt., 20 mL). The reaction mixture was heated to reflux for 72 h. The reaction was followed by GC-MS and upon consumption of the starting material, was then cooled to 0 °C. An aqueous solution of KOH (40 %, 30 mL) followed by  $Et_2O$  (30 mL) was then added to the reaction mixture. The layers were separated and the aqueous phase was washed with  $Et_2O$  (2 x 30 mL). The combined organic phases were dried over  $MgSO_4$ , filtered and concentrated. The residue was purified by flash chromatography (10% EtOAc/hexanes on silica gel) to yield 4.25 g of white solid (Yield: 90 %). **Rf**: 0.28 (10% EtOAc/hexanes). **Mp**: 112.8-113.6°C. (**Litt.**: 112.5-113.5°C).<sup>11</sup>  **$^1H$  NMR (400 MHz,  $CDCl_3$ )  $\delta$  (ppm)**: 8.43 (d,  $J = 2.5$  Hz, 1H), 7.58 (dd,  $J = 8.3$  Hz, 1H), 7.42 (dd,  $J = 8.4, 2.7$  Hz, 1H).  **$^{13}C$  NMR (100 MHz,  $CDCl_3$ )  $\delta$  (ppm)**: 152.1, 140.5, 136.3,

121.4, 115.4. **LR-MS (EI, 70eV) (*m/z*):** 283 ( $M^+$ ), 75. **HR-MS (EI, 70eV): Calculated** ( $C_5H_3BrIN$ ): 282.8494; **Found:** 282.8493. The  $^1H$  and  $^{13}C$  NMR spectrum each correspond to that found in the literature.<sup>12</sup>

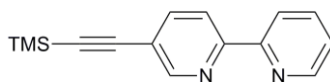
### 5-Bromo-2,2'-bipyridine (8):



To a solution of 2-bromopyridine (**7**) (4.80 mL, 50.4 mmol, 1.05 equiv.) in THF (65 mL) at  $-78\text{ }^\circ\text{C}$  was added *n*-BuLi 2.2 M in hexanes (24.0 mL, 52.8 mmol, 1.10 equiv.) over 40 min. The mixture was stirred for 30 min at  $-78\text{ }^\circ\text{C}$ , then a solution of  $ZnCl_2$  (7.19 g, 52.8 mmol, 1.10 equiv.) in THF (60 mL) was canulated in over 40 min. The mixture was stirred at room temperature for 2 h. The zincate solution was canulated into a mixture of 5-bromo-2-iodopyridine (**6**) (13.6 g, 48.0 mmol, 1.00 equiv.) and  $Pd(PPh_3)_4$  (2.91 g, 2.52 mmol, 5 mol %) in THF (60 mL). The reaction mixture was heated to reflux for 16 h. The reaction was followed by GC-MS. Upon cooling to room temperature, a gray solid precipitate was observed. The reaction mixture was concentrated under reduced pressure, but not dried. The suspension was cooled to  $-20\text{ }^\circ\text{C}$ . The gray solid was filtered and washed with cold THF (2 x 20 mL). It was added to an aqueous solution of EDTA: $NaHCO_3$  (sat.) (1:1, 15 mL) then stirred for 2 h at room temperature. To the mixture was added DCM and then the phases were separated. The organic phase was further washed with an aqueous solution of EDTA: $NaHCO_3$  (sat.) (1:1, 2 x 15 mL). The organic phase was dried over  $MgSO_4$  and concentrated under reduced pressure. The residue was purified by flash chromatography (15% EtOAc/hexanes on silica gel) to yield 7.00 g of white solid (Yield: 60%). **R<sub>f</sub>**: 0.45 (10% EtOAc/hexanes). **Mp**:  $72\text{--}73.8\text{ }^\circ\text{C}$ . (**Litt.**:  $74\text{--}75\text{ }^\circ\text{C}$ ).<sup>13</sup>  **$^1H$  NMR (300 MHz,  $CDCl_3$ )  $\delta$  (ppm):** 8.72 (d,  $J = 2.2$  Hz, 1H), 8.68 (d,  $J = 4.7$  Hz, 1H), 8.38 (d,  $J = 8.0$  Hz, 1H), 8.32 (d,  $J = 8.5$  Hz, 1H), 7.96 (dd,  $J = 8.5, 2.4$  Hz, 1H), 7.82 (td,  $J = 7.8, 1.8$  Hz, 1H), 7.33 (ddd,  $J = 7.3, 4.7, 1.1$  Hz, 1H).  **$^{13}C$  NMR (75 MHz,  $CDCl_3$ )  $\delta$  (ppm):** 155.1, 154.6, 150.1, 149.2, 139.4, 137.0, 123.9, 122.3, 121.1, 120.9. **LR-MS (EI, 70eV) (*m/z*):** 234 ( $M^+$ ), 155, 128. **HR-MS (EI, 70eV): Calculated** ( $C_{10}H_7BrN_2$ ): 233.9793; **Found:** 233.9797. The  $^1H$  and  $^{13}C$  NMR spectra each correspond to that found in the literature.<sup>13</sup>

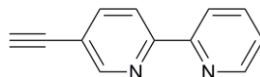


### 5-Trimethylsilylethynyl-2,2'-bipyridine (9):



To a solution of 5-bromo-2,2'-bipyridine (**8**) (2.00 g, 8.55 mmol, 1.00 equiv.) in THF (90 mL) and *i*-Pr<sub>2</sub>NH (30 mL) was added TMSA (2.90 mL, 20.5 mmol, 2.40 equiv.), Pd(PPh<sub>3</sub>)<sub>4</sub> (0.59 g, 0.51 mmol, 6 mol %) and CuI (0.25 mg, 1.37 mmol, 0.16 equiv.). The solution was degassed and stirred for 48 h at room temperature. The reaction was followed by GC-MS. The solvent was evaporated under reduced pressure. The residue was purified by flash chromatography (10% EtOAc/hexanes on silica gel) to yield 2.03 g of gray solid (Yield: 94%). **Rf**: 0.38 (10% EtOAc/hexanes). **Mp**: 53.2-54.7 °C. (**Litt.**: 55-56 °C).<sup>14</sup> **<sup>1</sup>H NMR (300 MHz, CDCl<sub>3</sub>) δ (ppm)**: 8.73 (d, *J* = 1.8 Hz, 1H), 8.68 (d, *J* = 4.3 Hz, 1H), 8.38 (dd, *J* = 11.7, 8.1 Hz, 2H), 7.87 (dd, *J* = 8.3, 2.2 Hz, 1H), 7.85 – 7.77 (m, 1H), 7.32 (ddd, *J* = 7.3, 4.7, 0.9 Hz, 1H), 0.28 (s, 9H). **<sup>13</sup>C NMR (75 MHz, CDCl<sub>3</sub>) δ (ppm)**: 155.4, 154.9, 152.0, 149.1, 139.8, 136.9, 123.9, 121.4, 120.0, 101.7, 99.1, -0.3. **LR-MS (EI, 70eV) (*m/z*)**: 252 (M<sup>+</sup>), 237, 221. **HR-MS (EI, 70eV): Calculated (C<sub>15</sub>H<sub>16</sub>N<sub>2</sub>Si): 252.1083; Found: 252.1088.** The <sup>1</sup>H NMR spectrum corresponds to that found in the literature, but the <sup>13</sup>C NMR spectrum was found to be different.<sup>15</sup>

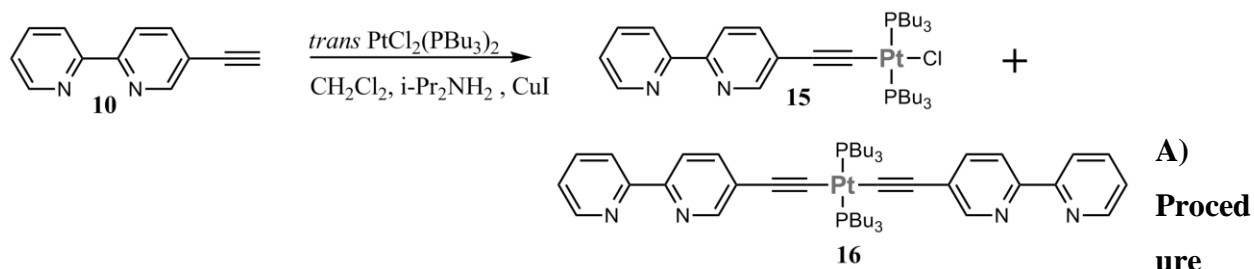
### 5-Ethynyl-2,2'-bipyridine (10) :



To a solution of the protected 5-trimethylsilylethynyl-2,2'-bipyridine (**9**) (0.10 g, 0.40 mmol, 1.00 equiv.) in MeOH (5 mL) was added K<sub>2</sub>CO<sub>3</sub> (0.13 g, 0.91 mmol, 2.30 equiv.). The reaction was stirred for 2 h at room temperature and followed by GC-MS. The reaction was poured into a solution of H<sub>2</sub>O/Et<sub>2</sub>O (1:1), the layers were separated and the organic phase was washed with H<sub>2</sub>O (twice). The combined aqueous fractions were extracted with Et<sub>2</sub>O (three times). The organic phase were combined and dried over MgSO<sub>4</sub>, the organic phase was filtered and then concentrated under reduced

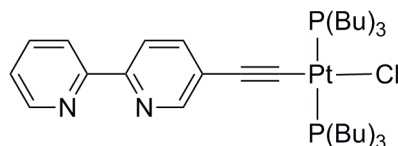
pressure to yield 0.07 g of light brown solid (Yield: 99 %). **Mp:** 87.6-88.5 °C. (**Litt.:** 87-89°C).<sup>15</sup> **Rf:** 0.30 (10% EtOAc/hexanes). **<sup>1</sup>H NMR (300 MHz, CDCl<sub>3</sub>) δ (ppm):** 8.78 (d, *J* = 1.4 Hz, 1H), 8.69 (d, *J* = 4.4 Hz, 1H), 8.40 (dd, *J* = 8.1, 4.3 Hz, 2H), 7.91 (dd, *J* = 8.2, 2.1 Hz, 1H), 7.83 (td, *J* = 7.9, 1.6 Hz, 1H), 7.33 (ddd, *J* = 7.4, 4.9, 0.5 Hz, 1H), 3.29 (s, 1H). **<sup>13</sup>C NMR (75 MHz, CDCl<sub>3</sub>) δ (ppm):** δ 155.4, 155.3, 152.2, 149.2, 140.0, 137.0, 124.0, 121.4, 120.2, 119.1, 81.32, 80.7. **LR-MS (EI, 70eV) (*m/z*):** 180 (M<sup>+</sup>). **HR-MS (EI, 70eV): Calculated (C<sub>12</sub>H<sub>8</sub>N<sub>2</sub>):** 180.0687; **Found:** 180.0682.

### Synthesis of 15 and 16:



leading to (15) as the major product:

***trans*-(5-Ethynyl-2,2'-bipyridine)-chloro-bis(tri-*n*-butylphosphine)platinum (15):**

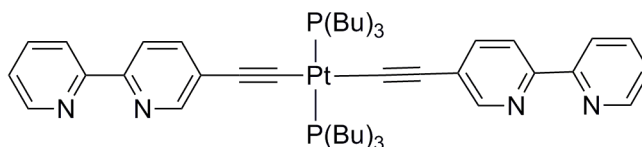


In A dry flask charged with excess *trans*-PtCl<sub>2</sub>(PBu<sub>3</sub>)<sub>2</sub> (0.99 g, 1.48 mmol, 8.90 equiv.), CuI (9.5 mg, 0.05 mmol, 0.30 equiv.) was added followed by DCM (50 mL) and *i*-Pr<sub>2</sub>NH (50 mL). The reaction mixture was purged with N<sub>2</sub> for 30 min, then 5-Ethynyl-2,2'-bipyridine (**10**) (30 mg, 0.17 mmol, 1.00 equiv.), dissolved in DCM (15 mL) and *i*-Pr<sub>2</sub>NH (15 mL), was added dropwise over 2 h. The mixture was stirred at room temperature for 16 h. The solvent was removed under reduced

pressure and the residue was redissolved in DCM (50 mL). The organic phase was washed with H<sub>2</sub>O twice then dried over MgSO<sub>4</sub> and concentrated under reduced pressure. The residue was purified by flash chromatography (50% DCM/hexanes on silica gel) to recuperate the excess *trans*-PtCl<sub>2</sub>(PBU<sub>3</sub>)<sub>2</sub>, then (30% EtOAc/hexanes) to yield 100 mg (Yield: 73%) of light yellow solid of **15** and finally flushed with (20% MeOH/DCM) to yield 42 mg (Yield: 13%) of **16**. **Rf**: 0.75 (30% EtOAc/hexanes). **Mp** = 67.3-69.7 °C; **<sup>1</sup>H NMR (400 MHz, CDCl<sub>3</sub>) δ (ppm)**: 8.65 (d, *J* = 4.7 Hz, 1H), 8.55 (d, *J* = 2.0 Hz, 1H), 8.34 (d, *J* = 8.0 Hz, 1H), 8.24 (d, *J* = 8.2 Hz, 1H), 7.79 (td, *J* = 7.7, 1.4 Hz, 1H), 7.61 (dd, *J* = 8.2, 1.9 Hz, 1H), 7.31 – 7.23 (m, 1H), 2.15 – 1.80 (m, 12H), 1.68 – 1.33 (m, 24H), 0.93 (dd, *J* = 13.1, 6.8 Hz, 18H). **<sup>13</sup>C NMR (75 MHz, CDCl<sub>3</sub>) δ (ppm)**: 156.2, 151.8, 151.1, 149.2, 138.1, 136.8, 125.7, 123.2, 120.8, 120.2, 98.2, 90.5, 26.4, 24.2, 22.2, 13.8. **<sup>31</sup>P NMR (162 MHz, CDCl<sub>3</sub>) δ (ppm)**: 8.45 (d, *J* = 2353.5 Hz). **LR-MS (EI, 70eV) (*m/z*)**: 814 (M<sup>+</sup>), 381, 202, 173. **HR-MS (EI, 70eV): Calculated (C<sub>36</sub>H<sub>61</sub>C<sub>11</sub>N<sub>2</sub>P<sub>2</sub>Pt): 812.3625; Found: 812.3600.**

## B) Procedure leading to (16) as the major product:

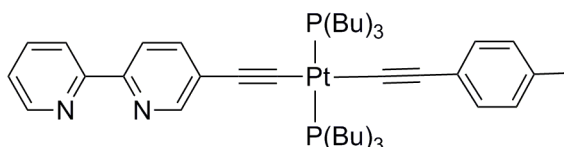
### *trans*-Bis(tri-*n*-butylphosphine)-bis(5-ethynyl-2,2'-bipyridine)platinum (16):



In A dry flask charged with excess *trans*-PtCl<sub>2</sub>(PBU<sub>3</sub>)<sub>2</sub> (0.40 g, 0.60 mmol, 4.00 equiv.), CuI (8.6 mg, 0.04 mmol, 0.3 equiv.) was added followed by DCM (30 mL) and *i*-Pr<sub>2</sub>NH (30 mL). The reaction mixture was purged with N<sub>2</sub> for 30 min, then 5-Ethynyl-2,2'-bipyridine (**10**) (27 mg, 0.15 mmol, 1.00 equiv.), dissolved in DCM (10 mL) and *i*-Pr<sub>2</sub>NH (10 mL), and added dropwise over 2 h. The mixture was stirred at room temperature for 16 h. The reaction was followed the same way as **15**. The residue was purified by flash chromatography (50% DCM/hexanes on silica gel) to recuperate the excess *trans*-PtCl<sub>2</sub>(PBU<sub>3</sub>)<sub>2</sub>, then (30% EtOAc/hexanes) to yield 8 mg (Yield: 7%) of light yellow solid of **15** and finally flushed with (20% MeOH/DCM) to yield 80 mg (Yield: 28%) of **16**. **Rf**: 0.18 (20% MeOH/DCM). **Mp**: 138.7-140.8°C. **<sup>1</sup>H NMR (400 MHz, CDCl<sub>3</sub>) δ (ppm)**: 8.58 (d, *J* = 4.1 Hz, 2H), 8.51 (s, 2H), 8.27 (d, *J* = 8.0 Hz, 2H), 8.18 (d, *J* = 8.2 Hz, 2H), 7.71 (td, *J* = 7.8, 0.9 Hz,

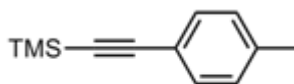
2H), 7.57 (dd,  $J = 8.2, 2.1$  Hz, 2H), 7.22 – 7.17 (m, 2H), 2.15 – 1.97 (m, 12H), 1.63 – 1.48 (m, 12H), 1.46 – 1.31 (m, 12H), 0.86 (t,  $J = 7.3$  Hz, 18H).  $^{13}\text{C}$  NMR (101 MHz,  $\text{CDCl}_3$ )  $\delta$  (ppm): 156.5, 151.9, 151.4, 149.4, 138.4, 137.0, 126.0, 123.4, 121.0, 120.4, 114.9, 106.5, 26.4, 24.7, 24.0, 13.8.  $^{31}\text{P}$  NMR (162 MHz,  $\text{CDCl}_3$ )  $\delta$  (ppm): 4.31 (d,  $J = 2328.0$  Hz). LR-MS (EI, 70eV) ( $m/z$ ): 957 ( $\text{M}^+$ ), 381, 173. HR-MS (EI, 70eV): Calculated ( $\text{C}_{48}\text{H}_{68}\text{N}_4\text{P}_2\text{Pt}$ ): 956.4546; Found: 956.4539

***trans*-(5-Ethynyl-2,2'-bipyridine)-4-tolyethynyl-bis(tri-*n*-butylphosphine)platinum (20):**



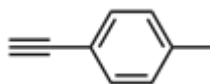
A dry flask charged with (**15**) (76 mg, 0.09, 1.00 equiv.), CuI (5.3 mg, 0.03 mmol, 0.30 equiv.), DCM (40 mL) and *i*-Pr<sub>2</sub>NH (6 mL) was purged with N<sub>2</sub> for 30 min. Excess 1-ethynyl-4-methylbenzene (**19**) (50 mg, 0.43 mmol, 4.60 equiv.), dissolved in DCM (10 mL), was then added. The mixture was stirred at room temperature for 16 h. The solvent was removed under reduced pressure and the residue was redissolved in DCM (20 ml). The organic phase was washed with H<sub>2</sub>O twice then dried over MgSO<sub>4</sub> and concentrated under reduced pressure. The residue was purified by flash chromatography (50% DCM/hexanes on silica gel) to yield 64 mg of yellow liquid (Yield: 78%). **R<sub>f</sub>**: 0.84 (50% DCM/hexanes).  $^1\text{H}$  NMR (400 MHz,  $\text{CDCl}_3$ )  $\delta$  (ppm): 8.65 (d,  $J = 3.4$  Hz, 1H), 8.57 (s, 1H), 8.36 – 8.31 (m, 1H), 8.23 (d,  $J = 8.4$  Hz, 1H), 7.83 – 7.74 (m, 1H), 7.64 (td,  $J = 8.3, 1.8$  Hz, 1H), 7.30 – 7.22 (m, 1H), 7.16 (d,  $J = 7.9$  Hz, 2H), 7.01 (d,  $J = 7.9$  Hz, 2H), 2.29 (s, 3H), 2.26 – 2.06 (m, 12H), 1.68 – 1.36 (m, 24H), 0.92 (t,  $J = 7.3$  Hz, 18H).  $^{13}\text{C}$  NMR (101 MHz,  $\text{CDCl}_3$ )  $\delta$  (ppm): 156.5, 151.7, 151.4, 149.4, 138.4, 137.0, 134.8, 130.8, 128.8, 126.2, 126.1, 123.3, 121.0, 120.4, 109.3, 106.1, 106.0, 105.9, 26.6, 24.7, 24.1, 21.5, 14.1.  $^{31}\text{P}$  NMR (162 MHz,  $\text{CDCl}_3$ )  $\delta$  (ppm): 4.17 (d,  $J = 2349.4$  Hz). LR-MS (EI, 70eV) ( $m/z$ ): 893 ( $\text{M}^+$ ); 381, 317. HR-MS (EI, 70eV): Calculated ( $\text{C}_{45}\text{H}_{68}\text{N}_2\text{P}_2\text{Pt}$ ): 892.4484. Found: 892.4470.

**1-Trimethylsilylethynyl-4-methylbenzene (18):**<sup>16</sup>



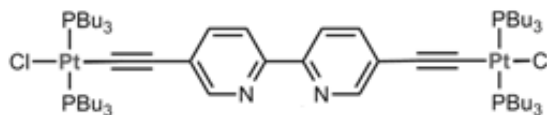
To a solution of  $\text{PdCl}_2(\text{PPh}_3)_2$  (65 mg, 0.09 mmol, 0.01 equiv.),  $\text{CuI}$  (82 mg, 0.46 mmol, 0.05 equiv.), 1-iodo-4-methylbenzene (**17**) (2.0 g, 9.2 mmol, 1.0 equiv.) in  $\text{Et}_3\text{N}$  (30 mL). The solution was degassed and then (TMSA) was added (1.3 ml, 9.2 mmol, 1.0 equiv.). The solution was stirred for 8 h at  $70^\circ\text{C}$  under  $\text{N}_2$ . The reaction was followed by GC-MS. The solution was diluted with ether and then treated with 0.1 N  $\text{HCl}_{\text{aq}}$  until the aqueous layer was at  $\text{pH} = 1$ . The aqueous solutions were extracted multiple times with ether. The organic phase was dried over  $\text{MgSO}_4$ , filtered on a Celite® plug and concentrated under reduced pressure to obtain the crude product. The product was purified by flash chromatography (10%  $\text{EtOAc}$ /hexanes on silica gel) to yield 1.55 g of brown liquid (Yield: 90%).  $R_f$ : 0.77 (100%Hexanes).  $^1\text{H NMR}$  (300 MHz,  $\text{CDCl}_3$ )  $\delta$  (ppm):  $\delta$  7.37 (d,  $J = 7.8$  Hz, 2H), 7.10 (d,  $J = 8.0$  Hz, 2H), 2.34 (s, 3H), 0.26 (s, 9H).  $^{13}\text{C NMR}$  (101 MHz,  $\text{CDCl}_3$ )  $\delta$  (ppm): 138.6, 131.8, 128.9, 120.0, 105.3, 93.15, 21.35, -0.13. **LR-MS (EI, 70eV) ( $m/z$ ):** 188 ( $\text{M}^+$ ), 173. **HR-MS (EI, 70eV): Calculated** ( $\text{C}_{10}\text{H}_{12}\text{BrNSi}$ ): 188.1021. **Found:** 188.1026. The  $^{13}\text{C}$  and  $^1\text{H}$  NMR spectrum corresponds to that found in the literature.<sup>16</sup>

### 1-Ethynyl-4-methylbenzene (**19**):<sup>16</sup>



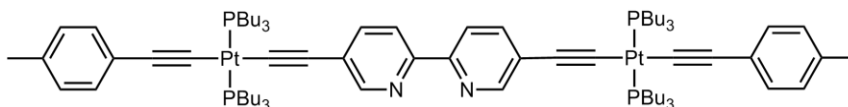
To a solution of the protected 1-trimethylsilylethynyl-4-methylbenzene (**18**) (150 mg, 0.80 mmol, 1.00 equiv.) in  $\text{MeOH}$  (4 mL) was added  $\text{K}_2\text{CO}_3$  (286 mg, 2.07 mmol, 2.60 equiv.). The reaction was stirred for 2 h at room temperature and followed by GC-MS. The reaction was poured into a solution of  $\text{H}_2\text{O}/\text{Et}_2\text{O}$  (1:1), the layers were separated and the organic phase was washed with  $\text{H}_2\text{O}$  (twice). The combined aqueous fractions were extracted with  $\text{Et}_2\text{O}$  (three times). The organic phase were combined and dried over  $\text{MgSO}_4$ , the organic phase was filtered and then concentrated under reduced pressure to yield 89 mg of brown liquid (Yield: 97 %).  $^1\text{H NMR}$  (300 MHz,  $\text{CDCl}_3$ )  $\delta$  (ppm): 7.38 (d,  $J = 8.1$  Hz, 2H), 7.12 (d,  $J = 8.0$  Hz, 2H), 3.03 (s, 3H), 2.35 (s, 1H). **LR-MS (EI, 70eV) ( $m/z$ ):** 116 ( $\text{M}^+$ ). **HR-MS (EI, 70eV): Calculated** ( $\text{C}_{12}\text{H}_8\text{N}_2$ ): 116.0626; **Found:** 116.0623.

***trans*-(5,5'-Ethynyl-2,2'-bipyridine)-dichloro-bis(tri-*n*-butylphosphine)platinum (21):**



A dry flask charged with *trans*-PtCl<sub>2</sub>(PBu<sub>3</sub>)<sub>2</sub> (0.73 mg, 1.1 mmol, 10 equiv.), CuI (4.50 mg, 0.03 mmol, 0.15 equiv.), DCM (40 mL) and *i*-Pr<sub>2</sub>NH (40 mL) was purged with N<sub>2</sub> for 30 min. 5,5'-diethynyl-2,2'-bipyridine (**5**) (0.22 mg, 0.11 mmol, 1.00 equiv.), dissolved in DCM (20 mL) and *i*-Pr<sub>2</sub>NH (20 mL) was then added. The mixture was stirred at room temperature for 16 h. The solvent was removed under reduced pressure and the residue was redissolved in DCM (30 mL). The organic phase was washed with H<sub>2</sub>O twice then dried over MgSO<sub>4</sub> and concentrated under reduced pressure. The residue was purified by flash chromatography (50% DCM/hexanes on silica gel) to yield 82 mg of yellow solid (Yield: 52%). **R<sub>f</sub>**: 0.52 (50% DCM/hexanes). **<sup>1</sup>H NMR (400 MHz, CDCl<sub>3</sub>) δ (ppm)**: 8.53 (d, *J* = 12.4 Hz, 2H), 8.19 (d, *J* = 9.1 Hz, 2H), 7.63 – 7.55 (m, 2H), 2.22 – 1.94 (m, 24H), 1.72 – 1.34 (m, 48H), 0.93 (t, *J* = 7.2 Hz, 36H). **<sup>13</sup>C NMR (101 MHz, CDCl<sub>3</sub>) δ (ppm)**: 152.3, 151.2, 138.0, 125.7, 120.2, 26.39, 24.3, 22.2, 14.1. **<sup>31</sup>P NMR (162 MHz, CDCl<sub>3</sub>) δ (ppm)**: δ 9.42 (d, *J* = 2359.7 Hz). The <sup>1</sup>H NMR spectrum corresponds to that found in the literature.<sup>17</sup>

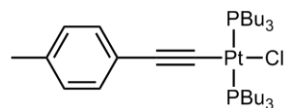
***trans*-(5,5'-Ethynyl-2,2'-bipyridine)-bis(4-tolylethynyl-bis(tri-*n*-butylphosphine)platinum) (22):**



A dry flask charged with *trans*-4-tolylethynyl -chloro-bis(tri-*n*-butylphosphine)platinum (**23**) (246 mg, 0.33 mmol, 2.10 equiv.), CuI (9.00 mg, 0.05 mmol, 0.30 equiv.), DCM (20 mL) and *i*-Pr<sub>2</sub>NH (8 mL) was purged with N<sub>2</sub> for 30 min. 5,5'-diethynyl-2,2'-bipyridine (**5**) (32.0 mg, 0.16 mmol, 1.00 equiv.), dissolved in DCM (10 mL), was then added. The mixture was stirred at room temperature for 16 h. The solvent was removed under reduced pressure and the residue was redissolved in DCM (30 mL). The organic phase was washed with H<sub>2</sub>O twice then dried over MgSO<sub>4</sub> and concentrated under

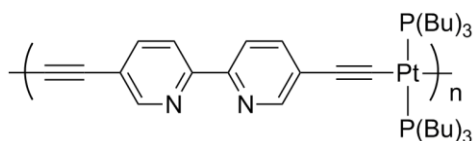
reduced pressure. The residue was purified by flash chromatography (10% EtOAc/hexanes on silica gel) to yield 64 mg of yellow liquid (Yield: 78%). **Mp:** 154.2-156.1°C. **Rf:** 0.86 (50% DCM/hexanes). **<sup>1</sup>H NMR (400 MHz, CDCl<sub>3</sub>) δ (ppm):** 8.48 (s, 2H), 8.11 (d, *J* = 8.2 Hz, 2H), 7.53 (d, *J* = 8.2 Hz, 2H), 7.10 (d, *J* = 7.8 Hz, 4H), 6.95 (d, *J* = 7.8 Hz, 4H), 2.22 (s, 6H), 2.17 – 1.94 (m, 24H), 1.63 – 1.46 (m, 24H), 1.46 – 1.29 (m, 24H), 0.85 (t, *J* = 7.2 Hz, 36H). **<sup>13</sup>C NMR (101 MHz, CDCl<sub>3</sub>) δ (ppm):** 151.8, 151.4, 138.3, 134.8, 130.8, 128.8, 126.1, 125.5, 120.1, 115.5, 109.3, 106.3, 106.1, 26.6, 24.7, 24.1, 21.3, 14.1. **<sup>31</sup>P NMR (162 MHz, CDCl<sub>3</sub>) δ (ppm):** 4.14 (d, *J* = 2347.0 Hz). **LR-MS (EI, 70eV) (*m/z*):** 1632 (M<sup>+</sup>), 598, 219. **HR-MS (EI, 70eV): Calculated (C<sub>80</sub>H<sub>128</sub>N<sub>2</sub>P<sub>4</sub>Pt<sub>2</sub>):** 1632.8423. **Found:** 1632.8384.

***trans*-4-Tolylethynyl-chloro-bis(tri-*n*-butylphosphine)platinum (23) :**



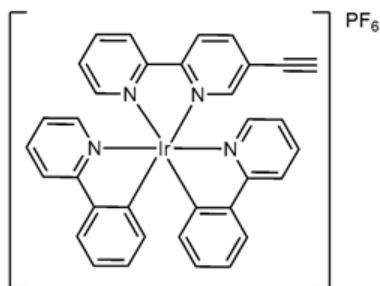
In A dry flask charged with excess *trans*-PtCl<sub>2</sub>(PBu<sub>3</sub>)<sub>2</sub> (1.47 g, 2.20 mmol, 5.10 equiv.), CuI (8.17 mg, 0.043 mmol, 0.10 equiv.), DCM (120 mL) and *i*-Pr<sub>2</sub>NH (10 mL). The reaction mixture was purged with N<sub>2</sub> for 30 min. 4-tolylethynyl (**19**) (50.0 mg, 0.43 mmol, 1.00 equiv.) dissolved in DCM (25 mL) and was added dropwise over 2 h. The mixture was stirred at room temperature for 16 h. The solvent was removed under reduced pressure. To the mixture was added DCM. The solvent was removed under reduced pressure and the residue was redissolved in DCM (50 mL). The organic phase was washed with H<sub>2</sub>O twice then dried over MgSO<sub>4</sub> and concentrated under reduced pressure. The residue was purified by flash chromatography (10% EtOAc/hexanes on silica gel) to recuperate the excess *trans*-PtCl<sub>2</sub>(PBu<sub>3</sub>)<sub>2</sub>, then (20% MeOH/DCM) to yield 70 mg of yellow oily liquid (Yield: 22%). **Rf:** 0.58 (50% DCM/hexanes). **<sup>1</sup>H NMR (300 MHz, CDCl<sub>3</sub>) δ (ppm):** 7.14 (d, *J* = 8.1 Hz, 2H), 7.02 (d, *J* = 8.0 Hz, 2H), 2.29 (s, 3H), 2.14 – 1.89 (m, 12H), 1.71 – 1.30 (m, 24H), 0.92 (t, *J* = 7.2 Hz, 18H). **<sup>13</sup>C NMR (101 MHz, CDCl<sub>3</sub>) δ (ppm) :** 135.0, 130.8, 128.9, 126.1, 101.1, 81.6, 26.4, 24.5, 22.16, 21.5, 14.1. **<sup>31</sup>P NMR (162 MHz, CDCl<sub>3</sub>) δ (ppm) :** 7.90 (d, *J* = 2377.4 Hz). **LR-MS (EI, 70eV) (*m/z*):** 748 (M<sup>+</sup>), 317. **HR-MS (EI, 70eV): Calculated (C<sub>33</sub>H<sub>61</sub>ClP<sub>2</sub>Pt):** 748.3564. **Found:** 748.3580.

### Pt-Polymer (24):



A dry flask charged with 5,5'-diethynyl-2,2'-bipyridine (**5**) (70.0 mg, 0.34 mmol, 1.00 equiv.), CuI (7.00 mg, 0.03 mmol, 0.10 equiv.), DCM (40 mL) and *i*-Pr<sub>2</sub>NH (40 mL) was purged with N<sub>2</sub> for 2 h. *trans*-PtCl<sub>2</sub>(P(Bu)<sub>3</sub>)<sub>2</sub> (230 mg, 0.34 mmol, 1.00 equiv.), dissolved in DCM (10 mL), was then added. The mixture was stirred at room temperature for 16 h and covered with Al foil. The solvent was removed under reduced pressure and the residue was redissolved in DCM (30 mL). The organic phase was washed with H<sub>2</sub>O twice then dried over MgSO<sub>4</sub> and concentrated under reduced pressure to yield 275 mg of brown solid (Yield: 96%). <sup>1</sup>H NMR (300 MHz, CDCl<sub>3</sub>) δ (ppm): 8.55 (s, 2H), 8.19 (d, *J* = 7.7 Hz, 2H), 7.61 (d, *J* = 8.4 Hz, 2H), 2.13 (s, 12), 1.80 – 1.30 (m, 24), 0.96 – 0.87 (m, 18). <sup>31</sup>P NMR (162 MHz, CDCl<sub>3</sub>) δ (ppm): 4.27 (d, *J* = 2332.8 Hz), 0.47 (d, *J* = 2453.8 Hz). GPC-RI (in THF against polystyrene standards) *M*<sub>n</sub> = 1.22 × 10<sup>4</sup>, *M*<sub>w</sub> = 2.48 × 10<sup>4</sup>, PDI = 2.

### [Ir(ppy)<sub>2</sub>(5-Ethynyl-2,2'-bipyridine)] Hexafluorophosphate (**30**):<sup>18</sup>

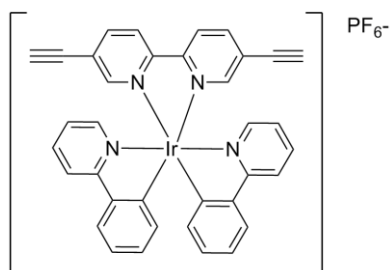


The dimeric complex [(ppy)<sub>2</sub>Ir-μ-Cl]<sub>2</sub> (86 mg, 0.08 mmol, 0.45 equiv.) was dissolved in DCM (6 mL) and methanol (6 mL) and 5-ethynyl-2,2'-bipyridine (**10**) (32 mg, 0.18 mmol, 1.00 equiv.) was added. The mixture was heated to 60 °C over 18 h. The color of the solution turned from orange to red. The solution was cooled to RT and extracted with water (3 × 50 mL), then washed with ether (3 × 50 mL) to remove unreacted bipyridine (**10**). To the aqueous solution was slowly added a solution



of  $\text{NH}_4\text{PF}_6$  (10 mL, 10 % w/w in  $\text{H}_2\text{O}$ ) under gentle stirring. The first drop caused the precipitation of an orange solid. The suspension was conserved for 2 h at 0 °C, filtered and the resulting solid was washed with cold water. The residue was purified by flash chromatography (10% MeOH/DCM on silica gel) to yield 110 mg of a red solid (Yield: 76%). **Rf**: 0.53 (10% MeOH/DCM). **Mp**: >350 °C.  **$^1\text{H}$  NMR (300 MHz,  $\text{CDCl}_3$ )  $\delta$  (ppm)**: 8.68 (d,  $J$  = 6.5 Hz, 2H), 8.17 (dd,  $J$  = 13.1, 4.8 Hz, 2H), 7.98 – 7.86 (m, 4H), 7.78 (t,  $J$  = 7.6 Hz, 2H), 7.69 (dd,  $J$  = 7.7, 4.0 Hz, 2H), 7.50 (t,  $J$  = 6.9 Hz, 2H), 7.42 (t,  $J$  = 6.9, 1H), 7.05 (t,  $J$  = 6.9 Hz, 4H), 6.98 – 6.86 (m, 2H), 6.27 (t,  $J$  = 6.6 Hz, 2H), 3.35 (s, 1H).  **$^{13}\text{C}$  NMR (75 MHz,  $\text{CDCl}_3$ )  $\delta$  (ppm)**: 168.0, 167.8, 155.4, 155.2, 152.8, 150.5, 149.8, 149.7, 148.9, 143.6, 143.5, 140.2, 138.5, 138.4, 131.9, 131.8, 131.2, 131.1, 128.5, 126.3, 125.2, 125.1, 125.0, 123.9, 123.7, 123.7, 123.1, 123.0, 120.0, 119.9, 85.6, 78.3. **LR-MS (EI, 70eV) ( $m/z$ )**: 681 ( $\text{M}^+$ ); 381, 317, 75. **HR-MS (EI, 70eV): Calculated ( $\text{C}_{34}\text{H}_{24}\text{IrN}_4$ )**: 681.1630. **Found**: 681.1649. The  $^1\text{H}$  and  $^{13}\text{C}$  NMR spectra each correspond to that found in the literature.<sup>18</sup> The structure was resolved by single crystal X-ray diffractometry and has been deposited into the CCDB.

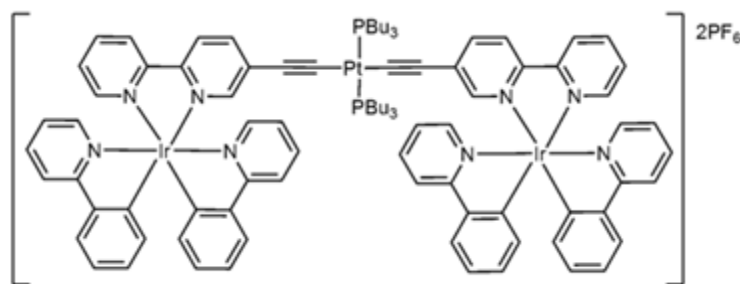
**[Ir(ppy)<sub>2</sub>(5,5'-Ethyynyl-2,2'-bipyridine)] Hexafluorophosphate (31):**



The dimeric complex  $[(\text{ppy})_2\text{Ir}-\mu\text{-Cl}]_2$  (82.8 mg, 0.08 mmol, 0.45 equiv.) was dissolved in DCM (6 mL) and methanol (6 mL), then 5,5'-diethynyl-2,2'-bipyridine (**5**) (35.0 mg, 0.17 mmol, 1.00 equiv.) was added. The mixture was heated to 60 °C over 18 h. The color of the solution turned from orange to red. The solution was cooled to RT and extracted with water (3 x 50 mL), then washed with ether (3 x 50 mL) to remove unreacted bipyridine (**5**). To the aqueous solution was slowly added a solution of  $\text{NH}_4\text{PF}_6$  (10 mL, 10 % w/w in  $\text{H}_2\text{O}$ ) under gentle stirring. The first drop caused the precipitation of an orange solid. The suspension was conserved for 2 h at 0 °C, filtered and the resulting solid was washed with cold water. The residue was purified by flash chromatography (10% MeOH/DCM on

silica gel) to yield 73 mg of a red solid (Yield:51%). **Rf**: 0.46 (10% MeOH/DCM). **Mp** = >350 °C. **<sup>1</sup>H NMR (400 MHz, CDCl<sub>3</sub>) δ (ppm)**: 8.67 (d, *J* = 8.3 Hz, 2H), 8.15 (d, *J* = 8.2 Hz, 2H), 7.96 – 7.91 (m, 4H), 7.80 (t, *J* = 7.6 Hz, 2H), 7.69 (d, *J* = 7.2 Hz, 2H), 7.50 (d, *J* = 5.7 Hz, 2H), 7.14 – 6.97 (m, 4H), 6.93 (t, *J* = 7.3 Hz, 2H), 6.25 (d, *J* = 7.1 Hz, 2H), 3.37 (s, 2H). **<sup>13</sup>C NMR (101 MHz, CDCl<sub>3</sub>) δ (ppm)**: 167.8, 154.6, 152.9, 149.1, 148.9, 142.9, 142.8, 138.6, 131.8, 131.1, 125.8, 125.1, 124.1, 123.8, 123.2, 120.0, 85.9, 78.3. **LR-MS (EI, 70eV) (*m/z*)**: 705 (M<sup>+</sup>); 501, 219. **HR-MS (EI, 70eV): Calculated (C<sub>36</sub>H<sub>24</sub>IrN<sub>4</sub>)**: 705.1632. **Found**: 705.1639.

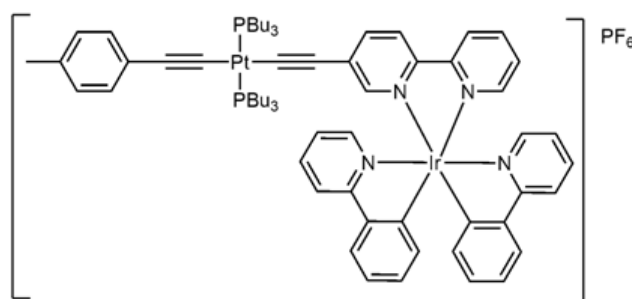
***trans*-Bis[Ir(ppy)<sub>2</sub>(5-ethynyl-2,2'-bipyridine)]-bis(tri-*n*-butylphosphine)platinum Hexafluorophosphate (32):**



The dimeric complex [(ppy)<sub>2</sub>Ir-μ-Cl]<sub>2</sub> (0.06 g, 0.05 mmol, 1.50 equiv.) was dissolved in DCM (6 mL) and methanol (6 mL) and Pt complex **16** (35 mg, 0.04 mmol, 1 equiv.) was added as a solid. The mixture was heated to 60 °C over 18 h. The reaction was followed the same way as described for **30** and **31** to yield 33 mg of a red solid (Yield: 40%). **Rf**: 0.52 (10% MeOH/DCM). **Mp**: >350 °C. **<sup>1</sup>H NMR (300 MHz, CDCl<sub>3</sub>) δ (ppm)**: 8.46 (t, *J* = 9.1 Hz, 4H), 8.00 (t, *J* = 8.1 Hz, 4H), 7.95 – 7.88 (m, 4H), 7.87 – 7.71 (m, 8H), 7.64 (d, *J* = 7.5 Hz, 4H), 7.60 – 7.52 (m, 2H), 7.46 (dd, *J* = 9.8, 5.6 Hz, 4H), 7.29 (d, *J* = 6.4 Hz, 4H), 6.99 (dt, *J* = 14.5, 6.8 Hz, 2H), 6.91 – 6.80 (m, 4H), 6.77 (d, *J* = 7.6 Hz, 2H), 6.23 (dd, *J* = 11.6, 7.6 Hz, 4H), 1.91 – 1.66 (m, 12), 1.48 – 1.22 (m, 24), 0.86 (t, *J* = 6.7 Hz, 18H). **<sup>13</sup>C NMR (75 MHz, CDCl<sub>3</sub>) δ (ppm)**: 167.9, 167.7, 155.8, 151.9, 151.0, 150.6, 150.3, 150.0, 148.7, 148.3, 143.5, 143.4, 140.3, 139.7, 138.1, 138.0, 131.6, 130.8, 130.6, 130.1, 130.0, 127.3, 126.3, 126.2, 124.8, 124.6, 123.4, 123.1, 122.6, 122.4, 119.7, 119.5, 110.1, 105.2, 26.2, 24.3, 23.8,

13.8.  $^{31}\text{P}$  NMR (162 MHz,  $\text{CDCl}_3$ )  $\delta$  (ppm): 4.38 (d,  $J = 2326.3$  Hz). LR-MS (EI, 70eV) ( $m/z$ ): 979 ( $\text{M}^{2+}$ ); 501, 360, 249. HR-MS (EI, 70eV): Calculated ( $\text{C}_{92}\text{H}_{100}\text{Ir}_2\text{N}_8\text{P}_2\text{Pt}$ ): 979.3216 ( $\text{M}^{2+}$ ); Found: 979.3270 ( $\text{M}^{2+}$ ).

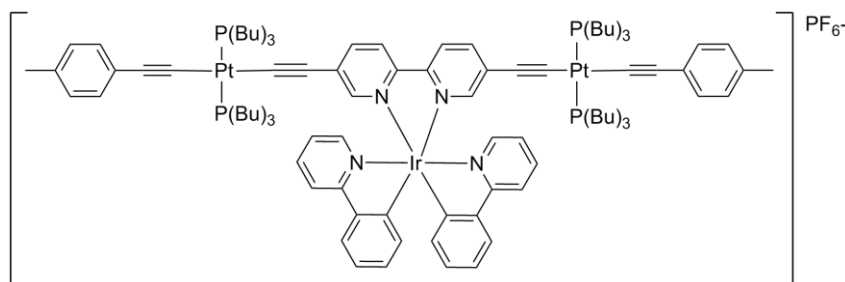
***trans*-[Ir(ppy)<sub>2</sub>(5-Ethynyl-2,2'-bipyridine)]-4-tolylethynyl-bis(tri-*n*-butylphosphine)platinum Hexafluorophosphate (33):**



The dimeric complex (**26**)  $[(\text{ppy})_2\text{Ir}-\mu\text{-Cl}]_2$  (15.20 mg, 0.01 mmol, 0.45 equiv.) was dissolved in DCM (5 mL) and methanol (5 mL), and **20** (28 mg, 0.03 mmol, 1.00 equiv.) was added and the mixture was heated to 60 °C over 18 h. The color of the solution turned from orange to red. The solution was cooled to RT and washed with water (3 x 50 mL) then extracted with ether (3x). The organic solution was evaporated to obtain the chloride complex as a red solid. This complex was dissolved in a minimum amount of methanol and a solution of  $\text{NH}_4\text{PF}_6$  (3 mL, 10% w/w in  $\text{H}_2\text{O}$ ) was slowly added under stirring. The resulting suspension was re-cooled to 0 °C for 2 h, filtered, washed with cold water and the solid was dried under vacuum. The residue was purified by flash chromatography (10% MeOH/DCM on silica gel) to yield 40 mg of red solid (Yield: 87%). **R<sub>f</sub>**: 0.47 (10% MeOH/DCM). **Mp**: >350 °C.  $^1\text{H}$  NMR (300 MHz,  $\text{CDCl}_3$ )  $\delta$  (ppm): 8.61 (d,  $J = 8.1$  Hz, 1H), 8.45 (d,  $J = 8.5$  Hz, 1H), 8.13 (t,  $J = 7.8$  Hz, 1H), 7.99 – 7.82 (m, 3H), 7.77 (t,  $J = 8.1$  Hz, 4H), 7.65 (dd,  $J = 16.7, 7.7$  Hz, 3H), 7.52 (t,  $J = 4.8$  Hz, 2H), 7.32 (dd,  $J = 12.5, 6.3$  Hz, 2H), 7.14 (d,  $J = 7.8$  Hz, 2H), 7.10 – 6.96 (m, 4H), 6.95 – 6.83 (m, 2H), 6.27 (d,  $J = 7.4$  Hz, 2H), 2.29 (s, 3H), 2.11 – 1.81 (m, 12H), 1.72 – 1.26 (m, 24H), 0.87 (t,  $J = 7.0$  Hz, 18H).  $^{13}\text{C}$  NMR (101 MHz,  $\text{CDCl}_3$ )  $\delta$  (ppm): 169.0, 168.8, 153.2, 153.1, 151.9, 151.7, 151.6, 151.0, 149.9, 149.5, 144.6, 144.5, 141.3, 141.0, 140.5, 140.3, 139.1, 139.0, 136.1, 132.8, 132.8, 132.0, 131.7, 131.4, 131.2, 129.8, 128.2, 127.5,

127.3, 126.0, 125.9, 125.7, 124.5, 124.2, 123.7, 123.4, 120.7, 120.5, 27.4, 25.4, 25.0, 22.4, 14.8.  $^{31}\text{P}$  NMR (162 MHz,  $\text{CDCl}_3$ )  $\delta$  (ppm): 5.28 (d,  $J = 2318.2$  Hz). LR-MS (EI, 70eV) ( $m/z$ ): 1394 ( $\text{M}^+$ ); Calculated ( $\text{C}_{67}\text{H}_{84}\text{IrN}_4\text{P}_2\text{Pt}$ ): 1394.5458. Found: 1394.5421.

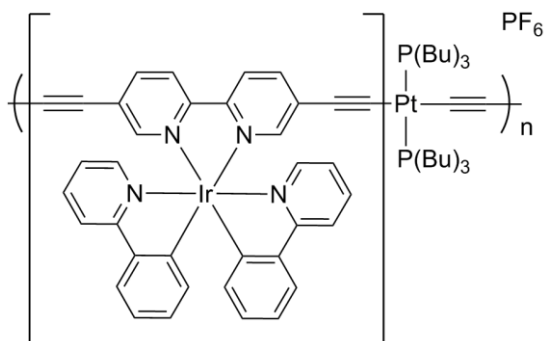
***trans*-[Ir(ppy) $_2$ (5,5'-Ethynyl-2,2'-bipyridine)]-bis(4-tolylethynyl-bis(tri-*n*-butylphosphine)platinum) Hexafluorophosphate (34):**



The dimeric complex  $[(\text{ppy})_2\text{Ir}-\mu\text{-Cl}]_2$  (6.00 mg, 0.01 mmol, 0.45 equiv.) was dissolved in DCM (6 mL) and methanol (6 mL), and *trans*-(5,5'-ethynyl-2,2'-bipyridine)-bis(4-tolylethynyl-bis(tri-*n*-butylphosphine)platinum) (**22**) (20 mg, 0.01 mmol, 1.00 equiv.) was added and the mixture was heated to 60 °C over 18 h. The solution was cooled to RT and washed with water (3 x 50 mL) then extracted with ether (3x). The organic solution was evaporated to obtain the chloride complex as a red solid. This complex was dissolved in a minimum amount of methanol and a solution of  $\text{NH}_4\text{PF}_6$  (3 mL, 10% w/w in  $\text{H}_2\text{O}$ ) was slowly added under stirring. The resulting suspension was re-cooled to 0 °C for 2 h, filtered, washed with cold water and the solid was dried under vacuum. The residue was purified by flash chromatography (10% MeOH/DCM on silica gel) to yield 26 mg of red solid (88%). **Rf**: 0.5 (10% MeOH/DCM). **Mp** = >350 °C.  $^1\text{H}$  NMR (400 MHz,  $\text{CDCl}_3$ )  $\delta$  (ppm): 8.43 (d,  $J = 8.4$  Hz, 2H), 7.89 (d,  $J = 8.0$  Hz, 2H), 7.85 – 7.74 (m, 4H), 7.71 (d,  $J = 1.6$  Hz, 2H), 7.68 – 7.57 (m, 4H), 7.54 (d,  $J = 5.4$  Hz, 2H), 7.13 (d,  $J = 7.8$  Hz, 4H), 7.06 – 6.94 (m, 6H), 6.86 (t,  $J = 7.3$  Hz, 2H), 6.25 (d,  $J = 7.4$  Hz, 2H), 2.29 (s, 6H), 2.08 – 1.84 (m, 24H), 1.56 – 1.44 (m, 24H), 1.40 – 1.31 (m, 24H), 0.86 (t,  $J = 7.0$  Hz, 36H).  $^{13}\text{C}$  NMR (101 MHz,  $\text{CDCl}_3$ )  $\delta$  (ppm): 168.0, 152.1, 151.3, 151.2, 148.85, 143.7, 140.7, 138.0, 135.0, 132.0, 130.8, 130.3, 129.5, 128.9, 126.5, 125.7, 124.8, 124.6, 124.5,

123.3, 122.5, 119.6, 110.3, 104.6, 26.5, 24.6, 24.0, 21.5, 14.1.  $^{31}\text{P}$  NMR (162 MHz,  $\text{CDCl}_3$ )  $\delta$  (ppm): 4.39 (d,  $J = 2326.8$  Hz). LR-MS (EI, 70eV) ( $m/z$ ): 2131 ( $\text{M}^+$ ). HR-MS (EI, 70eV): Calculated ( $\text{C}_{102}\text{H}_{144}\text{IrN}_4\text{P}_4\text{Pt}_2$ ): 2131.9275. Found: 2131.9272.

**Pt-Ir Polymer (36):**



A dry flask charged with  $[\text{Ir}(\text{ppy})_2(5,5'\text{-ethynyl-2,2'-bipyridine})]$  Hexafluorophosphate (**31**) (22 mg, 0.03 mmol, 1.00 equiv.), CuI (5.00 mg, 0.03 mmol, 1.00 equiv.), DCM (20 mL) and  $i\text{-Pr}_2\text{NH}$  (20 mL) was purged with  $\text{N}_2$  for 2 h.  $\text{trans-PtCl}_2(\text{PBU}_3)_2$  (17.5 mg, 0.03 mmol, 1.00 equiv.), dissolved in DCM (10 mL), was then added. The mixture was stirred at room temperature for 16 h and covered with Al foil. The solvent was removed under reduced pressure and the residue was redissolved in DCM (30 mL). The organic phase was washed with  $\text{H}_2\text{O}$  twice then dried over  $\text{MgSO}_4$  and concentrated under reduced pressure to yield 37 mg of brown solid (Yield: 80%).  $^1\text{H}$  NMR (300 MHz,  $\text{CDCl}_3$ )  $\delta$  (ppm): 8.62 – 8.07 (m, 6H), 7.94 (d,  $J = 7.7$  Hz, 2H), 7.89 – 7.67 (m, 5H), 7.63 (s, 1H), 7.59 – 7.32 (m, 2H), 7.16 – 6.78 (m, 4H), 6.27 (d,  $J = 6.6$  Hz, 1H), 2.15 – 1.72 (m, 12H), 1.70 – 1.05 (m, 24H), 1.06 – 0.59 (m, 18H).  $^{31}\text{P}$  NMR (162 MHz,  $\text{CDCl}_3$ )  $\delta$  (ppm): -7.10 (d,  $J = 2250.2$  Hz). GPC-RI (in THF against polystyrene standards)  $M_n = 1.18 \times 10^4$ ,  $M_w = 1.33 \times 10^4$ , PDI = 1.1.

**Photophysical characterization:** All samples were prepared in 2-methyltetrahydrofuran (2-MeTHF), which was distilled over  $\text{CaH}_2$  under nitrogen or HPLC grade acetonitrile (ACN) for the external reference. Absorption spectra were recorded at room temperature and at 77 K in a 1.0 cm capped quartz cuvette and an NMR tube inserted into a liquid nitrogen filled quartz dewar, respectively, using a Shimadzu UV-1800 double beam spectrophotometer. Molar absorptivity determination was verified by linear least squares fit of values obtained from at least three

independent solutions at varying concentrations with absorbances ranging from 0.01-2.6. Steady-state emission spectra were obtained by exciting at the lowest energy absorption maxima using a Horiba Jobin Yvon Fluorolog-3 spectrofluorometer equipped with double monochromators and a photomultiplier tube detector (Hamamatsu model R955). Emission quantum yields were determined using the optically dilute method.<sup>19,20</sup> A stock solution with absorbance of ca. 0.5 was prepared and then four dilutions were prepared with dilution factors of 40, 20, 13.3 and 10 to obtain solutions with absorbances of ca. 0.013, 0.025, 0.038 and 0.05, respectively. The Beer-Lambert law was found to be linear at the concentrations of the solutions. The emission spectra were then measured after the solutions were rigorously degassed with solvent-saturated nitrogen gas (N<sub>2</sub>) for 20 minutes prior to spectrum acquisition using septa-sealed quartz cells from Starna. For each sample, linearity between absorption and emission intensity was verified through linear regression analysis and additional measurements were acquired until the Pearson regression factor (R<sup>2</sup>) for the linear fit of the data set surpassed 0.9. Individual relative quantum yield values were calculated for each solution and the values reported represent the slope value. The equation  $\Phi_s = \Phi_r(A_r/A_s)(I_s/I_r)(n_s/n_r)^2$  was used to calculate the relative quantum yield of each of the sample, where  $\Phi_r$  is the absolute quantum yield of the reference,  $n$  is the refractive index of the solvent,  $A$  is the absorbance at the excitation wavelength, and  $I$  is the integrated area under the corrected emission curve. The subscripts  $s$  and  $r$  refer to the sample and reference, respectively. A solution of [Ru(bpy)<sub>3</sub>](PF<sub>6</sub>)<sub>2</sub> in ACN ( $\Phi_r = 9.5\%$ ) was used as the external reference.<sup>21</sup> The experimental uncertainty in the emission quantum yields is conservatively estimated to be 10%, though we have found that statistically we can reproduce PLQYs to 3% relative error. The emission lifetimes were measured on a TimeMaster model TM-3/2003 apparatus from PTI. The source was a nitrogen laser with high-resolution dye laser (fwhm ~1400 ps), and the excited state lifetimes were obtained from deconvolution or distribution lifetimes analysis.

**Computational Methodology.** Calculations were performed with Gaussian 09<sup>22</sup> at the Université de Sherbrooke with Mammouth super computer supported by Calcul Québec. The DFT<sup>23</sup> and TDDFT<sup>24</sup> were calculated with the B3LYP<sup>25</sup> method. The 3-21G\*<sup>26</sup> basis set was used for C, H and N, and VDZ (valence double  $\zeta$ ) with SBKJC effective core potentials<sup>26a,27</sup> for iridium and platinum. The predicted phosphorescence wavelengths were obtained by energy differences between the Triplet and Singlet optimized states.<sup>28</sup> The calculated absorption spectra and related MO contributions were obtained from the TD-DFT/Singlets output file and gausssum 2.1.<sup>29</sup> A THF quantum mechanical continuum solvation model was employed.<sup>30</sup>

## References:

- 1- G. B. Kauffman, L. A. Teter and J. E. Huheey, in *Inorg. Synth.*, John Wiley & Sons, Inc., **2007**, pp. 245.
- 2- W. L. F. Armarego and D. D. Perrin, *Purification of Laboratory Chemicals, 3rd edition*, Pergamon Press, Oxford, **1988**.
- 3- M. Nonoyama, *Bull. Chem. Soc. Japan*, **1974**, *47*, 767.
- 4- S. Ladouceur, D. Fortin, E. Zysman-Colman. *Inorg. Chem.*, **2010**, *49*, 5625.
- 5- F. Trécourt, G. Breton, V. Bonnet, F. Mongin, F. Marsais and G. Quéguiner *Tetrahedron* **2000**, *56*, 1349.
- 6- J. Bunzen, R. Hovorka and A. Lützen *J. Org. Chem.*, **2009**, *74* (15), 5228.
- 7- C. Grave, D. Lentz, A. Schäfer, P. Samorì, J. P. Rabe, P. Franke, and A. D. Schlüter *J. Am. Chem. Soc.*, **2003**, *125* (23), 6907.
- 8- P. N. W. Baxter. *Chem. Eur. J.* **2003**, *9*, 5011.
- 9- S. Ladouceur, A. M. Soliman, E. Zysman-Colman, *Synthesis*, **2011**, *22*, 3604.
- 10- V. Grosshenny, F. M. Romero, R. Ziessel, *J. Org. Chem.* **1997**, *62*, 1491.
- 11- U. Lehmann and A. D. Schlüter, *Eur. J. Org. Chem.*, **2000**, *2000*, 3483.
- 12- J. J. Song and N. K. Yee, *J. Org. Chem.*, **2000**, *66*, 605.
- 13- S.-H. Kim and R. D. Rieke, *Tetrahedron Lett.*, **2009**, *50*, 5329-5331.
- 14- A. Lützen and M. Hapke, *Eur. J. Org. Chem.*, **2002**, *2002*, 2292.
- 15- V. Grosshenny, F. M. Romero and R. Ziessel, *J. Org. Chem.*, **1997**, *62*, 1491.
- 16- a)N. E. Leadbeater, B. J. Tominack, *Tetrahedron Lett.* **2003**, *44*, 8653; b)Y. Wang, B. Huang, S. Sheng, M. Cai, *J. Chem. Res.* **2007**, *2007*, 728.
- 17- K. Ogawa, F. Guo, K. S. Schanze, *J. Photochem. Photobiol., A* **2009**, *207*, 79.
- 18- A. A. Rachford, R. Ziessel, T. Bura, P. Retailleau and F. N. Castellano, *Inorg. Chem.*, **2010**, *49*, 3730.
- 19- G. A. Crosby and J. N. Demas, *J. Phys. Chem.*, **1971**, *75*, 991.
- 20- S. Fery-Forgues and D. Lavabre, *J. Chem. Educ.*, **1999**, *76*, 1260.
- 21- H. Ishida, S. Tobita, Y. Hasegawa, R. Katoh and K. Nozaki, *Coord. Chem. Rev.*, **2010**, *254*, 2449.
- 22- M. J. Frisch, G. W. Trucks, H. B. Schlegel, G. E. Scuseria, M. A. Robb, J. R. Cheeseman, V. G. Zakrzewski, J. A. Montgomery, R. E. Stratmann, J. C. Burant, S. Dapprich, M. J.M., A. D. Daniels,

K. N. Kudin, M. C. Strain, O. Farkas, J. Tomasi, V. Barone, M. Cossi, R. Cammi, B. Mennucci, C. Pomelli, C. Adamo, S. Clifford, J. Ochterski, G. A. Peterson, P. Y. Ayala, Q. Cui, K. Morokuma, A. Malik, A. D. Rabuck, K. Raghavachari, J. B. Foresman, J. Cioslowski, J. V. Ortiz, A. G. Baboul, B. B. Stefanov, G. Liu, A. Liashenko, P. Piskorz, I. Komaromi, R. Gomperts, R. L. Martin, M. Challacombe, P. M. W. Gill, B. G. Johnson, W. Chen, M. W. Wong, J. L. Andres, M. Head-Gordon, E. S. Replogle and J. A. Pople, *Gaussian 98 (Revision A.6)*, Gaussian Inc., Pittsburgh, PA, 1998.

23- (a) P. Hohenberg and W. Kohn, *Phys. Rev.*, 1964, **136**, B864; (b) W. Kohn and L. J. Sham, *Phys. Rev.*, 1965, **140**, A1133; (c) in *The Challenge of d and f Electrons*, eds. D. R. Salahub and M. C. Zerner, ACS, Washington, DC, 1989; (d) R. G. Parr and W. Yang, *Density-functional theory of atoms and molecules*, Oxford Univ. Press, Oxford, 1989.

24- (a) R. E. Stratmann, G. E. Scuseria and M. J. Frisch, *J. Chem. Phys.*, **1998**, *109*, 8218; (b) R. Bauernschmitt and R. Ahlrichs, *Chem. Phys. Lett.*, **1996**, *256*, 454; (c) M. E. Casida, C. Jamorski, K. C. Casida and D. R. Salahub, *J. Chem. Phys.*, **1998**, *108*, 4439

25- (a) A. D. Becke, *J. Chem. Phys.*, 1993, **98**, 5648-5652; (b) C. Lee, W. Yang and R. G. Parr, *Phys. Rev. B*, 1988, **37**, 785-789; (c) B. Miehlich, A. Savin, H. Stoll and H. Preuss, *Chem. Phys. Lett.*, 1989, **157**, 200-206.

26- (a) J. S. Binkley, J. A. Pople and W. J. Hehre, *J. Am. Chem. Soc.*, **1980**, *102*, 939; (b) M. S. Gordon, J. S. Binkley, J. A. Pople, W. J. Pietro and W. J. Hehre, *J. Am. Chem. Soc.*, **1982**, *104*, 2797; (c) W. J. Pietro, M. M. Francl, W. J. Hehre, D. J. Defrees, J. A. Pople and J. S. Binkley, *J. Am. Chem. Soc.*, **1982**, *104*, 5039; (d) K. D. Dobbs and W. J. Hehre, *J. Comp. Chem.*, 1986, **7**, 359; (e) K. D. Dobbs and W. J. Hehre, *J. Comp. Chem.*, **1987**, *8*, 861; (f) K. D. Dobbs and W. J. Hehre, *J. Comp. Chem.*, **1987**, *8*, 880.

27- (a) W. J. Stevens, W. J. Basch and M. Krauss, *J. Chem. Phys.*, **1984**, *81*, 6026; (b) W. J. Stevens, M. Krauss, H. Basch and P. G. Jasien, *Can. J. Chem.*, 1992, **70**, 612; (c) T. R. Cundari and W. J. Stevens, *J. Chem. Phys.*, **1993**, *98*, 5555-5565.

28- (a) M. S. Lowry, W. R. Hudson, R. A. Pascal Jr. and S. Bernhard, *J. Am. Chem. Soc.*, **2004**, *126*, 14129; (b) S. Ladouceur, D. Fortin and E. Zysman-Colman, *Inorg. Chem.*, **2010**, *49*, 5625.

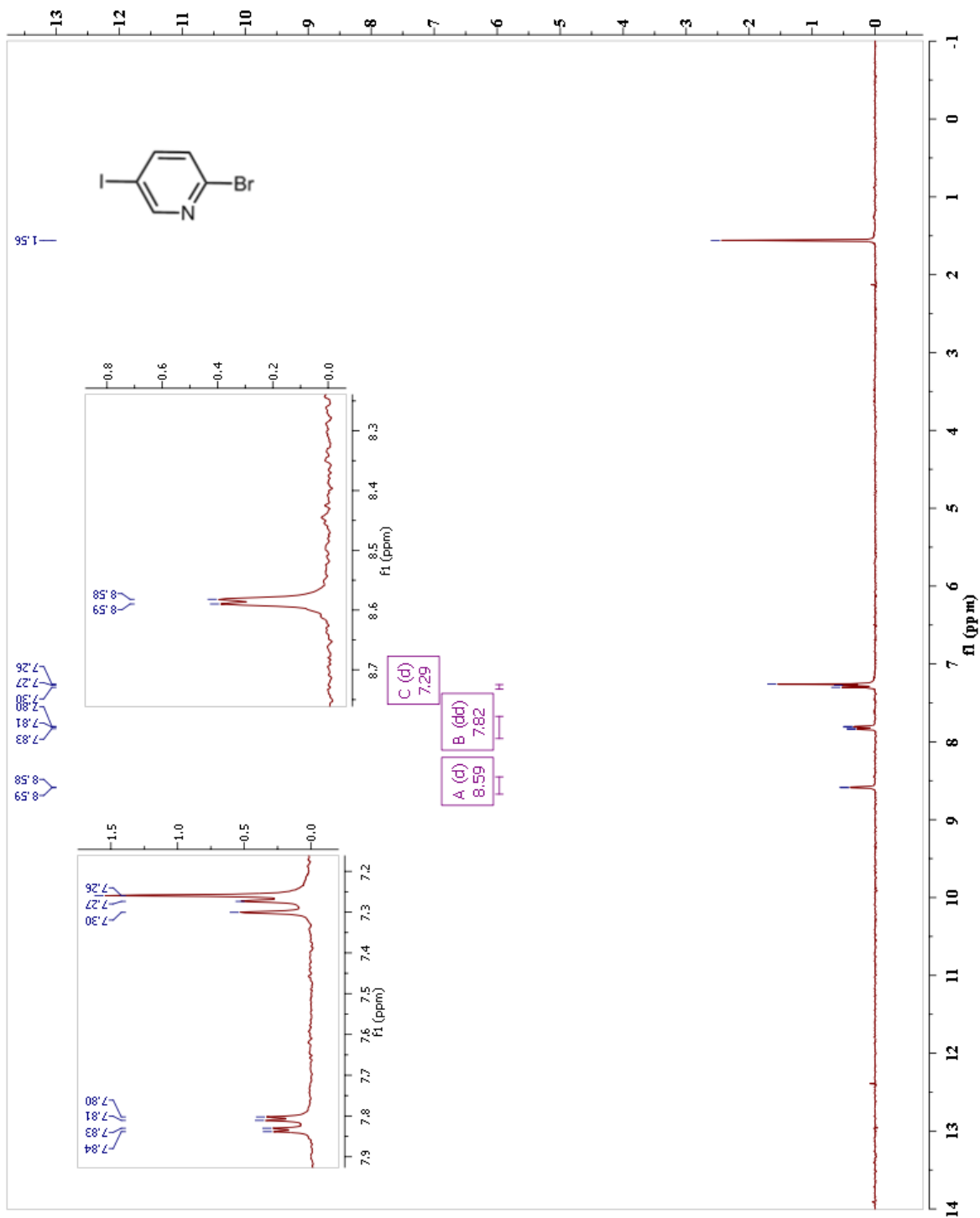
29- N. M. O'Boyle, *GaussSum 2.0*, Dublin City University; Dublin Ireland, 2006.

30- J. Tomasi, B. Mennucci and R. Cammi, *Chem. Rev.*, **2005**, *105*, 2999.



# ANNEX 1: SPECTRA OF NUCLEAR MAGNETIC RESONANCE OF PROTON.

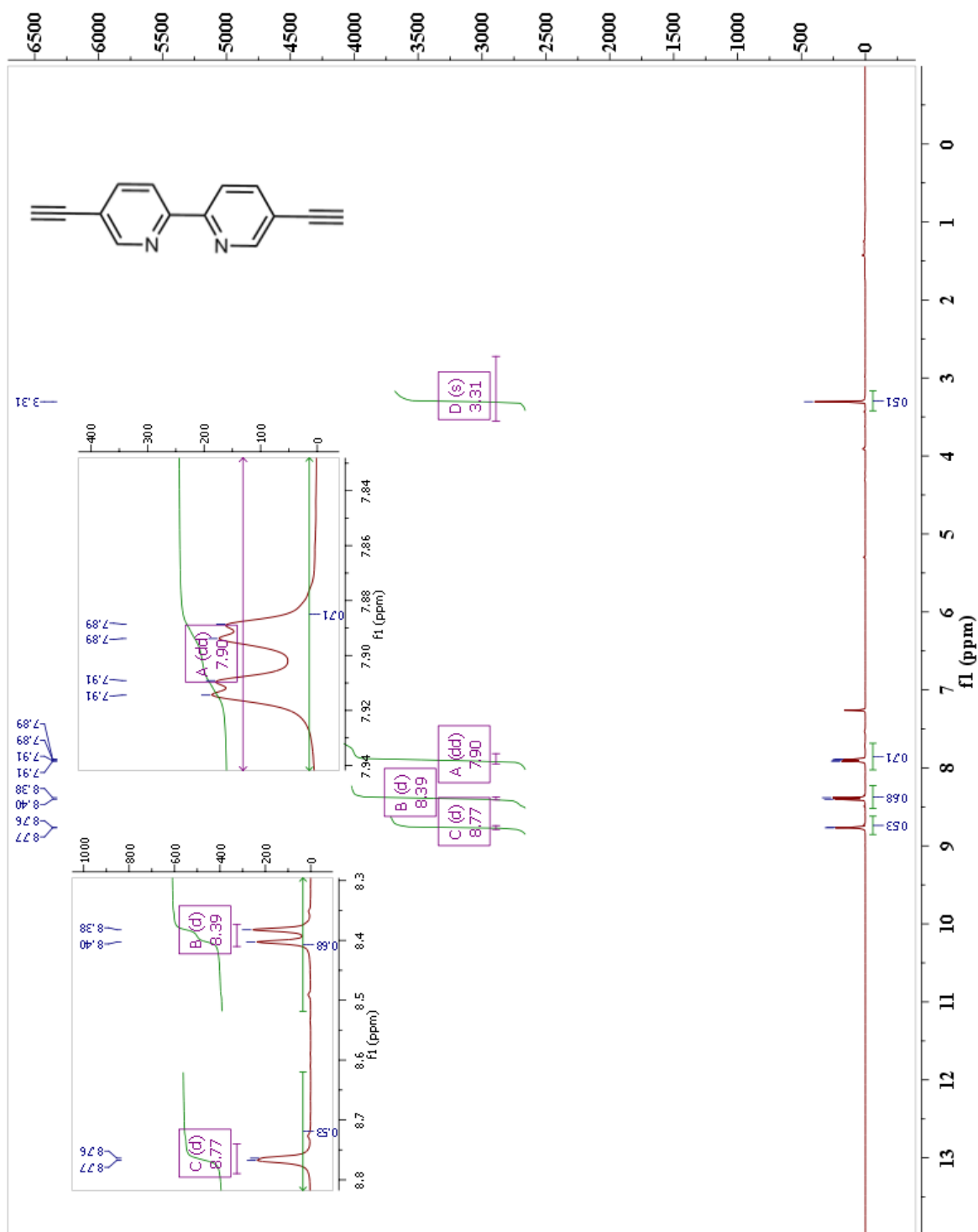
## 2-Bromo-5-iodopyridine (2):



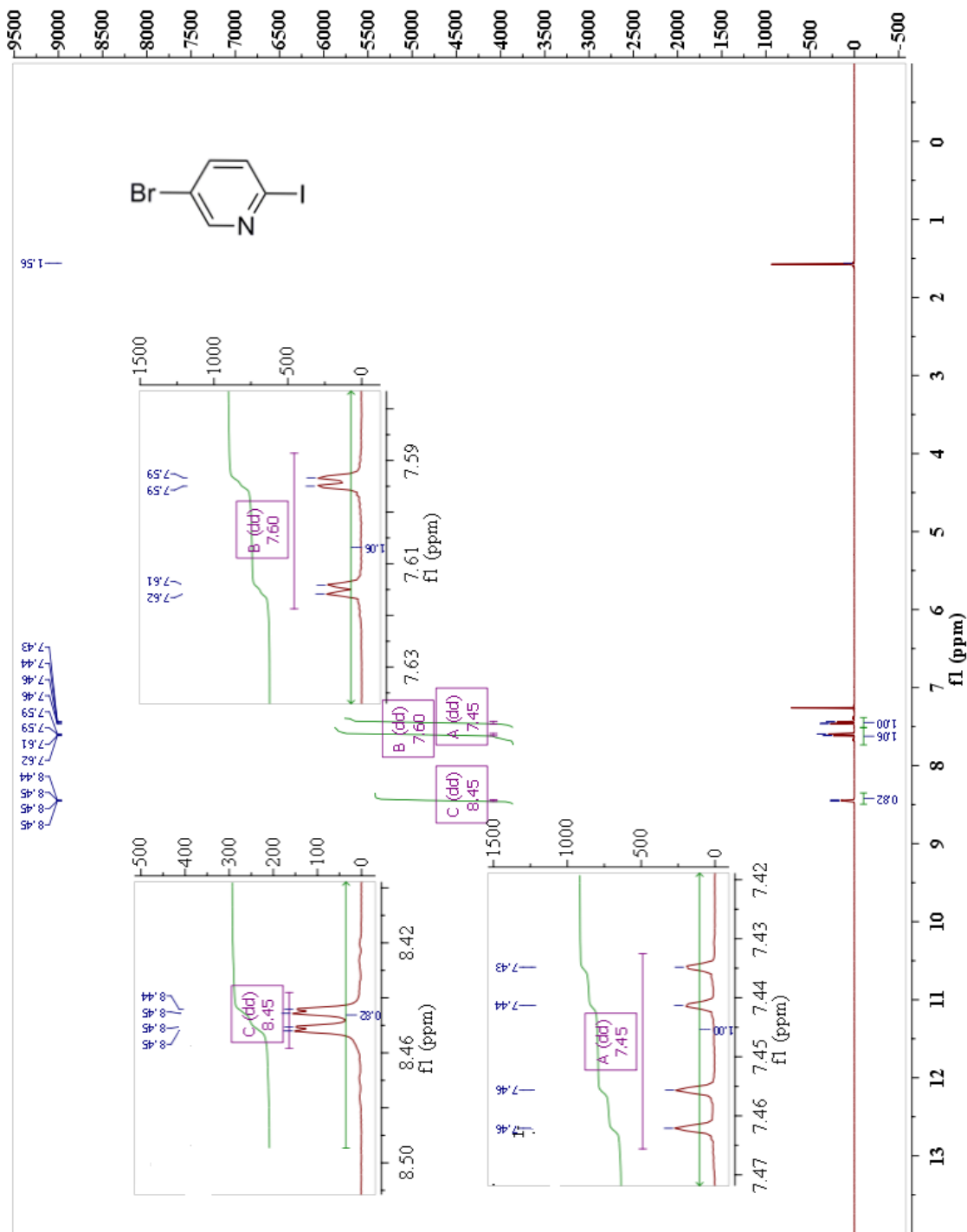




### 5,5'-Diethynyl-2,2'-bipyridine (5):

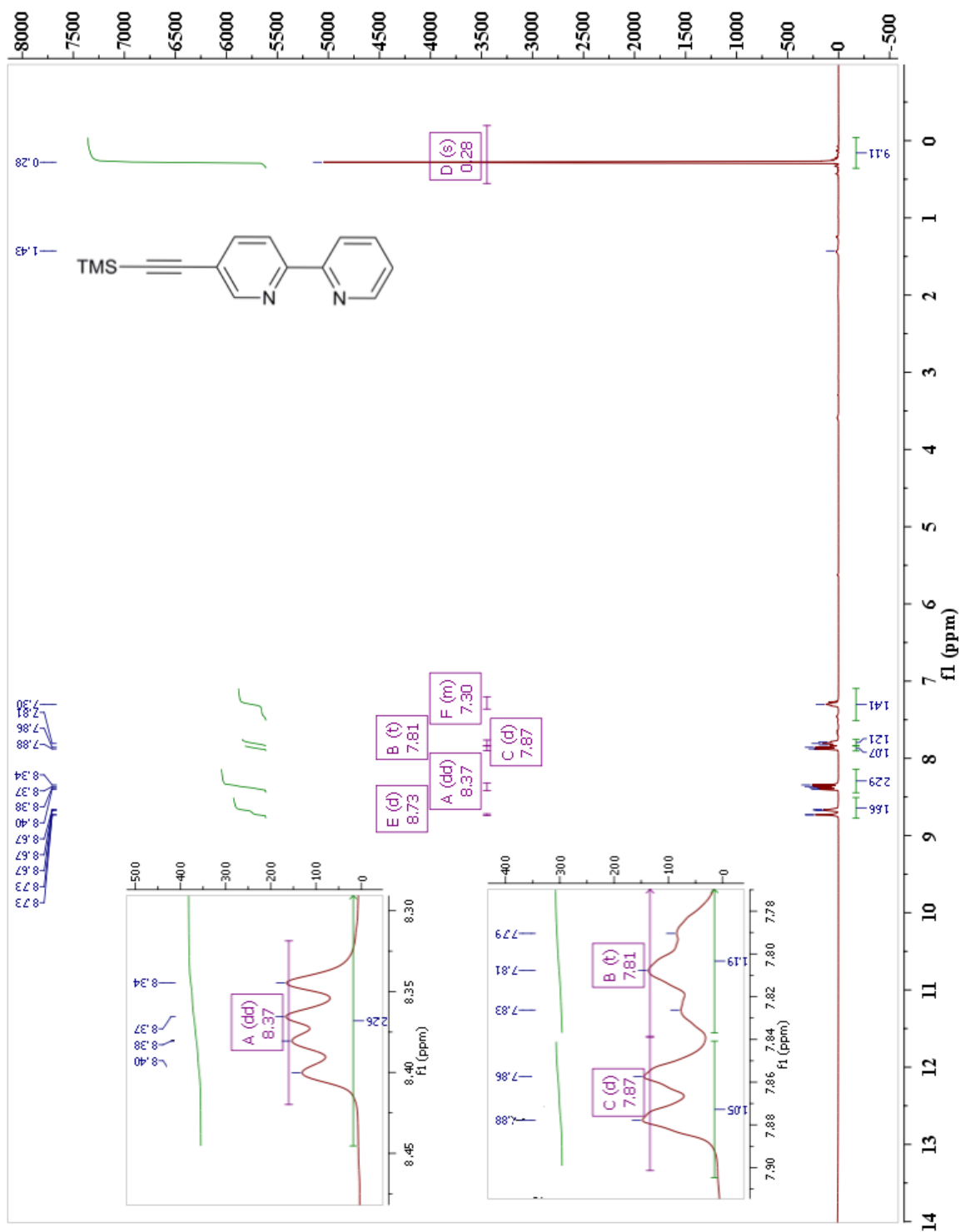


**5-Bromo-2-iodopyridine (6):**

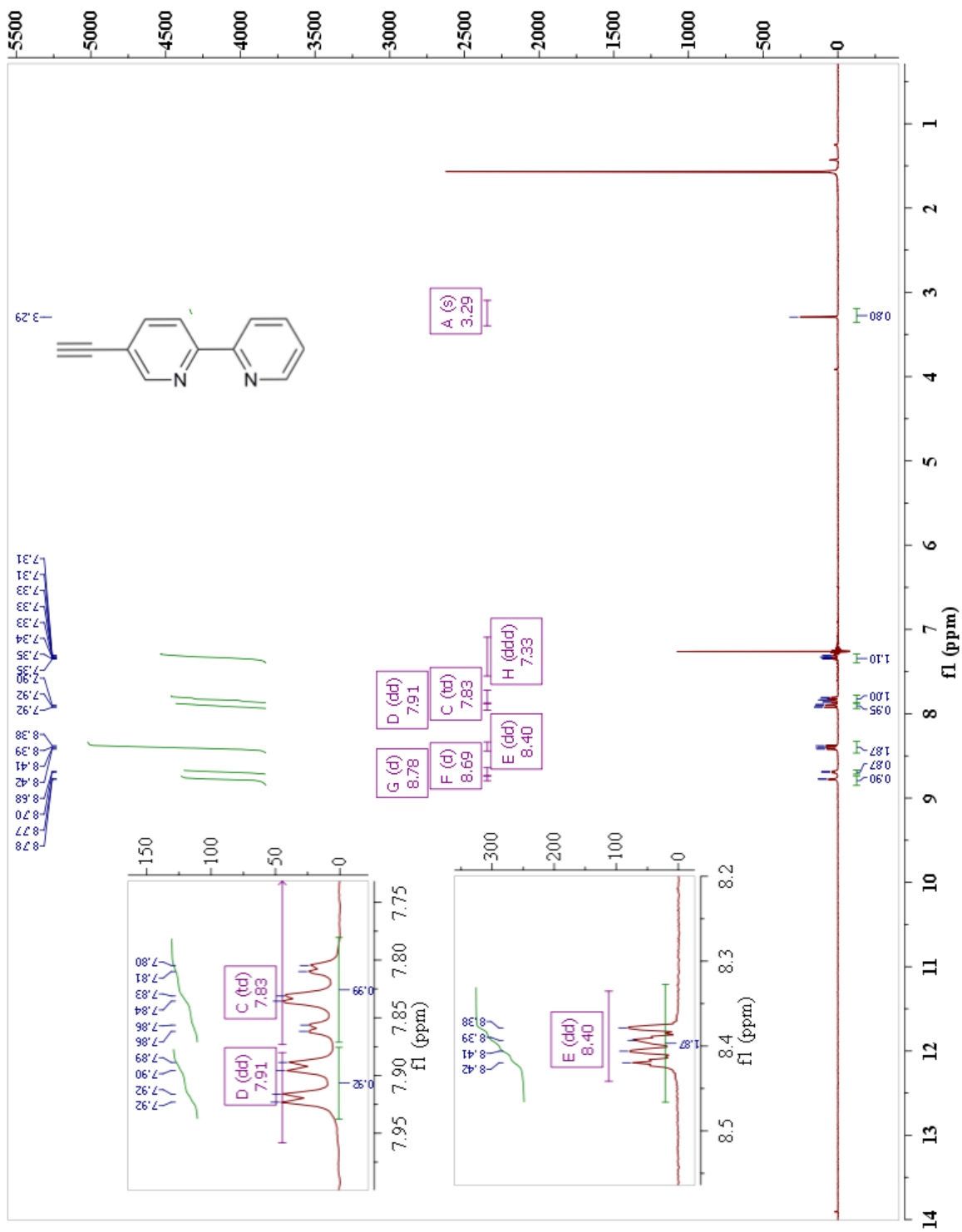




**5-Trimethylsilylethynyl-2,2'-bipyridine (9):**



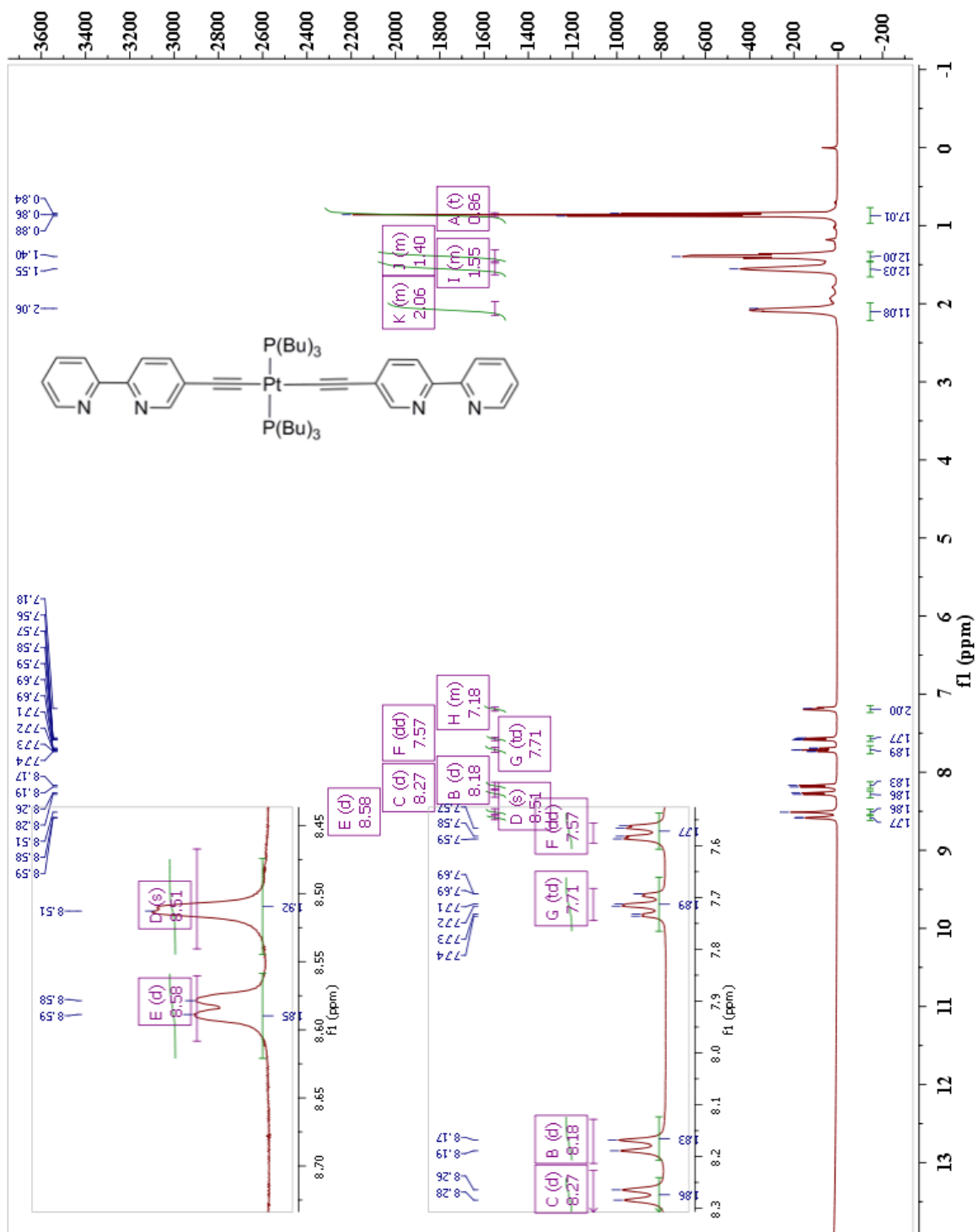
5-Ethynyl-2,2'-bipyridine (10) :



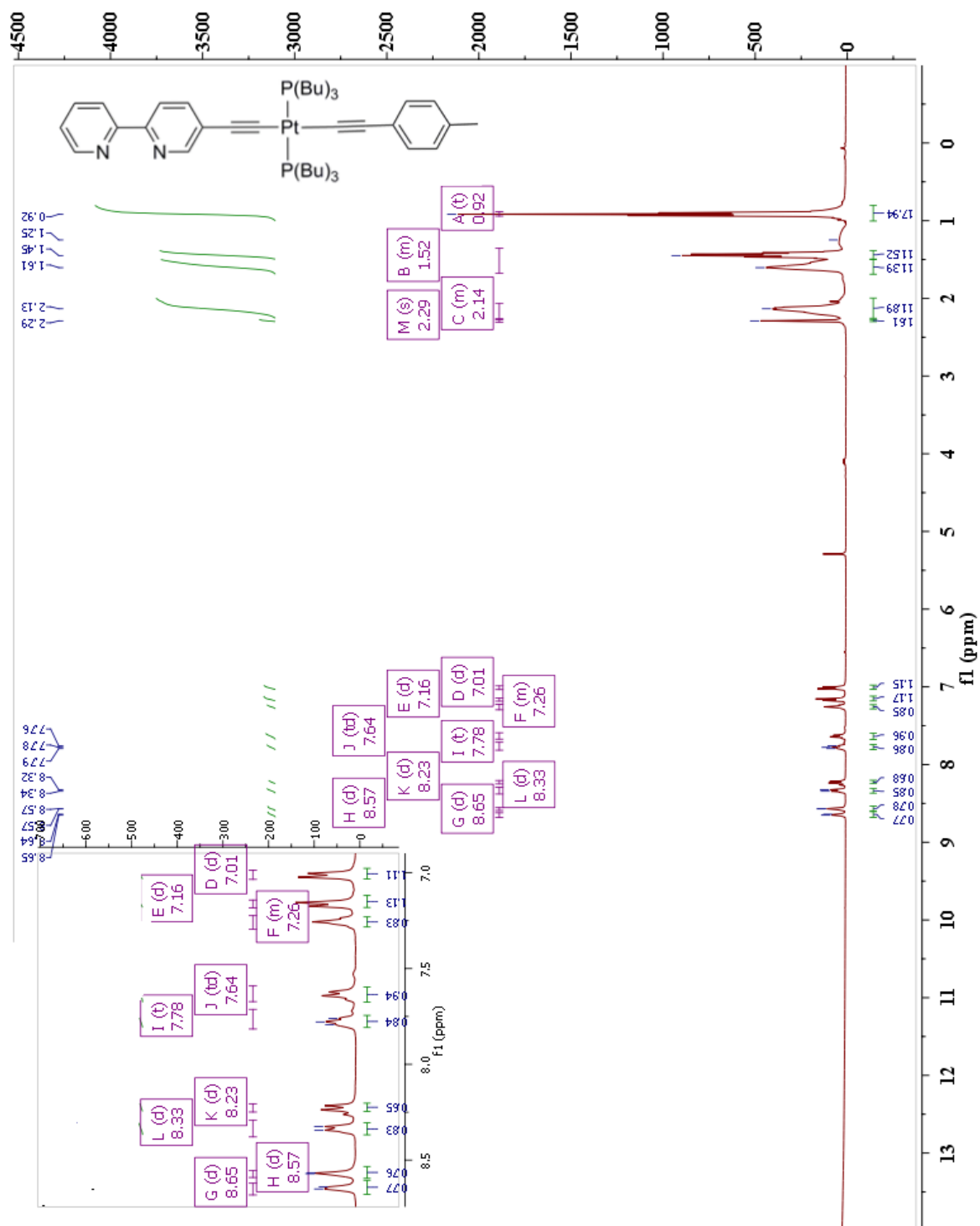




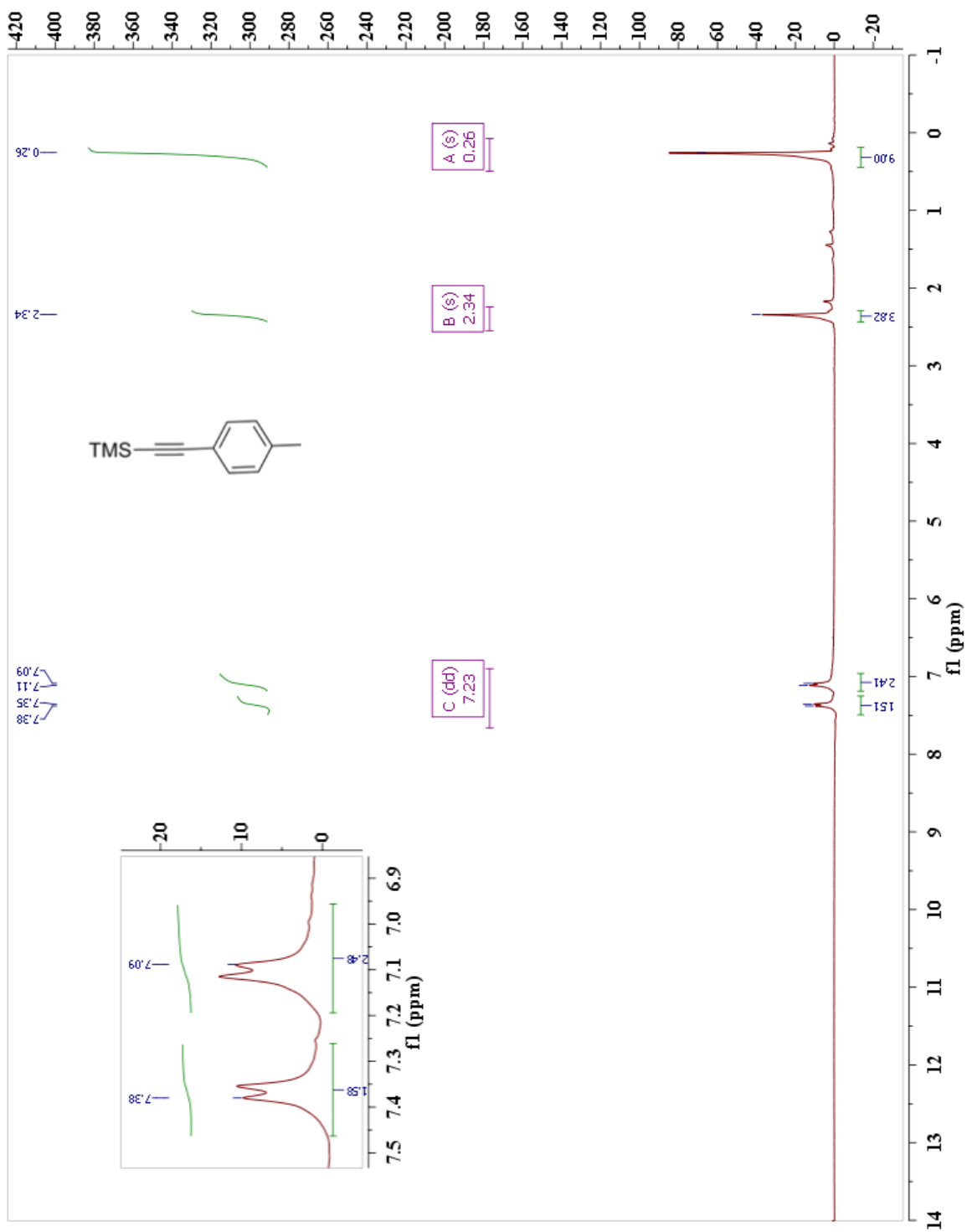
***trans*-Bis(tri-*n*-butylphosphine)-bis(5-ethynyl-2,2'-bipyridine)platinum (16):**



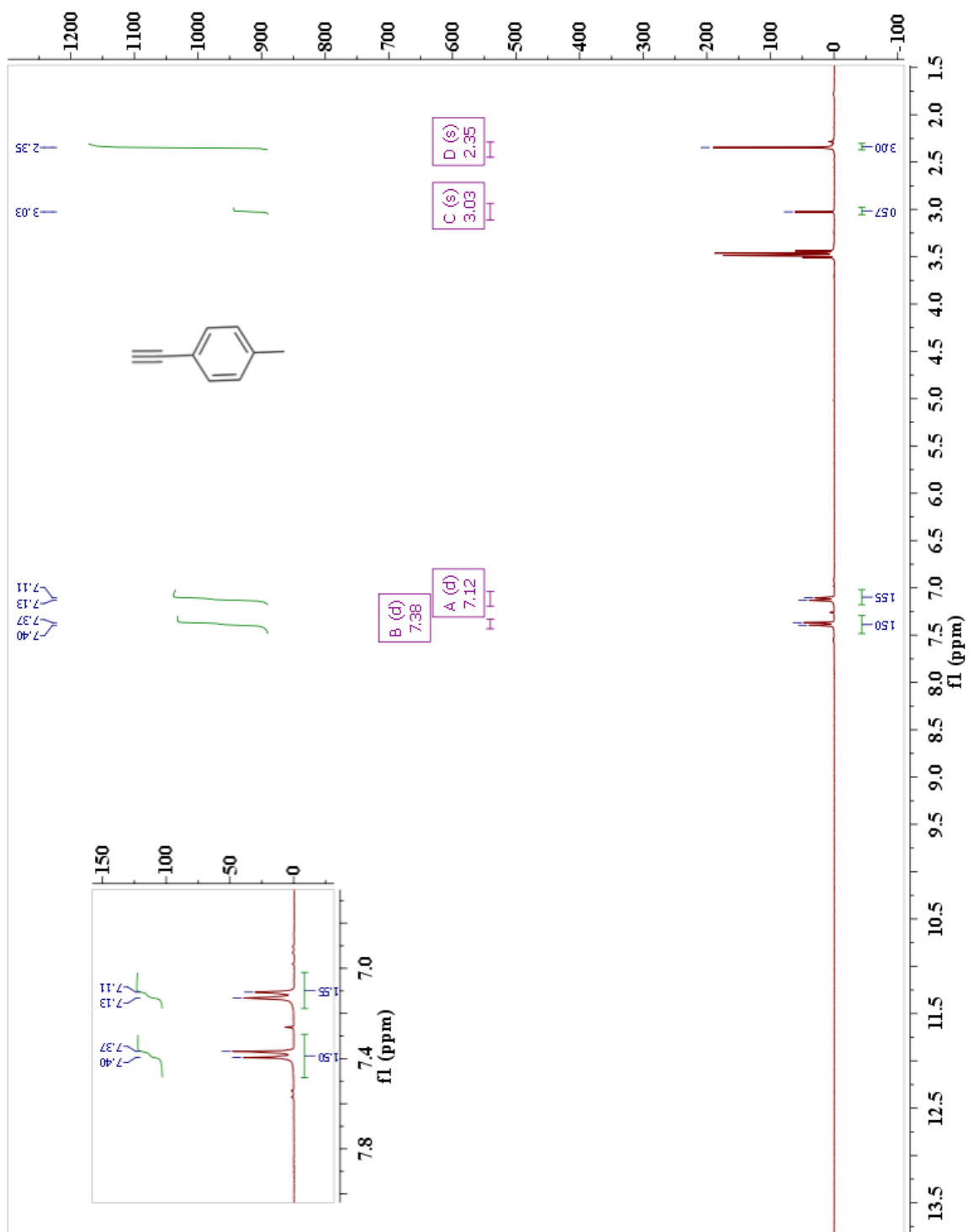
***trans*-(5-Ethynyl-2,2'-bipyridine)-4-tolyethynyl-bis(tri-*n*-butylphosphine)platinum (20):**



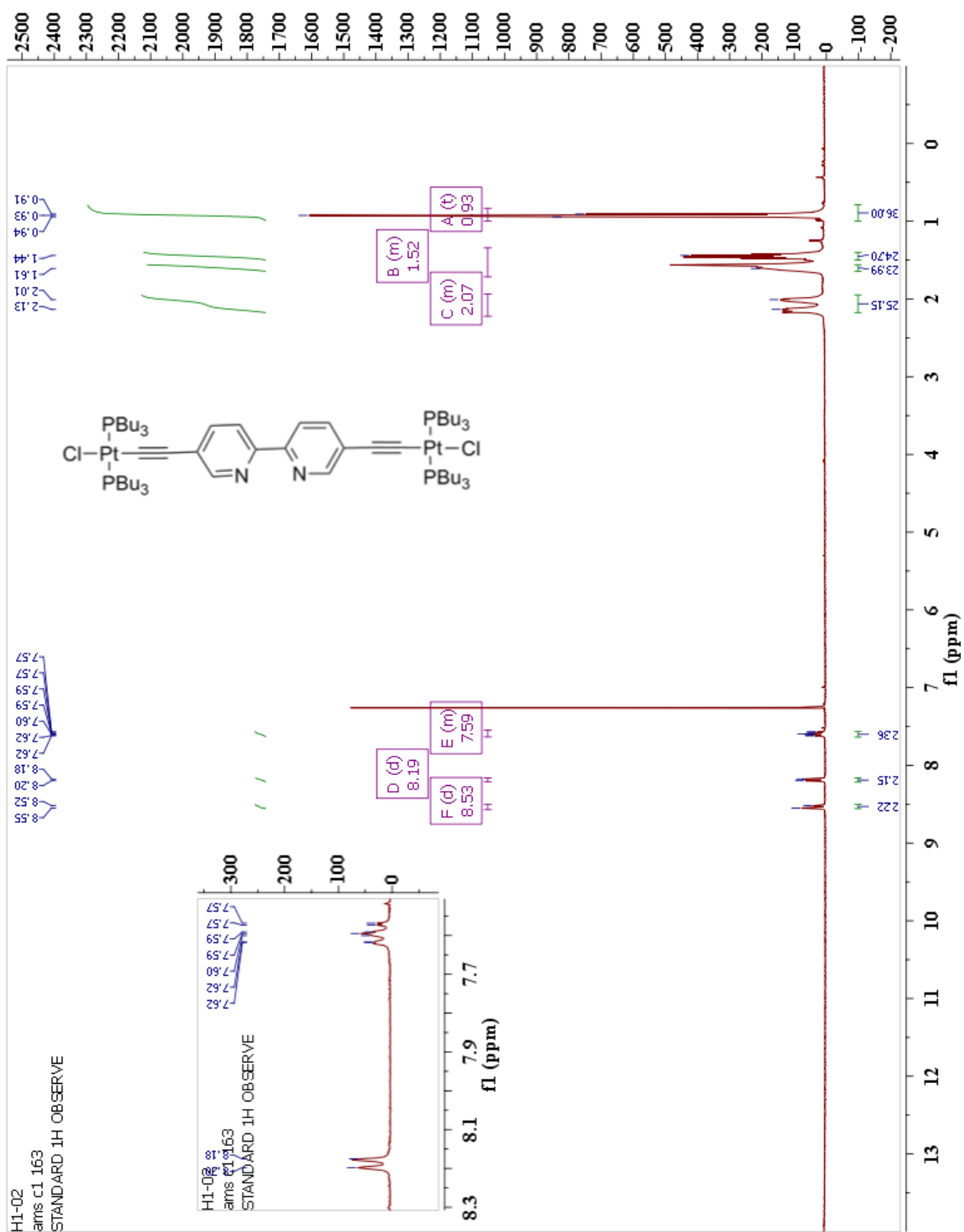
# 1-Trimethylsilylethynyl-4-methylbenzene (18):



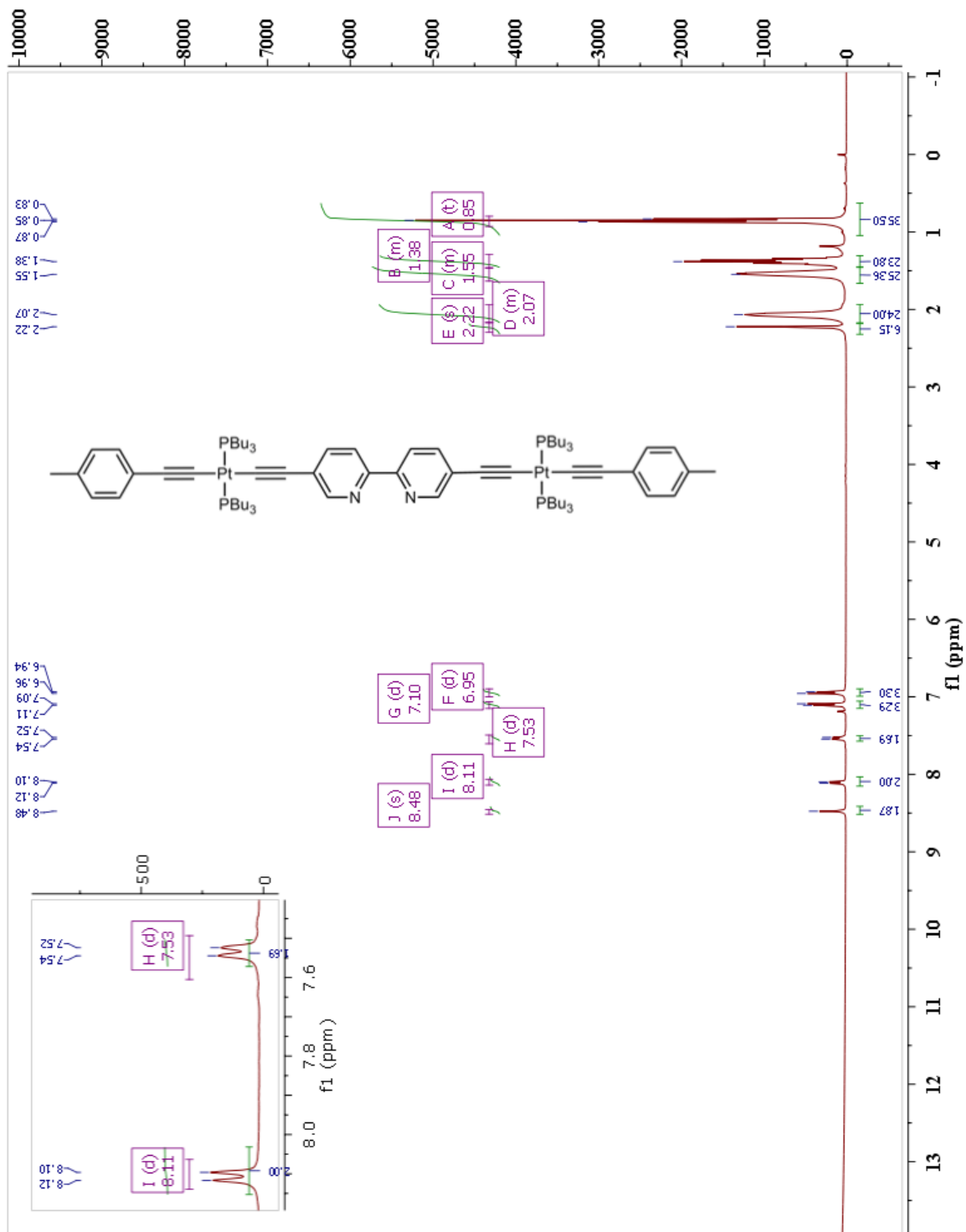
# 1-Ethynyl-4-methylbenzene (19):



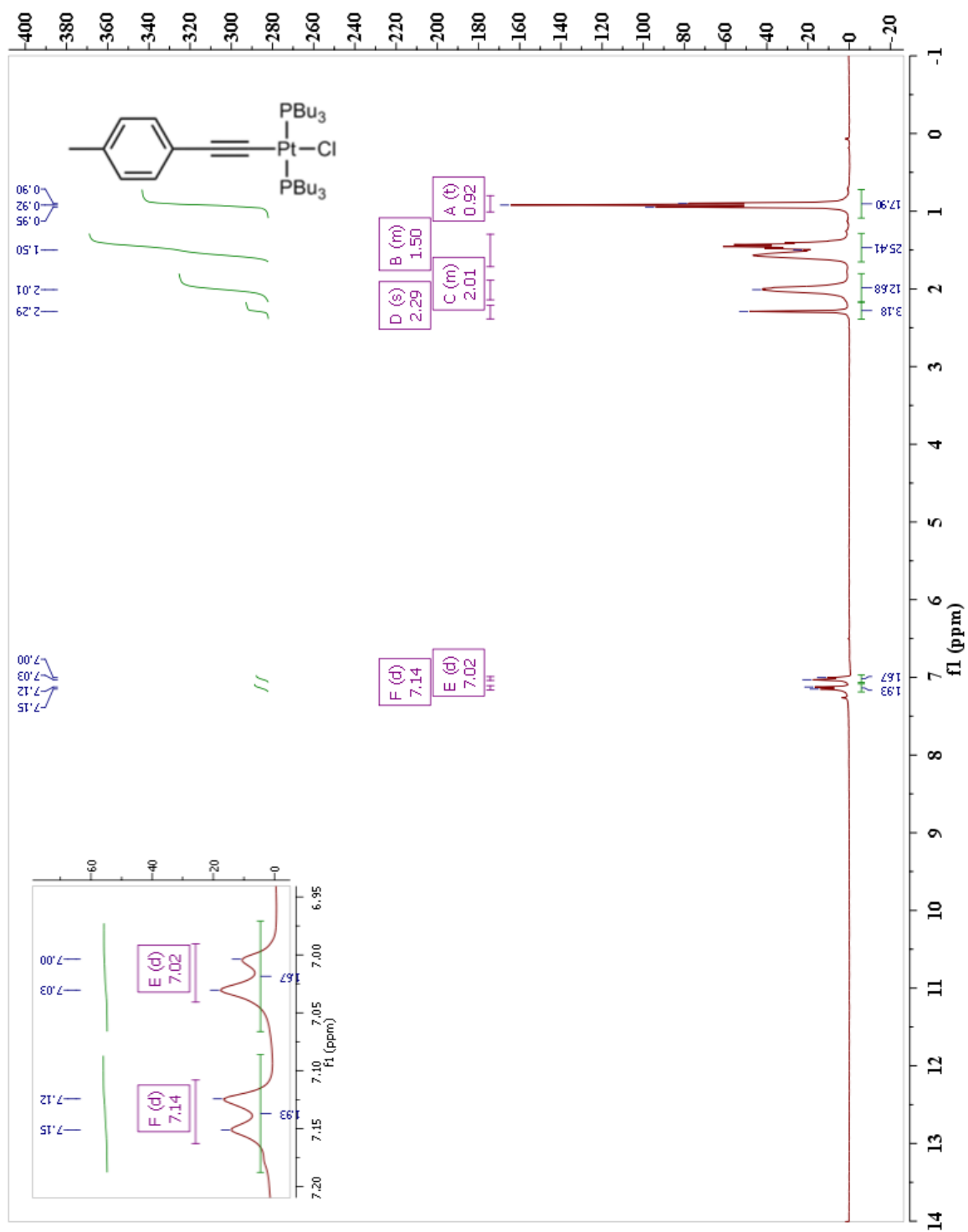
***trans*-(5,5'-Ethynyl-2,2'-bipyridine)-dichloro-bis(tri-*n*-butylphosphine)platinum (21):**



***trans*-(5,5'-Ethynyl-2,2'-bipyridine)-bis(4-tolylethynyl-bis(*tri-n*-butylphosphine)platinum) (22):**

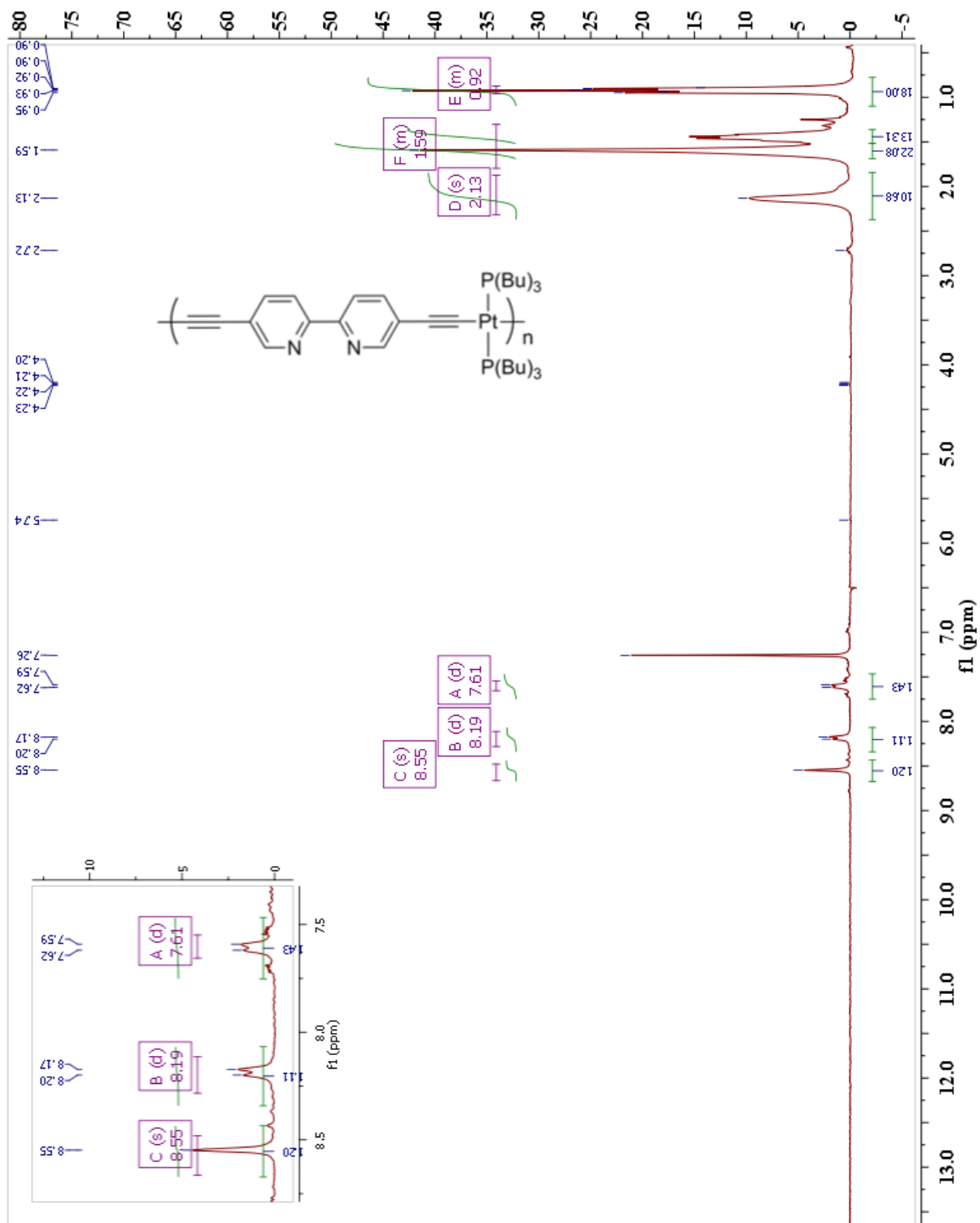


***trans*-4-Tolylethynyl-chloro-bis(tri-*n*-butylphosphine)platinum (23) :**

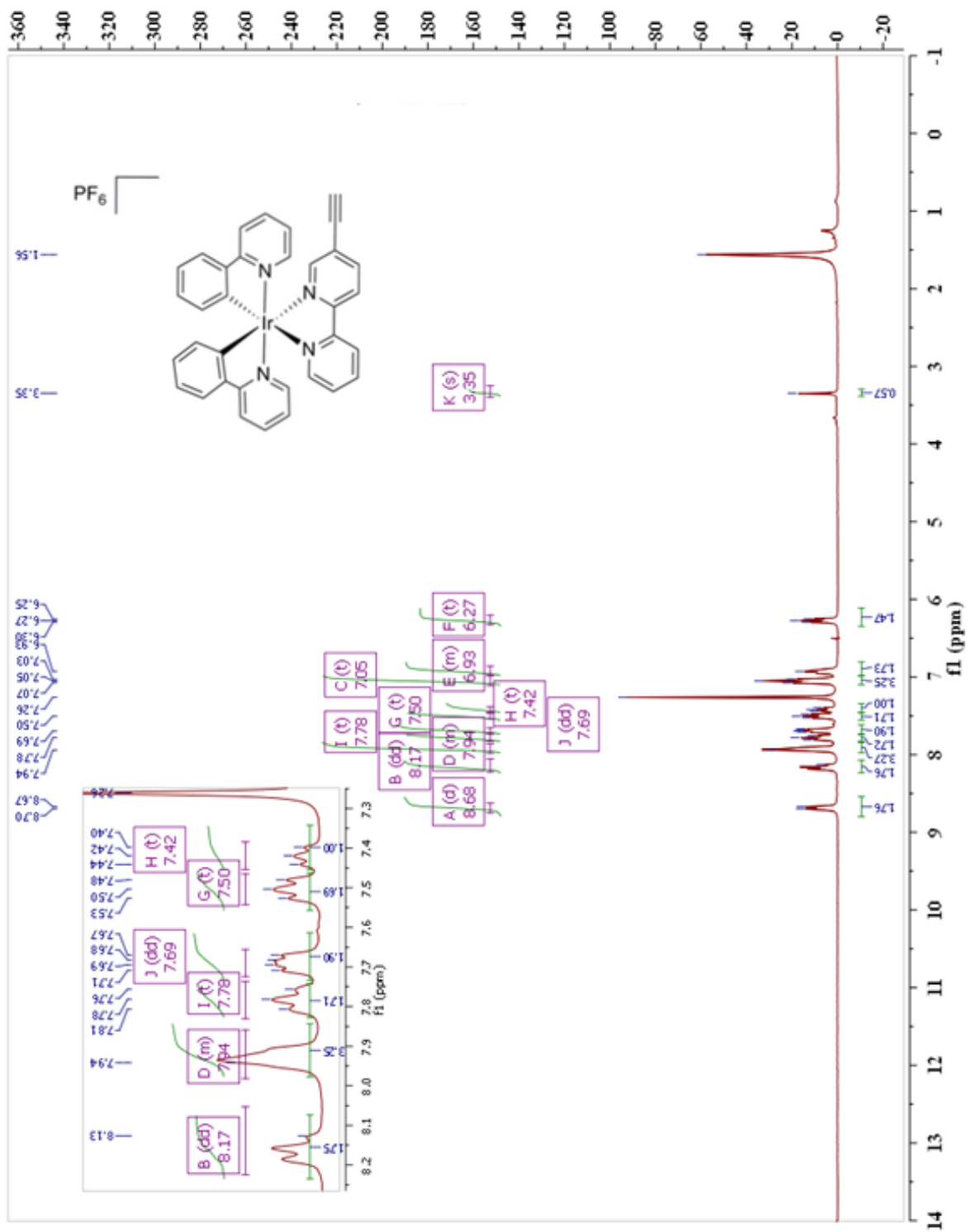




**Pt-Polymer (24):**

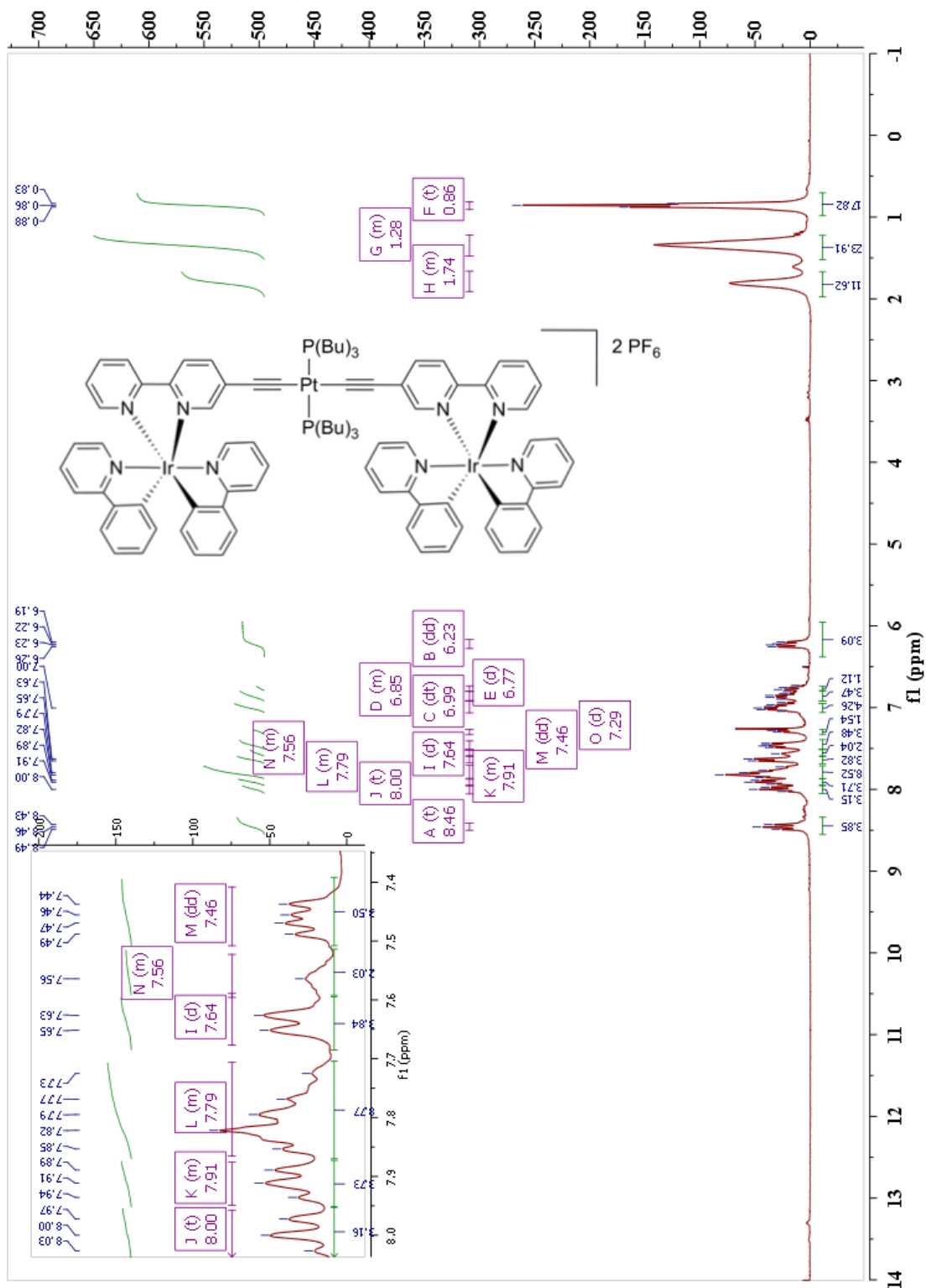


**[Ir(ppy)<sub>2</sub>(5-Ethynyl-2,2'-bipyridine)] Hexafluorophosphate (30):**

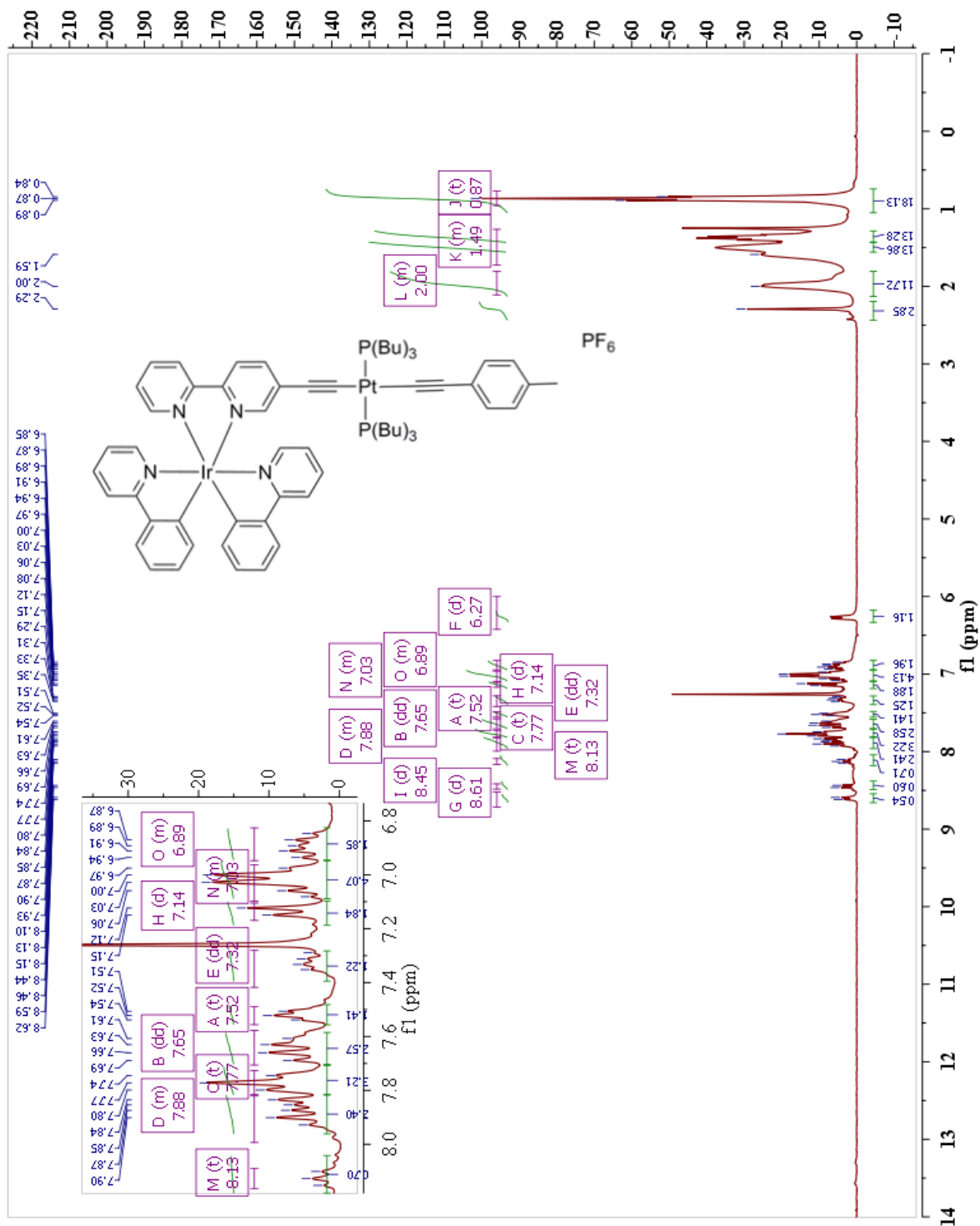




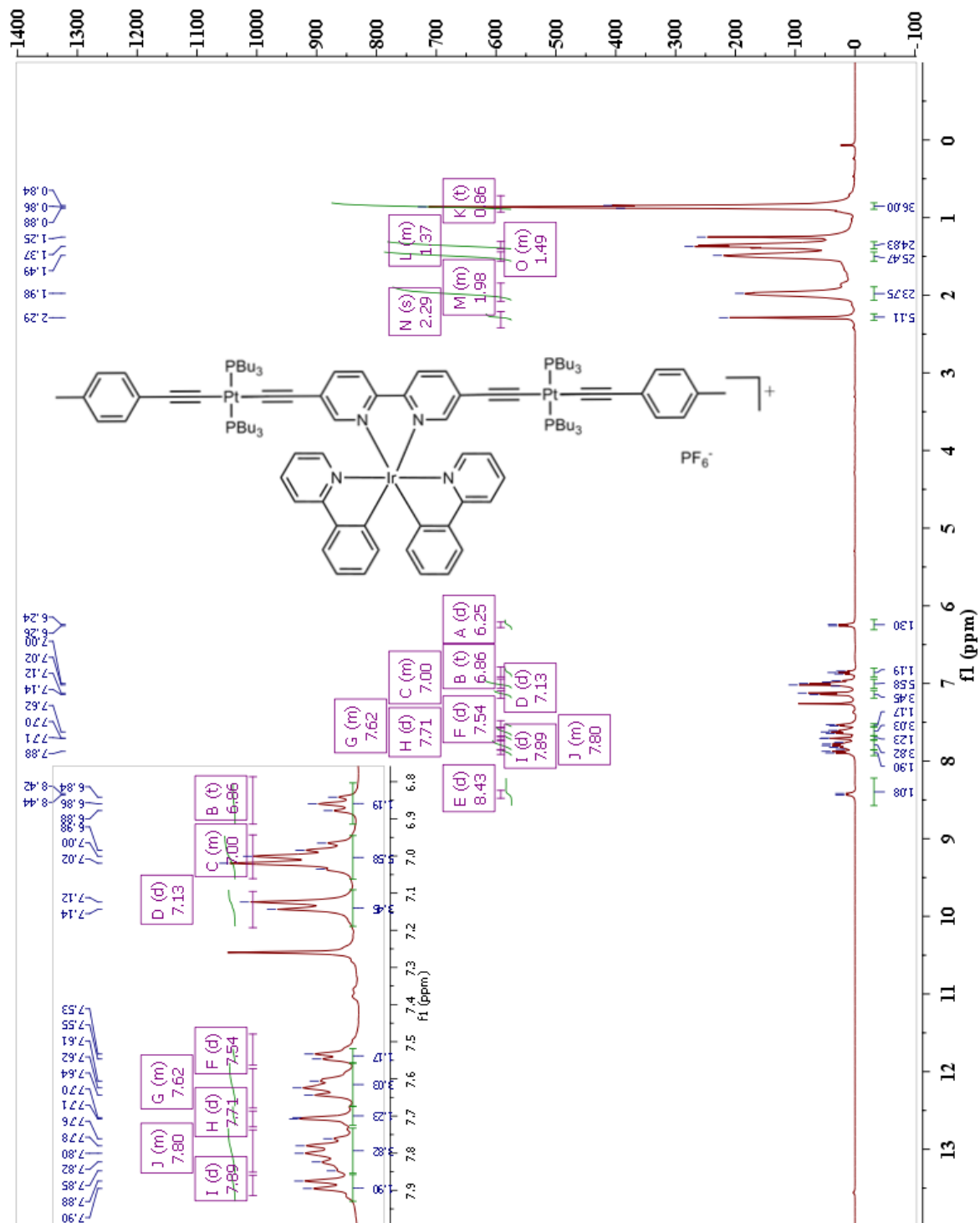
***trans*-Bis[Ir(ppy)<sub>2</sub>(5-Ethynyl-2,2'-bipyridine)]-bis(tri-*n*-butylphosphine)platinum  
Hexafluorophosphate (32):**



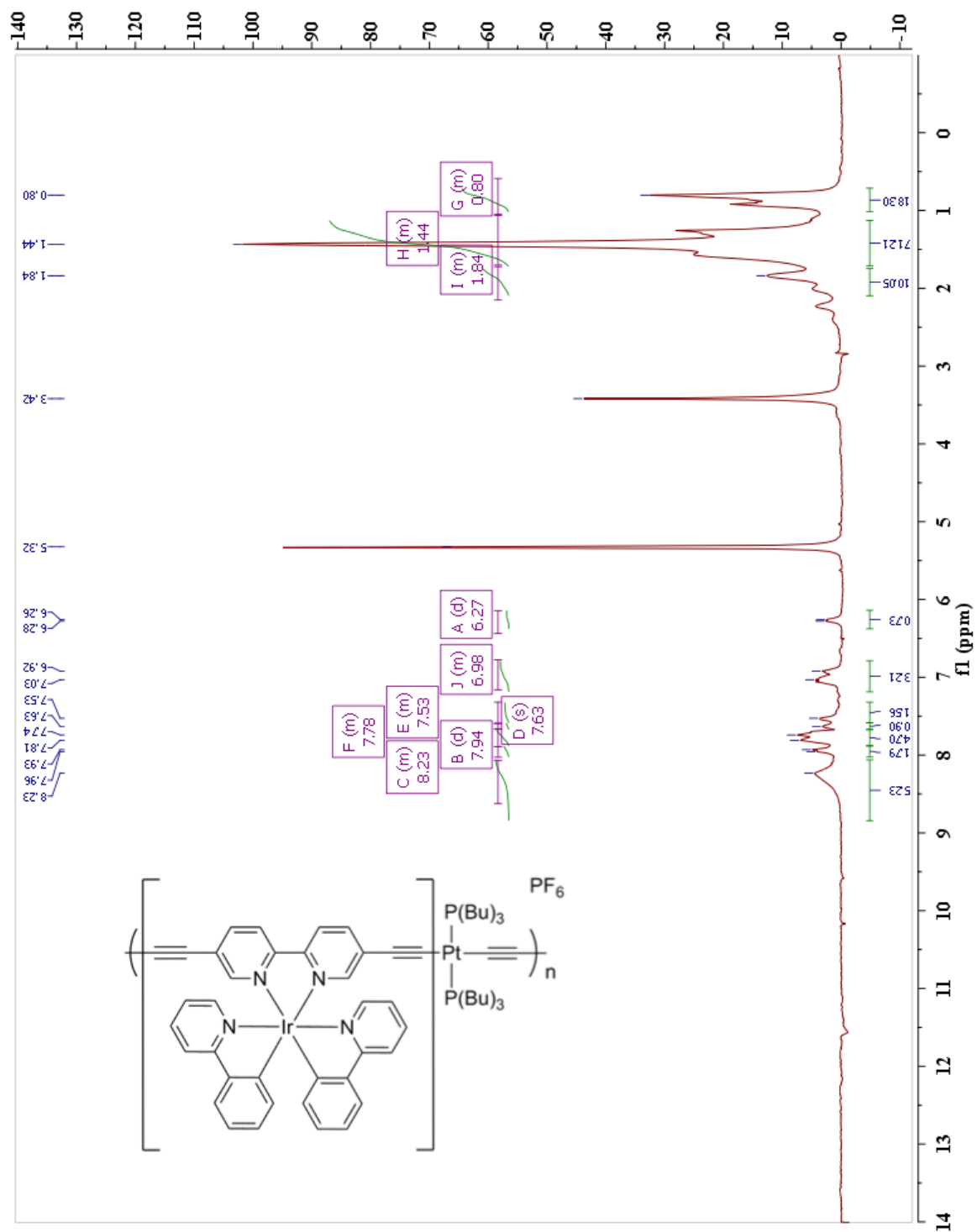
***trans*-[Ir(ppy)<sub>2</sub>(5-Ethynyl-2,2'-bipyridine)]-4-tolylethynyl-bis(tri-*n*-butylphosphine)platinum Hexafluorophosphate (33):**



***trans*-[Ir(ppy)<sub>2</sub>(5,5'-Ethynyl-2,2'-bipyridine)]-bis(4-tolylethynyl-bis(*tri-n*-butylphosphine)platinum) Hexafluorophosphate (34):**

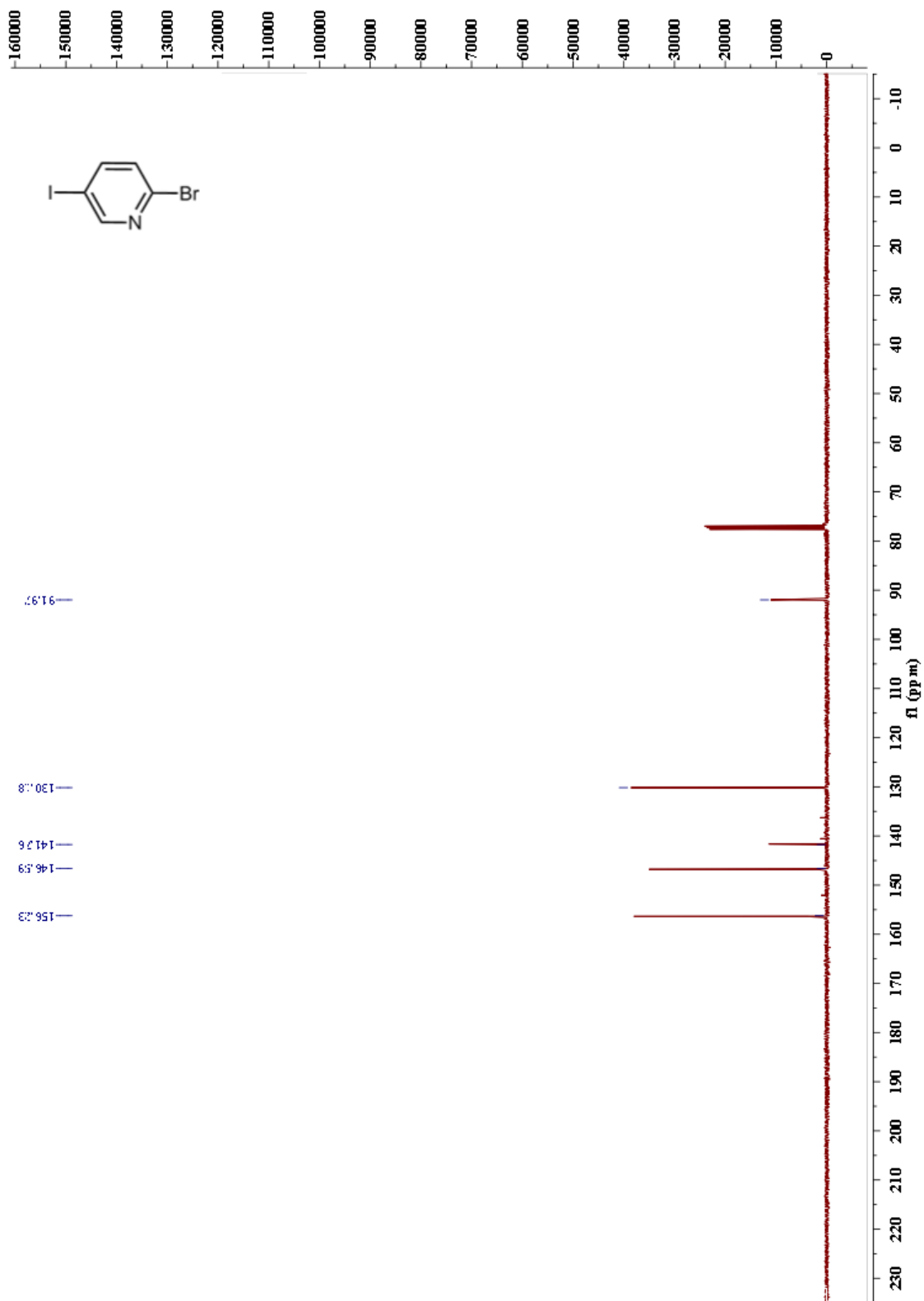


**Pt-Ir Polymer (36):**



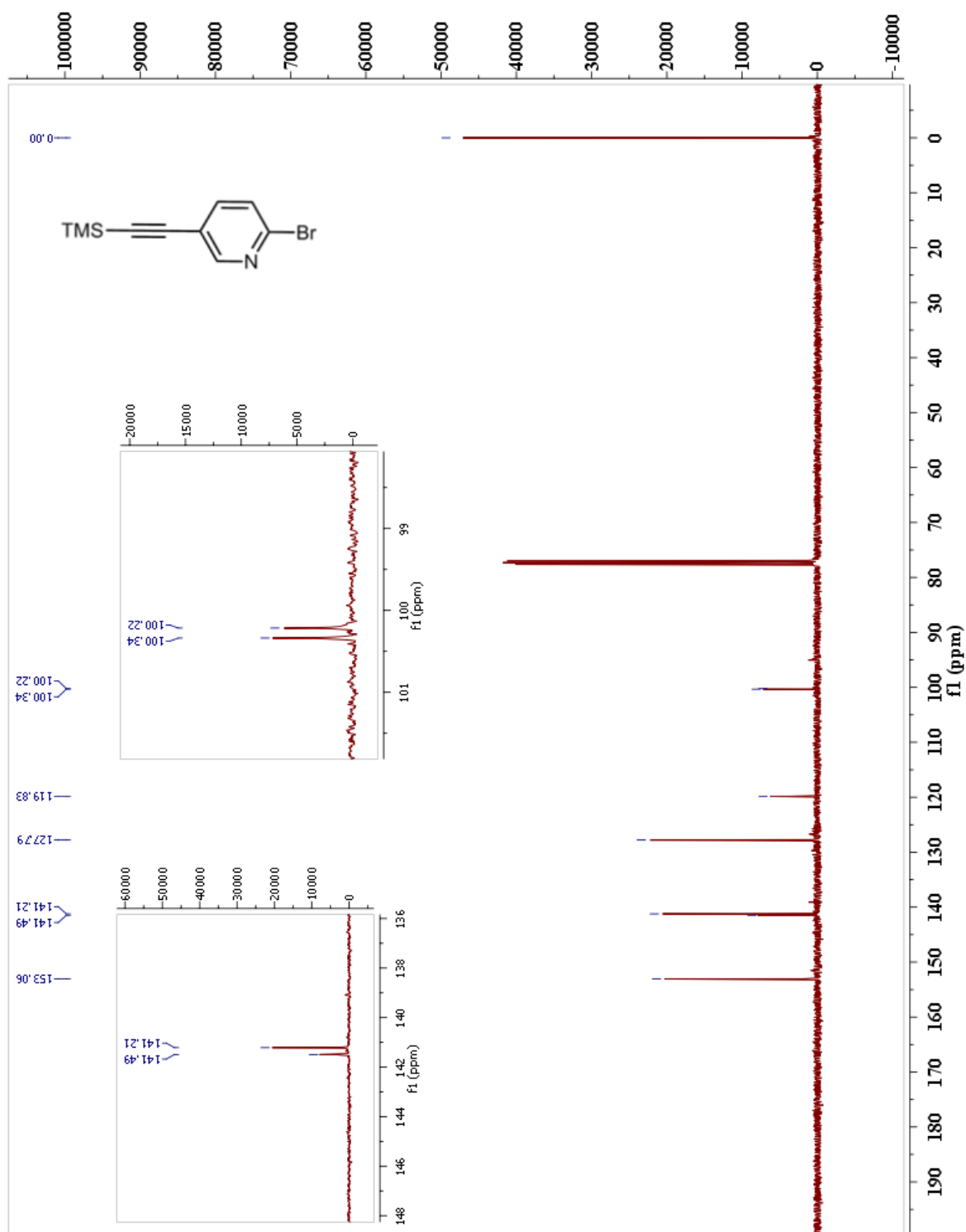
## ANNEX 2: SPECTRA OF NUCLEAR MAGNETIC RESONANCE OF CARBONS.

### 2-Bromo-5-iodopyridine (2):

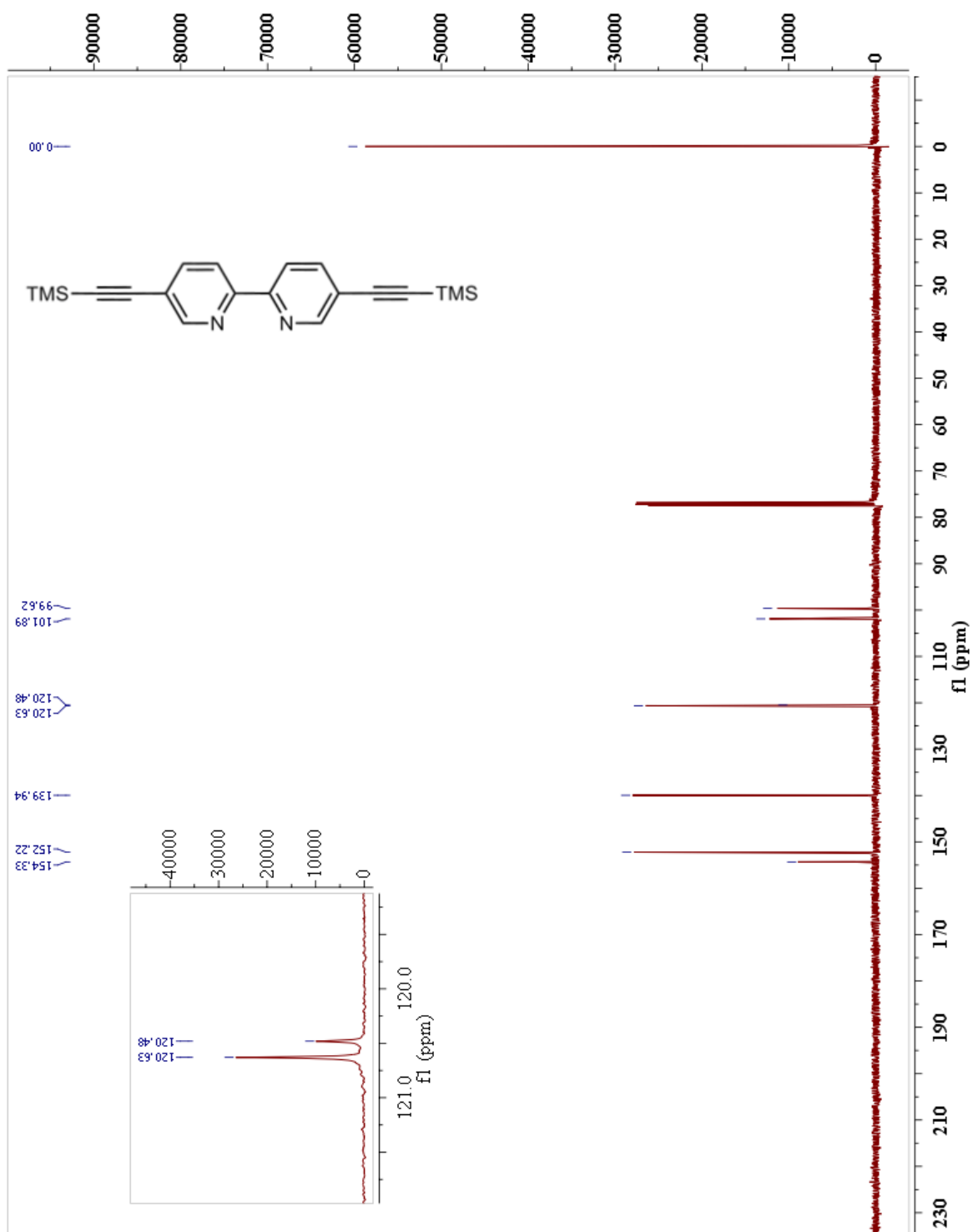




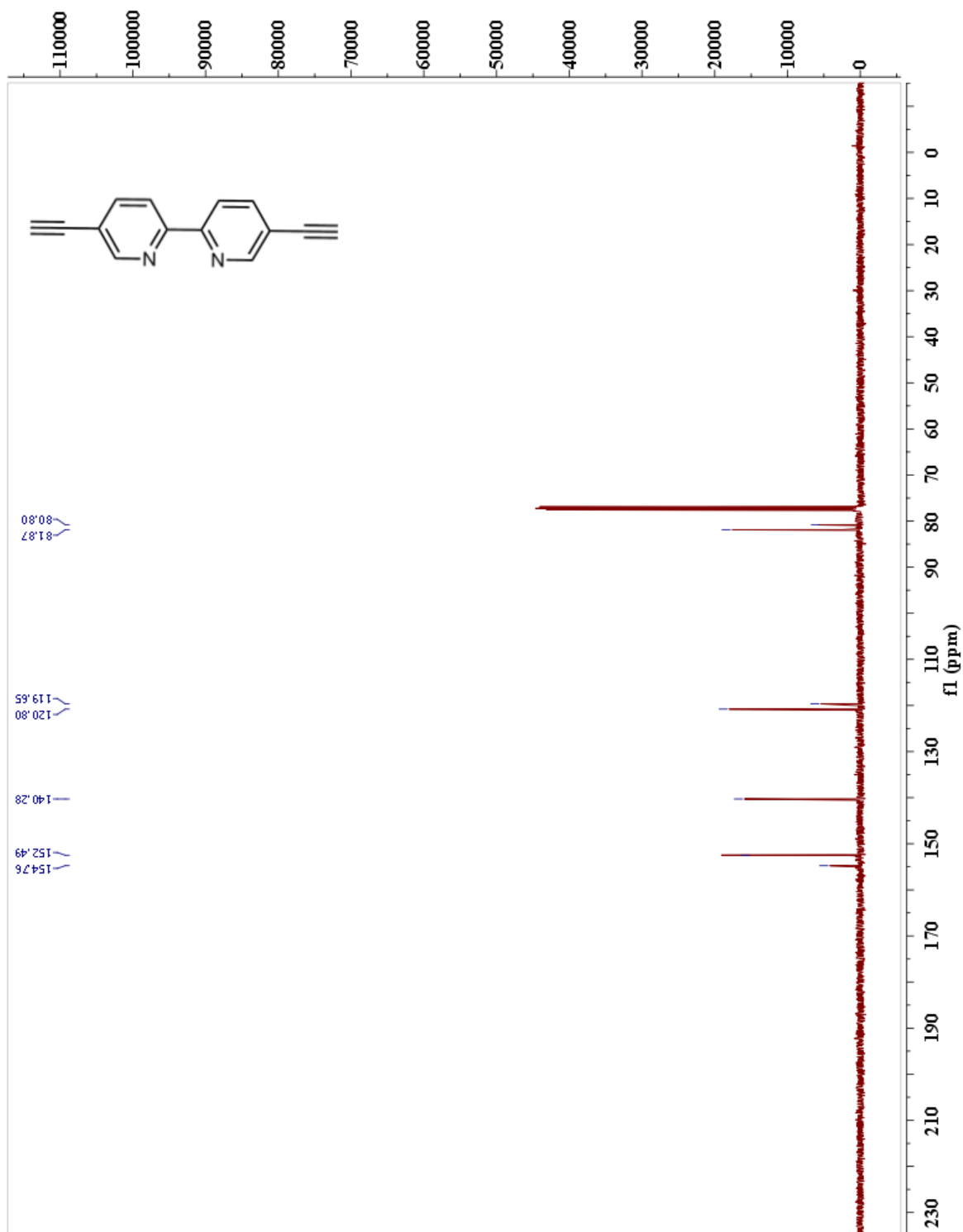
### 2-Bromo-5-((trimethylsilyl)ethynyl)pyridine (3):



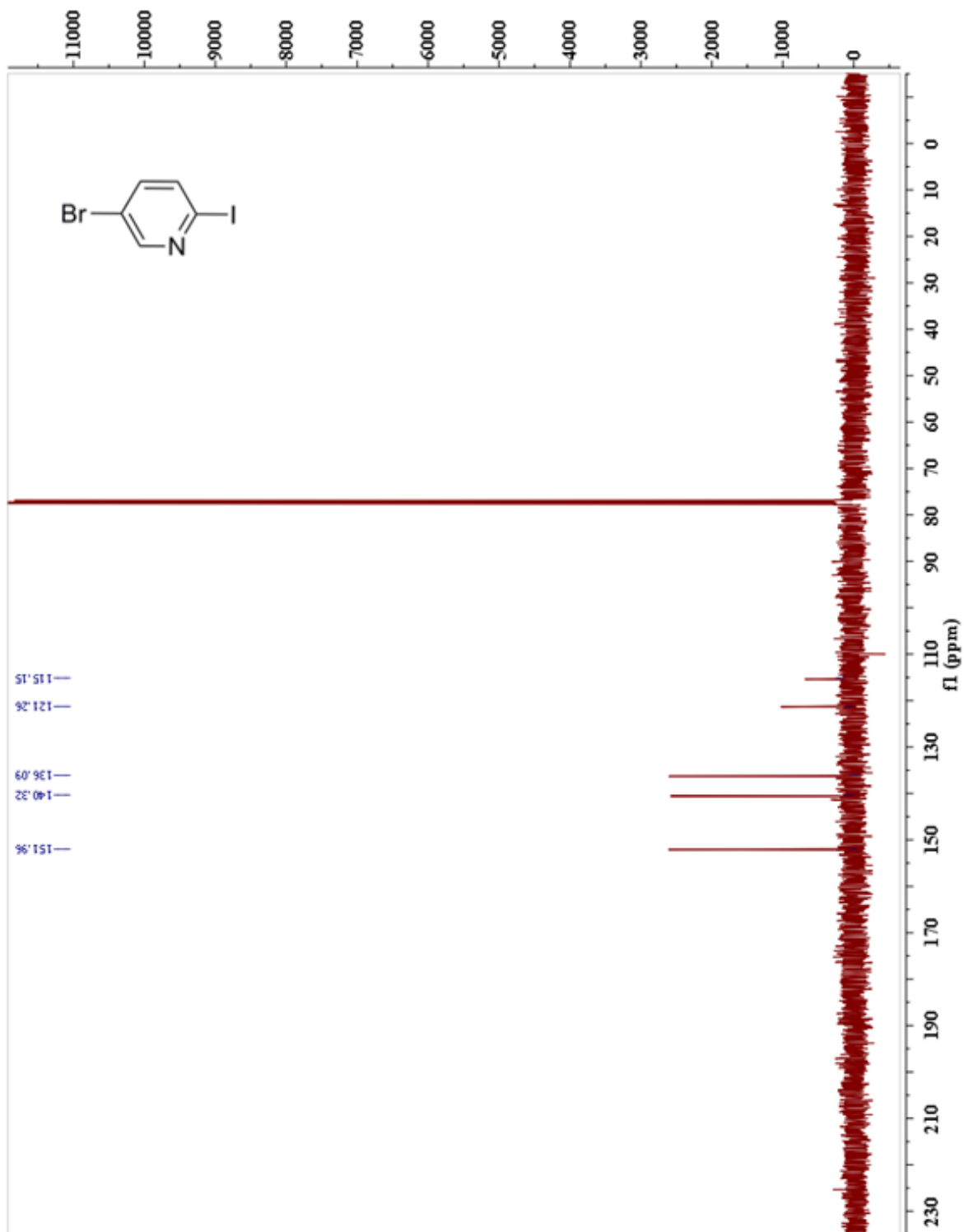
**5,5'-Bis((trimethylsilyl)ethynyl)-2,2'-bipyridine (4):**



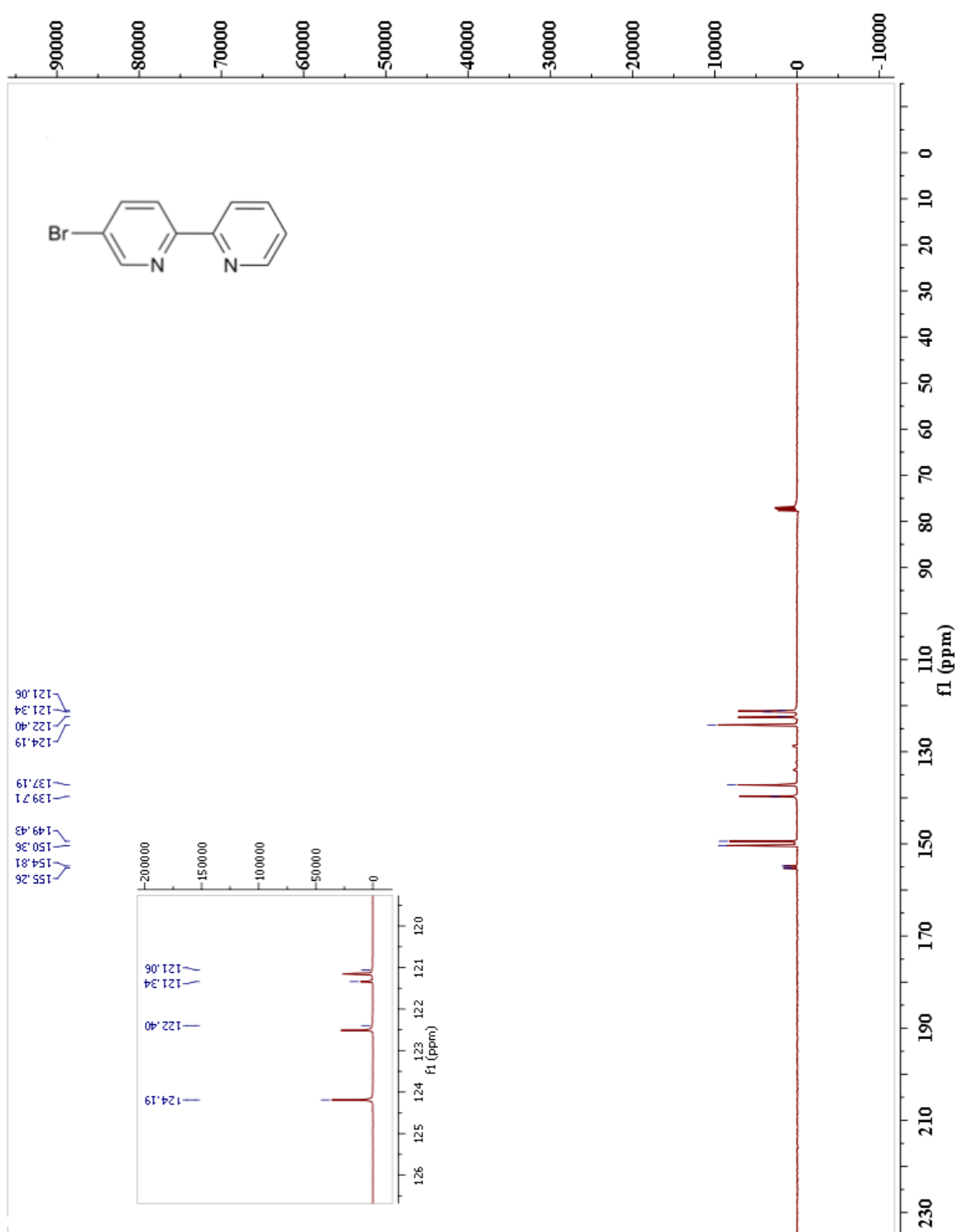
### 5,5'-Diethynyl-2,2'-bipyridine (5):



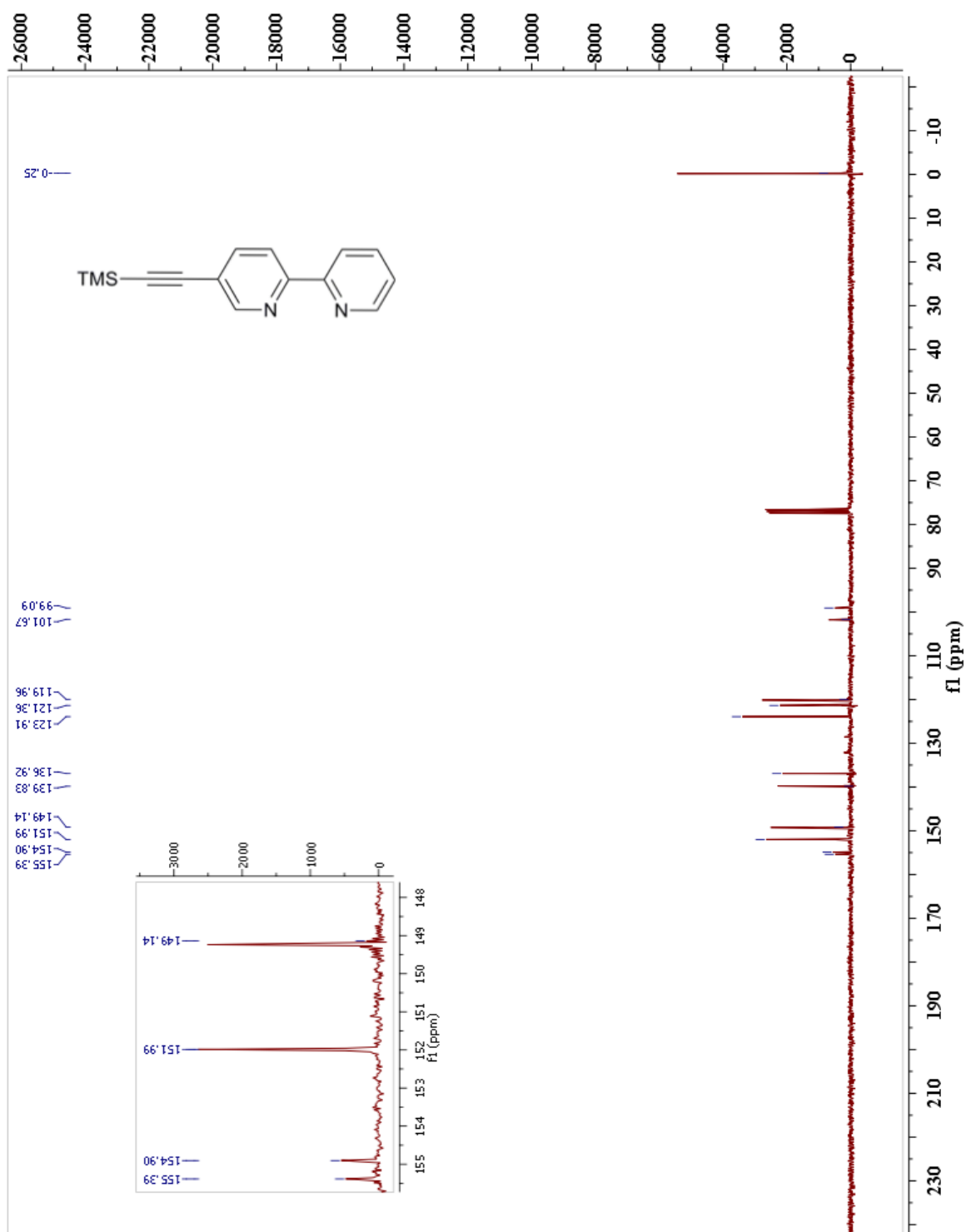
5-Bromo-2-iodopyridine (6):



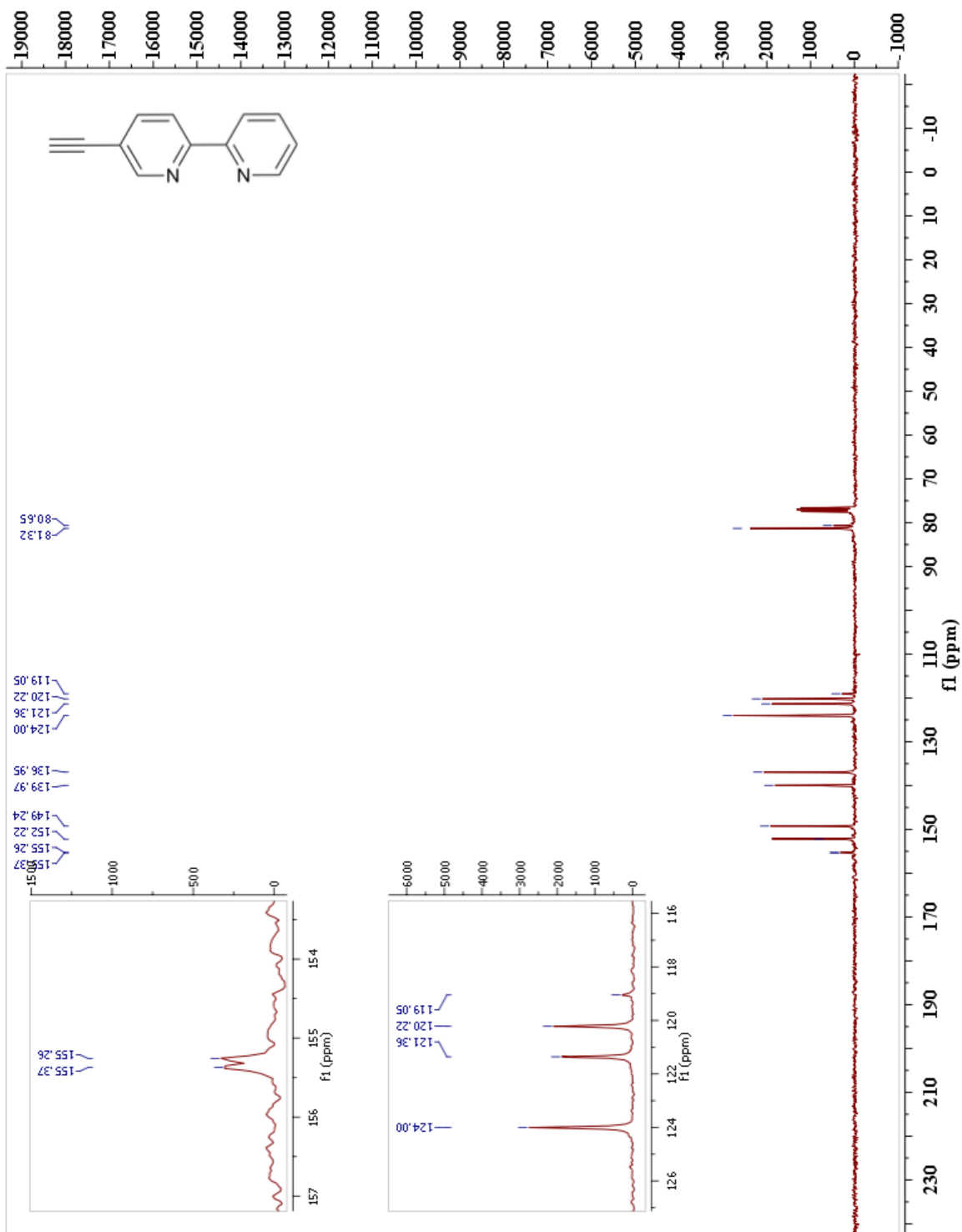
### 5-Bromo-2,2'-bipyridine (8):



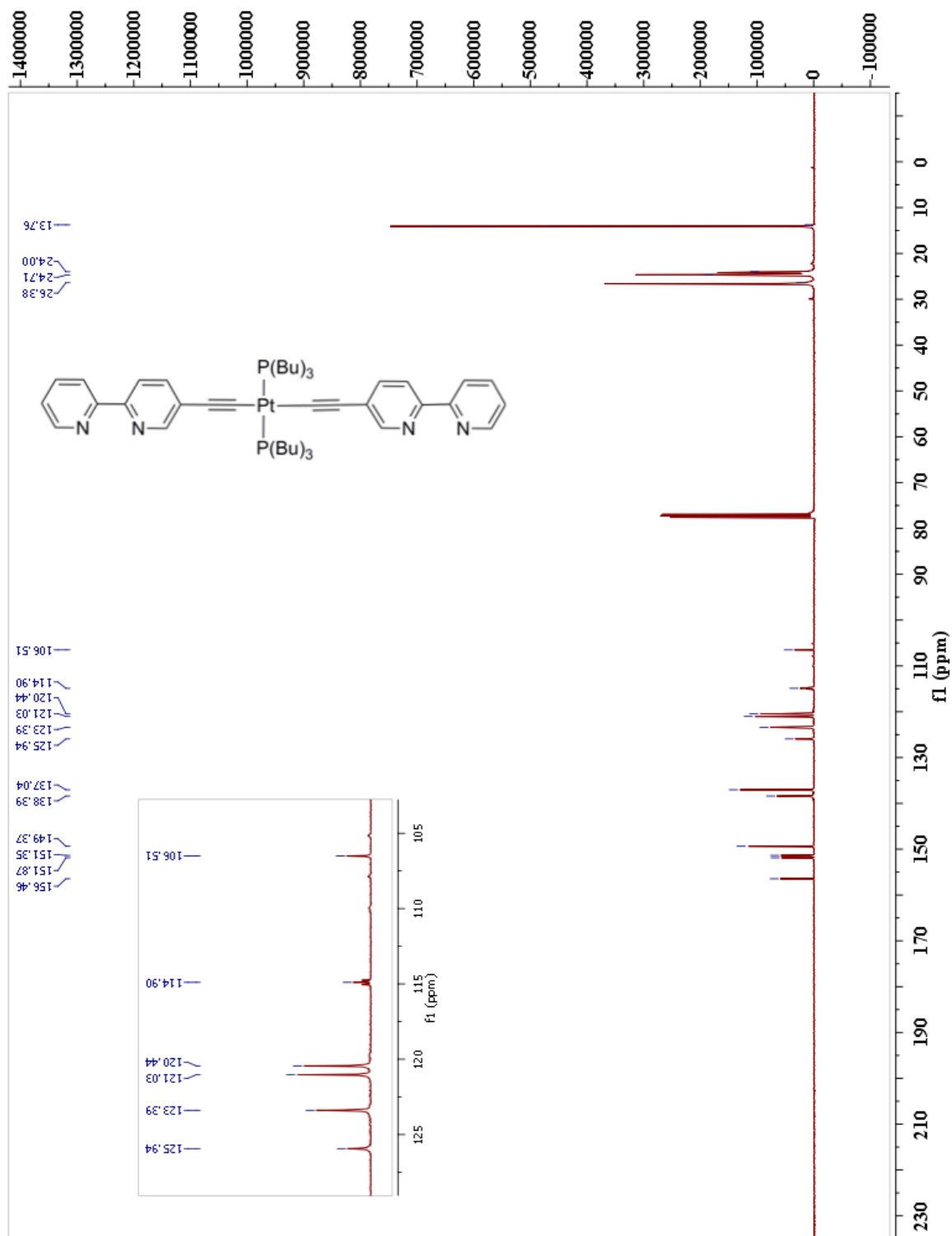
### 5-Trimethylsilylethynyl-2,2'-bipyridine (9):



5-Ethynyl-2,2'-bipyridine (10) :

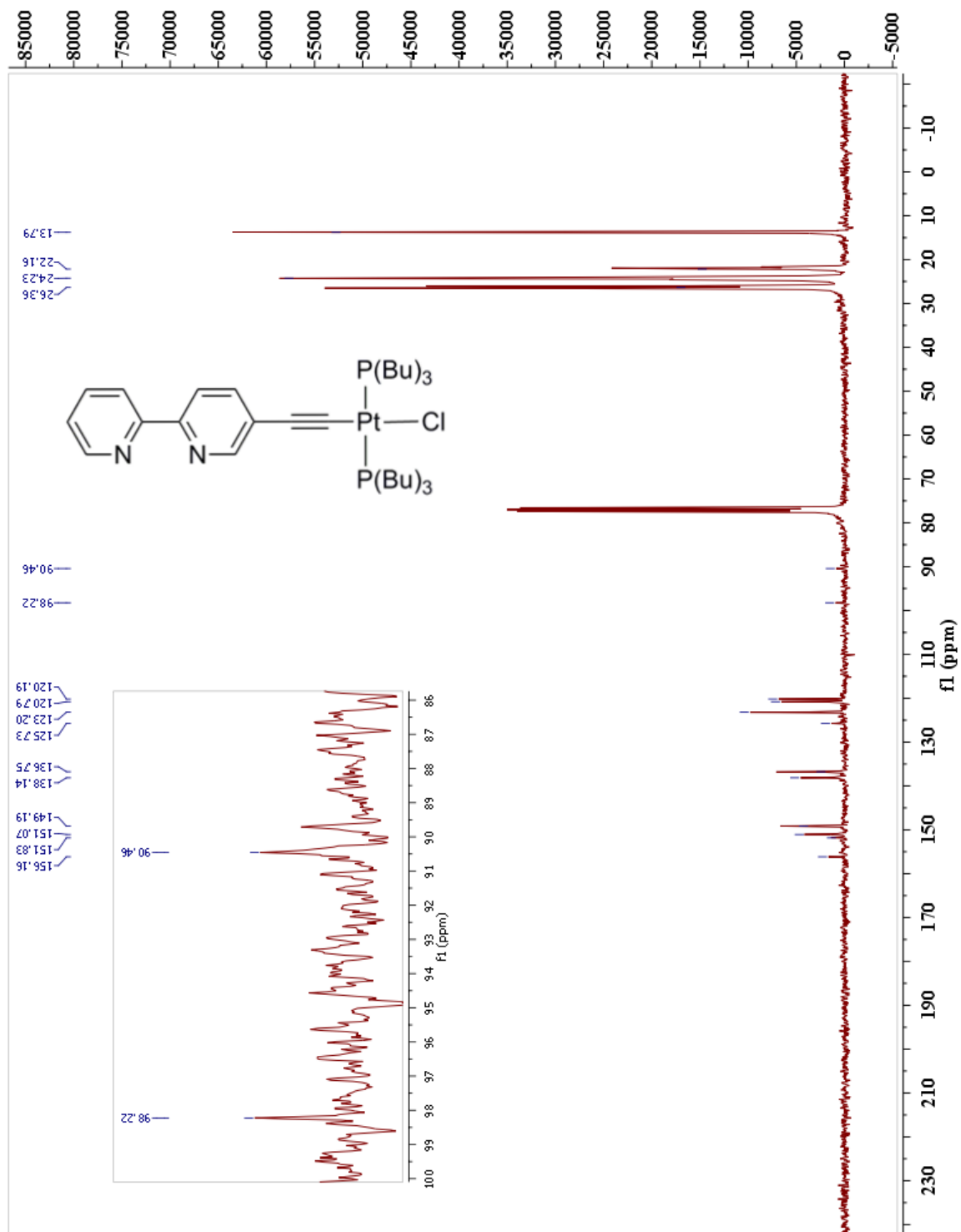


***trans*-(5-Ethynyl-2,2'-bipyridine)-chloro-bis(tri-*n*-butylphosphine)platinum (15):**

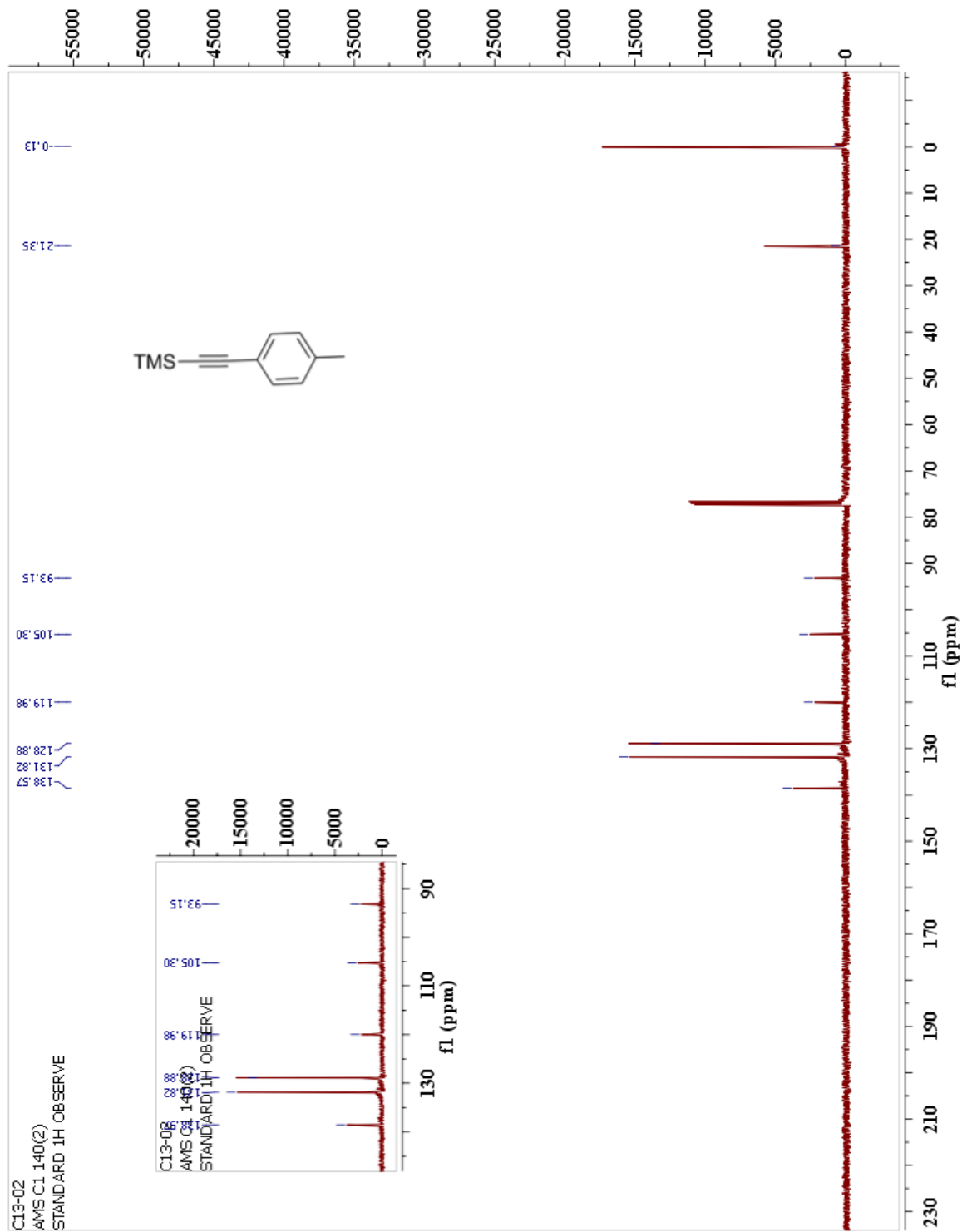




***trans*-Bis(tri-*n*-butylphosphine)-bis(5-ethynyl-2,2'-bipyridine)platinum (16):**

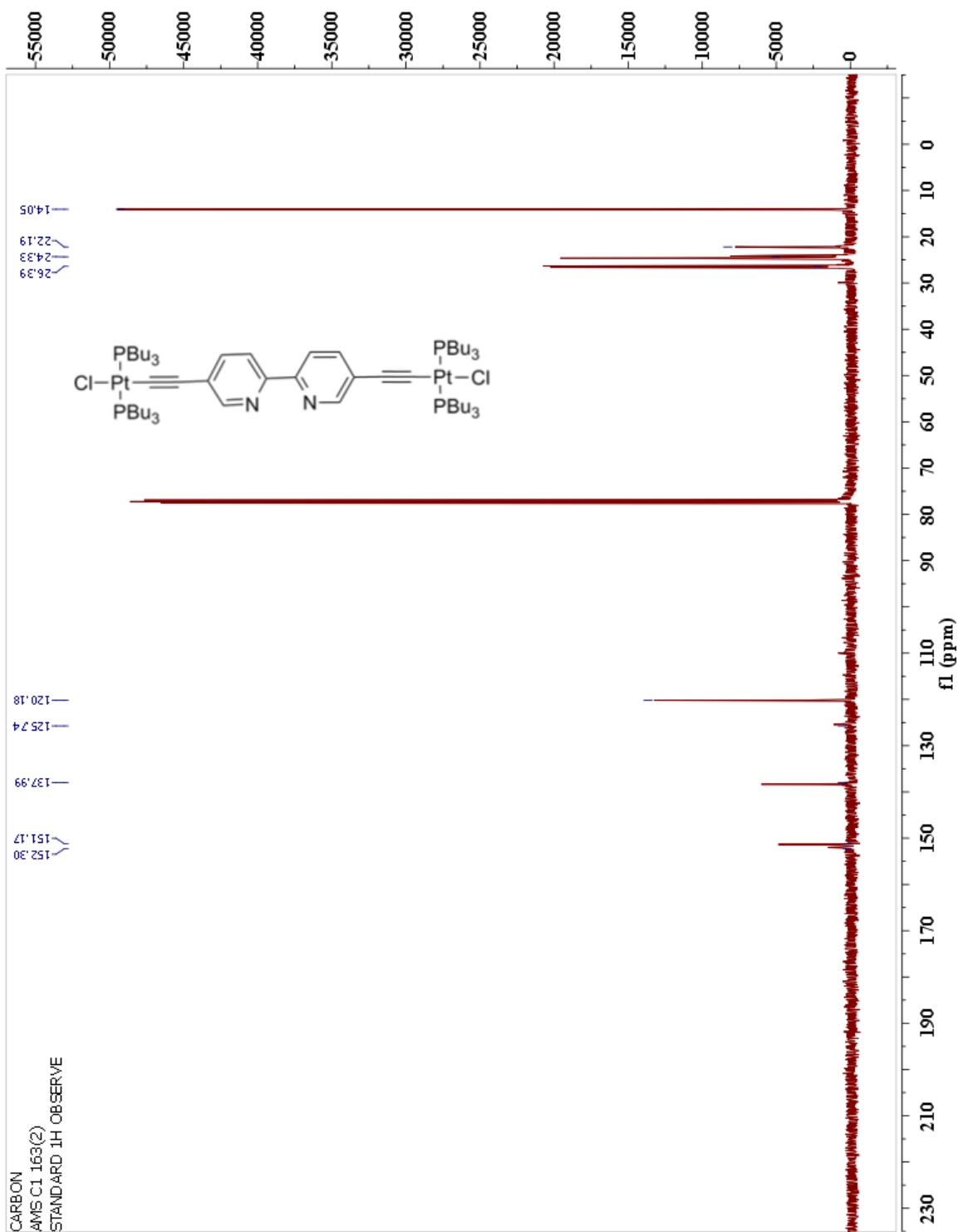


# 1-Trimethylsilylethynyl-4-methylbenzene (18):

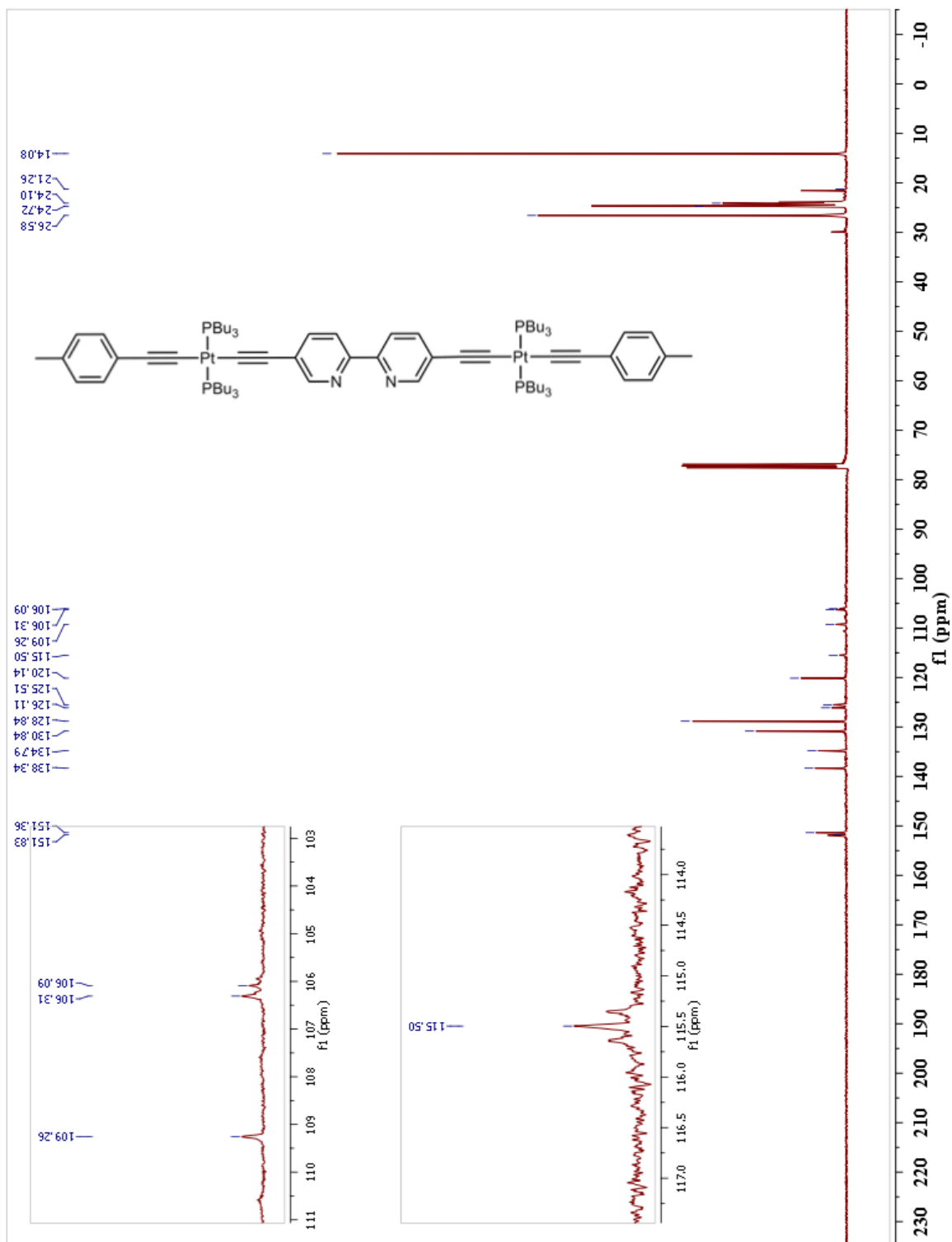




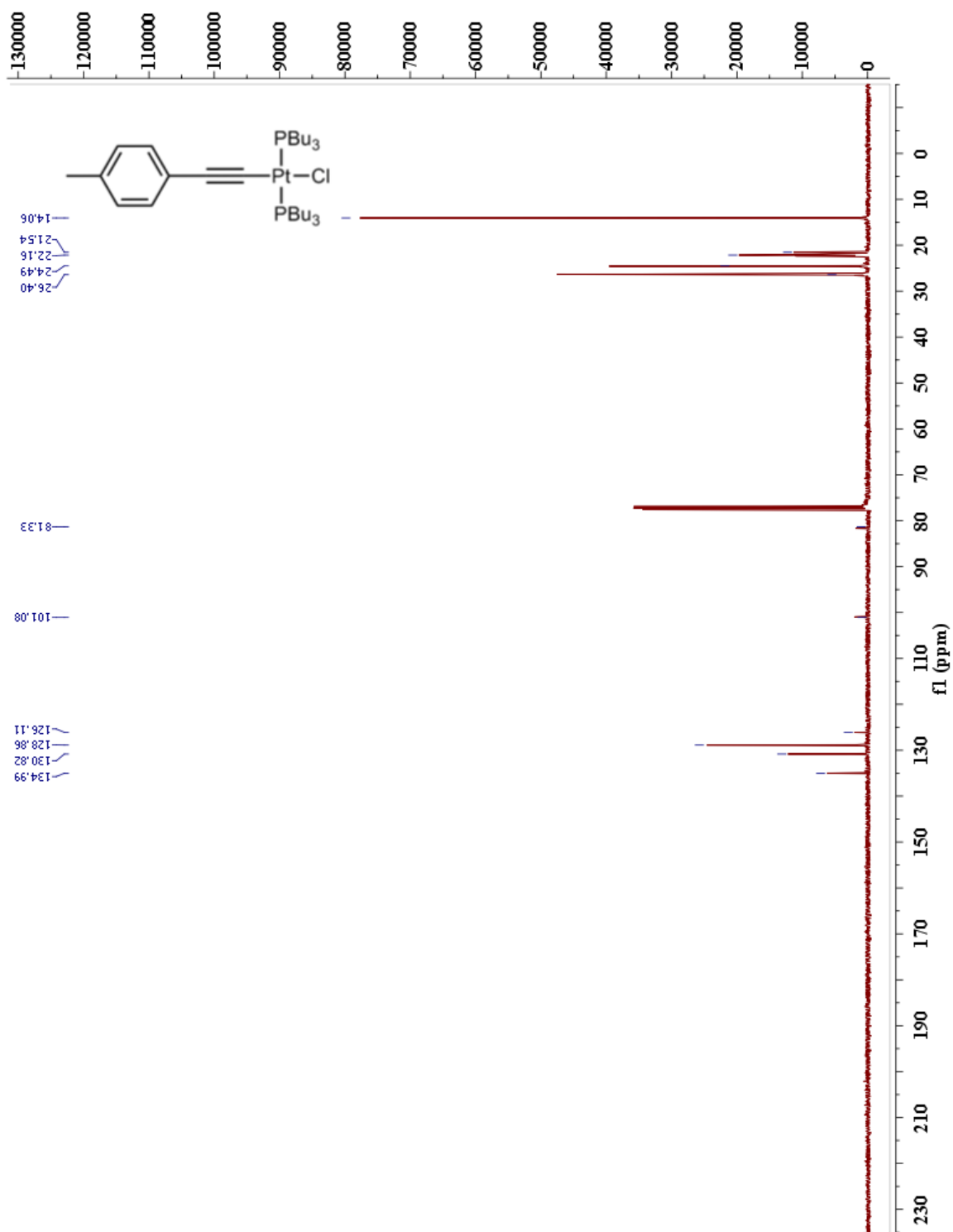
***trans*-(5,5'-Ethynyl-2,2'-bipyridine)-dichloro-bis(tri-*n*-butylphosphine)platinum (21):**



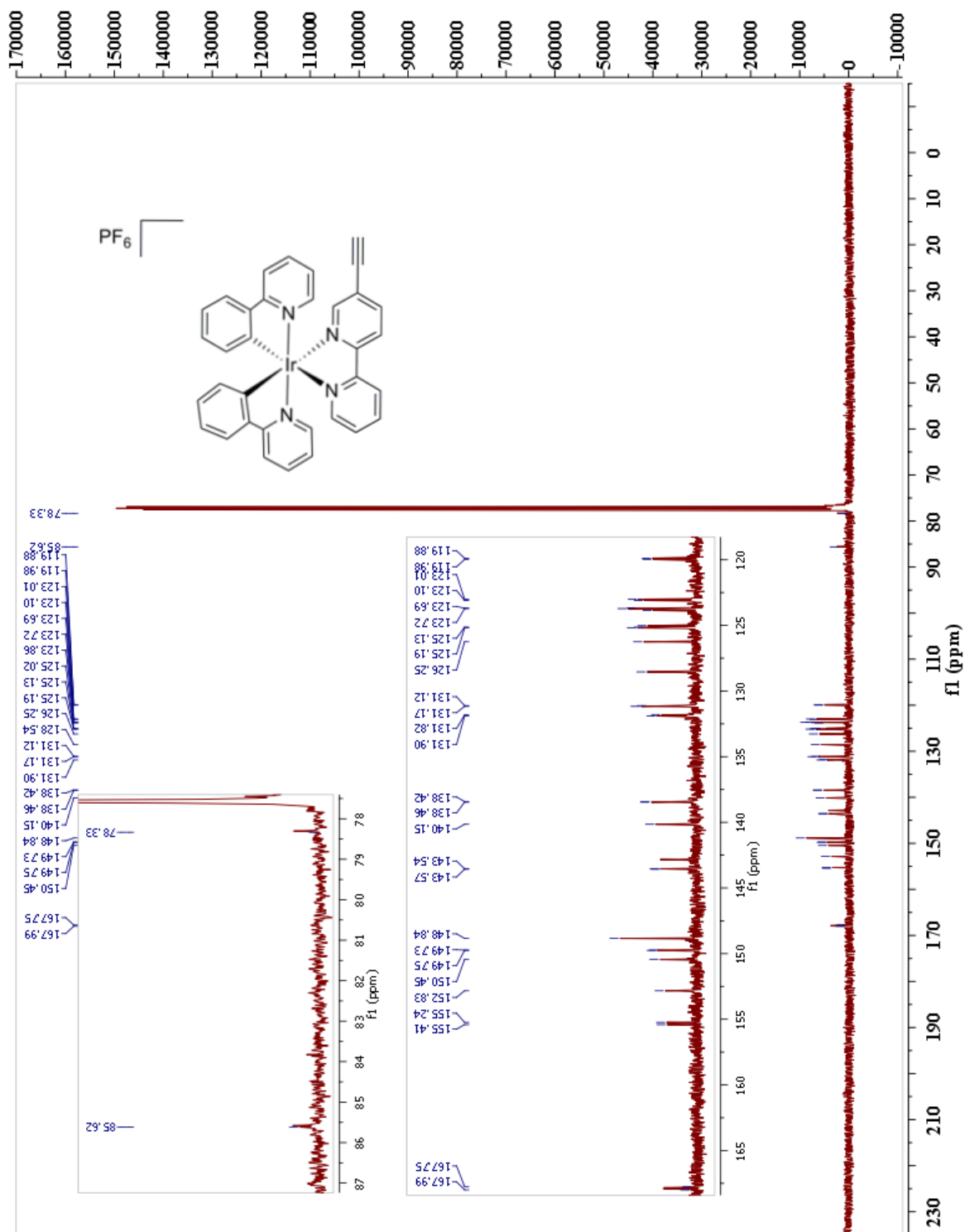
***trans*-(5,5'-Ethynyl-2,2'-bipyridine)-bis(4-tolylethynyl-bis(tri-*n*-butylphosphine)platinum) (22):**



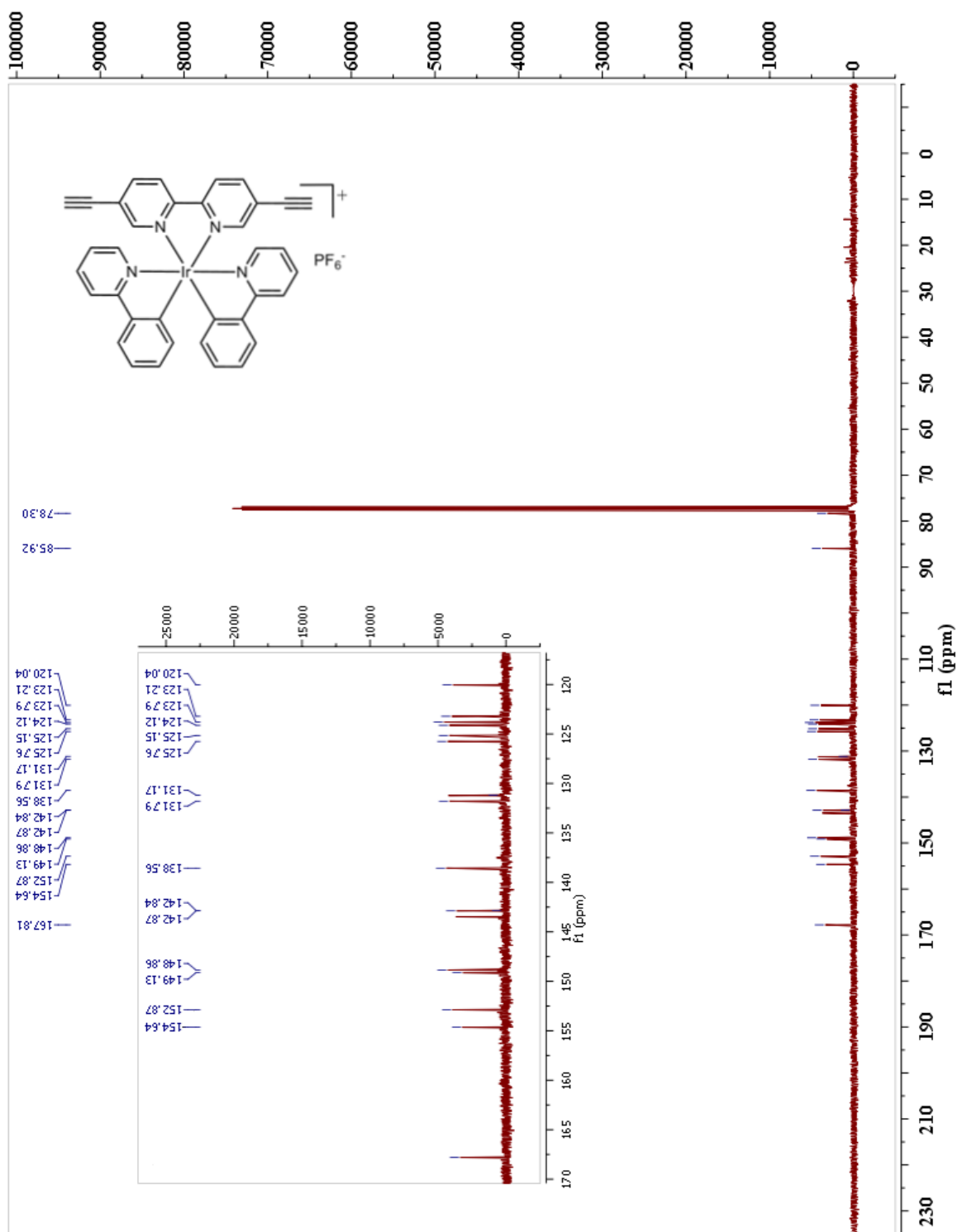
***trans*-4-Tolyethynyl-chloro-bis(tri-*n*-butylphosphine)platinum (23) :**



**[Ir(ppy)<sub>2</sub>(5-Ethynyl-2,2'-bipyridine)] Hexafluorophosphate (30):**

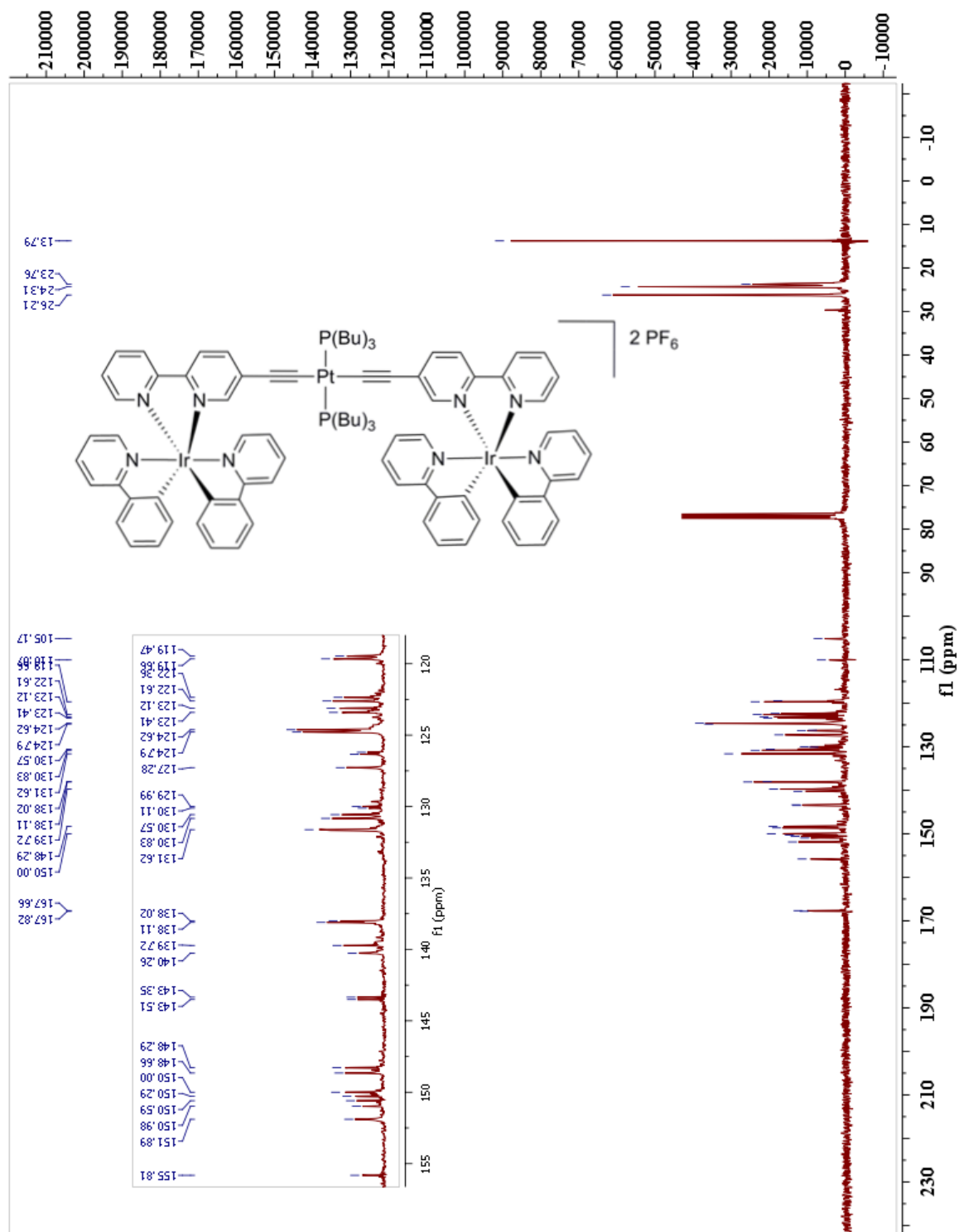


**[Ir(ppy)<sub>2</sub>(5,5'-Ethynyl-2,2'-bipyridine)] Hexafluorophosphate (31):**

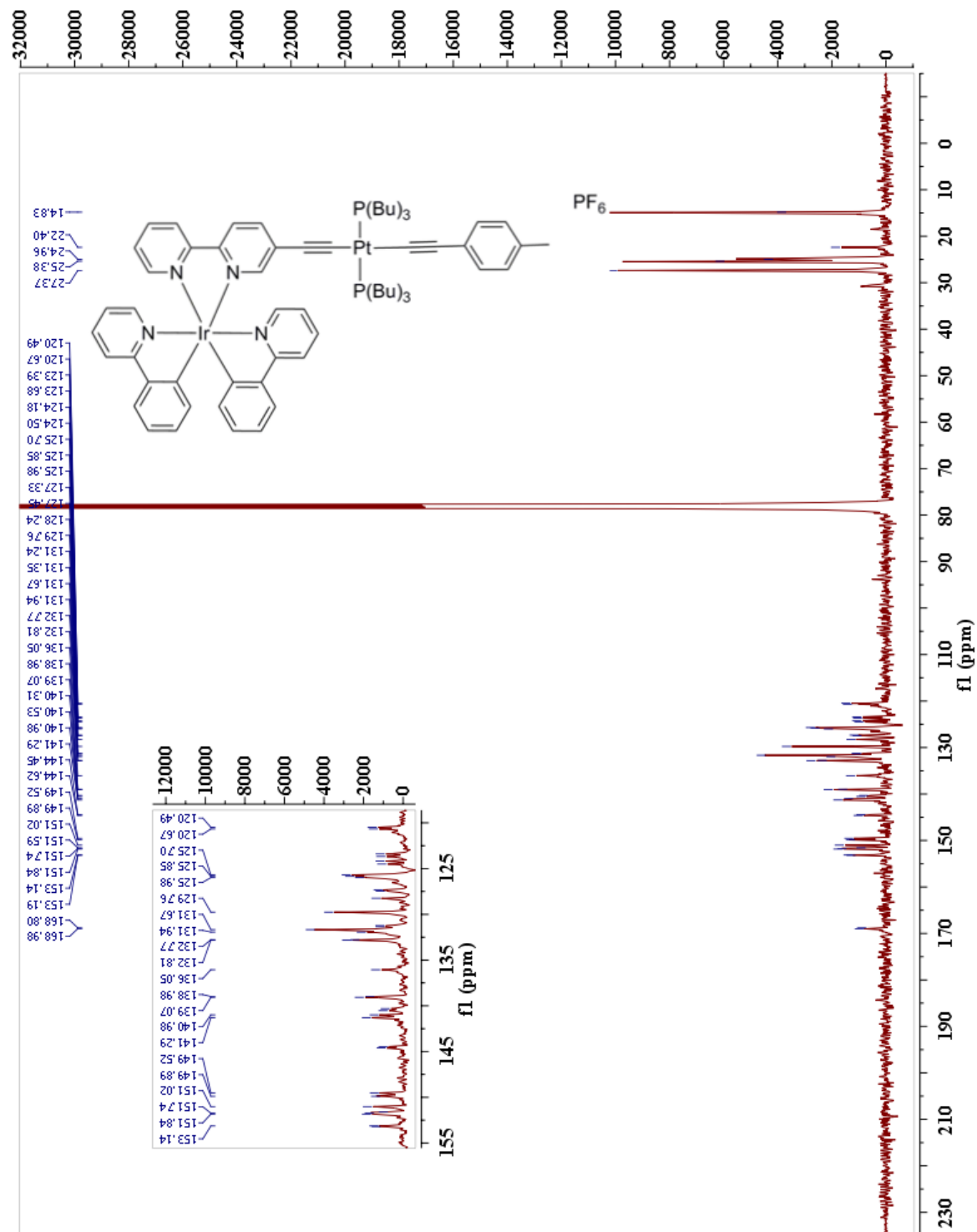




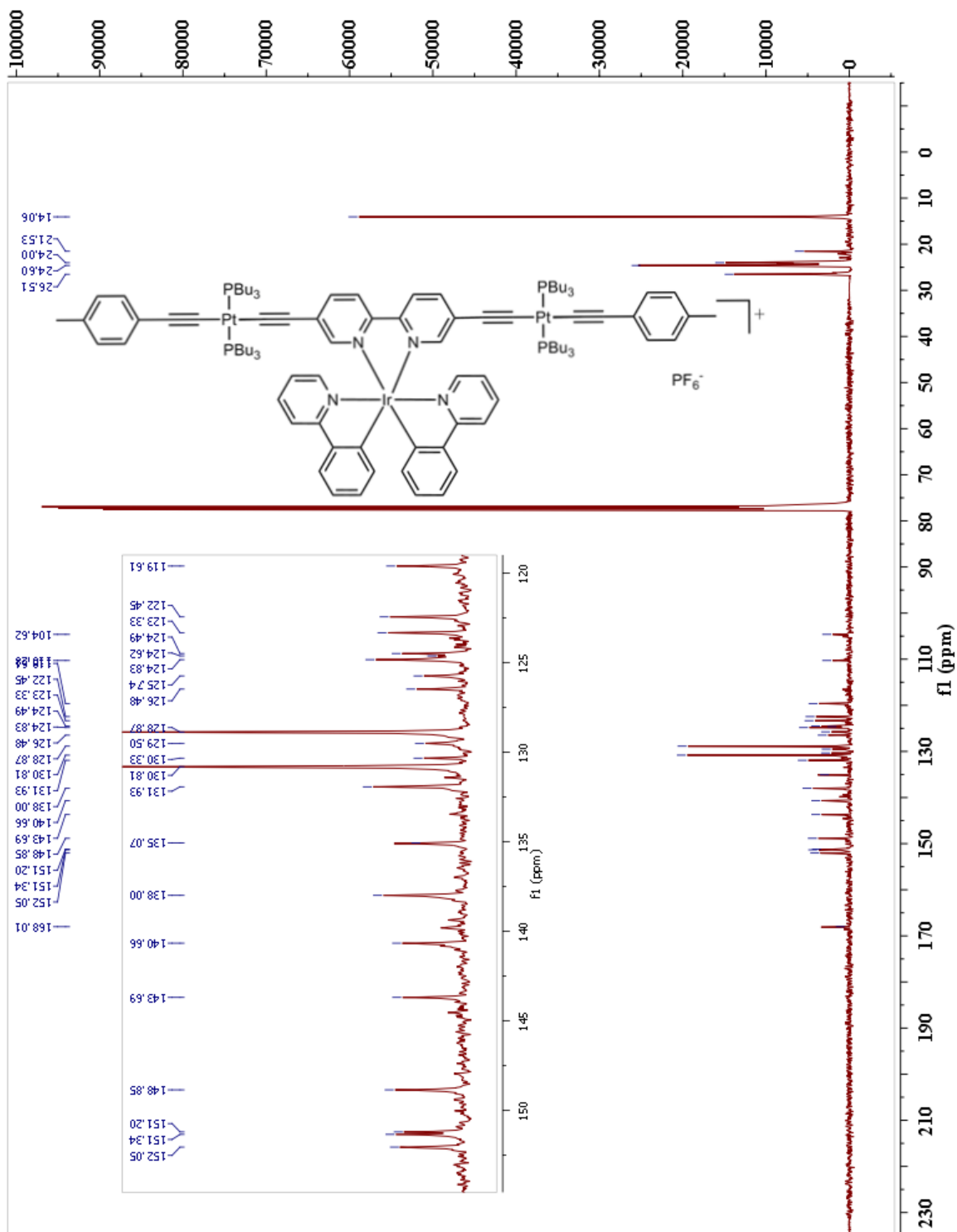
***trans*-Bis[Ir(ppy)<sub>2</sub>(5-ethynyl-2,2'-bipyridine)]-bis(tri-*n*-butylphosphine)platinum  
Hexafluorophosphate (32):**



***trans*-[Ir(ppy)<sub>2</sub>(5-Ethynyl-2,2'-bipyridine)]-4-tolylethynyl-bis(tri-*n*-butylphosphine)platinum  
Hexafluorophosphate (33):**

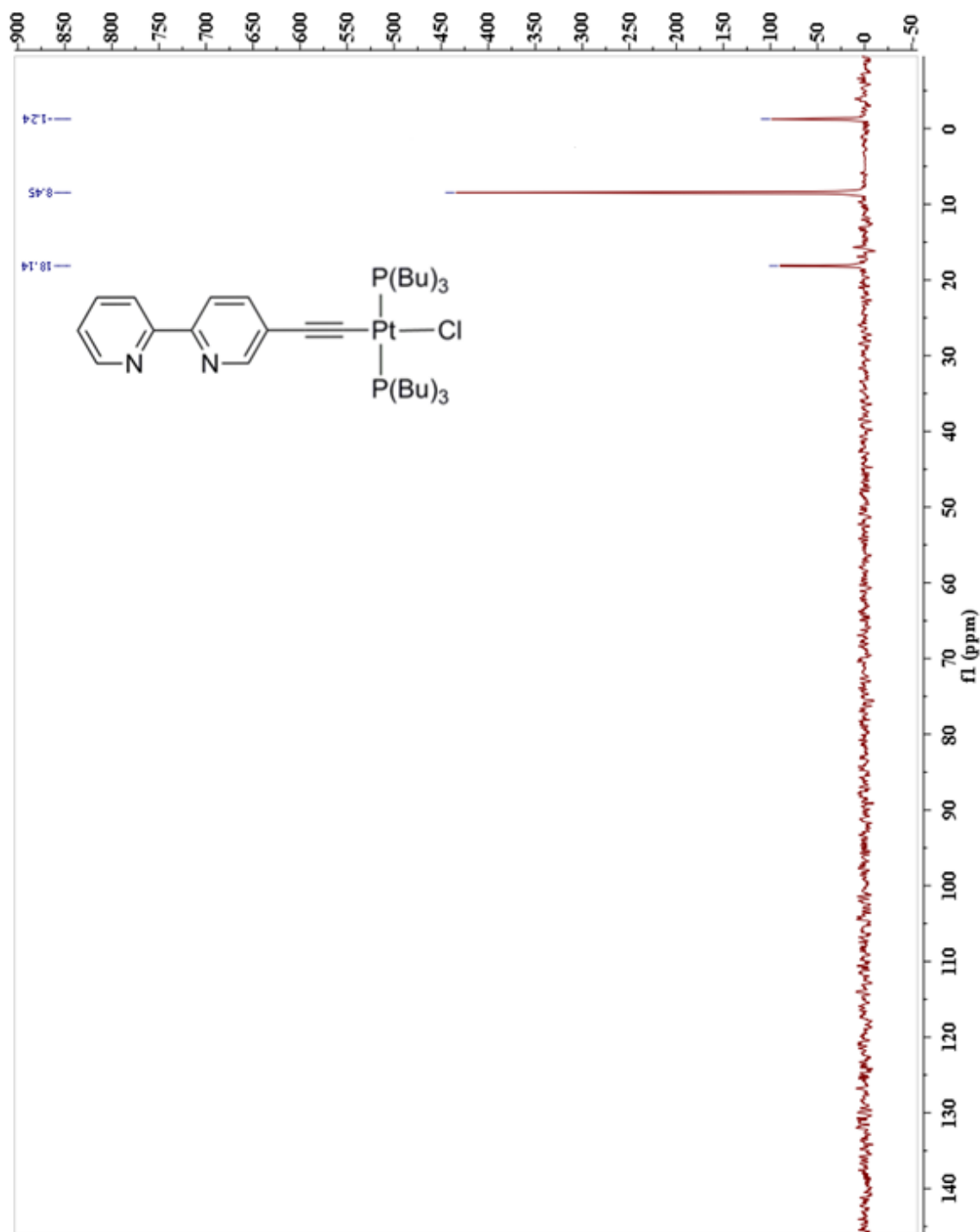


***trans*-[Ir(ppy)<sub>2</sub>(5,5'-Ethynyl-2,2'-bipyridine)]-bis(4-tolylethynyl-bis(tri-*n*-butylphosphine)platinum) Hexafluorophosphate (34):**

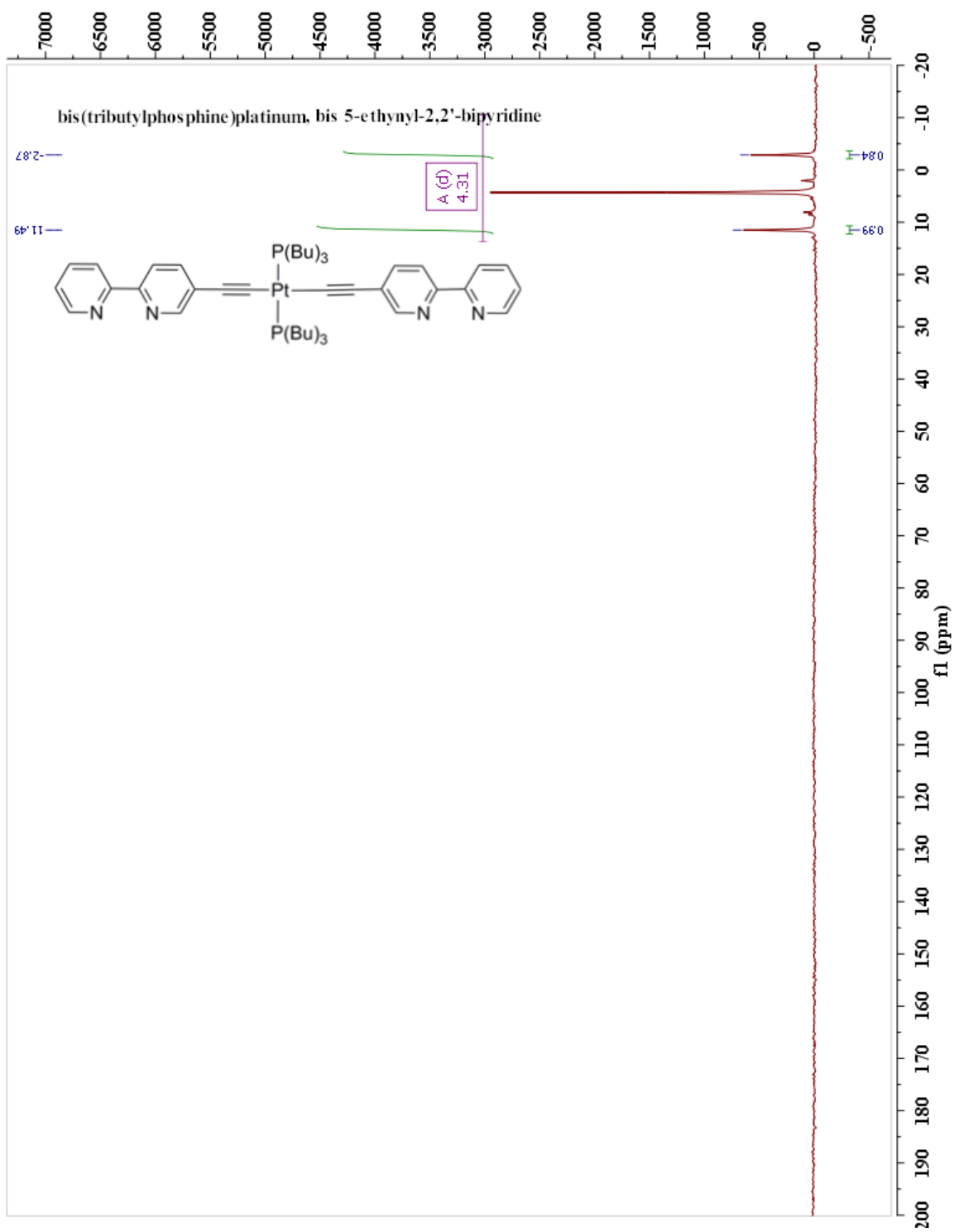


### ANNEX 3: SPECTRA OF NUCLEAR MAGNETIC RESONANCE OF PHOSPHORE.

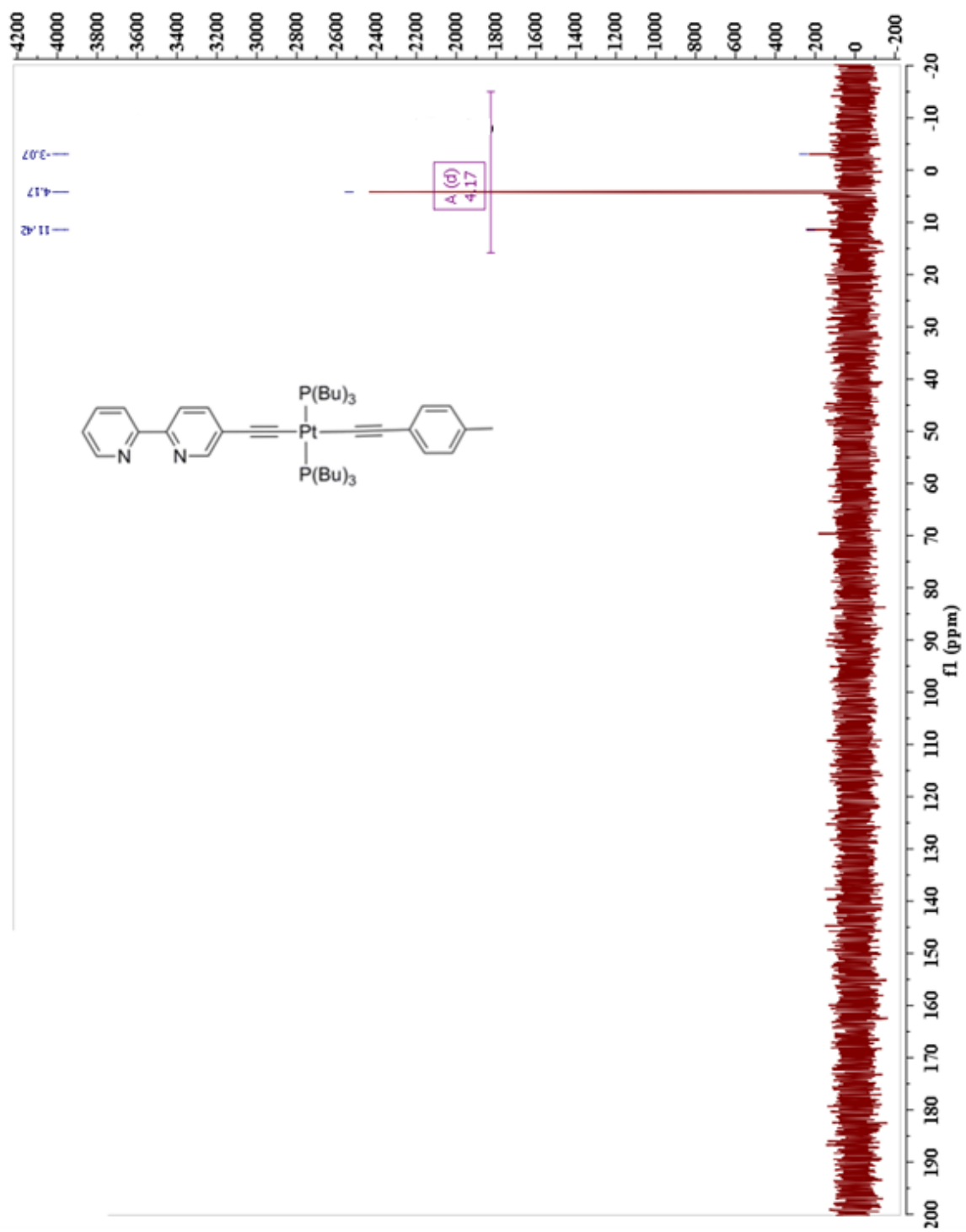
#### *trans*-(5-Ethynyl-2,2'-bipyridine)-chloro-bis(tri-*n*-butylphosphine)platinum (15):



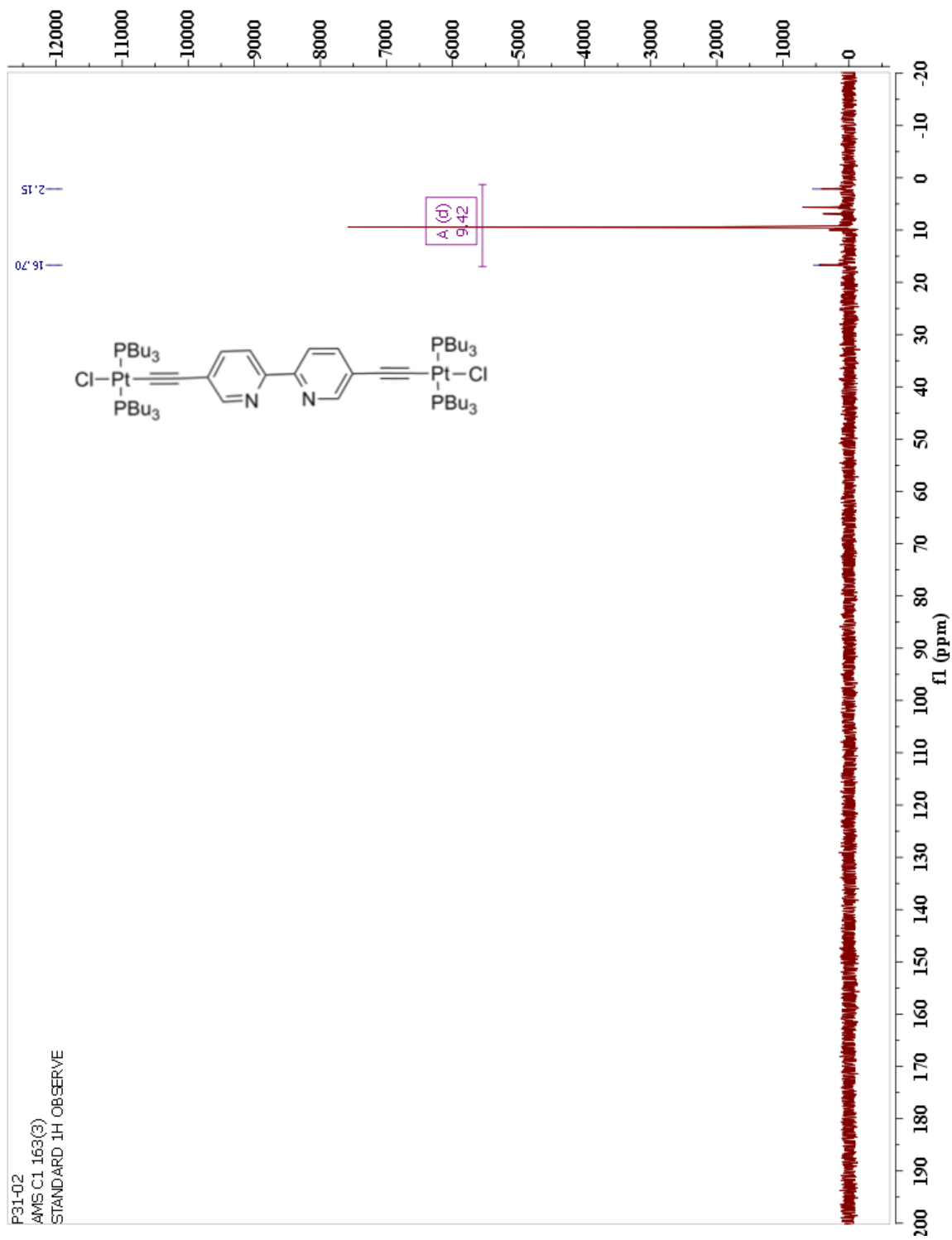
***trans*-Bis(tri-*n*-butylphosphine)-bis(5-ethynyl-2,2'-bipyridine)platinum (16):**



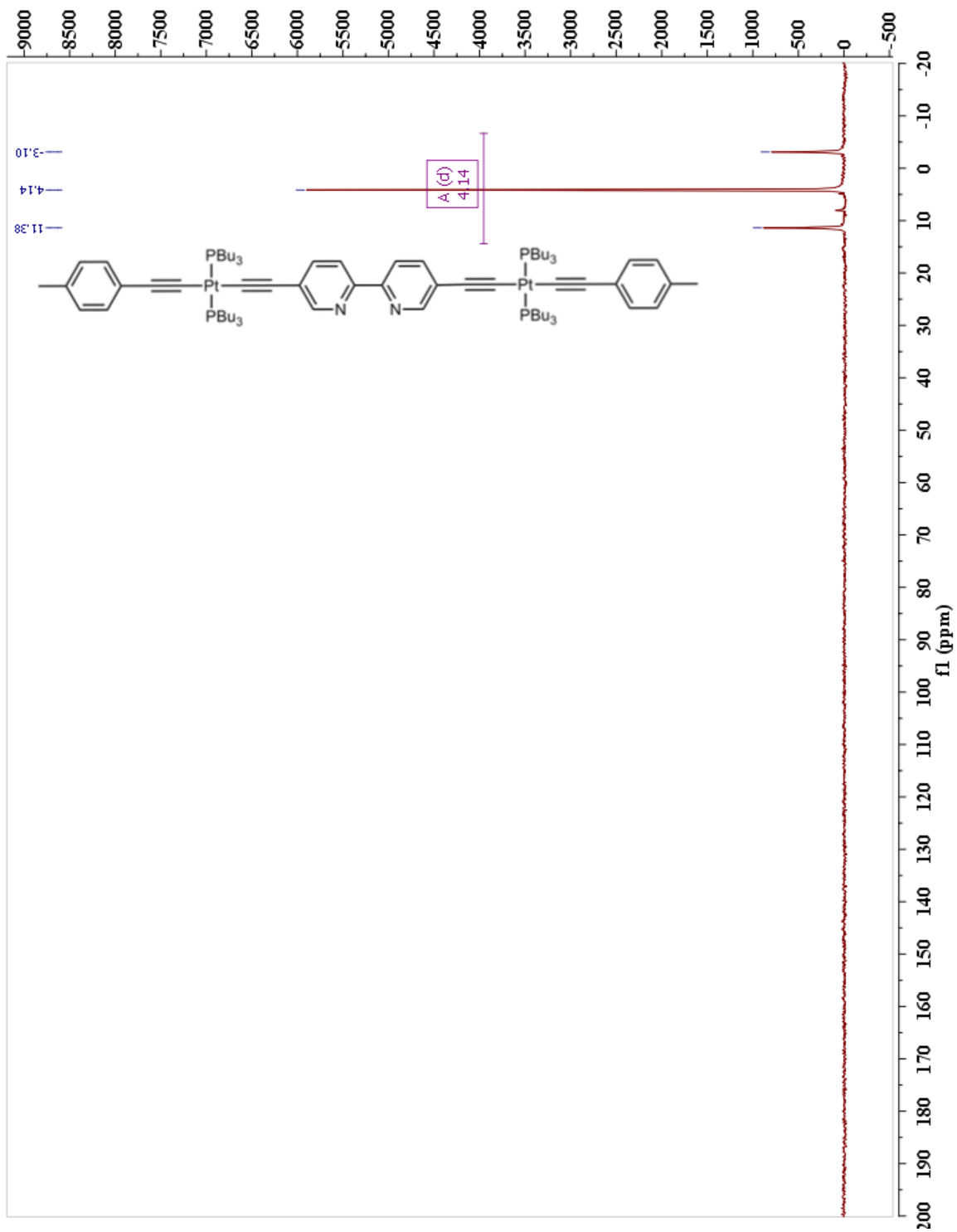
***trans*-(5-Ethynyl-2,2'-bipyridine)-4-tolyethynyl-bis(tri-*n*-butylphosphine)platinum (20):**



***trans*-(5,5'-Ethynyl-2,2'-bipyridine)-dichloro-bis(tri-*n*-butylphosphine)platinum (21):**

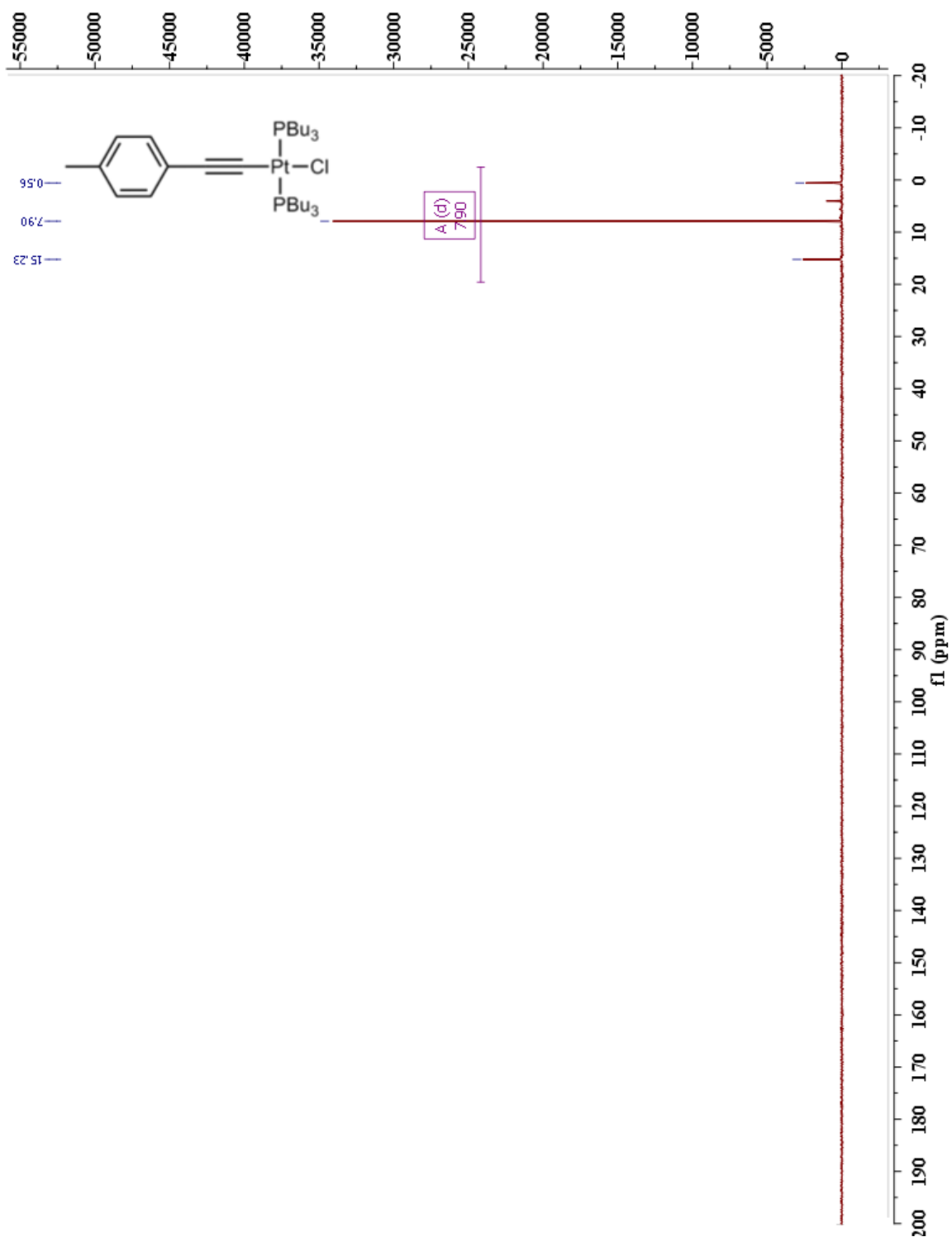


***trans*-(5,5'-Ethynyl-2,2'-bipyridine)-bis(4-tolylethynyl-bis(tri-*n*-butylphosphine)platinum) (22):**

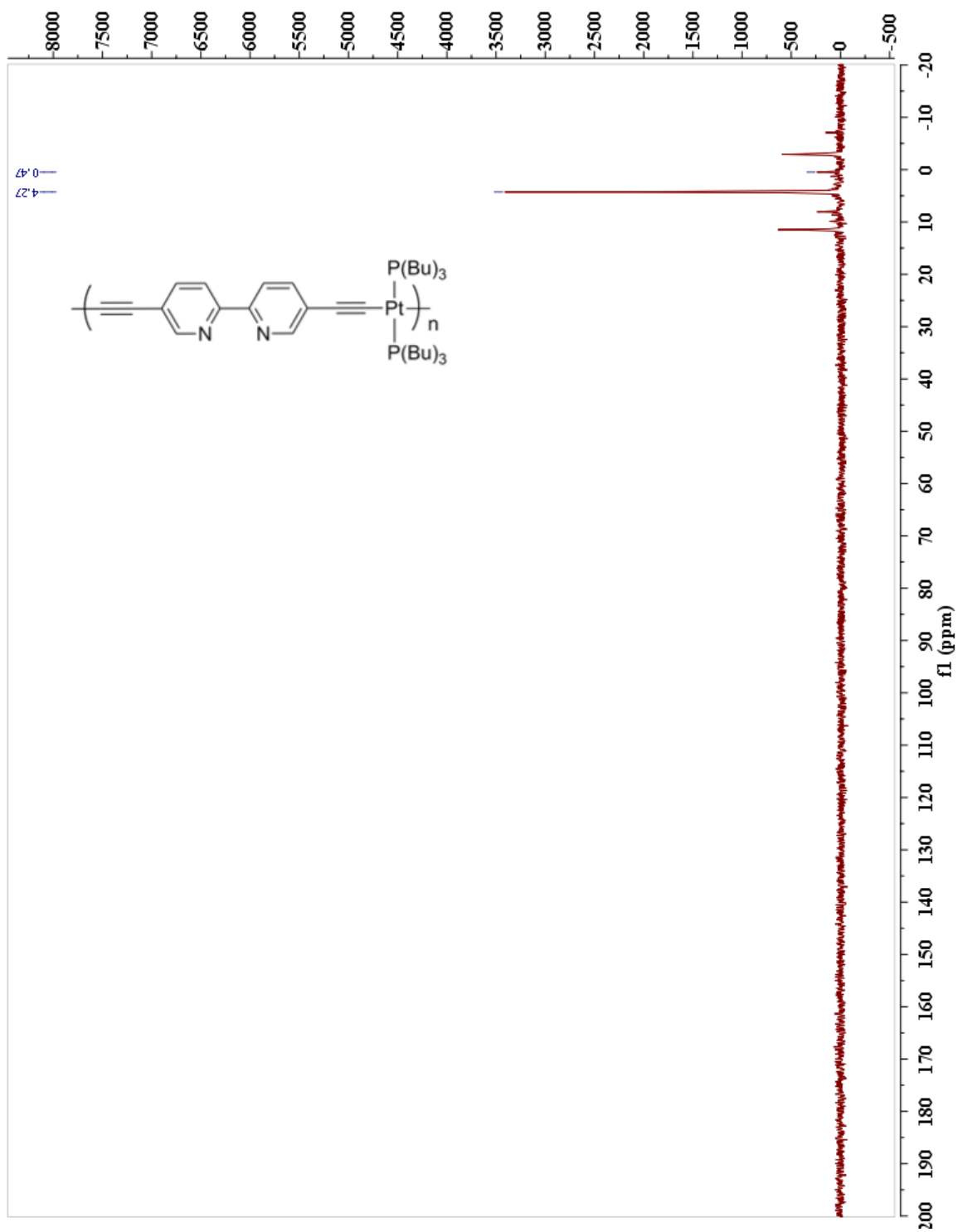




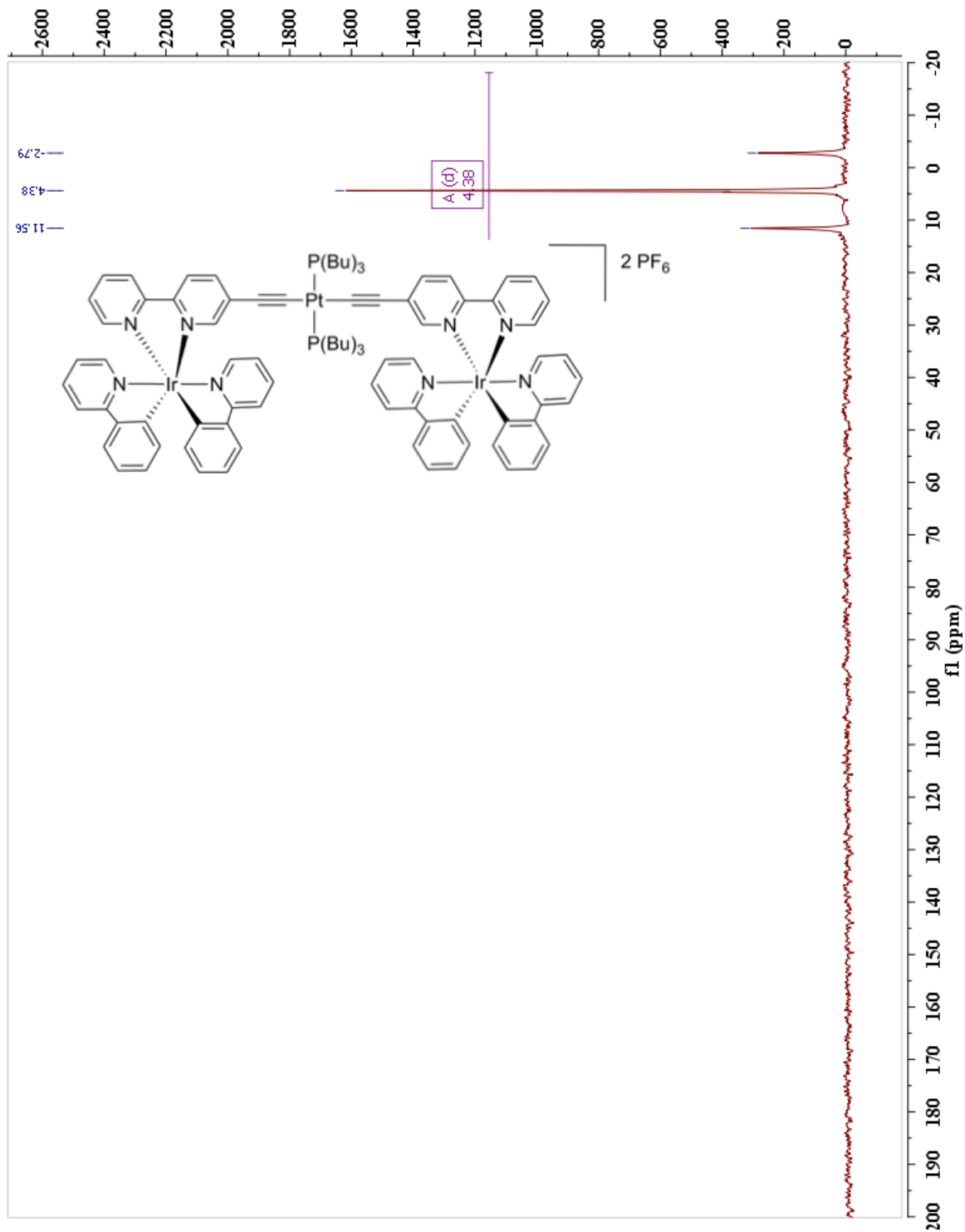
***trans*-4-Tolylethynyl-chloro-bis(tri-*n*-butylphosphine)platinum (23) :**



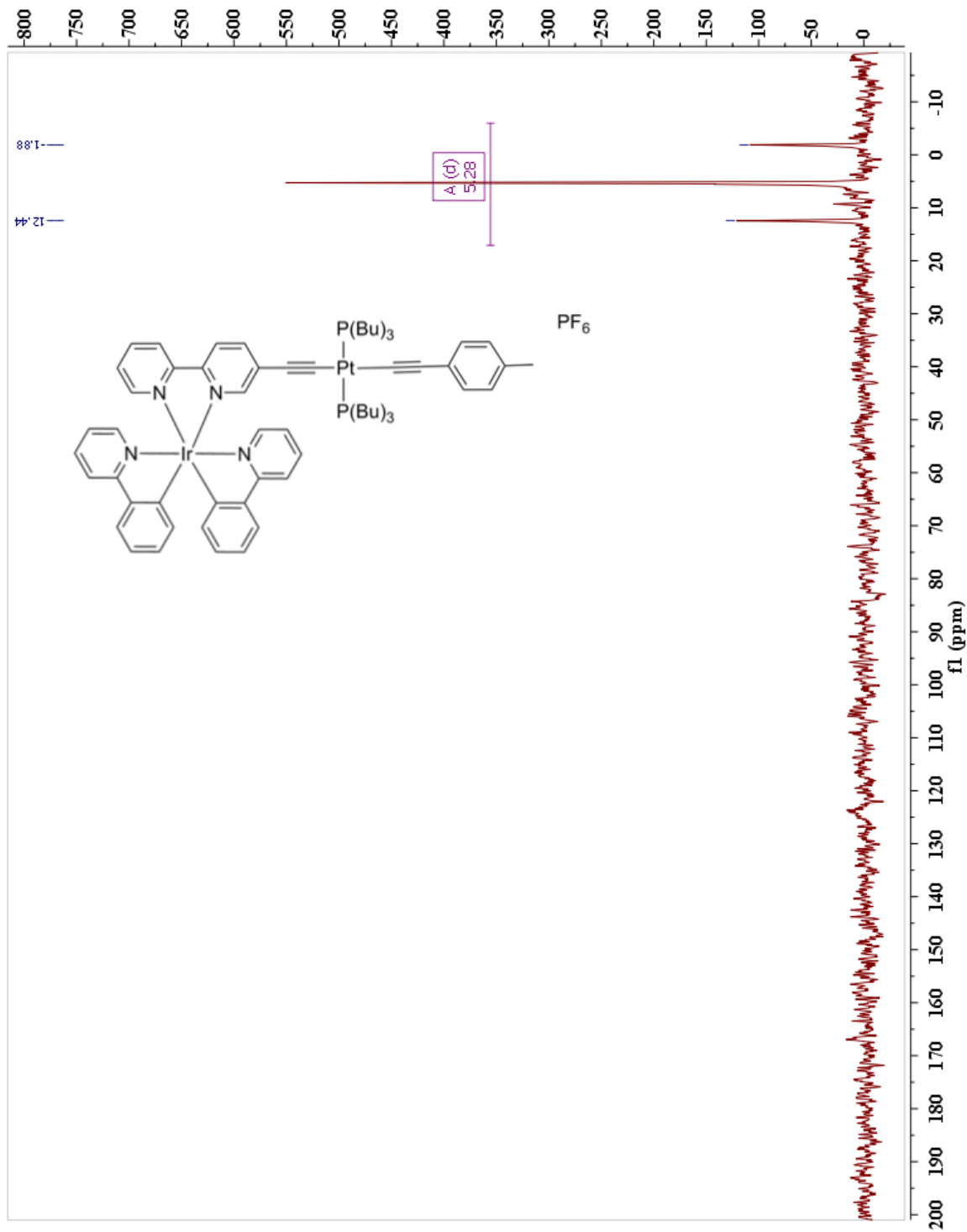
**Pt-Polymer (24):**



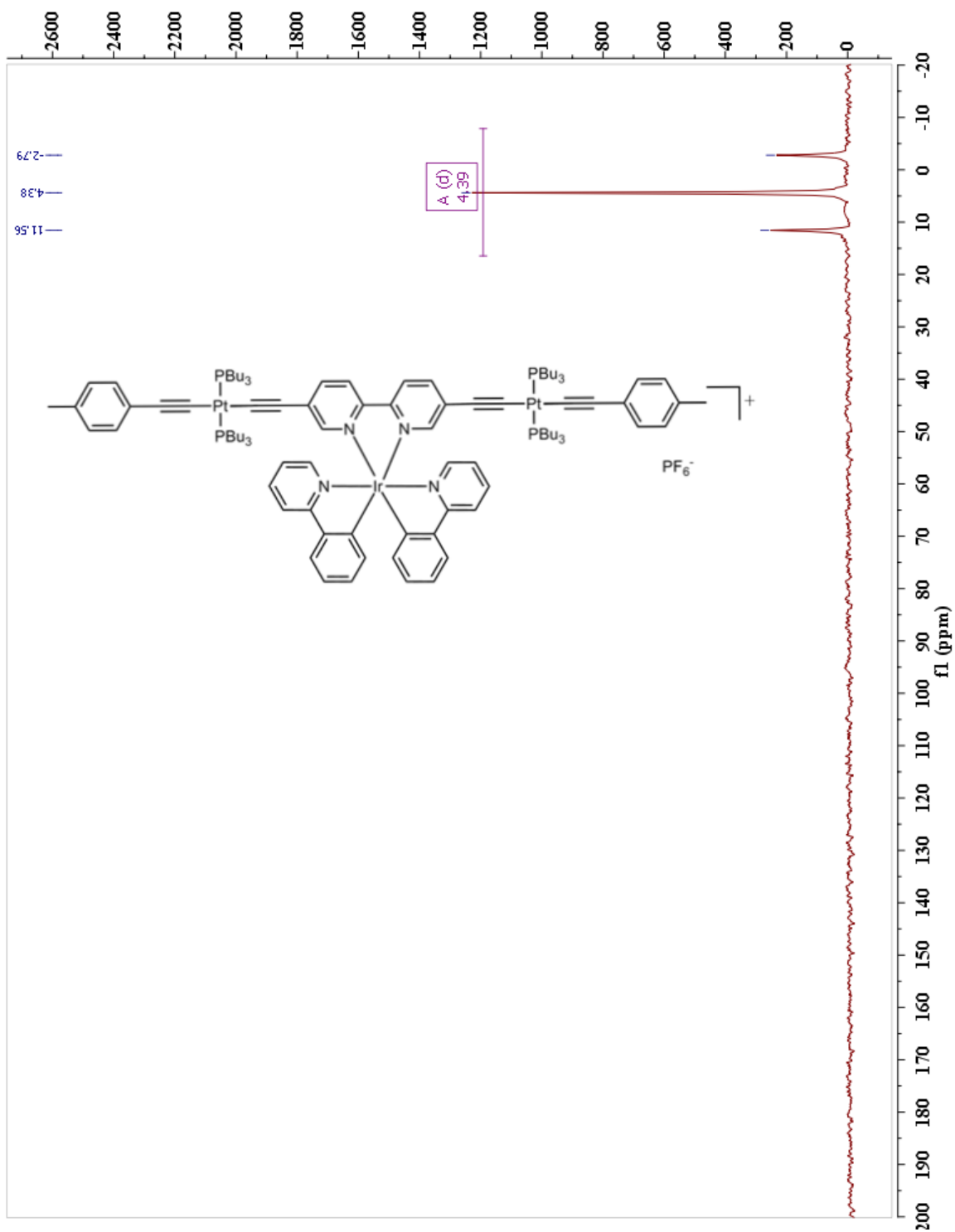
***trans*-Bis[Ir(ppy)<sub>2</sub>(5-ethynyl-2,2'-bipyridine)]-bis(tri-*n*-butylphosphine)platinum  
Hexafluorophosphate (32):**



***trans*-[Ir(ppy)<sub>2</sub>(5-Ethynyl-2,2'-bipyridine)]-4-tolylethynyl-bis(tri-*n*-butylphosphine)platinum  
Hexafluorophosphate (33):**



***trans*-[Ir(ppy)<sub>2</sub>(5,5'-Ethynyl-2,2'-bipyridine)]-bis(4-tolylethynyl-bis(tri-*n*-butylphosphine)platinum) Hexafluorophosphate (34):**



# Pt-Ir Polymer (36):

